The Mechanical Properties of a Three-Dimensional Stochastic Fibrous Network with Cross-linking

by

YANHUI MA

A thesis submitted in partial fulfilment for the degree of

Doctor of Philosophy

Cardiff School of Engineering

Cardiff University

2016

DECLARATION

This work has not been submitted in substance for any other degree or award at this or any other university or place of learning, nor is being submitted concurrently in candidature for any degree or other award.

Signed …… (Yanhui Ma) Date ……

STATEMENT 1

This thesis is being submitted in partial fulfillment of the requirements for the degree of ……(insert MCh, MD, MPhil, PhD etc, as appropriate)

Signed …… (Yanhui Ma) Date ……

STATEMENT 2

This thesis is the result of my own independent work/investigation, except where otherwise stated.
Other sources are acknowledged by explicit references. The views expressed are my own.

Signed …… (Yanhui Ma) Date ……

STATEMENT 3

I hereby give consent for my thesis, if accepted, to be available for photocopying and for inter-library loan, and for the title and summary to be made available to outside organisations.

Signed …… (Yanhui Ma) Date ……

I dedicate this to my parents, my family and my friends who have always lovingly supported me.

Acknowledgements

First I would like to express a great deal of gratitude to my supervisors, Dr. Hanxing Zhu, and Dr. Richard Perks for giving me this opportunity to carry out this research. A great deal of thanks is owed to Dr. Hanxing Zhu for his patient guidance about how to build up the geometrical models, treat the cross-linkers, identify the dominant deformation mechanisms, extract useful results, and prepare the dissertation and research papers, and for his continued encouragement over the course of my postgraduate study. I am greatly inspired by Dr. Zhu's attitude to novelty and high quality of research.

I would like to thank Prof. David Kennedy who has been internal examiner of my annual review for three years, for his advice on my research. I would also like to show appreciation to Dr. Shunqi Pan, Prof. Andrew Quantock and Dr. Rob Young for their support and kind help- I think if they had not appeared in my life, I would not have found that doing research is fun, and be choosing to stay in academia after my PhD. I would like to thank Prof. Gengkai Hu and Prof. Xiaoning Liu from Beijing Institute of Technology for recommending me to study in Cardiff and providing the help at the beginning of my PhD. I would also like to express my gratitude for an award from the PGR International Experience Fund which provided me with the opportunity to study in Prof. Peter Pinsky's lab in Stanford University as a Visiting Student Researcher for one month. I would like to thank Prof. Pinsky for his valuable guidance.

I would like to thank my friends and colleagues for their company, thank my training partners in Badminton Club for making me strong physically. I also would like to thank all the administration staff in the Research office for their kind help.

I am thankful to China Scholarship Council and Cardiff University School of Engineering for the sponsorship which allowed me to conduct this research.

Finally, I would like to thank my family for always supporting and encouraging me throughout the course of my education. In particular I owe my deepest gratitude to my loving parents, who always think that their daughter is the best. Mum and Dad, I love you so much!

Abstract

Fibrous materials are promising for a wide range of engineering applications due to their low density and high stiffness and strength. Stochastic filamentous networks can be widely found in biomaterials at the micro- and nano-scales. The objective of this study is to investigate the mechanical properties of macro-sized, micro-sized and nano-sized stochastic fibrous networks with cross-linking.

A continuum mechanics-based three-dimensional periodic beam model has been developed to describe stochastic fibrous materials by the Finite Element Method (FEM). Relative density is a key parameter to elucidate the mechanical properties of porous fibrous materials. The relative density of the beam model developed in this study can be adjusted by changing the concentration of the cross-linker, the fibre aspect ratio and the coefficient of overlap. In general, the non-dimensional Young's moduli and shear moduli increase with increasing relative density. The simulation and analytical model have suggested that strut bending is the dominant deformation mechanism for stochastic fibrous materials.

Based on the total strain energy density, scalar measures of characteristic stress and strain have been applied to reveal the yielding of stochastic fibrous materials. The effect of relative density on uniaxial yield strength of stochastic fibrous materials shows a quadratic function in the x direction and a cubic function in the z direction.

When the dimensions of fibrous structures are reduced to the micro- or nano-scale, the stiffness is much different from that of their macro-sized counterparts. Strain gradient effects at the micro-meter scale, and the surface elasticity and initial stress effects at the nano-meter scale have been incorporated into the deformation mechanism of fibrous materials. For both of the micro- and nano-sized fibrous structure, the smaller the diameter, the larger the non-dimensional Young's moduli and shear moduli. Generally speaking, the dimensionless stiffness of nano-sized stochastic fibrous structures is larger than their micro-sized counterparts. The size-dependent effects investigated in this study could provide good reference points for scientists in tissue engineering and serve as a guide in the design of MEMS and NEMS.

Contents

List of Figures

List of Tables

List of abbreviations

ECM	Extra-cellular matrix
CSK	Cytoskeleton
FEM	Finite element method
MFSS	Metal fibre sintered sheets
CAMBOSS	Cambridge bonded steel sheets
CAMBRASS	Cambridge brazed steel sheets
FEA	Finite element analysis
RVE	Representative volume element
MSC	Mesenchymal stem cells
MEMS	Micro-electro-mechanical systems
NEMS	Nano-electro-mechanical systems

Nomenclature

A	Area of cross section
b	Magnitude of the Burger's vector
C_{ijkl}	Components of fourth-order stiffness tensor
c	Overlap coefficient
D	Indention size
D_b	Bending rigidity
D_t	Torsion rigidity
D_c	Axial stretching or compression rigidity
d	Diameter of fibre
d'	Diameter of inserted beam
d_1, d_2	Diameters of three-section inserted beam
d_e	Equivalent diameter
E	Young's modulus
E^*	Calibrated Young's modulus
E_1, E_3	Young's modulus in the x and z directions
E_s	Young's modulus of solid material
E_t	Tangent modulus after yielding
E_e	Equivalent Young's modulus
F_r	Reaction force
$F_A, F_A,$	Force
F_s, F_t	Force calculated from simulation and theory
f	Surface stress
f_{ij}	Components of the surface stress tensor
f_{ij}^0	Components of initial surface stress tensor
G	Shear modulus
G_{12}	In-plane shear modulus
G_{13}	Shear modulus in the x-z plane
H	Hardness
I	Second moment of area
I_P	Polar second moment of area

K	Bulk modulus
k	Fibre concentration factor
L	Length of fibre
L_0	Original length of fibre
$L_A, L_{A'}$	Couple of force
l_{in}	Intrinsic length scale
l_m	Material intrinsic length at micro-meter scale
l_n	Material intrinsic length at nano-meter scale
l_c	Mean distance between any two intersection points
M	Bending moment
N	Number of fibres in stochastic fibrous materials
N_c	Concentration of cross-linker
P	Concentrated load
Q	Shearing force
S	Surface elastic constant
S_{ijkl}	Components of the surface elastic modulus tensor
T	Torsional moment
t	Thickness
W	Total elastic strain energy density
$\overline{W}$	Normalized strain energy density
$\widehat{W}$	Homogenized strain energy density
W_h, W_d	Hydrostatic and deviatoric energy density
$\boldsymbol{X_A}, \boldsymbol{X_B}$	Position vectors of particle A and B
X_{11}, X_{33}	Yield strain in the x and z directions
Y_{11}, Y_{33}	Yield strength in the x and z directions
x_c, y_c	Centre point of fibre
x_0, y_0	Original coordinates
ρ	Relative density
$u_{i1}^{ref}, u_{i2}^{ref}$	Translational displacement of the reference node chosen on opposite edges
u_{i1}, u_{i2}	Translational displacement of all the other nodes but the reference nodes
θ	Orientation of fibre

θ_{i1}, θ_{i2}	Rotational displacement of all the nodes chose on opposite edges of the mesh
$\boldsymbol{\varepsilon}$	Strain tensor
ε_{kl}	Components of surface strain tensor
ε_0^L	Initial strain
σ_s	Yield strength of solid material
σ_{ij}	Components of stress tensor
σ_e, ε_e	Effective stress and strain
σ_m, ε_v	Mean stress and volumetric strain
$\hat{\sigma}, \hat{\varepsilon}$	Characteristic stress and strain
ν_s	Poisson's ratio of solid material
ν_e	Equivalent Poisson's ratio
ν_{12}, ν_{21}	In-plane Poisson's ratio
ν_{13}, ν_{31}	Out-of-plane Poisson's ratio
$\boldsymbol{\chi}$	Symmetric curvature tensor
ρ_S	Density of statistically stored dislocation
ρ_G	Density of geometrically necessary dislocation
ζ	Strain scalar measure
γ	plastic shear strain
λ	Local length scale of the deformation field
δ_{ij}	Kronecker delta
δ	Length of inserted beam
τ_{12}	Shear stress in the x-y plane
$\Delta_x, \Delta_y, \Delta_z$	Deflection in the x, y and z directions

Chapter 1 Introduction

1.1 Research background and objectives

Porous materials with attractive thermal, acoustic, electrical and mechanical properties provide a wide range of engineering applications. Cellular materials like foam and honeycomb have been extensively studied[1–6]. Fibrous materials are another type of porous material with low density and high stiffness and strength; however, limited research has been carried out especially on simulation and analytical models.

Porous fibrous materials consisting of a metallic fibre network can be used as the core of sandwich panels. An understanding of the elasto-plastic behaviour of fibrous materials is important in order to fulfil structural applications. Stochastic filamentous networks can be widely found in biomaterials at the micron- and nano-scales. For instance, a typical extra-cellular matrix (ECM) is composed of structural protein nanofibres such as collagen with a diameter in the order of micrometers[7]. The cytoskeleton (CSK) is a network of filamentous proteins within a cell's cytoplasm, composed of filamentous actin (F-actin), microtubules and intermediate filaments with diameters in the order of nanometers[8]. The elasticity of a cell is governed by the cytoskeleton. It is crucial to build quantitative mechanical models describing the complicated behaviour of the cytoskeleton and predicting the effects of the filamentous network parameters, such as, the number of cross-linkers, the density of filaments on the elasticity. To the best of our knowledge, however, the three-dimensional model of the stochastic fibrous network with cross-linkers taken into account has never been reported.

To analyse the mechanical properties of stochastic fibrous materials, some conventional theories may not apply to materials with a dimension at the micro- or nano-scale. In general, the strain gradient effect plays a dominant role in deformation at the micro-meter scale. At the nano-meter scale, surface elasticity and initial strain (stress) effects are of great importance in the mechanical behaviour. It is important to investigate the size-dependent and tunable mechanical properties of micro- and nano-sized stochastic fibrous structures.

The key objectives and contributions of this research work are composed of four parts which are presented in four different chapters (Chapter3-6). They are:

1. Develop a continuum mechanics-based three-dimensional periodic beam model to describe the stochastic fibrous materials by the Finite Element Method(FEM). Investigate the geometrical properties of a three-dimensional random beam model in which all the parameters can be adjusted, for example, the diameter, the length, the orientation, the concentration of cross-linkers, overlap coefficient, among others.
2. Delineate how the key features in the anisotropic structure affect its stiffness. Investigate the role of a cross-linker and how the relative density affects the elastic properties of the stochastic filamentous network. The beam model developed in this study is proved to be transversely isotropic, thus there are five independent elastic constants investigated.
3. Delineate how the key features in the anisotropic structure affect its strength. Characteristic stress and strain derived from strain energy density have been applied to reveal the yielding of fibrous materials. Develop analytical models together with the FE simulation to reveal the relationship between the yield strength and relative density of the stochastic fibrous structure.

4. Investigate the size-dependent and tunable rigidities of stochastic fibrous materials. The effects of strain gradient at the micro-meter scale and the effects of surface elasticity and initial stresses/strains are incorporated into all the deformation mechanisms in the analysis of stochastic fibrous structures.

1.2 **Thesis organisation**

This thesis is organised as follows: Chapter 2 presents a literature review of past studies. It describes the applications of porous fibrous materials in engineering and the methods to investigate their mechanical properties. Also, it introduces strain gradient effects at the micro-scale and the surface effects at the nano-scale. Chapter 3 describes the three-dimensional periodic beam model which is used to represent the stochastic fibrous network with cross-linking. By using the random beam model, the elasticity of the cytoskeletal network composed of filamentous materials is investigated in Chapter 4. Chapter 5 reveals the dependence of yielding strength on the relative density of the stochastic structure. It shows that the dimension of the inserted beam representing the cross-linker in the fibrous network plays an important role in the strength anisotropy. In Chapter 6, the size-dependent effects on the relationships between the relative density and the elastic constants of micro- and nano-sized fibrous structures are investigated. Finally, a brief summary of the work has been concluded in Chapter 7. In addition, it presents the research limitation followed by recommendations for future work.

Chapter 2 Literature Review

2.1 **Porous materials**

Porous materials have been of great interest to engineers and scientists due to the attractive thermal, acoustic, electrical and mechanical properties and the fact that porous materials provide a wide range of different engineering applications. Foam and honeycomb which can also be categorized as cellular materials have been extensively studied[1–6]. As Gibson and Ashby[4] described, the four major applications of cellular materials in engineering are thermal insulation, packaging, structural use and buoyancy attributed to thermal conductivity, high compressive strength and stiffness and low density. With the same attractive properties as cellular properties, porous fibrous materials are less researched and less understood in comparison because of their more complex geometry. Some techniques have been developed to produce fibrous materials, for instance, fibre pull-out techniques[9] for porous metal fibre sintered sheets(MFSSs)[10] which can be used as the core of sandwich panels; the electrospinning techniques[11] for polymer fibre scaffold applied in drug delivery and tissue engineering[12], among others. In addition, the cytoskeleton which governs many mechanical behaviours of the cell is a network of stochastic filamentous proteins[13]. A typical extra-cellular matrix (ECM) is composed of structural protein nanofibres such as collagen with a diameter in the order of micrometers[7]. The promising applications of stochastic fibrous networks as biomaterials in tissue engineering are elucidated in Section 2.3.

2.1.1 Cellular and fibrous materials

Porous (permeable) cellular and fibrous materials can be made from metals, polymers, ceramics and even composites depending on the properties required in industry. Apart from man-made engineering porous materials, they are abundant in nature, such as cancellous bone, wood, cork, sponge and sheep's wool. Generally speaking, cellular solids include honeycombs and foams. Gibson and Ashby[4] conducted a comprehensive study on the mechanical, thermal, electrical and acoustic properties of cellular solids. In the architecture of cellular materials, cells are distinct. A single idealized unit cell can be used to represent the microstructural features of cellular materials, e.g., 2D honeycombs in which the unit cells can be triangle, square or hexagon. Many micromechanical models of honeycomb and foams have been developed to investigate the macro mechanical behaviour of cellular materials[1–4, 6, 14–16]. By contrast, the architectures of fibrous materials are much more complicated especially for stochastic fibrous networks, e.g., felt, as it is very hard to find any individual cells in their architecture. Paper is a kind of stochastic fibrous material, which is, to some extent, the most familiar one to most of us. Randomly orientated fibres are recruited into the network by sintering, welding or adhesive bonding with other fibres. Thus for the fibrous materials, the joints are the intersections between two fibres, whereas a typical joint of open-cell foam is a solid anchor for three or more cell edges as shown in Figure2.1[17].

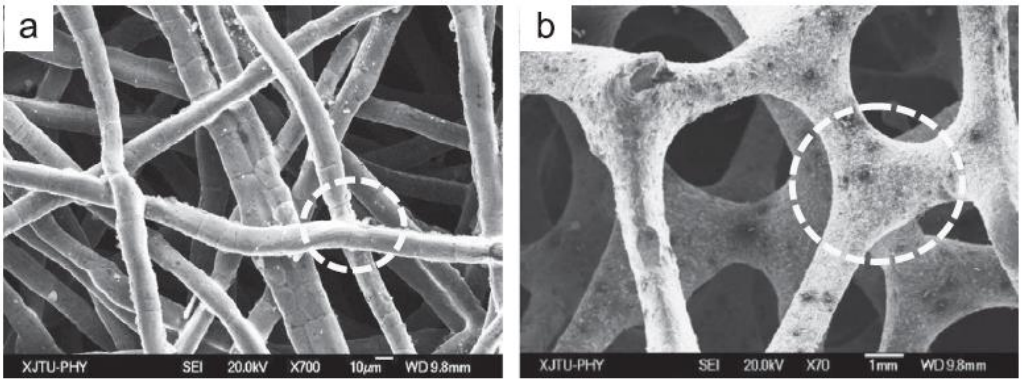

Figure 2.1. Comparison of the architectures of (a) a metal fibre network and (b) an open cell aluminium foam[17].

2.1.2 Metal fibre sintered sheets

Porous metal fibre sintered sheets(MFSSs) are a typical metal fibrous material with low density and high stiffness with potential for functional and structural applications. MFSSs are produced by overlapping the randomly distributed fibres by air-laid web-forming technology before compressing and sintering into a three-dimensional material with fibre network[9]. Experiments show that the MFSSs are transversely isotropic in the x-y plane (in-plane) which is perpendicular to the thickness direction (z-axis) as shown in Figure 2.2[17]. As MFSSs can be used as the core of sandwich structures, the stiffness and strength of MFSSs under shear are crucial. Shear tests based on a non-contact, optical, full-field deformation measurement system have been conducted to observe the shear response of MFSSs. It has been suggested that the in-plane shear modulus and strength are both linearly dependent upon the relative density (i.e., the ratio of the volume (mass) of the metal fibres to that of the fibrous structure) of MFSSs, while the transverse shear modulus and strength have quartic and cubic dependence upon the relative density respectively[18]. The discrepancy between the shear response of in-plane and out-of-plane of MFSSs is believed to be resulted from

different dominant deformation mechanisms. The latter is fibre bending, whereas the former is fibre stretching/compression. Experimental results show that the in-plane shear modulus and yield strength are much larger than their out-of-plane counterparts. Nevertheless, the transverse yield strain is larger than the in-plane yield strain under shear[18]. The uniaxial tension and compression tests of MFSSs show that both the in-plane stiffness and yield strength are much higher than those in the transverse direction[17], which could be attributed to the architecture of MFSSs as it is a multi-layered structure as shown in Figure 2.2 and the sintering quality of fibre joints could be uneven. Moreover, Poisson's ratio in the thickness direction $\nu_{31} = \nu_{32}$ is close to 0, which implies that the transverse loading can hardly trigger any contraction or expansion in the x and y directions.

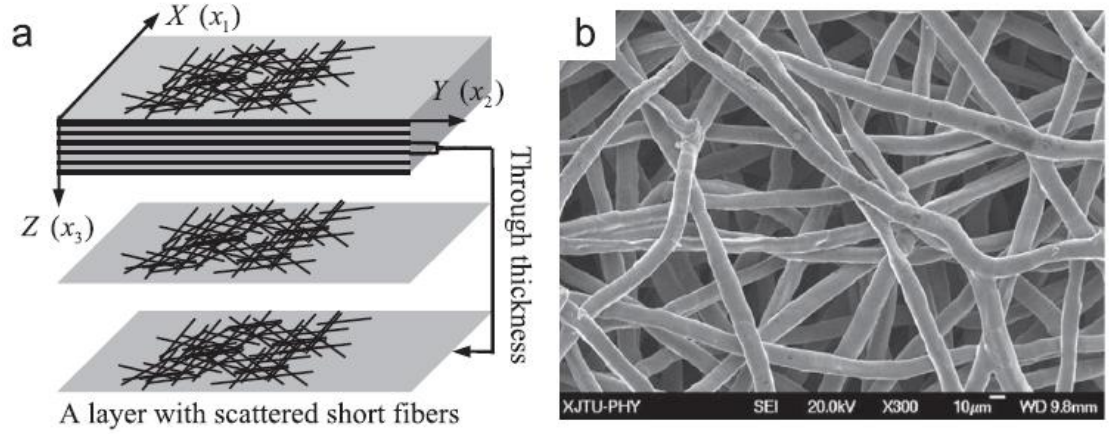

Figure 2.2. (a) Illustration of multi-layered structure of porous metal fibre sintered sheets(MFSSs) and (b)photography of MFSSs in the x-y plane[17].

2.1.3 The connectivity in the fibre network

The connectivity in the fibre network plays a significant role in the mechanical properties. It was found that the porous structure with high nodal connectivity is stretching dominated [10, 17]. In contrast, the deformation mode of the isotropic, two-

dimensional, perfect hexagonal honeycomb is a combination of stretching and bending, when the nodal connectivity is low[2, 19]. Jin *et al* developed a two-dimensional micromechanics random beam model to investigate the in-pane elasto-plastic behaviour of MFSSs[10]. In his model, all the fibres are completely overlapped with each other to form a two-dimensional stochastic fibre network, which leads to very strong bonding connection and high nodal connectivity between fibres. The simulation results showed that the in-plane Young's modulus and bulk modulus have a linear correlation with the relative density[10]. Gibson and Ashby [4] have suggested that a linear dependence of the modulus of a cellular solid upon its relative density implies the stretching dominated deformation mechanism.

Fibre network materials can be served as the core in the sandwich structures with high stiffness and low density, while keeping the thickness low. Markaki and Clyne [20, 21] have experimentally studied the mechanics of three variants of thin, ultra-light, stainless-steel, sandwich sheet material, two of which are Cambridge Bonded Steel Sheets (CAMBOSS) and Cambridge Brazed Steel Sheets (CAMBRASS). CAMBOSS and CAMBRASS share the same architecture and the only difference lies in the processing of connection between plates and metal fibre material. In CAMBOSS, fibres are connected by epoxy adhesive bonding, while the fibres in CAMBRASS are bonded by brazing at a temperature of 1000° for a period of about 5min. Experimental results showed that the stiffness of CAMBRASS is significantly higher than that of CAMBOSS[20]. It implies that the bonding quality or the strength of connection between fibres can greatly affect the stiffness of fibre network materials. Xi *et al* proposed that the mechanical properties of metal fibre porous materials are highly dependent upon the fibre-fibre joints and the number of metallurgy nodes[9]. The

mechanical properties are enhanced with increasing sintering contact points per unit volume and the bonding intensity.

The joint bonding quality can vary according to the method of preparation of the fibrous mat. The bonding can be done by welding, brazing, sintering or adhesive bonding. In Finite Element (FE) modelling, beams are mostly utilized to represent the fibres and the method of connection between beams is crucial. In the model of Jin *et al* [10], as all the fibres are overlapped into a two-dimensional network, the connection can be regarded as very rigid. Sastry and co-workers [21–23] proposed a technique for modelling fibre-fibre joints in which the connection realized by the torsion spring can be regarded as flexible. However, the mechanical properties of a fibrous network with flexible bonding were not given. The idea that the connectivity between fibres cannot be fully described by a single connection point in the beam modelling is very encouraging.

2.2 **Method to investigate stochastic fibrous materials**

The mechanical behaviour of porous fibrous materials can be investigated by tension/compression and shear tests. Experimental results of porous metal fibre sintered sheets (MFSSs) conducted by Zhao *et al*[18] suggest that the in-plane stiffness and strength are much higher than those in the out-of-plane direction, which is different with foam or honeycomb. Experiments showed that metal fibre porous materials show higher compressive strength than the aluminium foams[24]. Apart from the approaches of experimental tests, the properties of porous fibrous materials can be analysed by analytical models and the Finite Element Methods (FEM) based on the continuum solid mechanics.

2.2.1 Analytical framework

Some analytical models have been developed based on the assumption of affine deformation of the fibre network [25–28]. For a two-dimensional fibre network made of one single material, the Young's modulus can be expressed as[20]

$$E_c = \frac{3\rho tan^2\theta}{16s^2} E_f \tag{2.1}$$

where E_f is the Young's modulus of the constituent fibre material, θ is the inclined angle of the fibre, ρ is the relative density and s is the segment aspect ratio (L/d). It is assumed that for each fibre segment, one end is fixed and the other is free and applied by an external load W as shown in Figure 2.3 [20]. Also, it is assumed that all the fibres are inclined at the same angle and would behave similarly. On the basis of these assumptions, the Young's modulus of the fibre network derived from the beam bending theory is found to depend upon the inclination angle, relative density and the aspect ratio. This simple analytical model sheds light on the micromechanics of fibre network materials. However, in the real situation the boundary conditions are different, as most of the fibre segments would be embedded with each other at both ends. The orientation of fibres is random for stochastic fibrous materials. It has been suggested that structural randomness plays a significant role in the mechanical properties of fibre network materials [29]. The relationship between the in-plane Young's modulus and the relative density of the fibre network obtained from the analytical model mentioned above is consistent with the simulation results from Jin *et al* [10], based on the two-dimensional random beam model. The magneto-mechanical characteristics have been studied by an analytical model using ferromagnetic fibres under the influence of a magnetic field [26,30], in which a magnetic stiffness has been incorporated. In addition, by using the analytical method, the resistance of delamination of the thin,

ultra-light, stainless-steel sandwich sheet has been predicted [31] and the effect of the presence of a compliant matrix in the fibre network has been investigated [26].

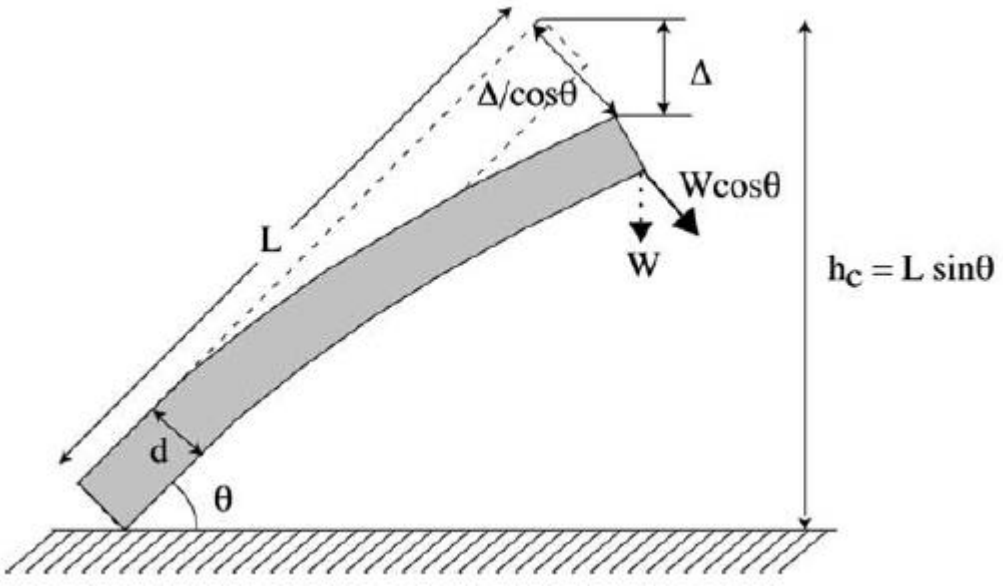

Figure 2.3. Illustration of the elastic bending of a fibre inclined at an angle θ and with an applied vertical load, W [20].

2.2.2 X-ray tomography

X-ray computed tomography is a technique to produce cross-sectional images from different angles, contributing to construction of 3-D architecture. With the development of the capability of digital image capture, X-ray computed tomography has become a very useful non-destructive tool in material science [32]. X-ray tomography has been utilized to extract the reliable architectural characteristics from the very complicated stochastic porous fibrous network and to reconstruct it [27, 29] as shown in Figure 2.4. Geometrical parameters, such as fibre orientation, segment length and distribution, and the number of intersections between fibres can be obtained from X-ray computed tomography. The structural details can be revealed by X-ray tomography; however, this technique is computationally challenging as it needs a

series of algorithms to extract the architectural parameter from the raw data. Also, it has suggested that the fibre network architectural characteristics are sensitive to the adopted algorithms of image processing, for instance, the segmentation method, thresholding, deconvolution, among others [29]. Finite element models are an attractive approach to construct the complex stochastic fibre network based on the basic geometrical parameters extracted from X-ray computed tomography.

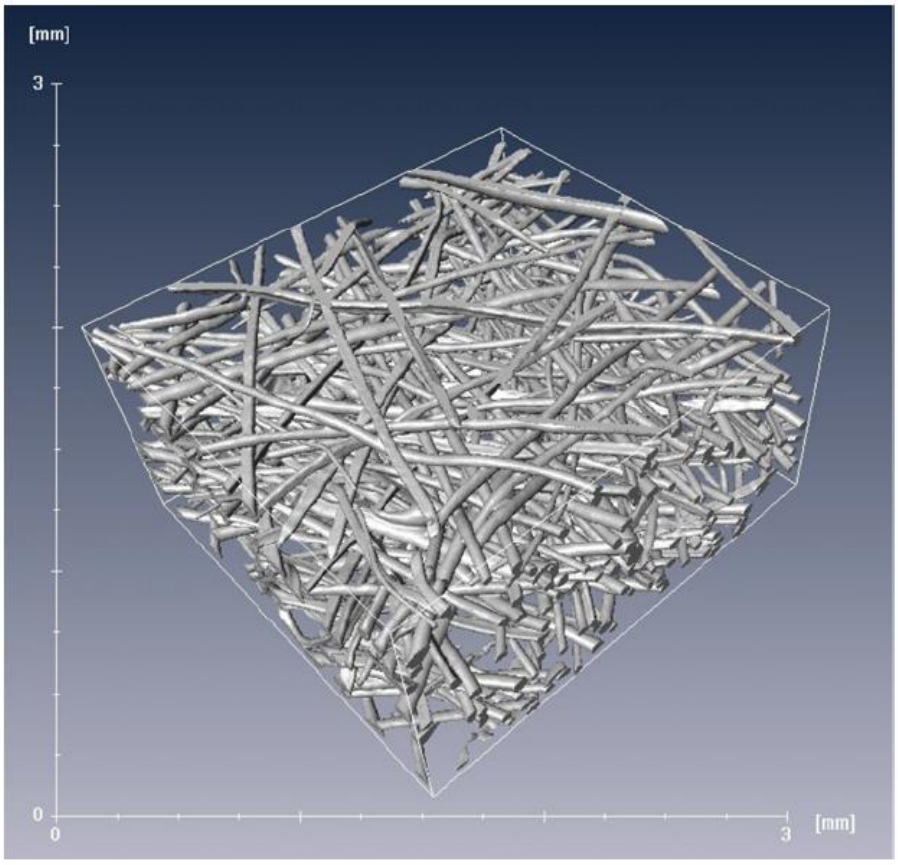

Figure 2.4. 3-D reconstruction from the X-ray computed tomography of stochastic fibrous materials [28].

2.2.3 Finite Element Method (FEM)

The finite element method (FEM), which was originally developed for solving solid mechanics problems, offers a means to probe the mechanical properties of intricate porous material. A two-dimensional random irregular honeycomb has been

constructed and the effect of the irregularity on the mechanical properties of honeycomb has been observed with Finite Element Analysis(FEA) [2, 33, 34]. Jin *et al* [10] developed a two-dimensional micromechanics random beam model to investigate the in-plane elasto-plastic behaviour of MFSSs. Finite element method has been employed to investigate the tensile and compressive behaviour of random fibrous materials [35, 36]. A comprehensive study on the modelling of stochastic fibrous materials by mathematical treatment, for instance, the probability and distribution can be found in reference[37], however, the connection between fibres was not taken into consideration. The connection between fibres is a very key feature in the structure, especially when dealing with mechanical behaviours of three-dimensional fibrous structures. A three-dimensional model of the fibrous structure made of three different materials with joint bonding taken into account has been constructed by Liu *et al* [35].

The relative density plays a significant role in the mechanical properties of porous materials[1–4, 10], in which the stiffness and strength can be adjusted over a wide range by changing the relative density. Gibson and Ashby have put forward that the simplest and most straightforward way to analyse the mechanical properties of cellular materials is to use dimensional analysis [4], and it points out the dependence of mechanical properties on the relative density of the structure. However, the relative density is difficult to control in the manufacturing process. With the assistance of the FEM it is easier and more convenient to control the relative density and other key parameters in the model. In addition, optimized design of complex porous materials can be realized by finite element method.

It is suggested that the macroscopic stresses and strains can be determined by the microscopic stresses and strains over a representative volume element (RVE). RVE [38] was proposed to reveal the full-scale model by a representative ‘cell unit’ to

significantly reduce the computation complexity. RVE serves as a bridge linking the macroscopic mechanical properties with their microscopic counterparts. To meet the continuity and equilibrium between any two neighbouring RVEs, the representative volume element must be periodic [2].

Choosing an appropriate boundary condition is very important in the numerical simulation. Chen *et al* [14] analysed three types of boundary conditions: mixed boundary conditions, prescribed displacement boundary conditions and periodic boundary conditions as shown in Figure 2.5. The mixed boundary condition is representative of frictionless grips. The model with mixed boundary conditions has no tangential force and the bending moment at nodes on the boundary, which have been used by Silva *et al* [39] and Triantafyllidis and Schraad[40]. The prescribed displacement boundary conditions impose relatively stronger restrictions, which are representative of sticking grips. The prescribed displacement boundary conditions constrain both the translation displacement and rotation of every node on the boundary. The periodic boundary conditions[2] assume that the corresponding nodes on the opposite side of the mesh have the same expansion in the normal direction, the same displacement in the other directions and the same rotation in all the directions. It has been indicated that the periodic boundary conditions are more suitable than the mixed boundary conditions and prescribed displacement boundary conditions [2] to analyse the mechanical properties of a periodic RVE. The periodic boundary conditions are expressed as

$$u_{i1} - u_{i2} = u_{i1}^{ref} - u_{i2}^{ref} \qquad \theta_{i1} - \theta_{i2} = 0, \quad i = x, y, z, \tag{2.2}$$

where u_{i1}^{ref}, u_{i2}^{ref} are the translational displacements of the reference node chosen on the opposite edge of the mesh; u_{i1}, u_{i2} denote the translational displacements of all

the other nodes but the reference node chosen on the opposite sides; θ_{i1} and θ_{i2} represent the rotational displacements of the corresponding nodes on the opposite boundaries.

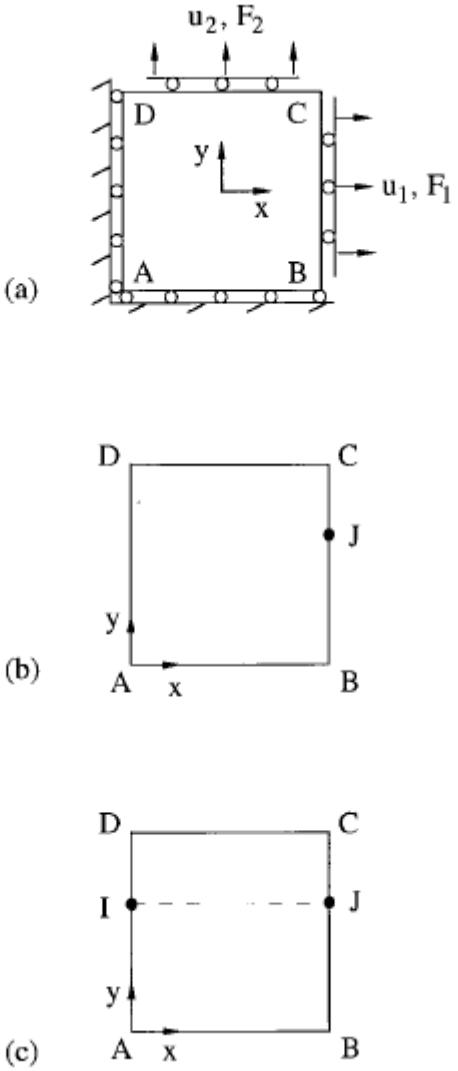

Figure 2.5. Three different types of boundary conditions: (a) mixed boundary conditions, (b) prescribed displacement boundary conditions and (c) periodic boundary conditions[14].

2.2.4 Characteristic stress and strain

Traditionally the yielding of a material is defined according to the von Mises yield criterion. However, it cannot be used to describe the yielding when a material is

subjected to hydrostatic loading as the Mises criterion is based on the distortional part of strain energy and when a material is under hydrostatic loading the von Mises equivalent stress is zero. Some researchers have put forward the characteristic stress and strain which combine the hydrostatic density energy and deviatoric density energy to probe the yielding of two-dimensional isotropic foam[14], two-dimensional anisotropic cellular materials[41] and three-dimensional transversely isotropic foams[42]. The deduction of characteristic stress and strain is based on the total strain energy density and different from those phenomenological yield criteria, for instance, a shape parameter needs to be given to describe the mean-effective stress[43]. It should be noted that the characteristic stress-strain curve is linear in the elastic regime and its slope is unique irrespective of the state of stress, i.e., all the curves under uniaxial and/or multiaxial loadings collapse on the same master line. Figure 2.6 shows the characteristic stress-strain plots under biaxial loading in the plane of isotropy and the plane of anisotropy for the transversely isotropic foam[42].

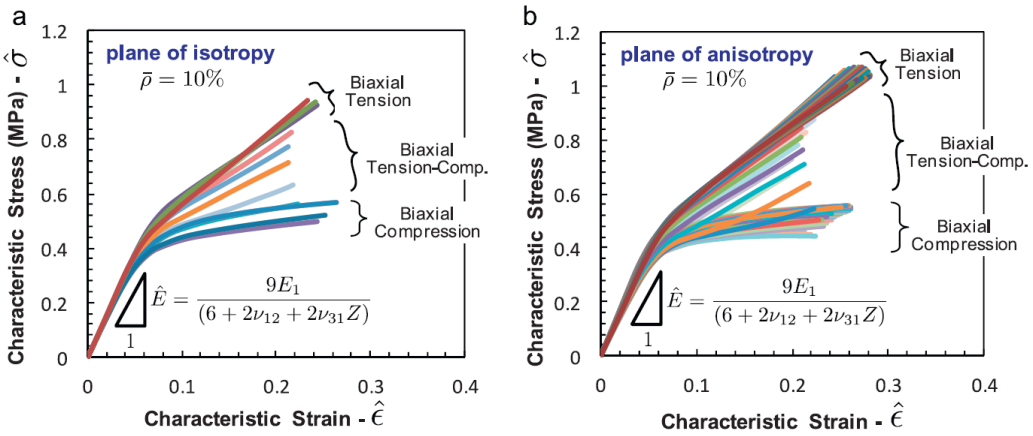

Figure 2.6. Characteristic stress-strain plots under biaxial loading in (a) plane of isotropy and (b) plane of anisotropy for the transversely isotropic foam[42].

The introduction of characteristic stress and strain facilitates to determine the onset of yielding under multiaxial loading conditions. For three dimensional transversely isotropic materials, the yield criterion based on the total strain energy density is given by [42]

$$\sigma_e{}^2 + \kappa^2 \sigma_m{}^2 = \left(1 + \frac{\kappa^2}{9}\right) Y_{11}{}^2 \tag{2.3}$$

where σ_e is the effective stress which is related to the deviatoric part of strain energy and σ_m is the mean stress associated with the hydrostatic part of strain energy. κ is a parameter carrying the information on stiffness and strength anisotropy and can be expressed by parameters Y_{11}, Y_{33}, X_{11}, X_{33}, ν_{12}, ν_{31},$E_1$and E_3, where Y_{11}, Y_{33} are the yield strengths when the material is subject to uniaxial loading in the x and z directions respectively, X_{11}, X_{33} are the corresponding yield strains. E_1, E_3 are the Young's moduli in the x and z directions. ν_{12}, ν_{31} are the Poisson's ratios. It implies that for transversely isotropic materials with the properties in the x direction the same as those in the y direction, based on only simple uniaxial loading tests (x and z) the yielding under any arbitrary stress state can be revealed. As most of the foams exhibit different mechanical responses under compression and tension, it is necessary to incorporate the pressure dependence in the yield criterion. Thus the final form of the yield criterion can be expressed as [42]

$$\sigma_e{}^2 + \kappa^2 \sigma_m{}^2 - 3(Y_{1t} + Y_{1c})\left(1 + \frac{\kappa^2}{9}\right)\sigma_m = -Y_{1t}Y_{1c}\left(1 + \frac{\kappa^2}{9}\right) \tag{2.4}$$

where Y_{1t} is the yield strength obtained from uniaxial tension and Y_{1c} is the yield strength under uniaxial compression. For materials which are not sensitive to hydrostatic pressure, $Y_{1t} = -Y_{1c}$ and Eq. (2.4) reduces to the form of Eq. (2.3). The yield surfaces in the space of effective stress versus mean stress are plotted in

Figure2.7 for transversely isotropic materials. The dashed line indicates that the response under compression is the same as that under tension and the solid line indicates the presence of the pressure dependence.

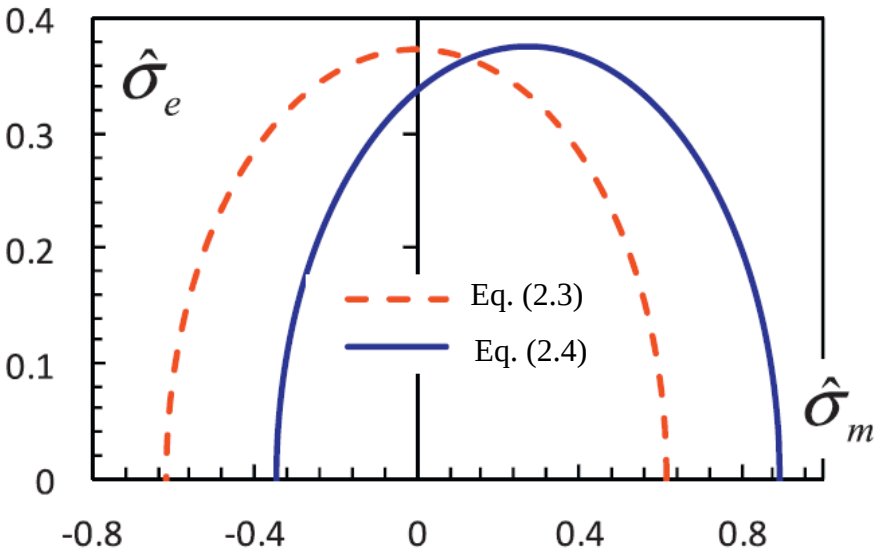

Figure 2.7. Yield surface in the mean–effective stress space. The dashed line indicates absence of linear pressure dependence and solid line indicates linear pressure dependence[42].

2.3 **Filamentous networks in tissue engineering**

Filamentous networks can be widely found in biomaterials at the micro- and nano-scales. For instance, cytoskeleton (CSK) is a network of filamentous proteins consisting of filamentous actin (F-actin), microtubules and intermediate filaments with diameters in the order of nanometers[8]. A typical extra-cellular matrix (ECM) is composed of structural protein nanofibres such as collagen with a diameter in the order of micrometers[7].

2.3.1 Cytoskeleton

The architecture of cytoskeleton is fibrous network as shown in Figure 2.8. Many mechanical behaviours of cells are determined largely by the networks of filamentous proteins called cytoskeleton. Like the bony skeleton, which gives the body stability, the cytoskeleton plays a significant role in maintaining each cell's shape, providing the strength and the ability to move. Cytoskeleton (CSK) is a network of filamentous proteins, composed of filamentous actin (F-actin), microtubules and intermediate filaments, within a cell's cytoplasm. The mechanical stiffness of intracellular material, to a great extent, is governed by the cytoskeleton[44]. Mechano-transduction describes the process by which cells recognize mechanical stimuli and react, which is of great significance for the attachment, growth and movement of all living cells and for adjusting a variety of physiological processes. A large array of physiological functions that involve specialized mechanisms of mechano-transduction have been delineated in terms of a broad spectrum of mechanosensitive behaviours[45]. As the fibrous networks throughout a cell, cytoskeleton, as well as extracellular matrix (ECM) and cell membrane protein intermediates, e.g., integrins, are crucial in the mechanisms of mechano-transduction. Cytoskeletal networks determine the cell stiffness and transmit the internal and external force during mechano-transduction. It has been proposed that the mechanical tension in the cytoskeleton, which is transmitted to the nucleus, is very important for the local control of cell-cycle progression, as the deformation of the nucleus regulates gene expression[46]. A tensionally integrated cytoskeleton model with sticks and strings was developed under different mechanical loads. It has been observed that the microfilaments within the cytoskeleton contribute the most to cell stiffness by generating and distributing tensions to all CSK filaments[47], which is consistent with the finding that networks with filamentous actin show a higher rigidity

in terms of the shear modulus than the networks with microtubules or intermediate filaments[48].

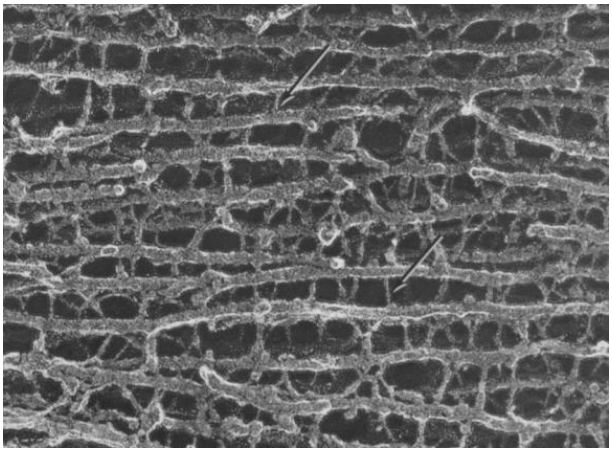

Figure 2.8. Axonal neurofilaments extensively cross-linked to each other within the neuronal cytoskeleton[49].

Some techniques have been developed to test the mechanical properties of the cytoskeletal networks within the cytoplasm in the living cell subjected to external stimuli, for instance, nanoparticle tracking based on ballistic intracellular nano-rheology[50] and atomic force microscopy[51]. These observations *in vivo* are of great importance to understanding the elasticity of the dynamic cellular processes. Considering the immense complexity of the living cell, the techniques conducted *in vivo* would not effectively render the mechanical properties of the cytoskeletal networks globally in an isolated cell which is due to the fact that normal cells are hardly viable when suspended in a fluid instead of being adhered to a solid[52]. One approach has been to build the reconstituted cytoskeletal networks *in vitro* to measure the mechanical elasticity of cytoskeleton[53]. Gardel *et al*[54] elucidated the mechanical response of reconstituted networks of cytoskeletal proteins *in vitro,* including the rheology of F-actin networks as well as the mechanics of microtubules and intermediate filament networks. It has been found that the reconstituted F-actin

networks cross-linked by the hinged filamins, which act as the actin-binding proteins, show dynamic elastic properties comparable to cellular processes in the living cell[55]. With the cross-linking protein recruiting actin filaments into networks, some related parameters, for instance, the physiological concentrations of actin (c_A) and the typical molar ratios of cross-linker and actin filament (R) play a large role in the rigidity of the cytoskeletal networks[53,55–57], i.e., small changes in the densities of cross-linker and actin filaments greatly affect the elasticity of the cytoskeletal networks[57]. It is not surprising that the architecture of the cytoskeleton can alter the elastic behaviour of the filamentous networks. It has been shown that the orientation of the filaments in the network can determine whether the main deformation mechanism of the filament is bending, stretching or compressing[58].

It is crucial to build quantitative mechanical models describing the complicated behaviour of the cytoskeleton and predicting the effects of network parameters. The varied mechanical behaviour of cells is largely determined by the cytoskeleton, thus the study of cytoskeletal networks will contribute to the understanding of cell mechanics.

2.3.2 Extracellular matrix

Sharing the similar architecture with the cytoskeleton, extracellular matrix does not exist in the cell but provides the structural supports to the surrounding cells[59]. The extracellular matrix(ECM) is typically organized as a three-dimensional fibre network composed of structural protein nanofibers, such as collagen with dimensions ranging from tens to hundreds of nanometres [7,60]. Increasing evidence has shown that mechanical stiffness of ECM plays a significant role in regulating cellular behaviours, including adhesion, proliferation and differentiation of mesenchymal stem

cells[52,61,62]. It is expected that a 3-D biomimetic ECM will play a similar role in supporting cell growth *in vitro,* as native ECM does *in vivo*. A more recent study has shown that collagen fibres' resistance to deformation affects stem cell spreading and differentiation[62]. It is also known that extra-cellular matrices consisting of collagen or fibrin fibres often have a much higher local stiffness than the bulk ECM[63]. Therefore, the mechanical stiffness of an ECM is not just dependent on its individual fibres but also on its 3-D network structures. It is important to model and characterise the mechanical properties of such network structures for their successful application in tissue engineering and regenerative medicine.

Collagen is the main component of extracellular matrix in all connective tissues, such as bone, skin, tendon, ligament and cornea, sclera, and so forth. Markaki *et al*[30] conducted a magneto-mechanical simulation of bone growth using the ferromagnetic fibre material and the application of a magnetic field. The concept that a porous and permeable implant could be treated as a scaffold for tissue growth has been well established[64]. The ferromagnetic fibre network in a magnetic field can be regarded as an *active* scaffold as the magnitude of elastic deformation of the fibre arrays can be induced and controlled. It is crucial to understand the mechanical properties of fibre networks, which facilitates the development of models for tissue engineering.

The collagen fibre alignments are different within different tissues. As shown in Figure 2.9, with an increase of the fibre concentration factor k, collagen fibres become more aligned along the preferred fibre orientation and the structures become anisotropic from isotropic in stiffness. The collagen fibres in skin tissue exhibit equal stiffness in all orientations, i.e., isotropy, in which $k = 0$. When $k = \infty$, all collagen fibres lie along the same orientation, which is relevant to tendons and ligaments. The

alignment of collagen fibres in sclera is stochastic and results in anisotropic mechanical behaviour ($k > 0$) [65].

In filamentous networks, cross-linking proteins can be found in the soft tissues, such as cornea. The cross-linker is significant in improving the visible-light transmission and enhancing the mechanical properties[66]. With more cross-linking, the cornea is stronger, whereas with less cross-linking, the cornea is weaker and easier to develop the keratoconus. Thus, the investigation of cross-linker is essential to gain an understanding of the elasticity of a material. In the model of stochastic fibre network, the connection between fibres should be emphasized.

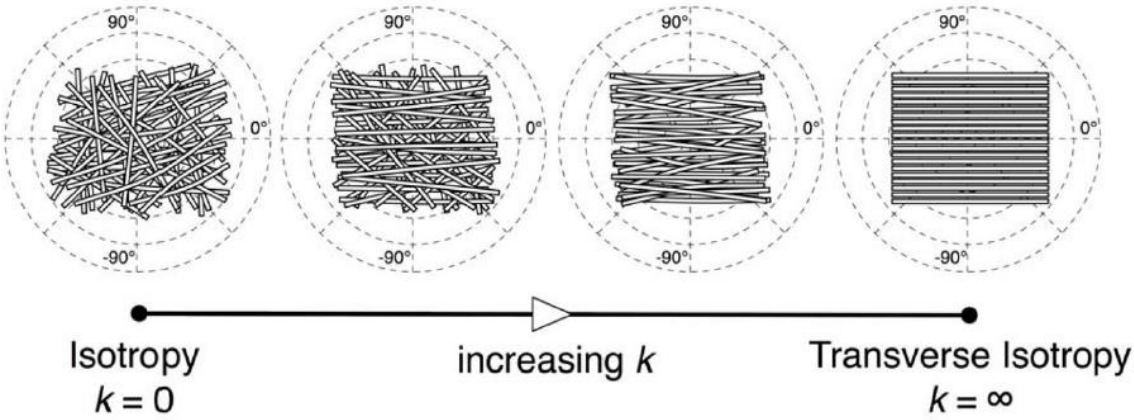

Figure 2.9. Collagen fibre alignments for different tissues. As the fibre concentration factor increases, collagen fibres become more aligned along the preferred fibre orientation[65].

2.4 **Size-dependent effects**

Filamentous networks can be widely found in biomaterials at the micro- and nano-scales. The mechanical properties of macro-sized fibrous materials has been studied[10,17]. However, when the dimensions of fibrous structures are reduced to the micro- or nano-scale, the stiffness or rigidity is much different from their macro-sized counterparts. At the micro scale, the strain gradient has a dominant effect on the mechanical behaviour. It has been generally recognised that at the nanometre scale, the surface elasticity and initial strain (stress) effects are of great importance.

2.4.1 Strain gradient effects at micro-scale

Extensive experimental investigations have shown that the deformation behaviours of metals[67–69] and polymers[70,71] at the micron and sub-micron levels are size dependent. Some plasticity phenomena have suggested that the smaller is the size, the stronger is the response. As can be seen from Figure 2.10[67], the thin copper wires with different diameters in the range of 12-170 μm display different normalized torsional strengths. This behaviour cannot be explained by conventional theory, which is only applicable for macro-sized structure. In Figure 2.10, if the constitutive law is size independent, all the plots would fall on the same curve. Thus, it is clear that an intrinsic material length scale l is required to enter the constitutive law and interpret the size-dependent behaviour.

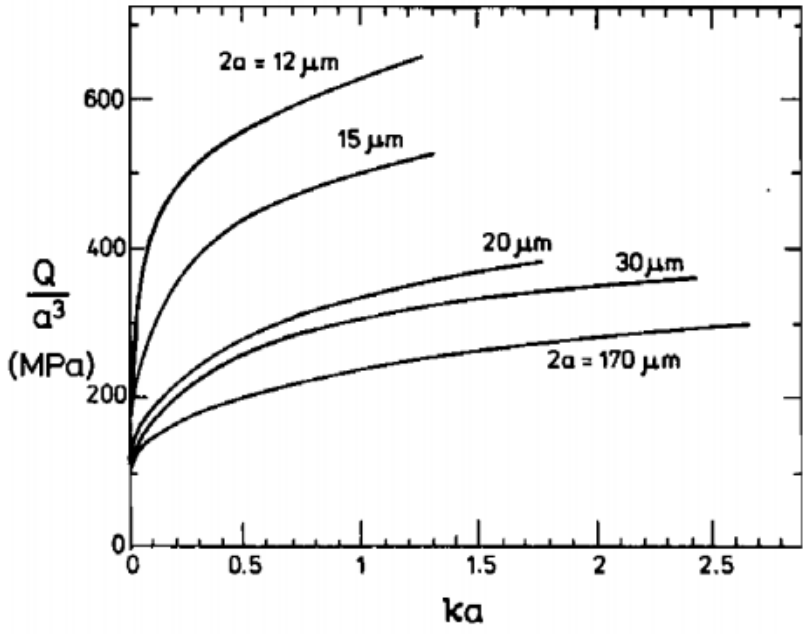

Figure 2.10. Torsional response of copper wires of diameter $\boldsymbol{2a}$ in the range 12-170$\boldsymbol{\mu m}$[67].

The size-dependent effects can be explained by couple stress theories[72–76]. In the conventional mechanics, it is believed that the applied load can only drive a material particle to translate and accelerate along the direction of exerted force. In the classical couple stress theories for linear elastic materials, a couple contributing to the rotation of the material particle is introduced. Figure 2.11[77] briefly shows an equivalent system of forces. In a system of material particles, a force F_A applied on the particle *A*, as shown in Figure 2.11(a), can be equivalent to a force F_A' applied on the particle *B* and a couple of force L_A' applied to the system, as shown in Figure2.11(c), by translating the force from particle *A* to particle *B* as shown in Figure2.11(b). The couple can be specified as

$$\boldsymbol{L_A' = (X_B - X_A) \times F_A} \tag{2.5}$$

where $\boldsymbol{X}_A$ and $\boldsymbol{X}_B$ are the position vectors of particle *A* and *B*. The Cosserats[78] firstly considered systematically couple-stress in the mechanics of an elastic medium. In couple stress theory, the couple acting across the surface is a central consideration in addition to the force.

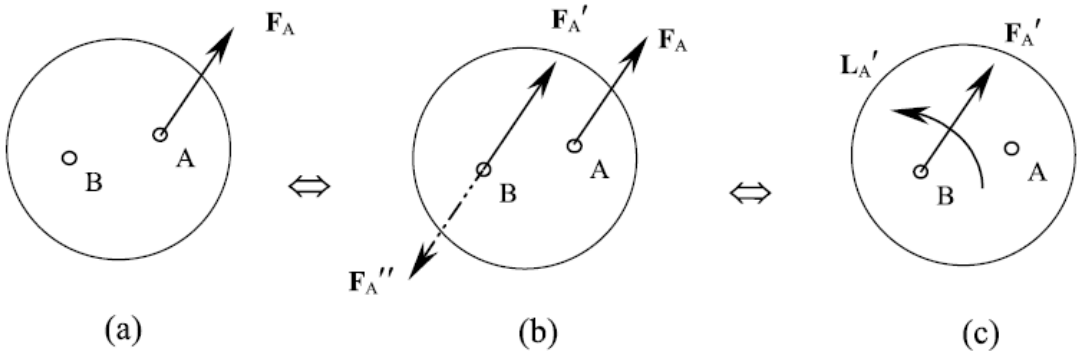

Figure 2.11. A force applied on the particle *A* can be equivalent to a force on the particle *B* and a couple applied to the system[77].

In the framework of couple stress, the principle of virtual work is formulated in terms of the gradient of translation $\boldsymbol{u}$ as well as rotation $\boldsymbol{\theta}$ which in conventional theory is not included. The deformation energy density of a volume V of deformable body takes the form as[77,79]

$$\int_V \delta w dV = \int_V (\delta \boldsymbol{\varepsilon} : \boldsymbol{\sigma} + \delta \boldsymbol{\chi} : \boldsymbol{m}) dV \tag{2.6}$$

where *w* is the deformation energy density per unit volume, $\boldsymbol{\varepsilon}$ is the strain tensor and $\boldsymbol{\chi}$ is the symmetric curvature tensor. $\boldsymbol{\varepsilon}$ and $\boldsymbol{\chi}$ are conjugated to the symmetric stress tensor $\boldsymbol{\sigma}$ and the deviatoric couple stress tensor $\boldsymbol{m}$, respectively. $\boldsymbol{\varepsilon}$ and $\boldsymbol{\chi}$ are the symmetric parts of the translation gradient and the rotation gradient respectively, defined as

$$\boldsymbol{\varepsilon} = \frac{1}{2}(\boldsymbol{u} \otimes \boldsymbol{\nabla} + \boldsymbol{\nabla} \otimes \boldsymbol{u}) \tag{2.7}$$

$$\boldsymbol{\chi} = \frac{1}{2}(\boldsymbol{\theta} \otimes \boldsymbol{\nabla} + \boldsymbol{\nabla} \otimes \boldsymbol{\theta}) \tag{2.8}$$

It is important to note that the symmetric curvature tensor $\boldsymbol{\chi}$ can be expressed in terms of the strain gradient[79]. The strain gradient theory of plasticity assumes that the yield stress depends on not only the strain, but also the strain gradient which fits the couple stress framework with higher order stress. Some researchers have been engaging in the development of mechanism-based strain gradient (MSG) theory of plasticity, in which an intrinsic material length scale is involved in modelling the size dependent effect in the micron to submicron range[79–83]. A strain gradient version of deformation theory and flow theory[79] is proposed, based on the couple stresses which are neglected in the conventional theories. Fleck *et al*[67] have developed a strain gradient theory of plasticity by hypothesizing that the hardening is governed by the sum of the density of statistically stored dislocations ρ_S and the geometrically necessary dislocations ρ_G. In materials science, a dislocation is a crystallographic defect. The randomly trapped dislocations are referred to as statistically stored dislocations, and geometrically necessary dislocations are extra storages of material defects resulted from the non-uniform plastic deformation[84–86]. Considering slip on a single system of a single crystal, it is suggested that the simplest possible relationship between flow stress τ on the slip plane and total density of statistically stored dislocations and geometrically necessary dislocations is given by[67]

$$\tau = CGb\sqrt{\rho_S + \rho_G} \tag{2.9}$$

where G is the shear modulus, b is the magnitude of the Burger's vector and C is a constant set to be 1/3 by Ashby[84].

It is assumed that the hardening is due to the accumulation of dislocations. Hardening due to statistically stored dislocations is assumed to be represented by the von Mises effective strain ε_e (or the invariant of the strain tensor $\boldsymbol{\varepsilon}$). Hardening due to geometrically necessary dislocations is assumed to scale with a scalar measure of strain gradient χ_e (or the invariant of the symmetric curvature tensor $\boldsymbol{\chi}$)[79]. For the sake of mathematical convenience, it is assumed that the deformation energy density w is a function of the single strain scalar measure ζ which takes the form as

$$\zeta = \sqrt{{\varepsilon_e}^2 + l^2 {\chi_e}^2} \tag{2.10}$$

where l is the intrinsic material length scale, introduced into the constitutive law to model the size-dependent effects. In conventional plasticity theories, only the von Mises plastic strain/stress is treated as the scalar measure of yield criterion. Taking the strain gradient into account, the plasticity theories possess an intrinsic material length scale. The density of geometrically necessary dislocations is directly proportional to the gradient of plastic strain[67]. Plastic strain gradients could be caused by the geometry of loading as shown in Figure 2.12(a, b)[67], or by the local boundary conditions as shown in Figure 2.12(c, d), or by the material itself containing microstructures as shown in Figure 2.12(e, f). In the plastic twisting of a cylinder or bending of a beam, the plastic strain is finite at the surface, but zero along the axis of twist, or neutral axis of bending. In the indentation hardness test, the plastic strain is finite just beneath the indenter, but zero in the regime far from the indenter. In the plastic deformation of polycrystals, the plastic strains are non-uniform at the boundaries of the grains because of the mismatch of slip.

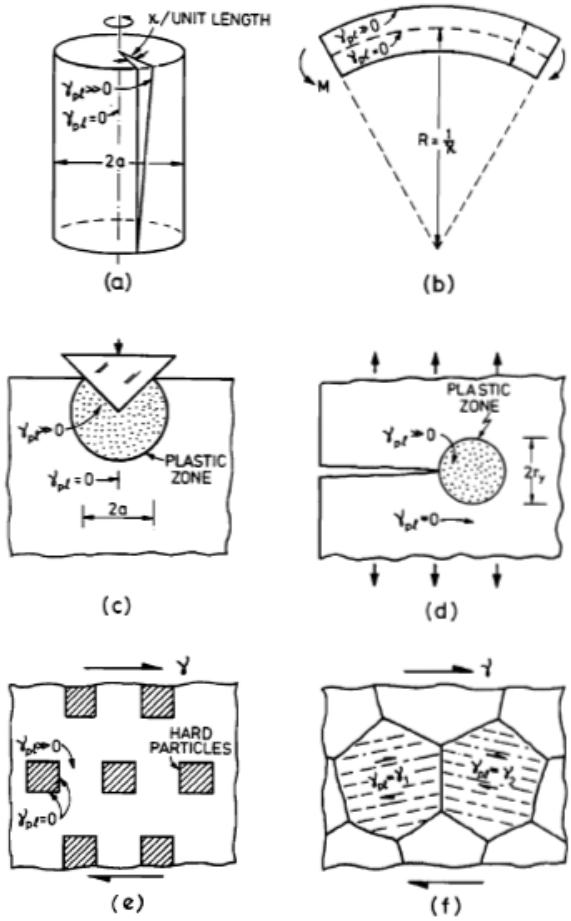

Figure 2.12. Plastic strain gradients could be caused by the geometry of loading (a, b), by the local boundary conditions (c, d), or by the material itself containing microstructures (e, f) [67].

The gradients of plastic strain result in the storage of geometrically necessary dislocations[84–86]. It has been suggested that the density of geometrically necessary dislocations is given by[84]

$$\rho_G \approx \frac{4\gamma}{b\lambda} \tag{2.11}$$

where b is the magnitude of the Burger's vector, γ is the macroscopic average plastic shear strain, and λ is the local length scale of the deformation field and varies with the cases shown in Figure 2.12. For instance, in the bending test, λ is half thickness of the beam; in the hardness test, λ is the indentation size. Approximately, the magnitude of

the plastic strain gradient is $\kappa \approx \gamma/\lambda$. Thus, $\rho_G \approx \kappa/b$. The density of statistically stored dislocations ρ_S (shaded band) and geometrically necessary dislocations ρ_G (solid line) against shear strain for pure copper is plotted in Figure 2.13. As can be seen from Figure 2.13, there is a regime where the density of geometrically necessary dislocations far exceeds the density of statistically stored dislocations, which implies that the hardening is mainly due to the strain gradient.

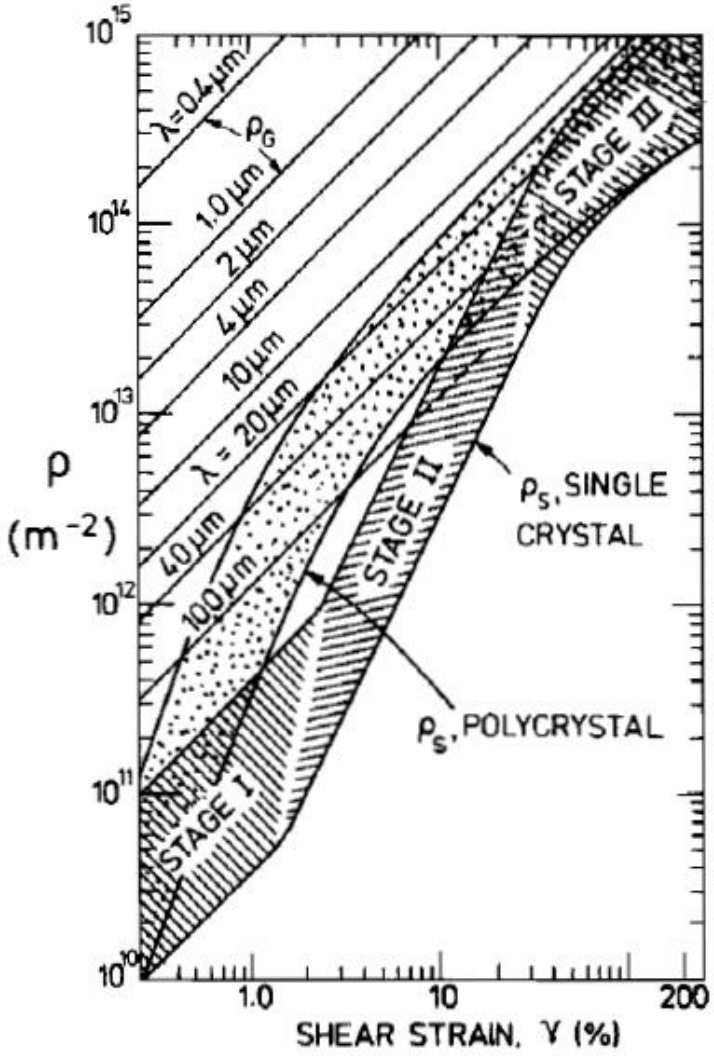

Figure 2.13. The density of statistically stored dislocations ρ_S is taken from the experimental data of Basinski and Basinski[87]. The density of geometrically necessary dislocations ρ_G with a variety of length scales λ is based on Eq(2.11) [67].

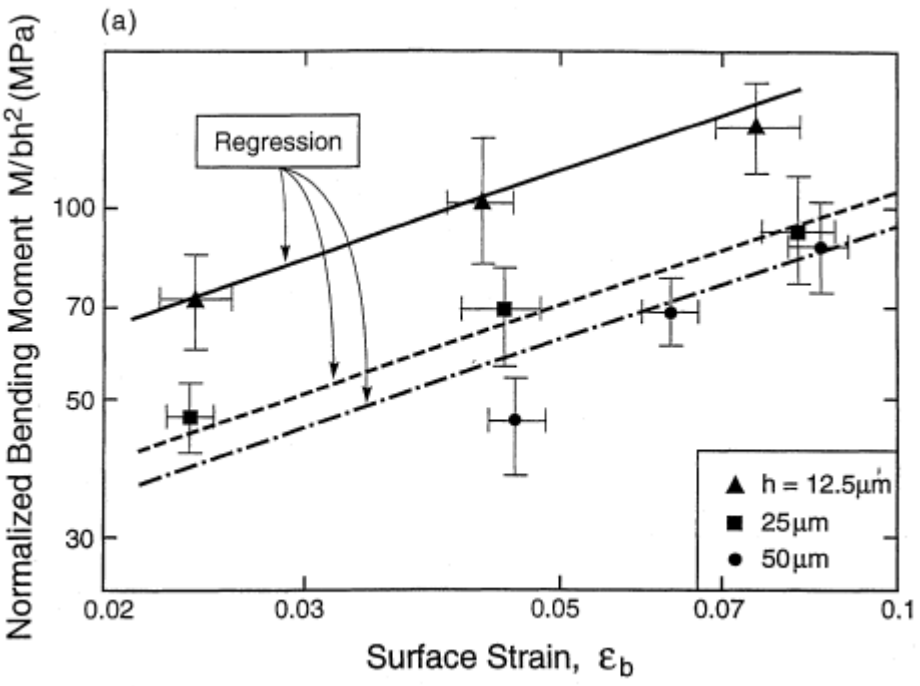

Figure 2.14. Plots of the normalized bending moment against the surface strain for all three foil thicknesses[68].

The strain gradient theory contains an intrinsic material length scale to account for the size dependent effects. Some experimental evidence has supported the presence of the length scale, for instance, the micro-torsion[67], micro-bending[68] and micro-indentation hardness test[69]. Fleck *et al*[67] carried out the torsion test of copper wire of diameter in the range of 12-170μm. As can be seen from Figure 2.10, the torsional strength increases with the decreasing wire diameter. In Figure 2.10, the group Q/a^3 can be interpreted as the magnitude of shear stress and the group κa could be interpreted as the magnitude of shear strain. If the shear stress in the copper wire depends only upon the shear strain and not strain gradient, all the curves in Figure 2.10 would completely overlap. Nevertheless, at $\kappa a = 0.3$, the Q/a^3 of copper wire of diameter $2a = 12\mu m$ is about three times that of diameter $2a = 170\mu m$. Thus, the micro-torsion test suggests that the strain gradient plays a significant role. Stolken *et al*[68] conducted a micro-bending test of thin nickel foil to determine the material

length scale. The normalized bending moment against the surface strain for the thin foil with three different thicknesses is plotted in Figure2.14. In the micro-bending test, it shows that the smaller is the thickness of the foil, the larger is the bending moment. This phenomenon results from the strain gradient and can be explained by adding a material length scale into the constitutive law. And the length scale obtained from the micro-bending test of nickel is in the range of 3-5 μm. A hardness test of silver was conducted by Ma *et al*[69] and it shows that the hardness is dependent on the size of the indentation for sizes below 10 μm. Hardness data plotted as a function of the indentation diameter is shown in Figure 2.15. Metal hardness H is three times the flow stress. Based on the theory of strain gradient plasticity, the hardness H is given by

$$H = Gb\sqrt{\rho_S + \rho_G} \tag{2.12}$$

By substituting Eq. (2.11) into the above equation, we obtain

$$H = Gb\sqrt{\rho_S + \frac{4\gamma}{bD}} \tag{2.13}$$

where D is the indentation size. Using Eq. (2.13), the relationship between the hardness and indentation size is plotted with the solid line in Figure 2.15. It can be seen that the experimental data fits very well with the theory of strain gradient plasticity. The hardness increases with the decreasing of indentation size. No size dependence is observed in the micro-tension tests. As shown in Figure2.16[67], the tension response of the thin copper wire is independent of wire diameter. It is suggested that the strain gradient in tension is negligible and the hardening is only due to the statistically stored dislocations without the storage of geometrically necessary dislocations in uniaxial micro-tension.

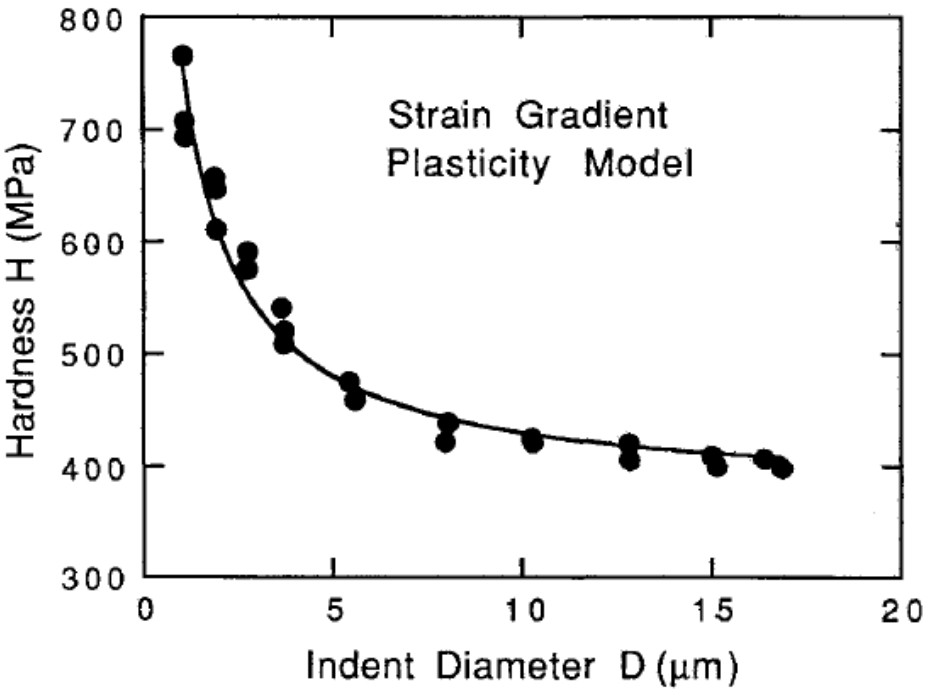

Figure 2.15. Plots of hardness data versus the indentation diameter in the micro-indentation test[69].

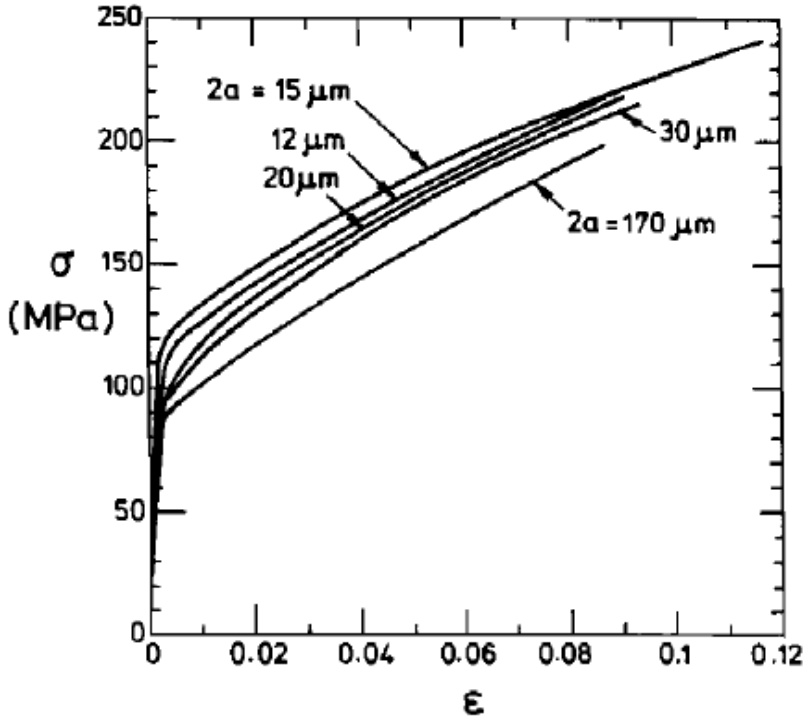

Figure 2.16. Tension response of the thin copper wire of diameter $\boldsymbol{2a}$ in the range 12-170$\boldsymbol{\mu m}$[67]

The intrinsic material length scale is generally believed to be at micron level and is related to the shear modulus, the yield strength and the Burger's vector of the material. The length scale l in the strain gradient plasticity is given by[80,88]

$$l = 3\alpha^2(\frac{G}{\sigma_y})^2 b \tag{2.14}$$

where G is the shear modulus, σ_y is the yield strength, b is the magnitude of the Burger's vector and α is an empirical coefficient in the range of 0.2-0.5. The intrinsic material length scale l carrying all the information of elasticity(G), plasticity(σ_y), and atomic nature of solids(b) varies from material to material. For typical metallic materials, the magnitude of Burger's vector b is in the order of 0.1nm, and $\frac{G}{\sigma_y}$ is in the order of 10^2. Thus, the intrinsic material length is in the order of microns, which fits the length scale observed in experiments[67–69].

Taking the size-dependent effect into account is significant in the analysis of mechanical behaviour of materials and structures whose dimension is in the order of microns, such as, micro-electro-mechanical systems (MEMS) with micro-sized features. In the conventional theories, the stiffness and strength of fibrous materials are dependent on the relative density, the orientation of the fibres and the slenderness of the fibres, but not on the absolute size. The strain gradient effects at the micron scale should be incorporated into all the deformation mechanisms in the analysis of the mechanical properties of fibrous materials. An intrinsic material length scale is required to scale with the strain gradient.

2.4.2 Surface elasticity and initial strains effects at the nano-scale

Size-dependence in the nano-sized structural element in terms of the mechanical properties has been investigated [89–94]. As can be seen from Figure2.17[90], the elastic modulus of silver and lead nanowires of diameter 30nm are almost twofold the elastic modulus of bulk Ag and Pb. The elastic constant increases with the decrease of the diameter of Ag and Pb nanowires of diameter in the range of 30-250 nm. When the diameters of nanowire are large enough, e.g., larger than 70nm for Ag, or larger than 100nm for Pb, the elastic moduli are size independent[90]. Nano-indentation experiments on nano-porous gold were conducted by Biener *et al*[92]. As can be seen from Figure 2.18, the hardness of nano-porous Au with a relative density of 0.25 increases with decreasing ligament (strut) diameter. The increase of elastic constant and yield strength of nano-sized structure with smaller diameter is attributed to the surface effects. For nanostructures, as the surface-to-volume ratio is large, the surface effects become predominant and can play a significant role in the deformation process. Surface change in interatomic potential give rises to a softer or stiffer property in nanoscale thin film and nanowire compared to the bulk[95,96]. A nanoscale continuum theory has been established to predict the elastic modulus of single-wall carbon nanotubes by incorporating interatomic potentials[97].

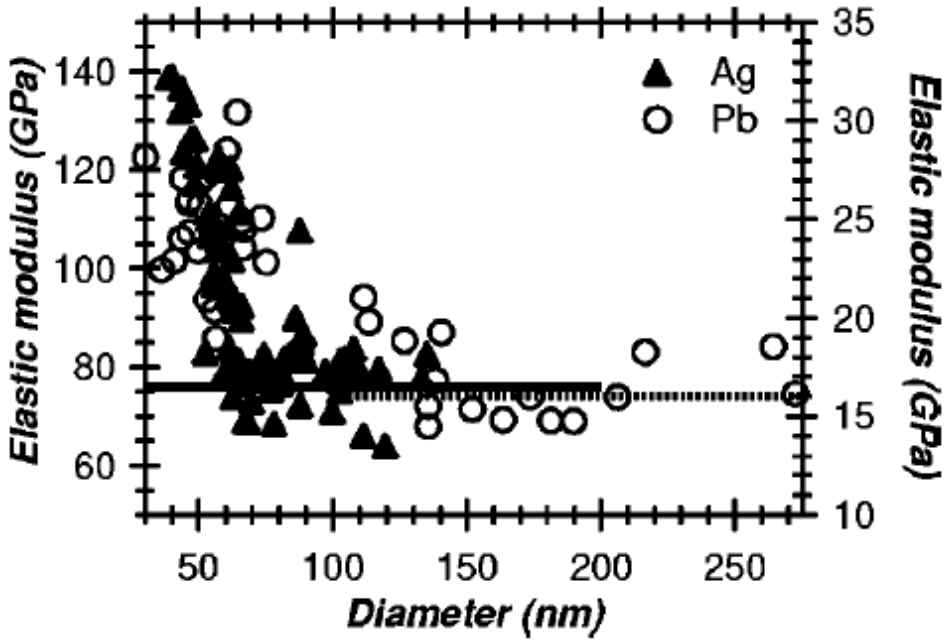

Figure 2.17. Measured elastic modulus for Ag and Pb nanowires as a function of the diameter. The solid line indicates the elastic modulus of bulk Ag and the dotted line indicates the elastic modulus of bulk Pb[90].

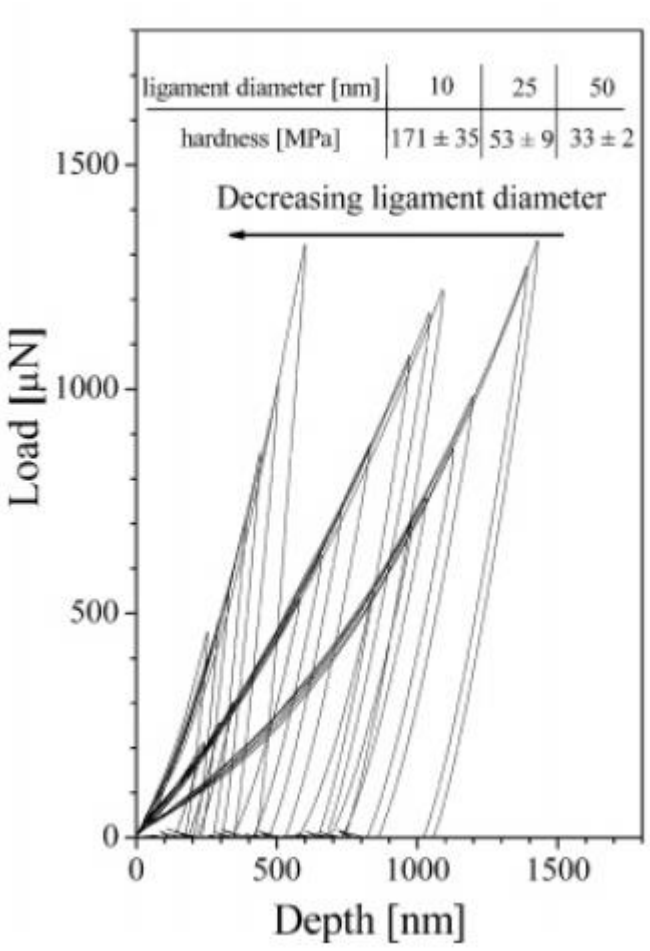

Figure 2.18. Nano-indentation experiment on nano-porous gold with a relative density of 0.25. The shift of the load-depth curves towards lower depths indicates that the hardness of nano-porous Au increases with the decrease of the ligament diameter[92].

Miller *et al*[89] developed a model to predict the size dependence of effective properties in the nanometer length scale. An intrinsic material length scale l_{in} which is identified as the ratio of the surface elastic modulus to the bulk elastic modulus has been introduced for the nano-sized structures. It is found that the non-dimensional difference in the elasticity of nanostructure from the continuum predictions satisfies

$$\frac{D - D_c}{D_c} = \alpha \frac{l_{in}}{L} \tag{2.15}$$

where D is the mechanical property at nano scale, for instance, the bending stiffness, D_c is its macro counterpart, α is a non-dimensional constant that depends on the geometry of the structural element and loading, L defines the size of the structure, for instance, L is the thickness of the plate in bending. l_{in} is the intrinsic length scale in nano-sized structures and is given by[90]

$$l_{in} = \frac{S}{E} \tag{2.16}$$

where the quantity S is the surface elastic constant and E is the corresponding elastic modulus of the bulk material. It should be noted that S can be positive or negative, thus l_{in} can be positive or negative. The predictions of the model in terms of the intrinsic length scale are tabulated in Table 2.1. The non-dimensional constant α is related to the material, the geometry of the structure and the loading. The absolute value of the intrinsic length scale is in the order of 0.1 nm for Al and Si. Therefore, in this case, when the size of Al or Si nanostructure is in the order of 10nm and above, the surface effects weaken, or even vanish. The role of surface effects is significant when the length scale of the structure becomes comparable with the atomic scale.

Table 2.1 summary of model predictions for size dependence of elastic properties [90].

Element	Loading	D_c	Material	Surface type	α	l_{in}(nm)
Plate	Tension	Eh	Al	(100)	2	-0.09298
Plate	Tension	Eh	Si	(100)1×1	2	-0.1012
Plate	Bending	EI	Al	(100)	6	-0.09298
Plate	Bending	EI	Si	(100)1×1	6	-0.1012
Bar	Tension	Eh	Al	(111)	$3\sqrt{2}$	0.02781
Bar	Tension	Eh	Si	(100)1×1	4	-0.1099
Bar	Bending	EI	Si	(100)1×1	8	-0.1012

Note that when the nano-sized structural element undergoes tension or bending, in the definition of intrinsic length scale, S and E are taken to be the surface Young's modulus and bulk Young's modulus, respectively. A theory for the prediction of the size dependence of torsional rigidities of nanostructures has been developed by Shenoy[91], in which model S and E are the surface shear modulus and bulk shear modulus, respectively.

Wang *et al*[98] proposed that many properties at the nano-scale obey a simple scaling law. For the non-dimensional mechanical properties of homogeneous nano-structured materials,

$$\frac{F(L)}{F(\infty)} = 1 + \alpha \frac{l_{in}}{L} \tag{2.17}$$

where $F(L)$ denotes the mechanical property at the nano scale L, $F(\infty)$ denotes the mechanical property of the bulk material, l_{in} is an intrinsic length scale related to the surface property. The scaling law Eq. (2.17) and the model developed by Miller *et al*[89] to predict the size dependence (see Eq. (2.15)) share the same form. Thus, l_{in} in Eq. (2.17) is identified as the ratio of surface elastic constant to the bulk elastic constant, when the scaling law is used to demonstrate the mechanical elasticity of nanostructures. Typically, the intrinsic length scale l_{in} of nano-sized metallic materials is in the order of 0.01-0.1nm [89,99]. The scaling law could give good predictions for $L > 3 - 5$nm in terms of the mechanical elasticity[98]. Moreover, with the scaling law, once determined the parameter αl_{in} with one or a few tests the corresponding mechanical property at any value of the size L can be obtained directly, which helps replace the various experimental measurements or numerical computations. Similarly, for general heterogeneous nano-structured materials, the scaling law is expressed as[98]

$$\frac{F(L)}{F(\infty)} = 1 + \frac{1}{L}\left(\alpha l_\lambda + \beta l_\mu\right) \tag{2.18}$$

where α and β are two non-dimensional constants, l_λ and l_μ denote two intrinsic length scales and take the form as[100]

$$l_\lambda = \lambda_s / E$$

$$l_\mu = \mu_s / E \tag{2.19}$$

where λ_s and μ_s are two surface elastic constants related to surface effects.

It is clear that the size-dependent mechanical behaviour of nano-sized structure can be predicted by introducing an intrinsic length scale for homogenous materials, or two intrinsic length scales for heterogeneous materials[91,100]. Apart from the surface elasticity, the initial surface stress plays an important role in the stiffness due to the large surface to volume ratio in nanostructures. Interestingly, the initial surface stress can be controlled by adjusting the amplitude of an applied electric potential[101–105]. For instance, experiments conducted by Biener *et al*[101] have shown that the initial surface stress of nano-porous gold can be controlled to reach 17-26N/m from 1.13N/m by adjusting the chemical energy. It is found that the surface stress and the charge in anion adsorption on Au are linearly correlated[104]. The surface stress as a function of the charge in three aqueous acid solutions of the perchlorate, sulphate and chloride ions are plotted in Figure 2.19[104]. It is seen that the surface stress depends linearly upon the charge, with little or no hysteresis, and the slopes for the three anions are listed in Table2.2. The values of the slopes of surface stress-charge curves are of the same sign and order of magnitude.

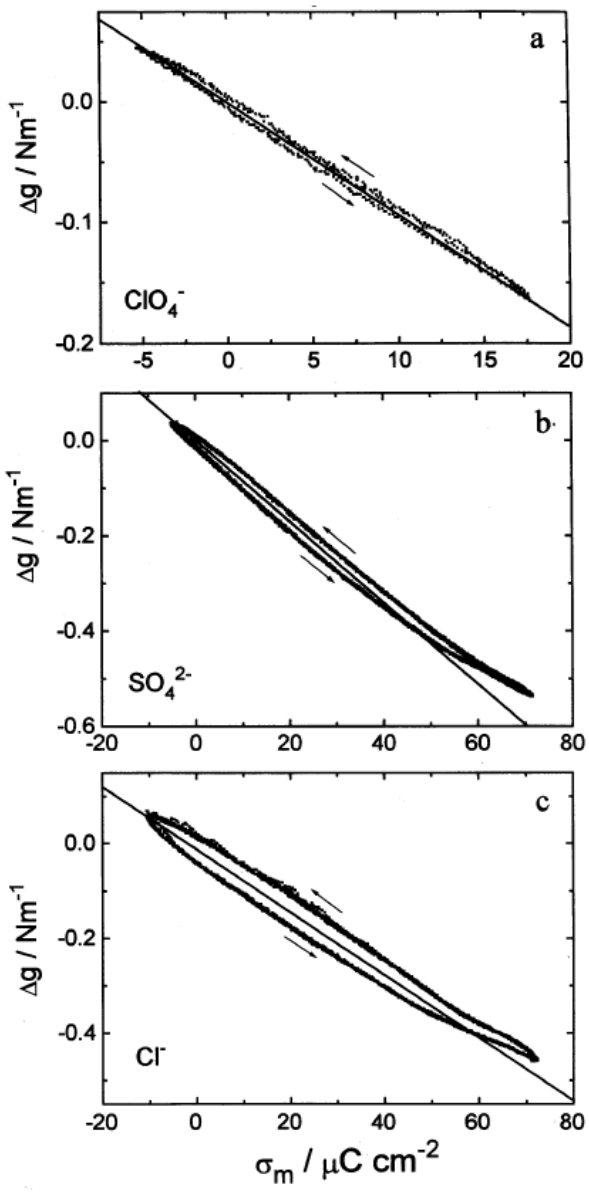

Figure 2.19. The surface stress as a function of the charge in three aqueous acid solutions of the perchlorate (a), sulphate (b) and chloride (c) ions[104].

Table 2.2 Slopes of the curves shown in Figure 2.19 for the three anions

Anion	ClO_4^-	SO_4^{2-}	Cl^-
Slope	-0.91	-0.85	-0.67

The surface stress can induce the deformation on the nanostructure. Materials that can change their dimensions in response to an applied voltage can serve as actuators in

various applications. The most familiar examples are the piezoelectric and electrostrictive ceramics. Extensive experiments have shown that charge-induced reversible strain can be found in nano-porous metals[101–103]. As can be seen from Figure 2.20[103], the reversible strain of nano-porous Pt increases almost linearly with increasing potential. It is suggested that the chemical energy can be converted into mechanical responses through nano-porous metals due to the high surface area. Since the surface stress depends linearly upon the charge, the relationship between the surface strain and the potential can be explained through the continuum mechanics. The dimensional change of nano-porous metal is caused by the charge-induced change in the surface stress[101]. The change of surface stress Δf in nanoporous gold is related to the dimensional change $\Delta l/l$ through[106]

$$\Delta f = -\frac{9K}{2\alpha_m \rho}\frac{\Delta l}{l} \tag{2.20}$$

where K is the bulk modulus of the solid, α_m is the specific surface area in the nano-porous metal and ρ is the bulk density. Based on Eq. (2.20), for a nano-porous Au with $K = 220Gpa$, $\rho = 19.3 \times 10^6 gm^{-3}$, $\alpha_m = 10 - 15 m^2 g^{-1}$, when the surface stress reaches to 17-26N/m by adjusting the chemical energy, the dimensional change or compressive strain could be 0.5%[101]. Thus the reversible strain of nano-porous metals in response to an applied potential can reach in the order of 0.1% or above which is comparable with the commercial piezoelectric ceramics.

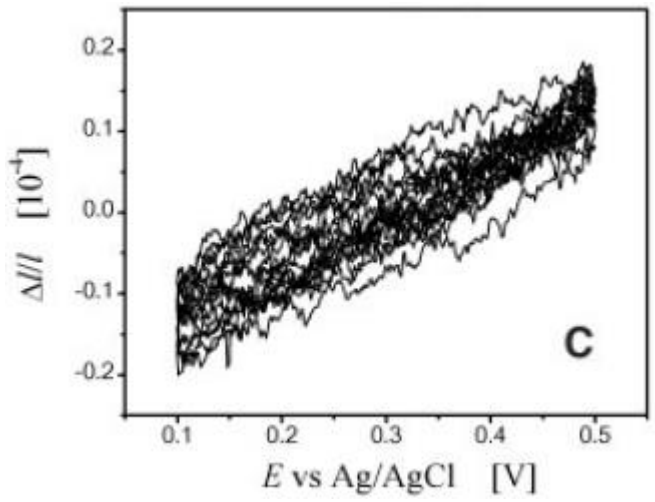

Figure 2.20. Reversible part of the strain of nano-porous Pt versus potential E for nine successive cycles. Results were measured in situ by dilatometer using H_2SO_4(0.5M) as the electrolyte[103].

For a free-standing isotropic thin film, Cammarata *et al* [107] showed that the in-plane elastic strain ε induced by the free surface stress f is

$$\varepsilon = -2f/Yt \tag{2.21}$$

where t is the thickness of the thin film and Y is an elastic modulus which is equal to $E/(1-\nu)$ for isotropic materials, where E is the Young's modulus and ν is the Poisson's ratio. Based on Eq. (2.21), with typical values for metals of $f = 1N/m$ and $Y = 100Gpa$, a thin film with thickness of 10nm would have a contractive in-plane strain of 0.2% which is comparable to the yield strain caused by an external stress. For a film with thickness of 2nm, the strain induced by surface stress could reach 1%, which is in excess of yield strain for metals.

For nanostructures, as the surface-to-volume ratio is large, surface effects play a dominant role in the mechanical behaviour when the size of structure dimension is small. The two main factors in surface effect are surface elasticity and initial surface

stress/strain. The former is size-dependent and increases with decreasing size of structure; the latter can be retained at a constant level, for example, by the application of an electrical potential. The linear constitutive relation of the surface can be expressed as [107]

$$f_{ij} = f_{ij}^0 + S_{ijkl}\varepsilon_{kl} \tag{2.22}$$

Where f_{ij} is the surface stress tensor, ε_{kl} is the surface strain tensor, S_{ijkl} is the surface elastic modulus tensor and f_{ij}^0 is the initial surface stress when the bulk is unstrained.

It's important to be noted that the surface stress is a different quantity from the surface energy in the case of solids. Cammarate clearly distinguished surface stress and surface energy concepts [107]. The surface free energy γ is defined as the reversible work per unit area involved to create a new solid surface. On the other hand, the surface stress f is defined as the reversible work per unit area involved to elastically stretch a solid surface. The surface stress tensor f_{ij} is related to the surface energy γ as [107]

$$f_{ij} = \gamma\delta_{ij} + \frac{\partial\gamma}{\partial\varepsilon_{ij}} \tag{2.23}$$

where δ_{ij} is the Kronecker delta (the function is 1, if $i = j$, and 0 otherwise). The surface stress and the surface energy share the same unit of N/m and generally they are in the same order of magnitude for solids.

The combined effects of surface elasticity and initial surface stresses on the bending stiffness of a core-shell nanowire(with two materials) and a simple nanowire(which is made of a single material)[93], and nanofilms[108] have been analysed. For

example, for a simple nanowire with a circular cross-section, the non-dimensional bending stiffness can be expressed as[93]

$$\frac{EI-(EI)_0}{(EI)_0}=\frac{8l_{in}}{d}-\frac{4\nu f_0}{Ed} \tag{2.24}$$

where E is the Young's modulus of the bulk material, d is the diameter of the nanowire, l_{in} is the intrinsic length scale in nanoscale (which is the ratio of surface elastic modulus to the bulk Young's modulus), f_0 is the initial surface stress and ν is the Poisson's ratio. $(EI)_0$ is the bending stiffness of macro-sized beam and equals $E\pi d^4/64$.

Chapter 3 Modelling Stochastic Fibrous Materials

A continuum mechanics-based, three-dimensional, periodic beam model has been constructed to describe stochastic fibrous materials. The establishment of a three-dimensional model is deduced progressively with two-dimension coordinates being considered first. Periodic boundary conditions are applied to analyse the mechanical properties in FE simulation. To determine the shear modulus of the stochastic fibrous material, an effective compressive strain and tensile strain in the transverse directions are imposed simultaneously. Since the plane of x-z of the stochastic beam model developed in this study exhibits anisotropy, geometry transformation is conducted to obtain the shear modulus.

3.1 **Introduction**

Porous materials have been of great interest to engineers and scientists due to their attractive thermal, acoustic, electrical and mechanical properties which are very promising in engineering applications. Foam and honeycomb, which can also be categorized as cellular materials, have been extensively studied[1–6]. With the same attractive properties as cellular properties, porous fibrous materials are less researched and less understood in comparison, because of their more complex geometry. Finite element method has been employed to investigate the tensile and compressive behaviour of random fibrous materials[35,36]. A comprehensive study on the

modelling of stochastic fibrous materials by mathematical treatment, for instance, the probability and distribution can be found in reference[37], however, the connection between fibres was not taken into consideration. The connection between fibres is a very key feature in the structure, especially when dealing with mechanical behaviours of the three-dimensional fibrous structures.

It is suggested that the macroscopic stresses and strains can be determined by the microscopic stresses and strains over a representative volume element (RVE). To meet the continuity and equilibrium between any two neighbouring RVEs, the representative volume element must be periodic[1,2]. It has been shown that the periodic boundary conditions are more suitable than the mixed boundary conditions and prescribed displacement boundary conditions[1,2] to analyse the mechanical properties of a periodic RVE.

In this chapter, a three-dimensional random beam model is introduced to represent the stochastic fibrous structure. In this study there are two ways to deal with the connection between fibres. As the fibrous network can be widely found, the connection could be soft in some materials and could be relatively rigid in other materials.

3.2 **Geometry of stochastic fibrous structure**

In this study, the model generated is of a three-dimensional stochastic fibrous structure with periodicity, which is complicated. Therefore the in-plane dimensions have been considered, before proceeding to consider the out-of-plane dimension, which is the thickness direction. In addition, the cross-linking, represented by beam element inserted between intersected fibres into the stochastic network has been incorporated,

as shown in Figure 3.1. All the information about the geometry, for instance, the location, orientation, connection and so forth, was generated by MATLAB before it is imported to ANSYS FE solver for the calculation. A flowchart demonstrating the process for generating the 3-D structure is given in Figure 3.2.

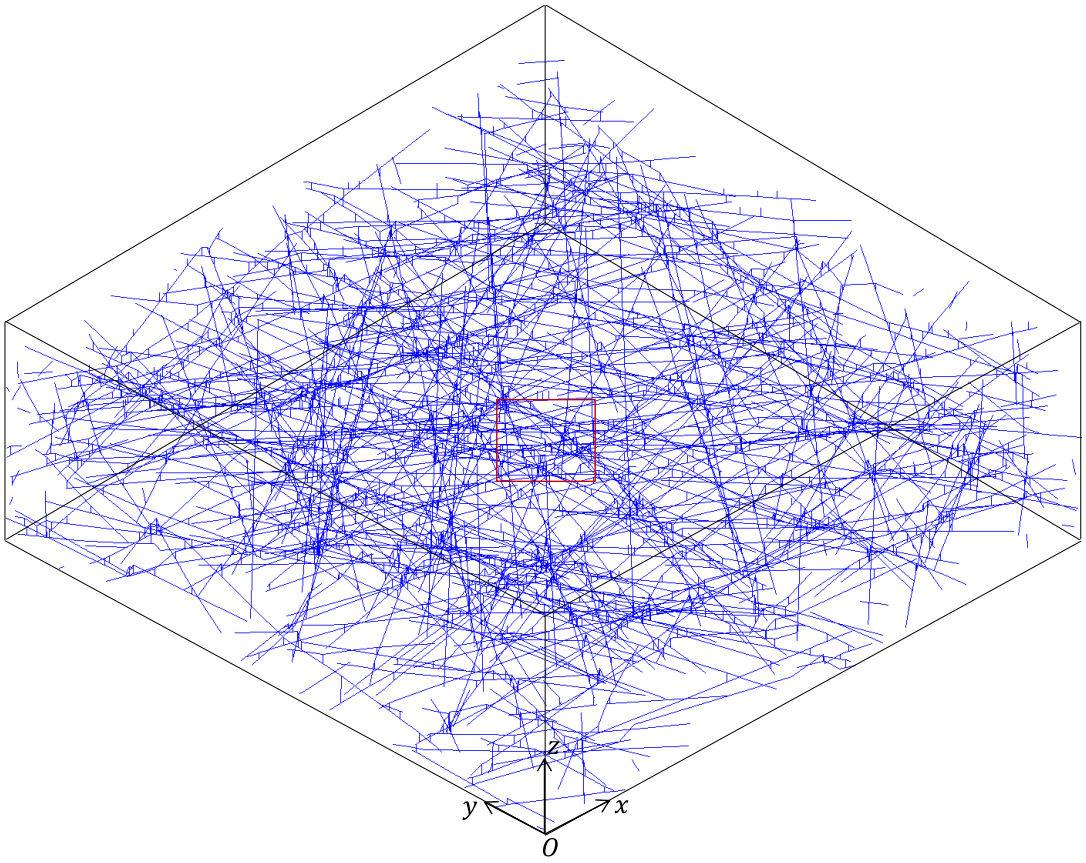

Figure 3.1. The isometric view of the beam model of the stochastic fibrous structure by FEM, where the fibres are represented by the polylines

3.2.1 Stochastic point and line process in two-dimensional space

An example of a few fibres stochastically distributed in the square region of $w \times w$ is shown in Figure 3.3. The location and orientation of all the fibres are random due to the manufacturing process of, for example, the metal fibre sintered sheet. The coordinate values (x_c, y_c) of the centre point and the angle θ of the line, which are used to render the location and orientation, respectively, are the important parameters

in this model. All the centre points of the lines denoting the fibres are random points, that is to say, these points are generated independently of one another and have the equal possibility to distribute in the given square region. We define the side length, w of the region as 1, for simplicity. The centre points (x_c, y_c) are randomly falling into the region of $\{(x_c, y_c)|0 < x_c < 1;\ 0 < y_c < 1\}$. As shown in Figure 3.3, O represents the origin of the coordinates. The random numbers are obtained from the MATLAB function *rand*, which generates uniformly distributed pseudorandom numbers. Even though the centre point of the fibre has been restricted in one inspection area, the fibre could lie in several inspection areas, which is attributed to the length L and orientation θ, of the fibre. In the stochastic model, the length, L is not uniform, continuously ranging from 0.8 to 1.2, as we set w as 1. And the orientation, θ ranges from 0 to π.

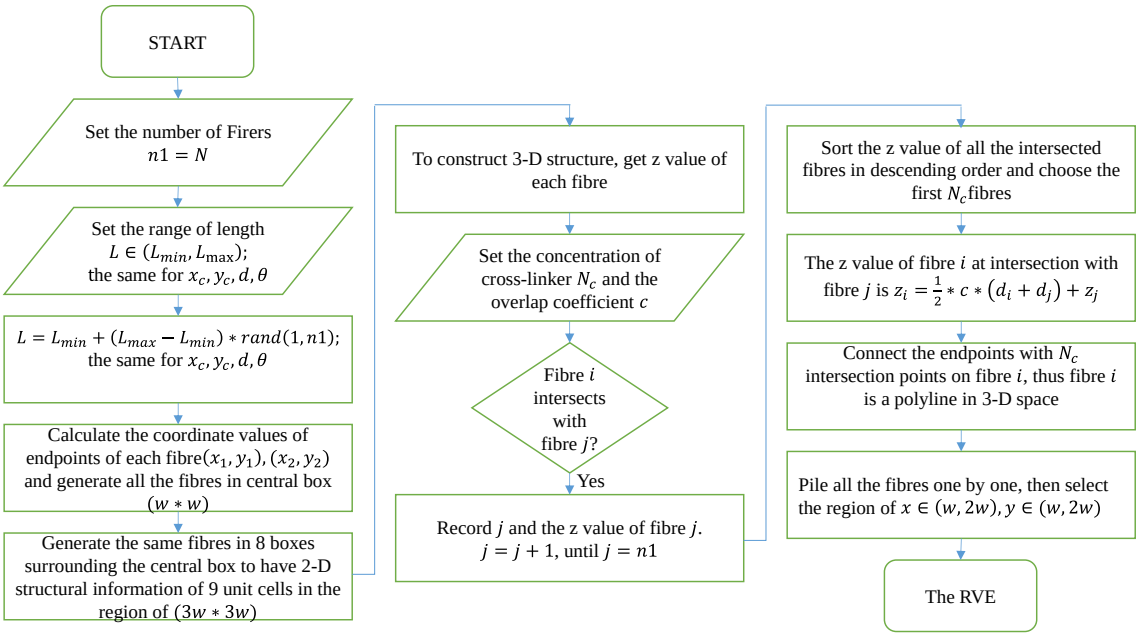

Figure 3.2. The flowchart of the construction process for a 3-D stochastic fibrous network.

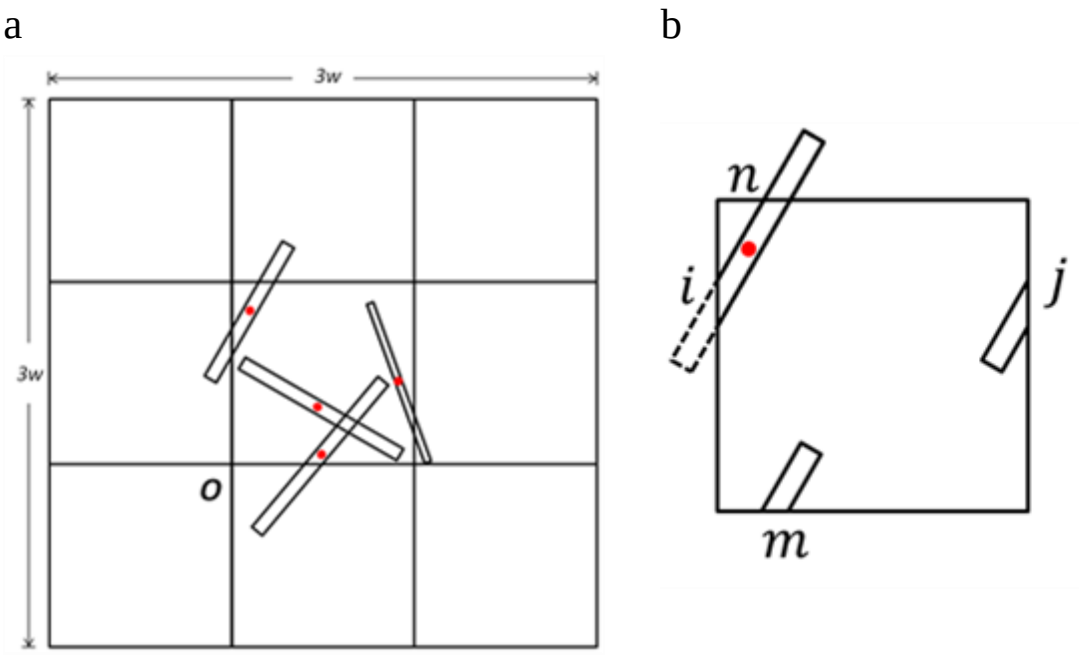

Figure 3.3. (a)Example of fibres stochastically distributed in the square region of w × w with the length ranging from 0.8w to 1.2w, and the red dot in the middle representing the centre point of the line.(b) operations to the fibre, whose centre point is in the given region, to obtain a periodic representative volume element (RVE).

3.2.2 Periodicity in x-y plane

As the fundamental constituent of continuum mechanics, a representative volume element (RVE) is adopted due to computational limitation. The RVE, which could be called the 'unit cell', must be periodic so as to meet the continuity and equilibrium between any two neighbouring RVEs. Thus, to consider the periodicity in two dimensional model, i.e., repetitive in the x-y plane, the operations are performed to all the fibres whose centre points are in the given square region, whereas the lines also exist in other regions. As can be seen from Figure 3.3(b), the fibre can be divided by the boundaries of the given region into two or three, at most, parts. The concept is to move the parts of the line, falling in other regions, into the given region by translating in the x or y direction by the side length of the given square. By this method, a periodic RVE can be obtained, which is just like the tessellation that is probably the most

familiar periodic object to most of us. It should be noted that the fibre with several parts scattered in the region needs to behave as a whole when the structure is subject to internal or external loadings. Periodic boundary conditions are applied on this periodic model, which can constrain those boundaries, such as paired nodes i and j in the x direction and paired nodes m and n in the y direction, shown in Figure 3.3(b). The periodic boundary conditions will be illustrated in Section 3.3.

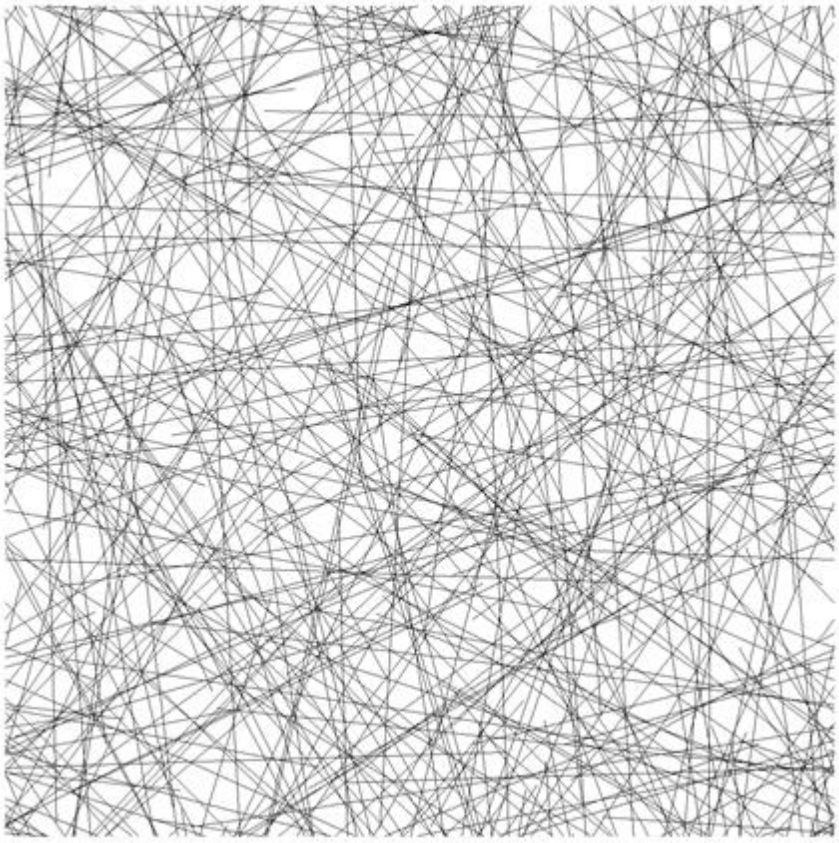

Figure 3.4. Stochastic periodic fibrous structure in two-dimensional space with the side length at 1(non-dimensional), length of fibre ranging from 0.8 to 1.2, number of fibres $\mathrm{N} = 200$. All the fibres are stochastically distributed in the plane, with uniformly random locations and orientations.

3.2.3 Establishment of the stochastic three-dimensional fibre model

The two-dimensional stochastic periodic fibrous structure shown in Figure 3.4 is, meanwhile, the projection of this three-dimensional fibrous structure. The three-

dimensional model is based on the two-dimensional one, but requires a more complex design in terms of the intersections between lines. Firstly, the geometry generated with straight lines which represent the fibres piling up in the thickness direction, i.e., in the z direction, is developed to delineate how to construct a spatial structure. All the information on the intersections between any two fibres is carried by the two-dimensional model, but there is processing sequence of the fibres when considering the growth in the out-of-plane dimension. Record the number of the intersected line with line i only if it is smaller than i. The z value of the first line is initialized as zero. The z value of each subsequent line can be determined by adding the diameter *d* (here the diameters of all the fibres are assumed uniform) onto the highest z value of its intersected lines. By piling up the fibres, one by one, until *N* fibres are layered in the model, a stochastic network is obtained, having a significant structural component in the third dimension, as shown in Figure 3.5. However, it is not true in the real sample, where a fibre bends away from another at the crossing point. Based on the three-dimensional model with straight lines, which introduces the concept of dealing with the z coordinate in the thickness direction, a periodical stochastic fibrous structure with polylines has been constructed, in which the concentration of cross-linking is incorporated. Before going on to the detailed polyline model setup, it should be acknowledged that a curved line model could be better in describing the real sample; however, it is unnecessary to use solid element instead of beam element in the simulation, as it would lead to enormous computational complexity, even when the number of fibres is around 10. Alternatively, extensive beam elements could be possible to fit the curvature of each curved lines. Given the huge number of elements, it would be too computationally expensive to generate the grid mesh for curved fibres and to carry out the analysis of mechanical behaviours. Simplification, by using

polylines to represent the structure, does not necessarily reduce the performance of the model, however, the innovative modelling method optimises the simulation both in efficiency and accuracy.

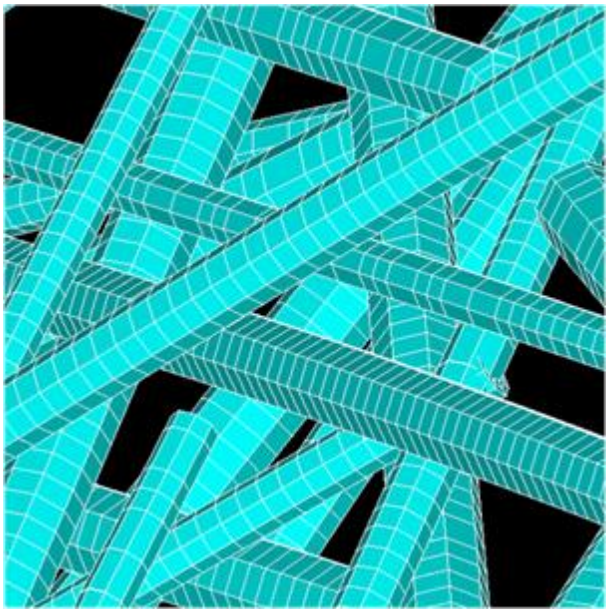

Figure 3.5. The three-dimensional stochastic beam model with straight lines in which fibres are layered, one by one, with few intersections with others. The diameter of the fibres in this model ranges uniformly from 0.01 to 0.02. The beams are 3-D display in ANSYS.

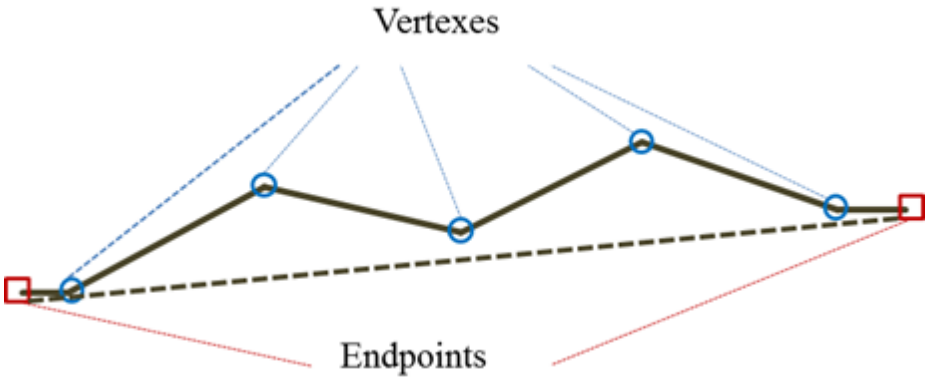

Figure 3.6. Polyline composed of more than one line segment with endpoints or vertexes on each of the segment. The vertexes represent the intersections in the fibrous material, and the number of vertexes is defined as the concentration of cross-linking in the network. The value of the slope of lines connecting each endpoint and its neighbouring vertex is assumed zero, and the length of the polyline is the same as that of the straight line connecting two endpoints, to simplify the calculation of relative density.

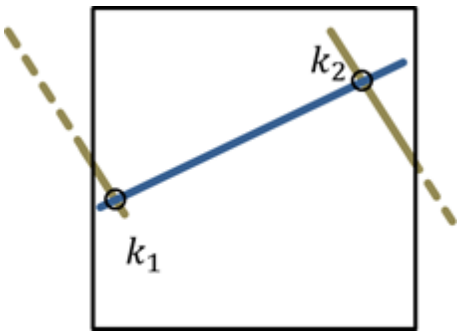

Figure 3.7. In the view of x-y plane, a fibre can intersect with the other fibre at two points due to the periodicity.

As we know in computer graphics, a polyline is a continuous line composed of more than one line segment, with endpoints or vertexes on each of the segments, as shown in Figure 3.6. In the model with polylines, the vertexes excluding the two endpoints are used to represent the intersection points. Thus, the number of intersections is controllable and adjustable, according to the manufacturing materials, and it is defined as the concentration of cross-linking, $N_c = L/l_c$, where l_c is the mean distance between any two intersection points along a fibre of length L. In the three-dimensional model with straight lines, shown in Figure 3.5, each line always has just one intersection, except for the case shown in Figure 3.7, where line i intersects with line$j$ at two intersection points for the sake of periodicity. Fewer contacts among fibres lead to weaker inter-fibre bonding, which consequently reduces the mechanical rigidity and strength of the fibrous material. In contrast, in the three-dimensional model with line segments, the fibre can drop down to connect with more fibres below, in which case the fibre volume fraction of the representative volume element(RVE) can be increased dramatically to reach comparable values in real material by adjusting the concentration of the cross-linking. Figure 3.8 shows the three-dimensional stochastic beam model with polylines.

Figure 3.8. The three-dimensional stochastic beam model with polylines developed in this study

In the numerical model, an innovation is introduced to deal with cross-linking in the three-dimensional random beam model. As shown in Figure 3.9, an additional beam with three nodes is inserted at the intersection point of two lines in the thickness direction (z direction). The inserted beams represent the cross-linker in the stochastic fibrous network. The three nodes in the inserted beam share the same x and y coordinate values with the two endpoint nodes on the two connected fibres/lines and the two midpoint nodes in the middle of the endpoint nodes vertically. A set of nodes $\{x_j^i\}$, ($i = 1,2,..N; j = 1,2,..L/l_c$; where N is the number of fibres) indicates the endpoint nodes of all the cross-linkers. By inserting beam elements at the intersections, it can be identified as a freely rotating cross-linker. As the strength of the stochastic fibrous material is sensitive to the diameter of the cross section of the inserted beam, in the study of plasticity the inserted beam has been divided into three sections (and seven nodes), with different/same cross section diameters, as shown in Figure 3.10. The dimensions of the inserted beam can affect the rigidity and strength of the fibrous structure, especially in the z direction, which is parallel to the axial direction of the

inserted beams. In the industrial process, if two metal fibres overlapped because of, for instance, high temperature, the middle of the intersection may be thinner than the two ends. The dependence of plastic behaviour of stochastic fibrous structure on the dimension of the cross-linker will be elucidated in Chapter 5.

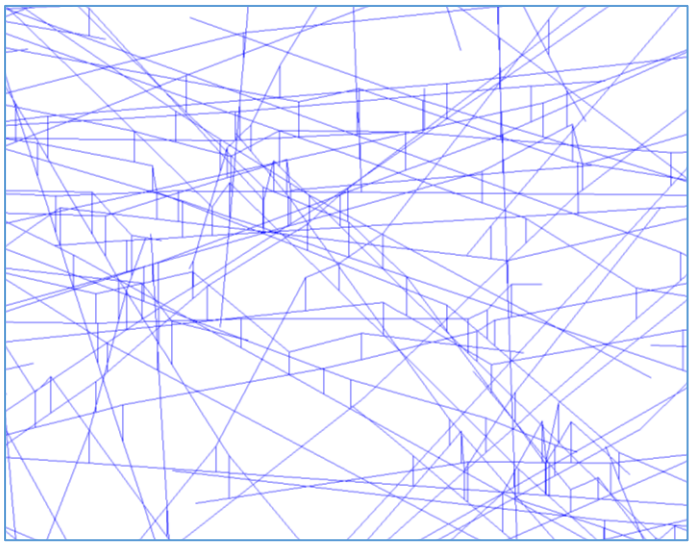

Figure 3.9. The cross-linking of the network represented by the beam element inserted between intersected fibres.

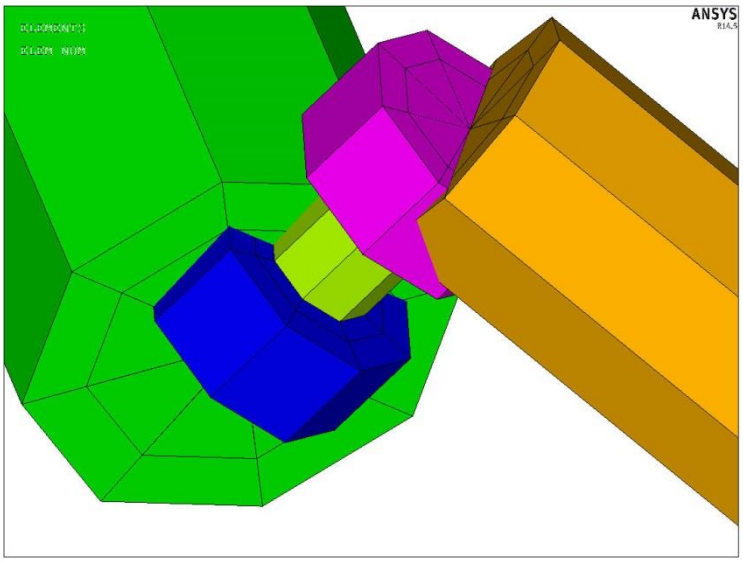

Figure 3.10. Three-section beam inserted between intersected fibres. The beams are 3D display in ANSYS.

To construct a stochastic fibrous structure in 3-D, the distance δ between the central axes of any two intersected fibres should be larger than zero. The Overlap coefficient c, defined as below, describes the degree of overlap between any two crossed lines (fibres), $c = \delta/d_0$, where d_0 is the sum of radii of the two crossed lines/fibres. For a two-dimensional model, δ equals zero and c is zero. The coefficient c is a variable to describe the extent of overlap within the range of [0, 1]. When c is zero, lines/fibres are completely overlapping, which is the same as two-dimensional fibrous network. Without any doubt the overlap coefficient will affect the length of the inserted beam, which is equal to the distance δ. The length of the inserted beam is a key parameter that determines the bearing capacity of a beam subjected to loads. Thus, the overlap coefficient is of significant importance in numerical modelling, especially when dealing with the cross-linkers as inserted beams. Also, the degree of overlap alters the thickness, t of the cross-linked structure.

Connections between fibres can be flexible cross-linkers which are represented by the additional inserted beams. Moreover, the two corresponding nodes in the set $\{x_j^i\}$ can be constrained by coupling their degrees of freedom. For instance, by coupling all the translation displacements UX, UY, UZ and all the rotation displacements ROTX, ROTY, ROTZ, it can be identified as a rigid cross-linker. It is not hard to understand that an increase in cross-linker numbers will give rise to a decrease in size in the z direction, i.e., the thickness of the structure, since the line/fibre needs to fall down to intersect with other lines/fibres in the three-dimensional modelling process, so that more cross-linkers can be generated.

3.2.4 Periodicity of the out-of-plane

Periodicity in the x-y plane has been described above, but periodicity in the z direction is conducted differently from that in the x and y directions, due to the different design and construction process. After building up the three-dimensional model with N fibres, another N fibres are continuously put up in the z direction, whose coordinates of x and y are the same as those of the previous N fibres correspondingly, for instance, $x(N+i) = x(i), y(N+i) = y(i), (i = 1,2,..N)$. In the establishment, $2N$ fibres are piled up progressively and the z coordinate of each fibre is decided by the ones below it. Note that it does not just double the previous RVE with N fibres vertically, whereas, for example, fibre $N+1$ intersects with fibres which are under it with a given concentration of intersection, i.e., fibre $N+1$ is not like the first fibre in the model, which is an initial straight line lying on the x-y plane. When the number of fibres, N is sufficiently large, there is a one-to-one correspondence between all the intersections on line N and line $2N$, of which the coordinate values in the x and y directions and the difference of z values of a pair of the intersection points are approximately the same. Figure 3.11 describes the construction of the periodicity in the z direction of the stochastic fibrous structure. Ideally, the shape of line $2N$ should be the same as that of line N, with the vertexes at the same position in the x and y directions. By taking the top N fibres from $N+1$ to $2N$, the three-dimensional periodic RVE is obtained in terms of the elasto-plastic behaviour of the stochastic fibrous structure. It is important to note that there would exist some additional isolated vertexes, or intersection points, where the beam elements have been inserted, when the top N fibres are taken away. For instance, as can be seen from Figure 3.11, there have been some inserted beam elements between line/fibre $N+1$ and lines/fibres below, whose numbers are smaller than N. To achieve the periodicity, the inserted beam elements are moved up and

inserted on the fibres whose numbers are added N to the numbers of their previously intersected fibres. Nodes A, B, C, D and nodes A', B', C', D' are constrained by applying periodic boundary conditions which will be illustrated in Section 3.3.

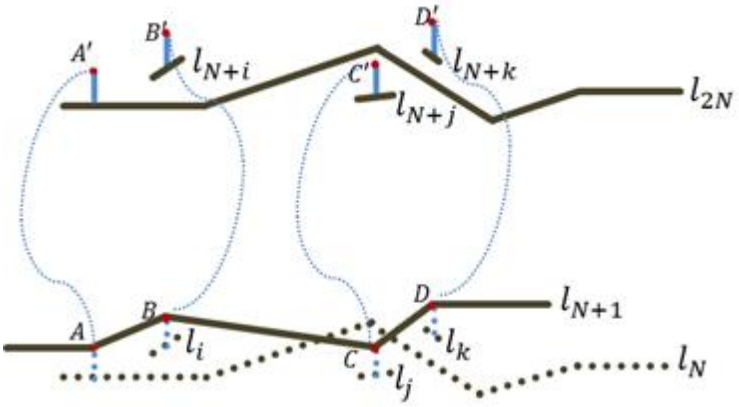

Figure 3.11. Schematic diagram to show the periodicity in out-of-plane. Ideally the shape of line N is the same as that of line $2N$, when the number of fibres is sufficiently large. When taking the top layer, consisting of N fibres, which is the representative volume element to be considered in the investigation, there would exist isolated beam elements indicated by the blue dotted lines. The isolated beam elements are moved up and periodic boundary conditions are applied on their nodes.

3.2.5 Relative density

The relative density is a key parameter to delineate the mechanical behaviour of cellular materials including fibrous materials[1–3,10]. By calculating the average value of all the distances between the constrained top and bottom nodes in the z direction, the thickness, t is obtained. Based on the thickness, the relative density of the fibrous material is specified by:

$$\rho = \frac{\sum_{i=1}^{N} L_i * (\frac{1}{4} * \pi {d_i}^2)}{(1 * 1 * t)} \tag{3.1}$$

where L_i are the fibre lengths, N is the number of fibres and d_i are the diameters of circular cross sections (in the model, the diameter is not uniform to maximally reveal

the industrial materials). Since the fibres are randomly distributed within the periodicity of w=1 in x and y directions, 1*1*t refers to the volume of the structure. Eq. (3.1) indicates the dependence of relative density on the geometry or the architecture of the structure, e.g., the length and the diameter of the line. Also, the thickness is a key parameter in determining the relative density of the structure. Note that the thickness t is an implicit function of the concentration of cross-linkers and the overlap degree, as well as the fibre diameters.

3.2.6 Statistical analysis

In this study periodical random structure has been constructed with the ranges of lengths, diameters and orientation of all the fibres taken into account. As the morphology of the fibrous network varies so much, one geometrical model alone is far from sufficient to describe the complexity of the stochastic fibrous structure in terms of its mechanical behaviours. The model is random, so in order to obtain the mechanical parameters, considerable calculation and statistical analysis are needed.

3.3 **Boundary conditions**

The geometry model of random beam has been developed above and some fundamentals are required in the finite element analysis. The type of element is 3 node beam element (BEAM 189) with circular cross section. BEAM 189 is an element suitable for analysing slender to moderately stubby/thick beam structures. This element is based on Timoshenko beam theory. Shear deformation effects are included. The constituting solid material of fibre is assumed to be elastic, perfectly plastic with

Young's modulus $E_s = 210GPa$ and Poisson ratio $\nu_s = 0.3$, and yield strength $\sigma_s = 290MPa$.

3.3.1 Periodic boundary conditions

Choosing an appropriate boundary condition is very important in the numerical simulation. Chen *et al* analysed three types of boundary conditions: mixed boundary conditions, prescribed displacement boundary conditions and periodic boundary conditions[14]. The mixed boundary condition is representative of frictionless grips. The model with mixed boundary conditions has no tangential force and the bending moment at nodes on the boundary. The prescribed displacement boundary conditions are relatively strong restrictions, which are representative of sticking grips. The prescribed displacement boundary conditions constrain both the translation displacement and rotation of every node on the boundary. Since the stochastic fibrous structure is periodic, then periodic boundary conditions can be applied to the beam model. In addition, it has been suggested that periodic boundary conditions are more suitable than mixed boundary conditions and prescribed displacement boundary conditions for a periodic RVE [1, 2]. The periodic boundary conditions assume that the corresponding nodes on the opposite edge of the mesh have the same expansion in the normal direction, the same displacement in other directions, and the same rotations in all directions. According to the definition of the periodic boundary conditions, the constraint equations used in the simulations are specified as follows:

$$u_i^{left} - u_j^{left} = u_{i\prime}^{right} - u_{j\prime}^{right} \tag{3.2}$$

$$v_i^{left} - v_j^{left} = v_{i\prime}^{right} - v_{j\prime}^{right} \tag{3.3}$$

$$w_i^{left} - w_j^{left} = w_{i\prime}^{right} - w_{j\prime}^{right} \tag{3.4}$$

$$\theta_i^{left} = \theta_{i'}^{right} \tag{3.5}$$

$$u_i^{top} - u_j^{top} = u_{i'}^{bottom} - u_{j'}^{bottom} \tag{3.6}$$

$$v_i^{top} - v_j^{top} = v_{i'}^{bottom} - v_{j'}^{bottom} \tag{3.7}$$

$$w_i^{top} - w_j^{top} = w_{i'}^{bottom} - w_{j'}^{bottom} \tag{3.8}$$

$$\theta_i^{top} = \theta_{i'}^{bottom} \tag{3.9}$$

$$u_i^{front} - u_j^{front} = u_{i'}^{back} - u_{j'}^{back} \tag{3.10}$$

$$v_i^{front} - v_j^{front} = v_{i'}^{back} - v_{j'}^{back} \tag{3.11}$$

$$w_i^{front} - w_j^{front} = w_{i'}^{back} - w_{j'}^{back} \tag{3.12}$$

$$\theta_i^{front} = \theta_{i'}^{back} \tag{3.13}$$

where i, j, i', j' are the boundary nodes, such as nodes $m, n,$ in Figure 3.3, and nodes A, A' in Figure 3.11. i, j are nodes on the left, top or front surface of the periodic random fibre model, and i', j' are the corresponding nodes on the right, bottom or back surface of the model. u, v and w indicate the displacement in the x, y and z directions respectively, and θ is the rotation in all directions collectively. Note that on each boundary, one pair of nodes is selected, serving as the reference nodes for the displacement constraints, i.e., all the other pairs of nodes are related to the same pair of nodes, for example in the x direction, and conform to Eq. (3.2) - (3.4).

3.3.2 Loading

We have set reference nodes on x-boundary, y-boundary and z –boundary, described above, to apply the periodic boundary conditions. For uniaxial loading, to take x-

directional loading as an example, the reference node on the left x-boundary is fixed with three displacements constrained, and to the corresponding node on the opposite boundary is applied a tensile or compressive strain in the x direction. For biaxial loading or triaxial loading, the proportional straining is applied on the reference nodes in two directions or three directions simultaneously, for instance, $\varepsilon_x : \varepsilon_y = 1:1$, $\varepsilon_x : \varepsilon_z = 1:-1$, $\varepsilon_x : \varepsilon_y : \varepsilon_z = 1:1:2$.

To obtain the Young's modulus, for instance, in the x direction of the stochastic fibrous structure, a uniaxial strain ε_x is applied on the reference node in the x direction. In FE simulation, reaction forces can be accessed after solving the model. The reaction force and action force exerted on the pair of reference nodes have the same value F_r, but with different signs. With the reaction force, the stress in the x direction can be calculated by

$$\sigma_x = F_r / A \tag{3.14}$$

where A is the area of the y-z plane of the stochastic fibrous structure whose normal direction is the x direction.

Thus the Young's modulus E_x can be specified by

$$E_x = \sigma_x / \varepsilon_x \tag{3.15}$$

To determine the shear modulus, for instance G_{12}, a shear strain γ_{12} is applied along two directions of the RVE, as shown in Figure 3.12. One reference node on the x-boundary is fixed with UY, UZ, ROTX, ROTY, ROTZ constrained, and to the corresponding node on the opposite x-boundary is applied a strain of γ_{12} in the y direction. One reference node on the y-boundary is fixed with UX constrained and to

the corresponding node, on the opposite y-boundary, a strain of γ_{12} is applied in the x direction. The displacement boundary conditions are expressed as

$$u_y(x_1, y, z) - u_y(0, y, z) = \gamma_{12} * x_1 \tag{3.16}$$

$$u_x(x, y_1, z) - u_x(x, 0, z) = \gamma_{12} * y_1 \tag{3.17}$$

In FE simulation, the shear stress, τ_{12} can be obtained by F_y/A_{yz} (or F_x/A_{xz}), where F_y is the reaction force extracted from the x-boundary reference nodes, and A_{yz} is the area of the y-z plane of the RVE.

Thus the shear modulus G_{12} can be expressed as

$$G_{12} = \frac{\tau_{12}}{2\gamma_{12}} \tag{3.18}$$

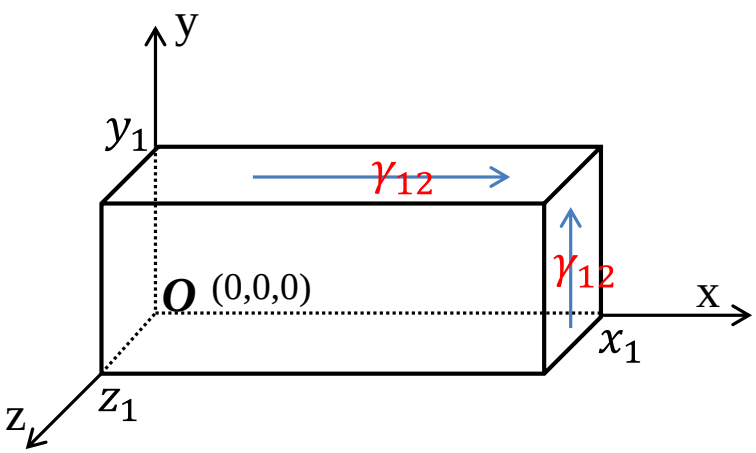

Figure 3.12. Shear displacement is applied along the x direction in the x-z plane, and along the y direction in the y-z plane to determine the shear modulus, G_{12}.

3.4 **Geometry transformation for shear loading**

Alternatively, to determine the shear modulus, an effective compressive strain in one direction and an effective tensile strain, with the same value, in the transverse direction are imposed simultaneously[1, 2]. As can be seen in the Mohr's circle for two-dimensional state of strain, shown in Figure 3.13, for the given coordinate system, the normal strain components, ε_1, ε_2 can be equivalent to the state of pure shear strain on a rotated coordinate system. The new coordinate system makes an angle, $\theta = 45°$ with the original coordinate system. By applying the normal strains in two transverse directions, the shear strain and stress through Mohr's circle and then the shear modulus can be determined. However, it should be noted that this method can be applied only when the material is isotropic. For instance, since the random beam model developed in this study is transversely isotropic in the x-y plane, an effective compressive strain and tensile strain can be applied to obtain the shear modulus, G_{12}, but not G_{13}.

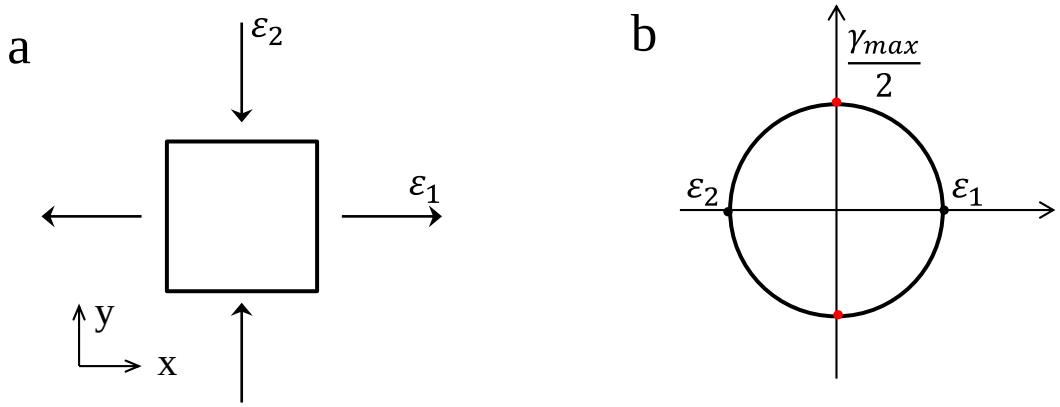

Figure 3.13. Mohr's circle for two-dimensional state of strain.

Considering a two-dimensional material, the elastic response follows Hook's law and can be written as

$$\sigma_1 = \frac{E_1}{1 - \nu_{12}\nu_{21}}\varepsilon_1 + \frac{\nu_{21}E_1}{1 - \nu_{12}\nu_{21}}\varepsilon_2 \tag{3.19}$$

$$\sigma_2 = \frac{\nu_{12}E_2}{1-\nu_{12}\nu_{21}}\varepsilon_1 + \frac{E_2}{1-\nu_{12}\nu_{21}}\varepsilon_2 \tag{3.20}$$

If the x-y plane is isotropic with $E_1 = E_2$ and $\nu_{12} = \nu_{21}$, when the material is subject to an effective tensile strain in the x direction and an effective compressive strain in the y direction($\varepsilon_1 = -\varepsilon_2$), the stresses become

$$\sigma_1 = \frac{E_1}{1+\nu_{12}}\varepsilon_1 \tag{3.21}$$

$$\sigma_2 = -\frac{E_1}{1+\nu_{12}}\varepsilon_1 \tag{3.22}$$

From Eq. (3.21) - (3.22), it can be seen that the normal stresses share the same value, but have a different sign. The Mohr's circle for two-dimensional state of stress, as shown in Figure 3.14a, suggests that the state of pure shear stress can be found in the new coordinate system, which makes an angle, $\theta = 45°$, with the original coordinate system. Thus, the coordinate systems for the state of pure shear strain and the state of pure shear stress coincide. So we can determine the shear modulus, G_{12} by this approach.

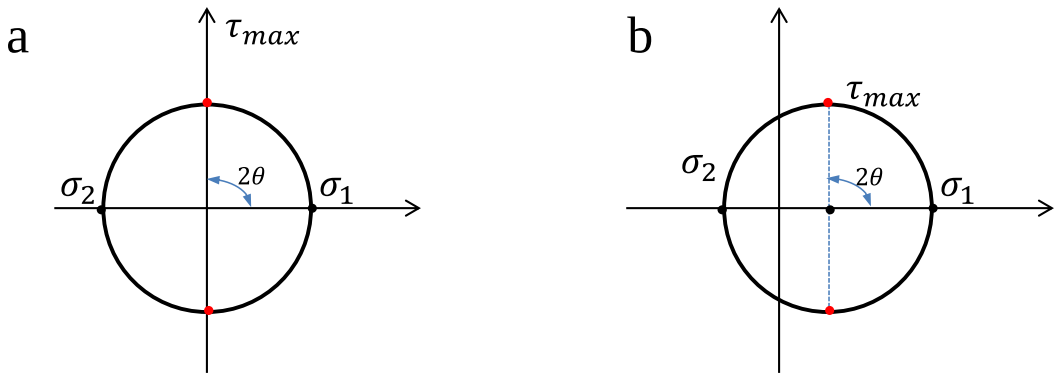

Figure 3.14. Mohr's circle for two-dimensional state of stress.

From the Eq. (3.19) - (3.20), it can be seen that if $E_1 \neq E_2$, the normal stresses would not satisfy $\sigma_1 = -\sigma_2$ when the material is subject to an effective compressive and tensile strain ($\varepsilon_1 = -\varepsilon_2$) simultaneously. As can be seen from Figure 3.14b, the state of stress at the 45° rotated coordinate system is not the state of pure shear stress ($\sigma \neq 0$). Therefore, the determination of shear modulus, G_{13} cannot use the above approach, as the stiffness of the stochastic fibrous structure in the x and z direction is different. The geometry transformation is required for shear loading. In the model developed in this study, as the fibres are layered one by one with cross-linkers inserted parallel to the z direction, the mechanical properties in the x direction are different from those in the z direction. In the new coordinate system, the properties of the stochastic fibrous material in the x' direction are the same as those in the z' direction, as shown in Figure 3.15. A new geometry based on the original RVE has been developed.

Firstly, control the thickness and make the x-z plane of RVE became a square. The new RVE in the $x'z'$ coordinate system is obtained by grouping four half old RVEs, as shown in Figure 3.15. An effective compressive strain in the z' direction and an effective tensile strain in the x' direction are imposed on the new geometry to determine the shear modulus, G_{13} of the stochastic fibrous material.

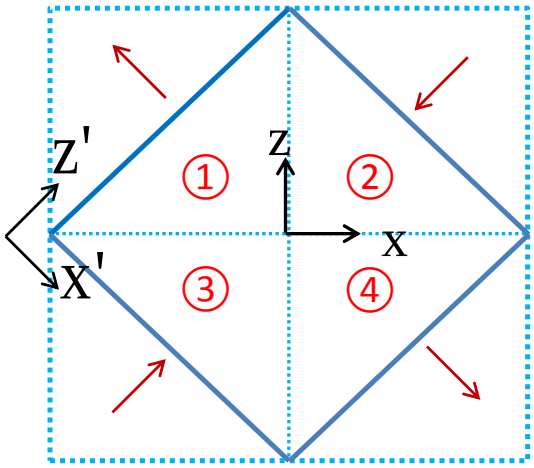

Figure 3.15. The geometry transformation for shear loading in the x-z directions.

In summary, the general idea for the geometry transformation is to apply the effective normal compressive/tensile strain on the 45° rotated coordinate system, in which the properties of the model in the x′ direction are the same as those in the z′ direction. This state of strain is equivalent to the state of pure shear strain on the previous x-z coordinate system after rotating the x′- z′ coordinate system back 45° in the Mohr's circle.

3.5 **Conclusions**

A three-dimensional random beam model has been developed to investigate the mechanical properties of stochastic fibrous materials. This introduces a novel way to deal with the connection between fibres by inserting an additional beam, which can be regarded as flexible cross-linker. Since the model is made of polylines, the relative density of the fibrous materials can be controlled by adjusting the concentration of intersections. To have more intersections, the fibre has to drop down to connect with others, which leads to a smaller thickness and a larger relative density. Apart from the

concentration of intersections, the coefficient of overlap can alter the thickness and relative density of the stochastic materials. Choosing an appropriate boundary condition is very important in the numerical simulation. Periodic boundary conditions have been applied to the periodic representative volume element (RVE). To determine the Young's modulus, an effective uniaxial tensile strain is imposed. To determine the shear modulus, a pair of shear strains is applied in transverse directions. Also, by applying the normal strains in two transverse directions, the shear strain and stress can be worked out through Mohr's circle and then the shear modulus is determined. However, it is worth noting that the rotated coordinate system of the state of pure shear strain and the state of pure shear stress coincides only when the material is isotropic. The beam model developed in this study shows anisotropy in the x-z plane. The approach to obtain the shear modulus, $G_{13,}$ by imposing an effective compressive strain in the x direction and an effective tensile strain in the z direction, does not suit this random beam model. Thus geometry transformation is conducted to work out the shear modulus, G_{13}.

Chapter 4 The Elastic Properties of Cytoskeletal Networks Based on a 3-D Stochastic Filament Model with FEA

Many mechanical behaviours of cells are determined largely by the networks of filamentous proteins called collectively the cytoskeleton. However, very little is known about how the macroscopic stress and strain are transmitted in the cytoskeletal networks. A continuum mechanics-based, three-dimensional, random-beam model of the filamentous structure of the cytoskeleton has been developed to investigate its elasticity by finite element analysis (FEA). The objective of this work has been to delineate how key features in anisotropic structure affect its stiffness. The periodic representative volume element (RVE) has been constructed for a stochastic filamentous structure with different concentrations of cross-linkers, degree of overlap and varying relative density. The results indicate the dominant deformation mechanism in the x direction gradually changes from bending to stretching with increasing relative density. In addition, there is a power law relationship between the Young's modulus in the z direction and the relative density.

4.1 **Introduction**

Cytoskeleton (CSK) is a network of filamentous proteins, composed of filamentous actin (F-actin), microtubules and intermediate filaments, within a cell's cytoplasm. More detailed information about the cytoskeleton can be found in Section 2.3.1. The

mechanical stiffness of intracellular material, to a great extent, is governed by the cytoskeleton[44]. It is crucial to build quantitative mechanical models describing the complicated behaviour of the cytoskeleton and predicting the effects of network parameters. The different mechanical behaviour of the cell is largely determined by the cytoskeleton, thus the study of cytoskeletal networks will contribute to the understanding of cell mechanics. As the cytoskeletal network is filamentous or cellular material, the relative density is a key parameter to elucidate the mechanical properties of cellular materials[1,2,10]. However, the relative density (i.e. the ratio of the volume (mass) of the filament to that of the cytoskeletal structure) is difficult to control in the process of building the reconstituted networks *in vitro*. Finite element method (FEM) which was originally developed for solving solid mechanics problems is a numerical method that offers a means to find the approximate solution. Computer modelling of the simplified cytoskeleton provides the opportunity to experimentally regulate microstructural features of the model. With the assistance of finite element method (FEM), a mechanical model of the cytoskeleton can be developed to probe the macroscopic stresses and strains. It is suggested that macroscopic stresses and strains can be determined by microscopic stresses and strain over a representative volume element (RVE). To begin with, a three-dimensional strut numerical model for stochastic cross-linked filaments has been constructed to quantitatively show the relationship between the macroscopic and microscopic elastic parameters in the randomly distributed filamentous structure. The objective has been to investigate the role of cross-linker and how the relative density affects the elastic properties of the stochastic filamentous network.

4.2 **Simulation methods**

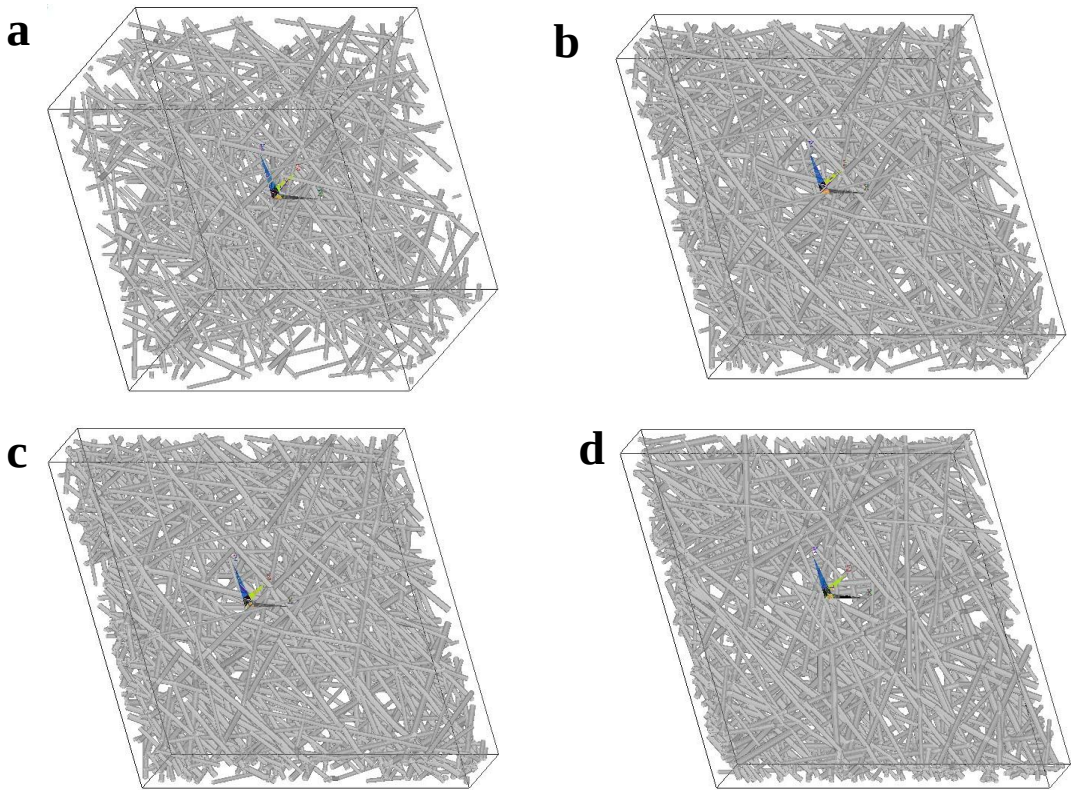

Figure 4.1. Three-dimensional random strut numerical models with different degree of overlap: (a) 0.95, (b) 0.6, (c) 0.5, (d) 0.4.

4.2.1 Periodical random beam model

A three-dimensional random strut numerical model is developed as shown in Figure4.1. The geometrical microstructure of the random beam model is generated by piling up randomly distributed lines/fibres one by one. The three-dimensional model is established progressively with two-dimensional coordinates being considered first. As the fundamental constituent of continuum mechanics, representative volume element (RVE) is adopted due to computational limitation. The RVE, which could be called 'unit cell', must be periodic. By creating *3w* x *3w* regions simultaneously in x direction and y direction with periodicity of *w*, the central region is selected to be periodic. The coordinates in 3-D space of every key point on the lines/fibres can be

derived by the relative positions and 2-D coordinates. Further construction details relating to the 3-D random beam mode can be found in Chapter 3. In addition, it has been suggested that the periodic boundary conditions are more suitable than the mixed boundary conditions and prescribed displacement boundary conditions[1, 2]. In the numerical simulation, the three-node beam element (BEAM189) based on the Timoshenko beam theory is utilized. The constituting solid material of a filament is assumed to be elastic with Young's modulus of 1.0. The non-dimensional equivalent Young's modulus is one of the main objectives of the study, with respect to the characteristic of fibrous structure. A stress-strain curve is given in Figure 4.2 for a filamentous network with the Young's modulus of constituting solid material $E_s = 210GPa$. As can be seen in Figure 4.2, the structure behaves linearly when the strain is sufficiently small. Due to the linearity, it is worth noting that by assuming a unit modulus of the solid material, the Young's modulus of the structure is equivalent with non-dimensional Young's modulus of the structure which is Young's modulus of the structure normalized against the Young's modulus of the solid material. As it has been indicated, the Poisson ratio of isotropic solids mostly varies between 0.1 and 0.5[109], the Poisson ratio of the filaments is set at 0.3. To measure the Young's modulus, or shear modulus, of the filamentous network, a uniaxial tensile or shear strain is applied across the periodic boundary conditions.

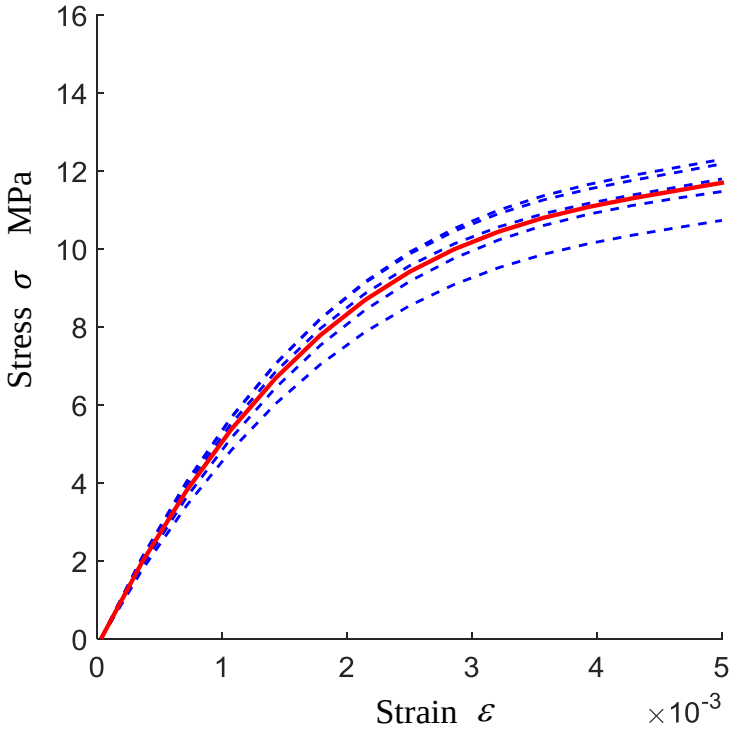

Figure 4.2. Stress-strain curves under uniaxial loading in the x direction. Red solid line was obtained from averaging the blue dashed lines.

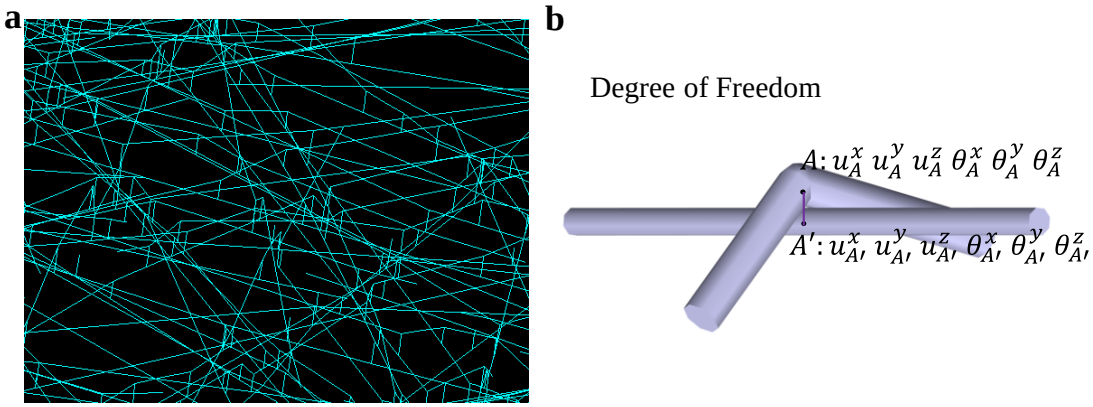

Figure 4.3. Two types of cross-linker in the three-dimensional random beam model: (a) flexible cross-linker by inserting an additional beam between intersected filaments; (b) comparatively firm cross-linker by constraining all the degrees of freedom of paired nodes.

4.2.2 Cross-linker

In the cytoskeletal networks of filamentous actin (F-actin), cross-linking proteins stabilize the network and strengthen the rigidity of the cytoskeleton. A myriad of

research publications have shown that the density or the concentration of cross-linkers largely determines the elastic properties of the filamentous actin networks *in vitro*[48,55,57,110–115]. The cross-linker concentration is defined by the ratio L/l_c, where l_c is the mean distance between cross-linkers along a filament of length L. In the numerical model, an innovative way to deal with the cross-linker is introduced in the three-dimensional random beam model. As shown in Figure 4.3, each filament is represented by a line of length L, and to effectively mimic the real F-actin network, the lengths are not uniform, ranging from 0.8 to 1.2, dimensionlessly. All the lines are deposited with random position and orientation with a range of 2π. An additional beam with three nodes is inserted at the intersection point of two lines in the thickness direction (z direction). The inserted beams represent the cross-linkers in the cytoskeletal networks. The three nodes on the inserted beam share the same x and y coordinate values, with the two endpoint nodes on the two connected lines, and the midpoint node in the middle of endpoint nodes vertically. A set of nodes $\{x_j^i\}$, ($i = 1,2,..N; j = 1,2,..L/l_c$; where N is the number of filaments) indicates the endpoint nodes of all the cross-linkers. By inserting beam element at the intersections, it can be identified as the freely rotating cross-linker. Moreover, we can constrain the two corresponding nodes in the set $\{x_j^i\}$, by coupling their degrees of freedom, as shown in Figure 4.3(b). For instance, by coupling all the translation displacements UX, UY, UZ, and all the rotation displacements, ROTX, ROTY, ROTZ, it can be identified as the comparatively firm cross-linker. It is not hard to understand that an increase in cross-linker numbers will give rise to a decrease in the size in the z direction, i.e., the thickness of the structure, since the line (beam) needs to fall down to intersect with other lines, in this three-dimensional model process, so that more cross-linkers can be generated.

4.2.3 Overlap coefficient

To construct a stochastic filamentous structure in 3-D, the distance δ between the central axes of any two intersected beams should be larger than zero. The Overlap coefficient c defined as below describes the degree of overlap between any two crossed lines (beams), $c = \delta/d_{0,}$ where d_0 is the sum of radii of the two crossed lines. For a two-dimensional model, δ equals zero and c is 0. The coefficient, c is a variable to describe the extent of overlap within the range of [0, 1]. When c is zero, lines are completely overlapping, which is the same as the two-dimensional model. Without any doubt that the overlap coefficient will affect the length of the inserted beam which is equal to the distance δ. The length of a beam is a key parameter that determines the bearing capacity of the beam subjected to loads. Thus, the overlap coefficient is of significant importance in the numerical modelling, especially when dealing with the cross-linker as an inserted beam. Also, the degree of overlap alters the thickness t of the cross-linked structure. Examples with different overlap coefficients have been shown in Figure 4.1. Even when coupling the intersection nodes instead of inserting beam element, the degree of overlap will make a difference to the elastic properties of the random beam model.

4.2.4 Relative density

It has been suggested that the macroscopic elasticity of cytoskeletal networks not only depends on the concentration of cross-linkers, but also upon the density of filaments in the networks[13]. Gibson and Ashby have shown that the simplest and most straightforward way to analyse the mechanical properties of cellular materials is to use dimensional analysis[4], which emphasises the dependence of mechanical properties on the relative density of the structure. By calculating the average value of all the

distances between the constrained top and bottom nodes in the z direction, the thickness t is obtained. Based on the thickness, the relative density of the fibrous material is specified by:

$$\rho = \frac{\sum_{i=1}^{N} L_i * (\frac{1}{4} * \pi {d_i}^2)}{(1 * 1 * t)} \tag{4.1}$$

where L_i are the filament lengths, N is the number of filaments and d_i are the diameters of the circular cross sections. Since the filaments are randomly distributed within the periodicity of w=1 in the x and y directions, $1 * 1 * t$ refers to the volume of the fibrous structure. From the Eq. (4.1), the dependence of relative density on the geometry or the architecture of the structure, e.g., the length and the diameter of the line is evident. Also, the thickness is a key parameter in determining the relative density of the structure. Note that the thickness of a fibrous network depends on the overlap coefficient, concentration of the cross-linkers, the filament diameter, and the number of the filaments.

4.2.5 Statistical analysis

As the morphology of cytoskeletal networks varies so much, one single geometrical model is inadequate to describe the complexity of the cytoskeleton. In this study periodical random structures have been constructed with a range of lengths, diameters and orientations of all the filaments taken into consideration. These random numbers are obtained from the function in MATLAB, which generates uniformly distributed pseudorandom numbers between 0 and 1. The model is random, so to get the mechanical parameters, massive calculation and statistical analysis are needed. Mean results and standard deviations are obtained from twenty independent, but similar structural models with the same set/combination of different parameters.

4.2.6 Mesh sensitivity

A mesh sensitivity study has been performed by changing the total number of filaments, *N* for samples having the concentration of cross-linker, $L/l_c = 6$. Twenty random models were investigated for each different total number of filaments, N=50, 75, 100, 150, 200, 400. Note that with more filaments, the cell size is getting larger in the thickness direction. Each fibrous structure was generated using a different list of random numbers, and had the same diameter range, $d \in [0.01,0.02]$, and the same overlap coefficient, $c = 0.95$. The statistical test of reaction force, Young's modulus in the x direction, and the relative density, were conducted and shown in Table 4.1. The results presented below were obtained by using the finite element solver of ANSYS APDL software. As can be seen from Table 4.1, the mean densities and Young's moduli in the x direction are almost the same in all the cases, N=50, 75, 100, 150, 200, 400. While the standard deviations for both Young's modulus and density are trending downward, i.e., the larger the number of filaments, the smaller will be the standard deviation. Theoretically, the reaction force of double layers should be twice as strong as that of a single layer (i.e., N=100 vs. N=50, N=200 vs. N=100…), when all the other conditions are completely the same. The ratio of the reaction forces of two corresponding cases are listed in Table 4.2, and the ratio is the mean value of twenty paired samples. It is worth noting that when the number of filaments increases, the ratio between the reaction forces of one and two layers approaches two. When N=200, the standard deviations of the density, the Young's modulus in the x direction and the reaction force are very small. Also, in consideration of computational efficiency, the finite element results shown below are the mean results over twenty random samples having a total number of filaments fixed at N=200.

Table 4.1. The statistics of the density, Young's modulus in the x direction and the reaction force over 20 samples for the number of filaments N=50, 75,100, 150, 200, 400, with the concentration of cross-linker at $L/l_c = 6$, the overlap coefficient at $c = 0.95$, and the mean slenderness ratio at 1.5%.

Descriptive Statistics

Density

	Mean	Std. Deviation	95% Confidence Interval for Mean		Minimum	Maximum
			Lower Bound	Upper Bound		
N=50	.06596645	.005283758	.06349358	.06843932	.058416	.073771
N=75	.06513645	.003876645	.06332212	.06695078	.057409	.072516
N=100	.06683480	.001796309	.06599410	.06767550	.064115	.070695
N=150	.06661080	.002495420	.06544291	.06777869	.062340	.071749
N=200	.06505695	.001890000	.06417240	.06594150	.062176	.068886
N=400	.06609510	.001473404	.06540553	.06678467	.063357	.068021

Young's modulus

	Mean	Std. Deviation	95% Confidence Interval for Mean		Minimum	Maximum
			Lower Bound	Upper Bound		
N=50	1.7530E-03	3.97268E-04	1.5671E-03	1.9389E-03	1.04E-03	2.49E-03
N=75	1.7964E-03	4.10587E-04	1.6042E-03	1.9886E-03	6.98E-04	2.60E-03
N=100	1.8155E-03	3.00902E-04	1.6747E-03	1.9563E-03	1.37E-03	2.45E-03
N=150	1.8214E-03	3.36228E-04	1.6641E-03	1.9788E-03	8.79E-04	2.42E-03
N=200	1.7985E-03	1.65315E-04	1.7211E-03	1.8759E-03	1.48E-03	2.13E-03
N=400	1.8225E-03	1.21952E-04	1.7654E-03	1.8796E-03	1.58E-03	2.10E-03

Reaction Force

	Mean	Std. Deviation	95% Confidence Interval for Mean		Minimum	Maximum
			Lower Bound	Upper Bound		
N=50	2.4386E-07	5.01092E-08	2.2041E-07	2.6731E-07	1.50E-07	3.41E-07
N=75	3.7608E-07	8.02353E-08	3.3853E-07	4.1363E-07	1.60E-07	5.40E-07
N=100	5.0458E-07	8.73045E-08	4.6372E-07	5.4544E-07	3.89E-07	6.87E-07
N=150	7.5251E-07	1.25882E-07	6.9359E-07	8.1142E-07	3.98E-07	9.83E-07
N=200	1.0010E-06	8.92792E-08	9.5918E-07	1.0427E-06	8.26E-07	1.17E-06
N=400	2.0143E-06	1.40250E-07	1.9487E-06	2.0800E-06	1.80E-06	2.36E-06

Table 4.2. The mean ratio of paired reaction forces over twenty random samples.

	N100/N50	N150/N75	N200/N100	N400/N200
Mean Ratio	2.162423	2.119755	2.045563	2.033126

4.3 **Numerical results**

4.3.1 Transversely isotropic properties

The two-dimensional networks of isotropic, homogenously cross-linked actin have been presented[116]. One of the significant features incorporated into the three-dimensional beam model is the anisotropic elasticity of the filamentous networks. Table 3 lists Young's moduli, shear moduli and Poisson's ratios of 20 models with the concentration of cross-linker $L/l_c = 10$, the overlap coefficient, c of 0.95 and the number of filaments N=200, the diameter ranging from 0.010 to 0.020.

It is shown that the mean values of Young's modulus and the Poisson's ratio for 20 models are almost identical in the x and y directions. The results suggest the elastic properties of random fibrous structures are isotropic in the x-y plane. In addition, the observed values of Young's modulus and Poisson's ratio satisfy:

$$\frac{E_x}{E_y} * \frac{\nu_{21}}{\nu_{12}} = 0.997155194 \text{ (The mean value)} \tag{4.2}$$

$$\frac{E_x}{E_z} * \frac{\nu_{31}}{\nu_{13}} = 1.004540088 \text{ (The mean value)} \tag{4.3}$$

$$\frac{E_y}{E_z} * \frac{\nu_{32}}{\nu_{23}} = 1.004046493 \text{ (The mean value)} \tag{4.4}$$

The above equations imply that the relationship between Young's modulus and Poisson's ratio is,

$$\frac{E_i}{E_j} = \frac{\nu_{ij}}{\nu_{ji}} \tag{4.5}$$

Table 4.3. The non-dimensional Young's moduli, shear moduli and Poisson's ratios of 20 periodic filamentous structures with 200 filaments, density of cross-linker $L/l_c = 10$, degree of overlap $c = 0.95$ and the mean value of aspect ratio at 1.5%.

	Ex	v12	v13	Ey	v21	v23
1	5.723E-03	0.285744	1.21925	5.795E-03	0.288937	1.57524
2	6.316E-03	0.301886	1.11942	5.618E-03	0.270425	1.34235
3	5.308E-03	0.333524	0.82134	4.765E-03	0.300303	0.82170
4	5.604E-03	0.279462	0.83292	6.006E-03	0.293877	0.98153
5	5.472E-03	0.273270	1.21001	4.926E-03	0.245830	1.09657
6	5.238E-03	0.280950	1.12880	5.429E-03	0.291075	1.19702
7	5.915E-03	0.323796	1.19239	5.347E-03	0.293300	0.88433
8	5.242E-03	0.307554	0.82397	4.896E-03	0.282599	1.22579
9	5.458E-03	0.240946	1.46975	5.079E-03	0.224540	1.51231
10	5.230E-03	0.282815	0.94208	6.565E-03	0.354410	1.31206
11	4.479E-03	0.298303	0.91895	5.003E-03	0.322426	0.86887
12	5.176E-03	0.273343	1.43650	5.609E-03	0.295320	1.20214
13	5.822E-03	0.263016	1.71740	5.647E-03	0.255191	1.13037
14	5.618E-03	0.333085	1.14812	3.910E-03	0.231321	1.06922
15	5.913E-03	0.327621	1.14331	5.407E-03	0.300466	1.05081
16	5.331E-03	0.267546	0.92498	6.422E-03	0.323592	1.38776
17	4.590E-03	0.295067	1.25848	4.608E-03	0.296369	1.04840
18	5.529E-03	0.345179	1.55146	4.915E-03	0.306887	0.82896
19	4.856E-03	0.252683	0.72066	6.960E-03	0.361404	1.71686
20	5.569E-03	0.300357	1.83414	5.644E-03	0.304396	1.14066
Mean	5.419E-03	0.29330735	1.17069665	5.427E-03	0.2921334	1.1696473
Std.	4.318E-04	0.02796125	0.29972837	6.995E-04	0.0342564	0.2423874

	Ez	v31	v32	G12	G13	G23
1	3.366E-05	0.00720060	0.00914950	2.236E-03	4.398E-05	4.070E-05
2	3.811E-05	0.00709433	0.00921579	2.323E-03	4.598E-05	3.939E-05
3	4.223E-05	0.00664811	0.00736513	1.919E-03	4.274E-05	4.506E-05
4	5.005E-05	0.00738592	0.00810776	2.247E-03	4.445E-05	4.301E-05
5	3.250E-05	0.00721327	0.00726901	2.066E-03	4.541E-05	4.065E-05
6	3.790E-05	0.00816300	0.00835671	2.074E-03	4.071E-05	4.086E-05
7	4.591E-05	0.00921959	0.00762749	2.152E-03	4.090E-05	4.200E-05
8	3.674E-05	0.00589903	0.00890294	1.952E-03	3.995E-05	3.911E-05
9	3.920E-05	0.01054560	0.01174210	2.138E-03	4.530E-05	3.952E-05
10	5.501E-05	0.00989064	0.01143940	2.247E-03	4.068E-05	4.829E-05
11	3.732E-05	0.00784442	0.00682279	1.798E-03	4.429E-05	4.007E-05
12	3.655E-05	0.00968536	0.00787307	2.099E-03	4.079E-05	4.262E-05
13	3.651E-05	0.01072680	0.00727374	2.277E-03	4.297E-05	4.144E-05
14	4.315E-05	0.00880258	0.01188460	1.875E-03	4.103E-05	3.945E-05
15	4.278E-05	0.00858839	0.00829631	2.156E-03	4.570E-05	4.482E-05
16	4.709E-05	0.00814191	0.01018070	2.276E-03	3.867E-05	4.897E-05
17	3.875E-05	0.01060450	0.00880013	1.770E-03	3.861E-05	4.397E-05
18	4.629E-05	0.01300300	0.00766342	1.972E-03	4.607E-05	4.212E-05
19	4.957E-05	0.00736959	0.01228270	2.284E-03	3.996E-05	4.907E-05
20	3.809E-05	0.01253120	0.00770028	2.152E-03	4.588E-05	4.288E-05
Mean	4.137E-05	0.00882789	0.00889768	2.101E-03	4.270E-05	4.270E-05
Std.	5.829E-06	0.00187897	0.00166724	1.645E-04	2.534E-06	3.069E-06

From the results it can be seen that the shear modulus, Young's modulus and Poisson's ratio in the x and y direction meet that,

$$\bar{G}_{12} = 0.5\bar{E}_x/(1+\bar{v}_{12}) \tag{4.6}$$

where E_x can be replaced by E_y, and ν_{12} can be replaced by ν_{21}. In addition, $G_{13} = G_{23}$, $\nu_{13} = \nu_{23}$, $\nu_{31} = \nu_{32}$. These all suggest that the stochastic fibrous structure is transversely isotropic. Note that the means of 20 samples in Table 4.3 give an isotropic response in the x and y direction, but for a given cell, for instance, cell 19, it can be anisotropic. The isotropy of macro structure can be reached by assembling different cells such as those tabulated in Table 4.3, rather than periodically replicating a single cell.

4.3.2 The dimension of inserted beam

In this model, the relatively flexible cross-linkers in the cytoskeletal network can be represented by inserted beam, as delineated above. Apart from the length, δ of the inserted beam, which can be determined by the overlap coefficient, $c = \delta/d_0$, the diameter, $d'$of the inserted beam is of great importance. It could be half the diameter of the filaments, or a third, or fourth, depending on the biomaterials. Here, the diameter of the inserted beam is determined from the stand point of solid mechanics, by studying the stiffness of the inserted beam. It is assumed that two overlapped solid bodies can be equivalent to a spatial structure consisting of two crossed beams and one inserted beam. As can be seen from Figure 4.4, two models have been constructed in which the same boundary conditions and the same loading are applied. One is utilized for simulation in the finite element software, the other one is for the theoretical solution.

The principle of virtual forces is one of the energy principles in structural mechanics. When the structure is subject to external force, the deflection, Δ, can be found by unite load method:

$$\Delta = \sum \int \frac{M\overline{M}}{EI} ds + \sum \int \frac{N\overline{N}}{EA} ds + \sum \int \frac{T\overline{T}}{GI_P} ds + \sum \int \mu \frac{Q\overline{Q}}{GA} ds \qquad (4.7)$$

where M, N, T and Q represent the bending moment, axial force, torsional moment and shearing force due to actual loading, respectively. $\overline{M}$, $\overline{N}$, $\overline{T}$, $\overline{Q}$ are the bending moment, axial force, torsional moment and shearing force due to virtual unit load, respectively. μ is 10/9. The materials of all the beams in Figure 4.4(b) are the same with the parameters: Young's modulus E, shear modulus G. The diameters of circular cross section in beam *AB* and beam *CD* are the same at d, which is the mean value of all the beams (lines) in the periodical stochastic filamentous structure (the second moment of the filament cross-sectional area $I = \frac{\pi d^4}{64}$, polar second moment of area $I_P = \frac{\pi d^4}{32}$, area of the cross section $A = \frac{\pi d^2}{4}$). The diameter d' of the inserted beam *BC* is to be determined.

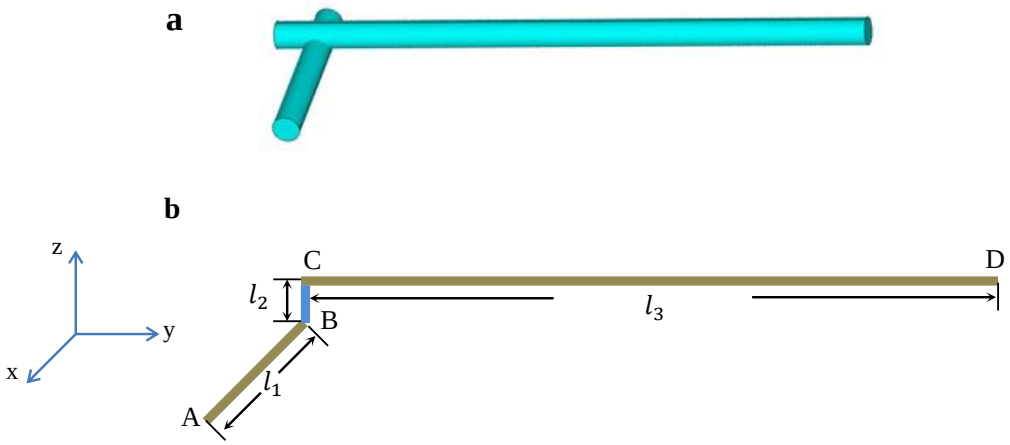

Figure 4.4. The schematic diagrams of the intersected beams in the model: (a) represents two overlapped solid bodies used in the simulation, (b) indicates spatial structure consisting of two crossed beams and one inserted beam, and this equivalent structure can be used in the theoretical solution.

Beam *CD*

F_x

$$\delta = \frac{10F_x l_3}{9GA}$$

Shearing force diagram Q

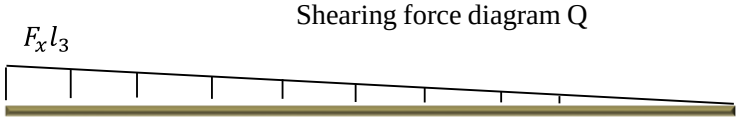

$$\delta = \frac{F_x {l_3}^3}{3EI}$$

Bending moment diagram M

Beam *BC*

$$\delta = \frac{10F_x l_2}{9G'A'}$$

Shearing force diagram Q

$$\delta = \frac{F_x {l_2}^3}{3E'I'}$$

Bending moment diagram M

$$\delta = \frac{F_x l_2 {l_3}^2}{G' {I_P}'}$$

Torsional moment diagram T

Beam *AB*

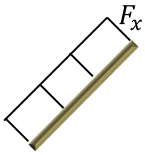

$$\delta = \frac{F_x l_1}{EA}$$

Axial force diagram N

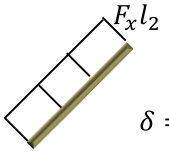

$$\delta = \frac{F_x {l_2}^2 l_1}{EI}$$

Bending moment diagram M_y

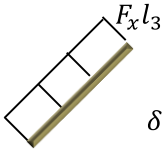

$$\delta = \frac{F_x {l_3}^2 l_1}{EI}$$

Bending moment diagram M_z

Figure 4.5. The internal force diagrams of the spatial structure shown in Figure 4.4(b) subjected to a force in the x direction.

For two interested beams/filaments AB and CD with AB in the x direction and CD in the y direction, as shown in Figure 4.4, end A is fixed (no displacement or rotation), and a force F_x is applied at end D in the x direction. The internal force diagrams are listed in Figure 4.5.

Thus, the displacement of end *D* in the x direction, Δ_x, can be obtained using structural mechanics, and expressed as:

$$\Delta_x = \frac{F_x {l_3}^3}{3EI} + \frac{10F_x l_3}{9GA} + \frac{F_x l_1}{EA} + \frac{F_x l_1 ({l_2}^2 + {l_3}^2)}{EI} + \frac{10F_x l_2}{9GA'} + \frac{F_x {l_2}^3}{3EI'} + \frac{F_x {l_3}^2 l_2}{G{I_P}'} \quad (4.8)$$

Now, alternatively, we mesh the two connected filaments, shown in Figure 4.4(a), into a large number of tetrahedral elements and use commercial finite element software ANSYS to obtain the displacement of end *D* in the x direction. With the force, F_x and deflection, Δ_x both known, the diameter, d' can be obtained by substituting values of F_x, Δ_x from simulation into Eq.(4.8).

In the simulation, a slenderness ratio sensitivity study has been performed, based on a simple solid undergoing a transverse loading, as shown in Table 4.4. It indicates that the accuracy of solid element solving the problem of beam is high.

Table 4.4. The effect of slenderness ratio in the solid simulation and theory of beam with one end fixed and one free end applied a transverse displacement 0.1.

Ratio(L/d) / Results	5	10	20	30	40	60
F_s(Simulation)	2.3366e-5	2.9494e-6	3.6892e-7	1.0927e-7	4.6083e-8	1.3649e-8
F_t(Theoretical)	2.3062e-5	2.9294e-6	3.6766e-7	1.0902e-7	4.6004e-8	1.3633e-8
Error $(F_s - F_t)/F_t$	1.32%	0.68%	0.34%	0.23%	0.17%	0.11%

It is not surprising that, with a fixed overlap coefficient, the overlapped volume between the two solid filaments would not alter with a change in the length of the two filaments. In Table 4.5, it can be seen that, when *c* is 0.4, the calculated diameter, d' of inserted beam encompassed by two solids with different dimensions shows small changes. It is also true in the case of *c*=0.95.

Table 4.5. The diameters of the inserted beam obtained from the combination of FEA simulation and theory of beam, with overlap coefficients at 0.4 and 0.95. In each case, the dimensions of the solids (beams) can be changed and show no significant effect on the value of diameter d'.

	c=0.4($l_2 = 0.4d$)	*c*=0.95($l_2 = 0.95d$)
$l_1 = 5d; l_3 = 20d$	0.863d	0.671d
$l_1 = 5d; l_3 = 40d$	0.887d	0.677d
$l_1 = 10d; l_3 = 40d$	0.865d	0.674d

Considering the possible errors that would occur in the simulation, the calibrations of Young's modulus *E* have been conducted in terms of different dimensions of the solids (beams). A model has been built with two solid filaments completely overlapped, in which no inserted beam is needed at the intersection, as the length, l_2 equals to zero (or *c*=0). Without any unknown variables, the results of FEA simulations can be compared with the theoretical results obtained from structural mechanics. When end A is fixed and a force F_x is applied at end *D* in the x direction, the displacement of the end *D* can be expressed as:

$$\Delta_x = \frac{F_x {l_3}^3}{3EI} + \frac{10F_x l_3}{9GA} + \frac{F_x l_1}{EA} + \frac{F_x {l_3}^2 l_1}{EI} \tag{4.9}$$

Table 4.6. The calibrated Young's modulus, E^* in three models with different dimensions of the beams.

	$l_1 = 5d; l_3 = 20d$	$l_1 = 5d; l_3 = 40d$	$l_1 = 10d; l_3 = 40d$
E^*	1.0390	1.0249	1.0195

In the simulation, the diameter, d is set as 0.2, the Young's modulus, E is 1, and Poisson's ratio, ν is 0.3. The force F_x or the deflection Δ_x can be obtained from the simulation, by substituting the values into Eq.(4.9), the calibrated E^* can be obtained as shown in Table 4.6. As can be seen from Table 4.7, with the calibration of Young's modulus, the effect of dimensions of solids on the diameter d' is smaller. It indicates that the introduction of calibrated Young's moduli, which are based on the beam dimensions, can effectively offset the influence of dimensions. Thus, the determination of the diameter of inserted beam is more accurate.

Table 4.7. The diameters of inserted beam, d' with overlap coefficient $c = 0.4$, and $c = 0.95$. Comparison between simulations with a normal Young's modulus E and a calibrated Young's modulus E^* with different dimensions of solids.

	$c = 0.4$ ($l_2 = 0.4d$)		$c = 0.95$ ($l_2 = 0.95d$)	
	with E	*with E**	*with E*	*with E**
$l_1 = 5d; l_3 = 20d$	*0.863d*	*0.777d*	*0.671d*	*0.653d*
$l_1 = 5d; l_3 = 40d$	*0.897d*	*0.798d*	*0.677d*	*0.661d*
$l_1 = 10d; l_3 = 40d$	*0.865d*	*0.780d*	*0.674d*	*0.659d*

Apply a force at end D in the z direction, and end A is fixed with no displacement or rotation. The displacement of end D in the z direction, Δ_z, can be expressed as:

$$\Delta_z = \frac{F_z {l_3}^3}{3EI} + \frac{10F_z l_3}{9GA} + \frac{F_z {l_3}^2 l_1}{GI_P} + \frac{10F_z l_1}{9GA} + \frac{F_z {l_1}^3}{3EI} + \frac{F_z l_2}{EA'} + \frac{F_z {l_3}^2 l_2}{EI'} \quad (4.10)$$

Similarly, with the force F_z or deflection Δ_z obtained from the simulation, the only unknown variable d' in Eq.(4.10) can be calculated. With a calibrated Young's modulus E^*, the diameters of inserted beam d' for different overlap coefficients are listed in Table 4.8.

Table 4.8. The diameters of inserted beam, d', with overlap coefficient $c = 0.4$, and $c = 0.95$ with different dimensions of solids when the structure is subjected to a loading in the z direction.

	$c = 0.4$ ($l_2 = 0.4d$) *with* E^*	$c = 0.95$ ($l_2 = 0.95d$) *with* E^*
$l_1 = 5d; l_3 = 20d$	*0.711d*	*0.588d*
$l_1 = 5d; l_3 = 40d$	*0.738d*	*0.597d*
$l_1 = 10d; l_3 = 40d$	*0.714d*	*0.594d*

As can be seen from Table 4.7 and 4.8, the diameter of inserted beam calculated from the equivalence of these structures shown in Figure 4.4 is slightly sensitive to the mode of loading. To have a values of d' satisfied both equations, Eq.(4.8) and Eq.(4.10), another variable could be freed, for instance, the Young's modulus of the inserted beam E'. Then two unknown variables related to the inserted beam *BC*, (E', d') could be obtained by solving these simultaneous equations. However, the results were not reasonable with a negative value of d'^2. Alternatively, μ could be freed, which was set as 10/9 in Eq.(4.8) in the part related to beam *BC*. Also no suitable value of the diameter d' was achieved.

When the loading is applied in the x direction, the inserted beam undergoes torsion, apart from the bending, which induces a relatively larger diameter d' compared to the case when the structure is subjected to a loading in the z direction. Torsion is of great importance in the elasticity of the filamentous networks. Thus, the numerical results, with respect to the elastic behaviour of a cytoskeleton with flexible cross-linkers, are

based on the beam model with the diameter of inserted beam at $d' = 0.780d(c = 0.4)$ and $d' = 0.659d(c = 0.95)$, which were obtained when the loading was applied in the x direction and the torsion was incorporated.

4.3.3 Five independent elastic constants

Generalized Hooke's law, which defines the most general linear relation between the stress and the strain, can be expressed as

$$\sigma_{ij} = C_{ijkl}\varepsilon_{kl} \tag{4.11}$$

where σ_{ij} and ε_{kl} are the components of stress tensor and strain tensor, and C_{ijkl} are the components of the fourth-order stiffness tensor of the material, respectively. For orthotropic material, there are three mutually orthogonal planes of reflection symmetry. The number of independent stiffness coefficients is 9 and the stiffness tensor can be expressed as

$$C = \begin{bmatrix} C_{1111} & C_{1122} & C_{1133} & 0 & 0 & 0 \\ & C_{2222} & C_{2233} & 0 & 0 & 0 \\ & & C_{3333} & 0 & 0 & 0 \\ & & & C_{2323} & 0 & 0 \\ & symm & & & C_{1313} & 0 \\ & & & & & C_{1212} \end{bmatrix} \tag{4.12}$$

For transversely isotropic material, the mechanical properties are symmetric about the z axis, which is normal to the plane of isotropy (x-y plane), in addition to the three mutually orthogonal planes of reflection symmetry. The properties in the x direction are identical to those in the y direction. The number of independent stiffness coefficients is then reduced to 5, and the stiffness tensor is given by

$$C = \begin{bmatrix} C_{1111} & C_{1122} & C_{1133} & 0 & 0 & 0 \\ & C_{1111} & C_{1133} & 0 & 0 & 0 \\ & & C_{3333} & 0 & 0 & 0 \\ & & & C_{2323} & 0 & 0 \\ & symm & & & C_{2323} & 0 \\ & & & & & C_{1212} \end{bmatrix} \tag{4.13}$$

where $C_{1212} = \frac{1}{2}(C_{1111} - C_{1122})$.

It has been suggested that the random beam model developed to represent a stochastic filamentous structure, is transversely isotropic. All the five independent elastic constants of the material and their dependence on the relative density are investigated in this section.

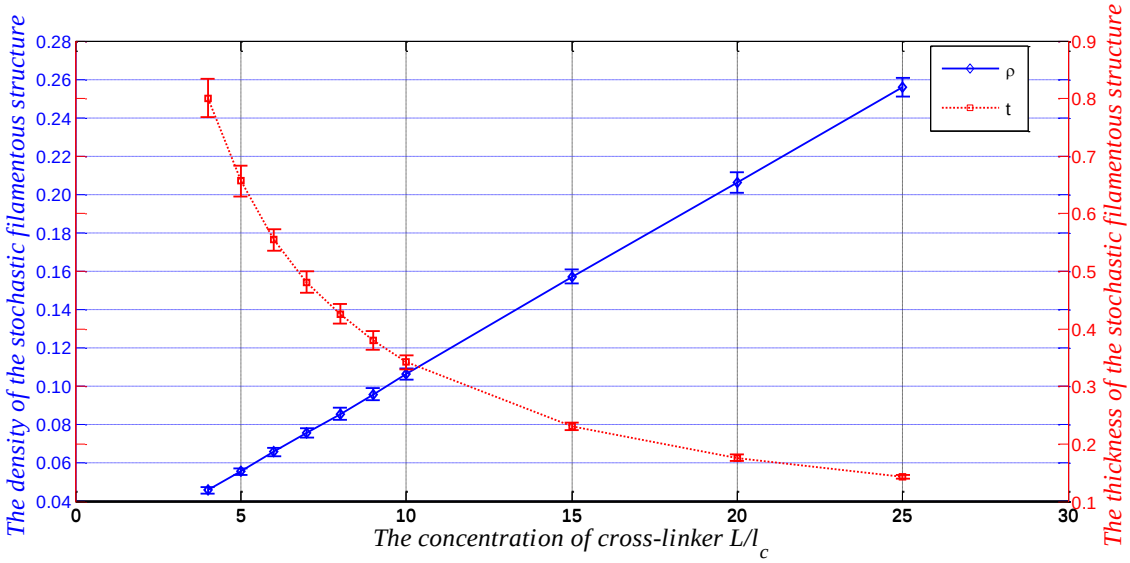

Figure 4.6. Effect of the concentration of cross-linkers, L/l_c , on the density (blue solid line), and thickness (red dashed line), of the stochastic filamentous structure.

It is not surprising that the density of the stochastic filamentous structure is increasing and the thickness is decreasing with increasing concentration of cross-linker, based on the three-dimensional beam model developed. The results are illustrated in Figure 4.6, and it can be seen that as the concentration of cross-linker, L/l_c , increases, there is a negative exponential decay in the thickness of the filamentous network. In contrast,

the relative density increases almost linearly. Thus, the effects of the density of cross-linker and the relative density on the elastic constants are equivalent, with the recognition that the former is in terms of geometry and the latter is an intrinsic parameter of the structure.

First, an analysis of the Young's modulus of the random beam model representing the cytoskeletal networks is given. As the structure is transversely isotropic in the x-y plane, i.e.,$E_x = E_y$, the Young's modulus is only tested in the x and z directions by imposing an effective tensile strain of 1% in the x and z directions in separate analyses. Here, for computational efficiency, the frequency and nonlinearity are ignored and attention is focused on the static networks of filament in the linear elastic regime. The applied strain is quite small due to the fact that, for many biopolymer networks, the onset of stiff-stiffening will occur when the strain is on the order of 5%[110]. It is worth noting that the compressive modulus and the extensional modulus are the same in this model in which a compressive strain of -1% and a tensile strain of 1% are imposed, respectively. The non-dimensional effective Young's moduli in the x and the z directions are obtained as functions of relative density by changing the concentration of cross-linker L/l_c with the degrees of overlap at $c = 0.4$ and $c = 0.95$, and are given in Figure 4.7. From the graphs, it can be seen that there is a discrepancy between the Young's moduli in the x and z directions, also, the overlap coefficient plays a significant role. The different tendencies show different deformation mechanisms in the x and z directions. Strut bending is the dominant deformation mechanism in the x direction for low-density filamentous networks, whose effective Young's modulus is proportional to $E_s\rho^3$, whereas for high-density filamentous networks, the mechanical properties and relative density follow a linear relationship, suggesting that strut stretching dominates the deformation. Since the relative density

is regulated by the concentration of cross-linkers, it implies that with more connectivity in the cytoskeleton, the deformation mechanism in the x direction is stretch-dominated, but with less connectivity; it is bending-dominated. The overlap coefficient can alter the critical value of density where the deformation mechanism transitions from strut bending to stretching as shown in Figure 4.7(a).

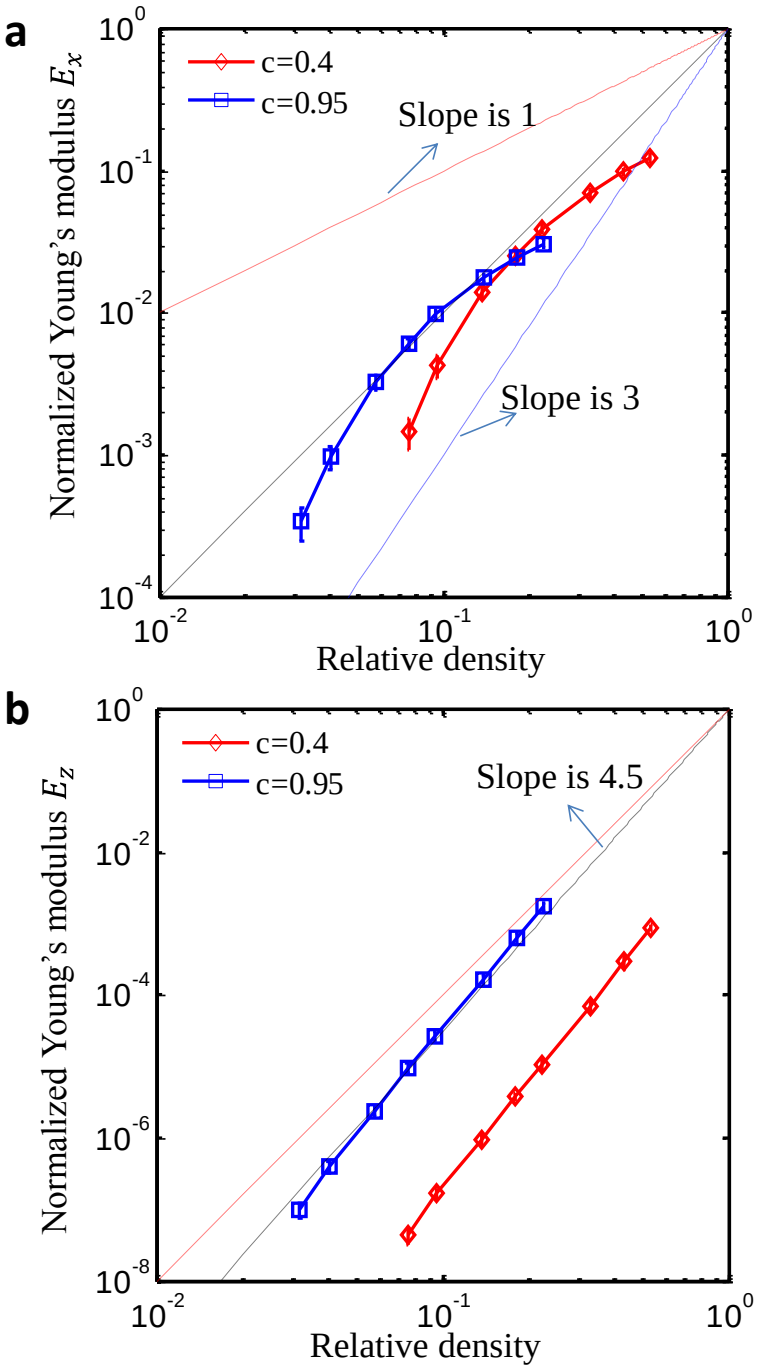

Figure 4.7. Effect of relative density on the non-dimensional Young's modulus in the x and z direction having a degree of overlap $c = 0.4$(red) and $c = 0.95$ (blue).

As for the deformation mechanism in the z direction of the random beam model, it shows distinctive features compared to that in the x direction. Bending-dominated deformation mechanism exists throughout the whole scale of relative density from low to high. In addition, the overlap degree does not affect the relationship between the elastic properties in the z direction and the relative density, as shown in Figure 4.7(b).

When a material is stretched in one direction, it usually tends to shrink in the other two perpendicular directions. Poisson ratio, i.e., the ratio of relative expansion to relative contraction, typically ranges between 0.1 and 0.5 for isotropic solid materials. However, it also can reach much higher and much lower values for porous materials. Figure 4.8 and Figure 4.9 present the effective Poisson's ratios as functions of relative density, by changing the concentration of cross-linkers, L/l_c with the degrees of overlap at $c = 0.4$ and $c = 0.95$. The Poisson's ratio, ν_{12} of the filamentous structure keeps constant at around 0.3 with the varying degrees of overlap and relative densities. There is much variation in the Poisson's ratio, ν_{13}, when the relative density is small, which is due to the fact that it is hard to get the low-density or low connectivity random strut model isotropic in the x-y plane. The non-monotonic relation between ν_{13} and relative density could be attributed to the switch of dominant deformation mechanism from bending to stretching. The Poisson's ratio, ν_{31} is identical to the Poisson's ratio ν_{32}, which confirms again that the elasticity of the beam model is transversely isotropic in the x-y plane. Also, similarly, the overlap coefficient is of great importance for the contractile ability in the z direction. When the concentration of cross-linkers, L/l_c is small, i.e., the relative density is small, the networks exhibits much greater lateral contraction in the z direction, when subjected to a tensile strain in the x direction. In contrast, when traction stress is exerted in the z direction, it triggers lower contraction in the two transverse directions (See Figure 4.9).

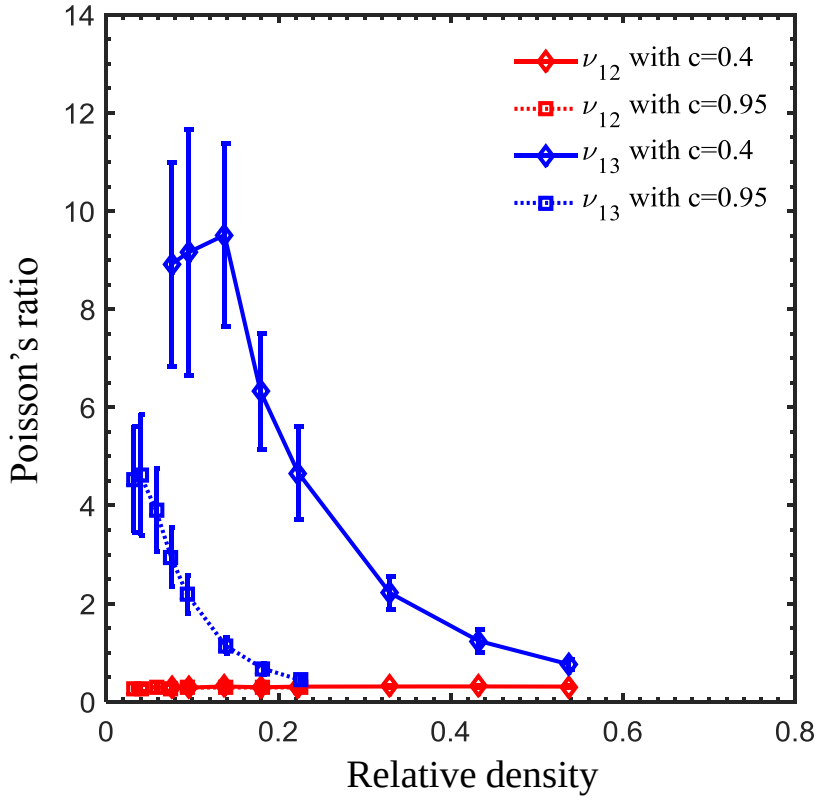

Figure 4.8. Effect of relative density on the Poisson's ratios ν_{12} and ν_{13}

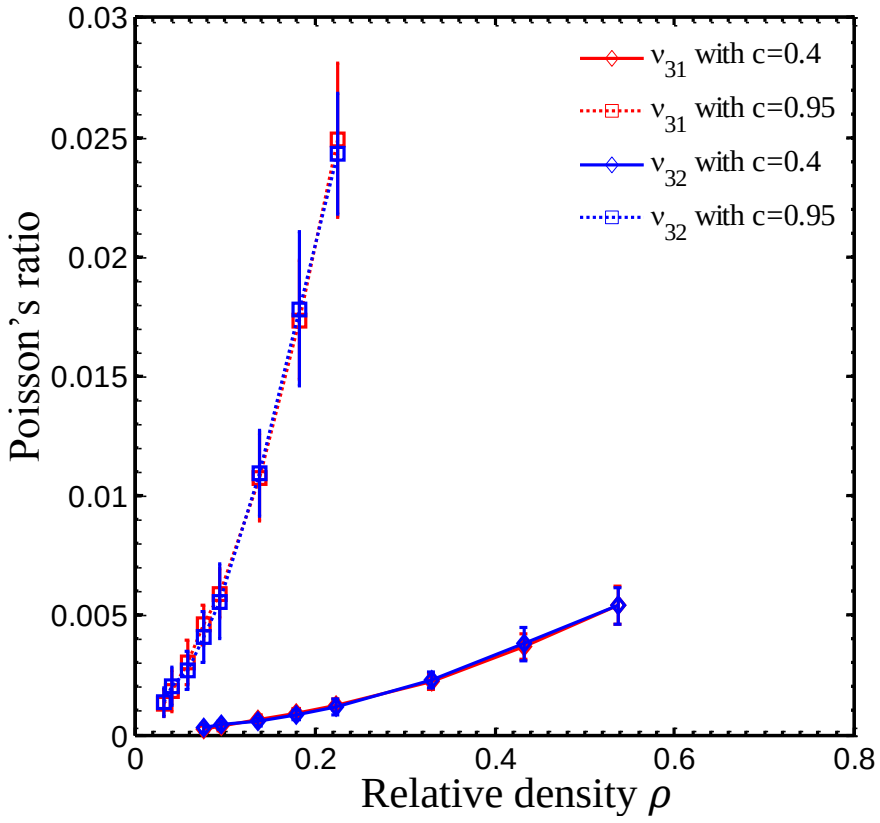

Figure 4.9. Effect of relative density on the Poisson's ratios ν_{31} and ν_{32}

To establish a good understanding of the elastic properties of a material, it is required to know all the independent elastic constants. A shear deformation is enforced by imposing an effective compressive strain of -1% in one direction and an effective tensile strain of 1% in its transverse direction, simultaneously. The non-dimensional effective shear moduli, as functions of relative density by changing the concentration of cross-linkers L/l_c with varying degree of overlap at $c = 0.4$ and $c = 0.95$, are given in Figure 4.10. It can be seen from the figure that the shear moduli in different planes with different degrees of overlap have a similar tendency. The tendency of shear modulus, G_{12}^* is in concert with that of the Young's modulus, E_x^*, which has strong agreement with the formula, $G_{12}^* = \frac{0.5E_x^*}{1+\nu_{12}}$, as the Poisson's ratio, ν_{12} is a constant, with varying relative densities.

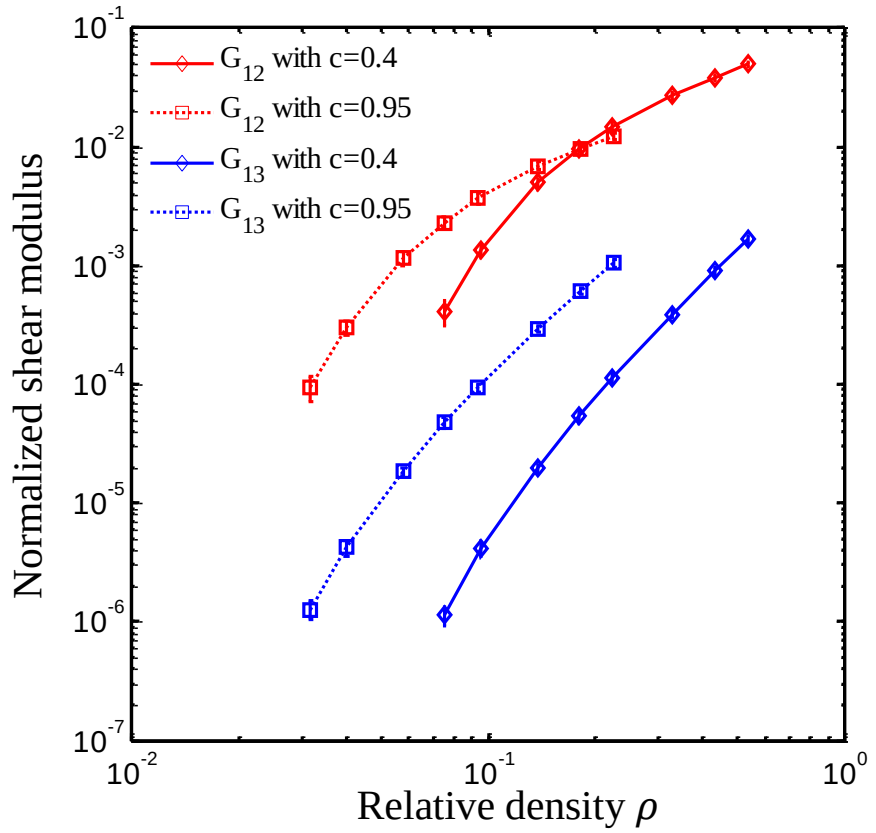

Figure 4.10. Effect of relative density on the non-dimensional shear moduli

4.3.4 Dependence of stiffness on the concentration of cross-linker

Concentration of cross-linkers plays a significant role in the stiffness of the cytoskeleton. In addition, by changing the concentration of cross-linkers, the relative density of cytoskeletal networks can be adjusted to vary over a wide range. As can be seen from Figure 4.11, relative density has been obtained by fixing the aspect ratio of filaments and changing the concentration of cross-linker $L/l_c = 3,\ 4,\ 6,\ 8,\ 10,\ 15,\ 20,\ 25$. The non-dimensional Young's modulus increases as the concentration of cross-linkers increases in the stochastic filamentous networks with different values of overlap coefficient and different aspect ratios of the filaments. For high-density filamentous networks, there is a linear relationship between the Young's modulus in the x direction and relative density, irrespective of the change of aspect ratios, as all the curves with various aspect ratios collapse along a single master line, as shown in Figure 4.11. When the overlap coefficient is small, for instance, $c = 0.4$ (Figure 4.11a), the relative density is comparatively high and the dominant deformation mechanism is stretching, especially when the concentration of cross-linkers is larger than 8. In contrast, when the overlap coefficient is larger, for instance, $c = 0.95$ (Figure 4.11b), the thickness of the networks is larger, which gives rise to a lower relative density (see Eq.(4.1)). Moreover, for the random beam model with a larger overlap degree, the inserted beams have a smaller diameter and a larger length; hence the main deformation mechanism of the stochastic filament network is bending.

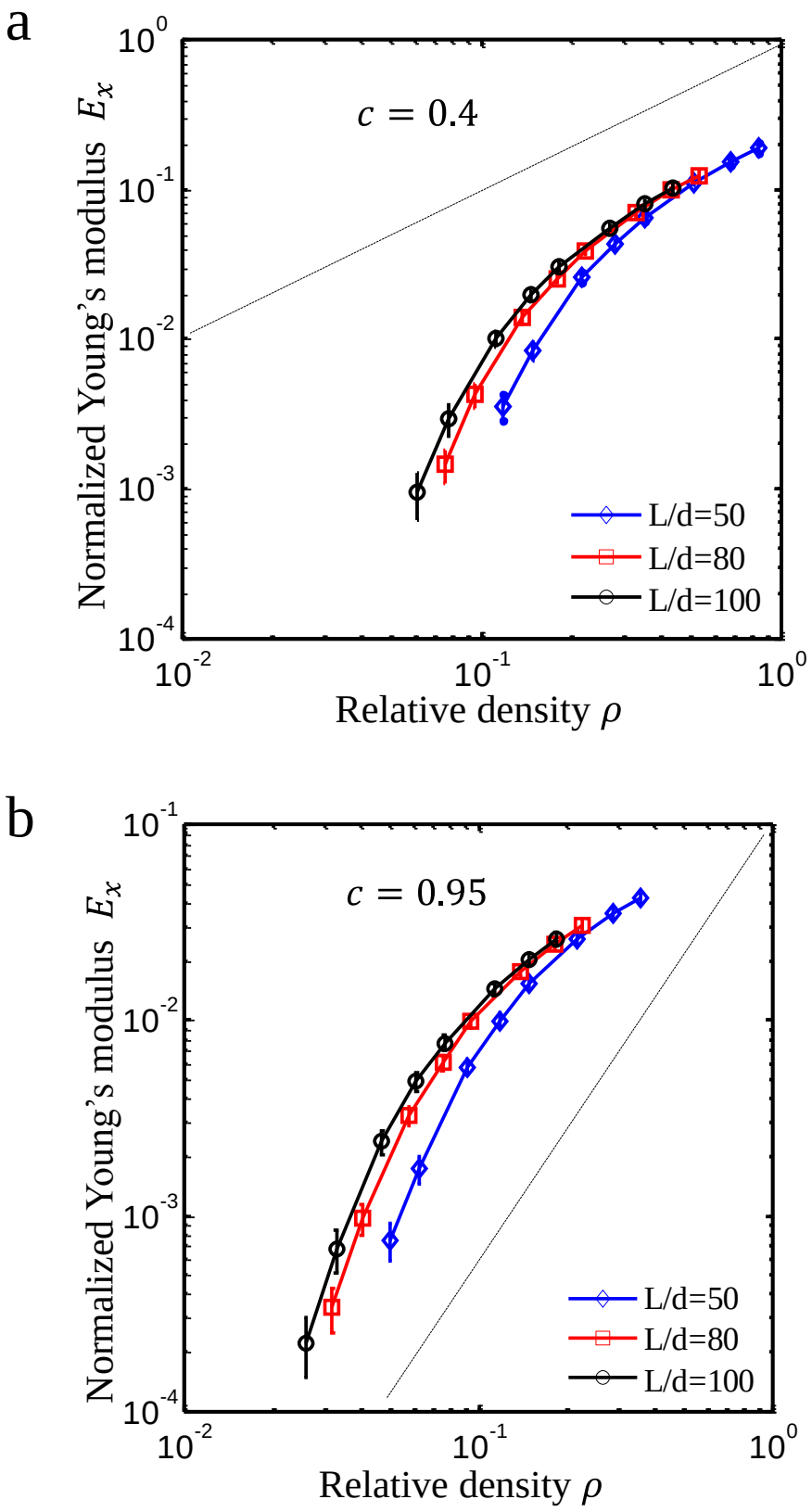

Figure 4.11. Effect of concentration of cross-linkers on the non-dimensional Young's modulus of stochastic filamentous networks having different values of overlap degree: (a) $c = 0.4$, (b) $c = 0.95$.

4.3.5 Dependence of stiffness on the aspect ratio of the networks

Figure 4.12 presents the normalised Young's modulus as a function of relative density for stochastic filamentous networks with different values of overlap degree. The relative density has been obtained by fixing the concentration of cross-linkers and changing the aspect ratio of the filaments $L/d = 40,\ 50, 80,\ 100, 125$. For varying degrees of overlap, the Young's modulus increases with increasing relative density. Interestingly, the change of aspect ratio of the filaments does not affect the deformation mechanism of filamentous networks, as the tendency of the curve between Young's modulus and relative density keeps almost consistent. However, concentration of cross-linker is the key factor in determining the deformation mechanism.

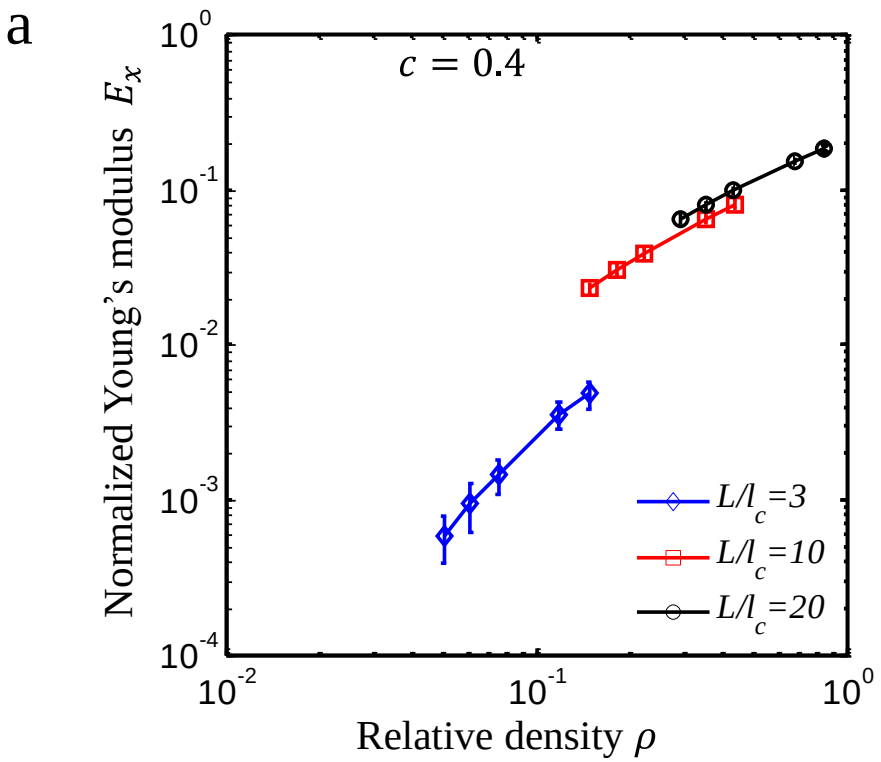

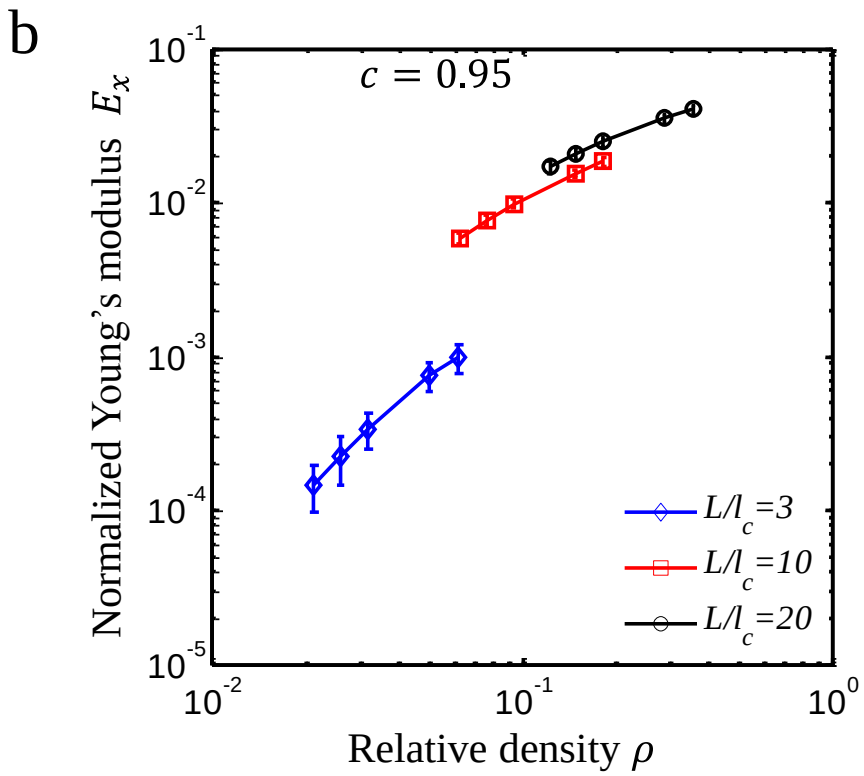

Figure 4.12. Effect of aspect ratio of filament on the non-dimensional Young's modulus of stochastic filamentous networks having different values of overlap degree: (a) $c = 0.4$, (b) $c = 0.95$.

4.3.6 Effect of cross-linker type

Finite element models of cytoskeletal networks have been developed to investigate the effect of relative density by changing the concentration of cross-linker L/l_c. It has suggested that the concentration of cross-linker can affect not only the stiffness of the stochastic filamentous networks, but also the deformation mechanism. The above analysis is based on the model with inserted beams representing the cross-linkers, which is a relatively flexible way to integrate the actin filaments into the cytoskeletal network. In the cytoskeleton, it has been found that there is a variety of cross-linking proteins with a range of mechanical properties[117]. By inserting the beam elements between the filaments, the connections between the filaments are treated as springs (i.e. deformable). Also, connections between the filaments could be treated as 'rigid

linkers' (i.e. not deformable). Naturally, different mechanical properties of cross-linkers will lead to different predictions of the elastic modulus of the cytoskeletal networks. The effects of cross-linker type on the Young's moduli in the x and z directions have been shown in Figure 4.13 and Figure 4. 14 with the same overlap coefficient, $c = 0.95$. With the beam elements inserted into the networks, the stiffness of the material is much lower than that when the intersections are treated as rigid connections. This is consistent with the findings of [55] concerning the stress-strain relationship of F-actin networks formed with different FLN mutants, especially when the strain is small. It is worth noting that, whether the cross-linkers are treated as deformable springs or rigid connections, increasing the concentration of cross-linkers, L/l_c , greatly improves the stiffness of the networks. This applies not only in cytoskeletal networks, but also in ECM, such as the lamellar architecture of cornea, where the cross-linker is significant in improving the visible-light transmission and enhancing the mechanical properties[66]. With more crosslinking, the cornea is stronger, whereas with less crosslinking, the cornea becomes weaker and may then become susceptible to developing disease, such as keratoconus. Thus, the investigation of cross-linkers is essential to gain an understanding of the elasticity of a material.

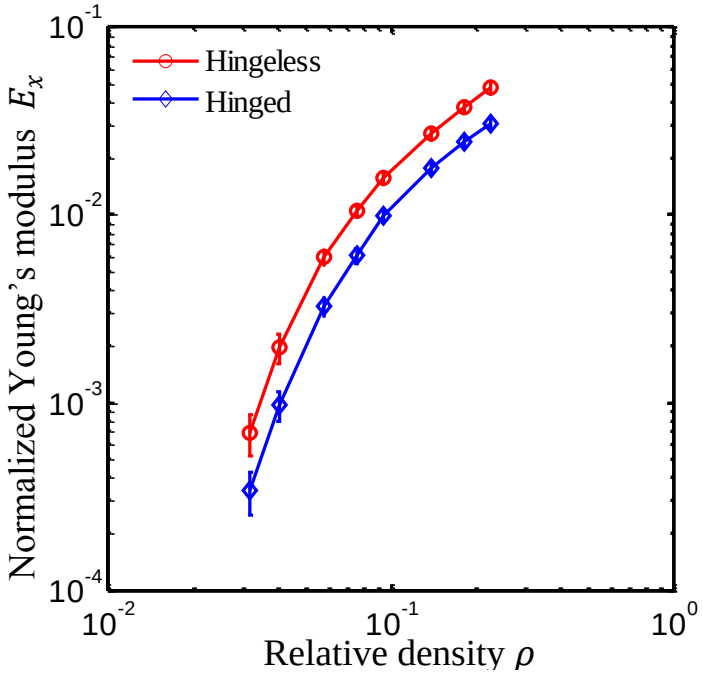

Figure 4.13. The non-dimensional Young's modulus in the x direction with two different types of cross-linker: hingeless (red) and hinged (blue).

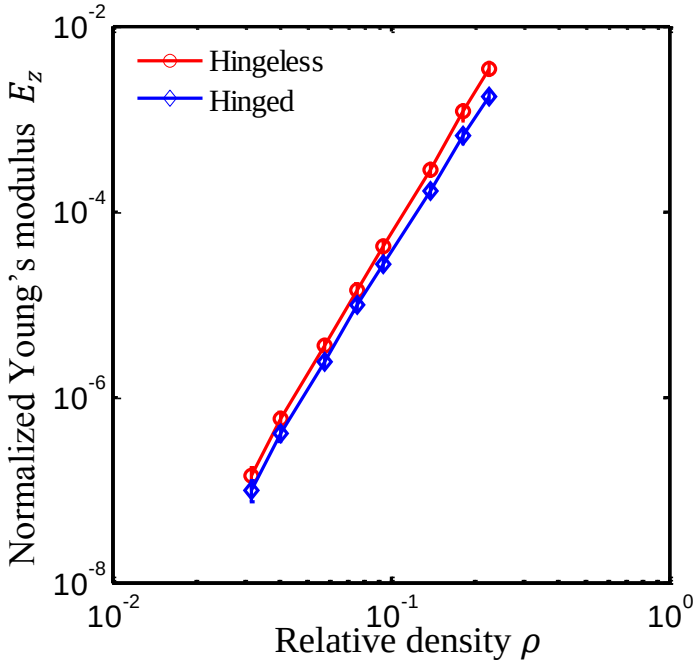

Figure 4.14. The non-dimensional Young's modulus in the z direction with two different types of cross-linker: rigid intersections (red) and inserted beams (blue).

4.4 **Analytical models**

In this part, we aim to obtain the Young's moduli using a simplified model shown in Figure 4.15 with dimensional analysis. All the fibres in the x direction are parallel to

each other and intersect with fibres lying in the y direction. At the intersection points, an additional beam is inserted in the z direction between any two intersected fibres. The concentration of intersections/cross-linkers is $N_c = L/l_c$, where L is the mean length of the fibres and l_c is the mean distance between any two neighbouring intersections. In addition, all the fibres are uniform and have the same diameter d. It may be noted that this simplified model is not equivalent to the random beam model presented above, as fibres in this model have a preferred orientation. However, this is not expected to introduce significant errors in terms of the dominant deformation mechanism of the filamentous structure. Properties of the structure shown in Figure4.15(a) in the x direction are the same as those in the y direction. The superposition of these structure at different orientation can get an isotropic behaviour in the x-y plane.

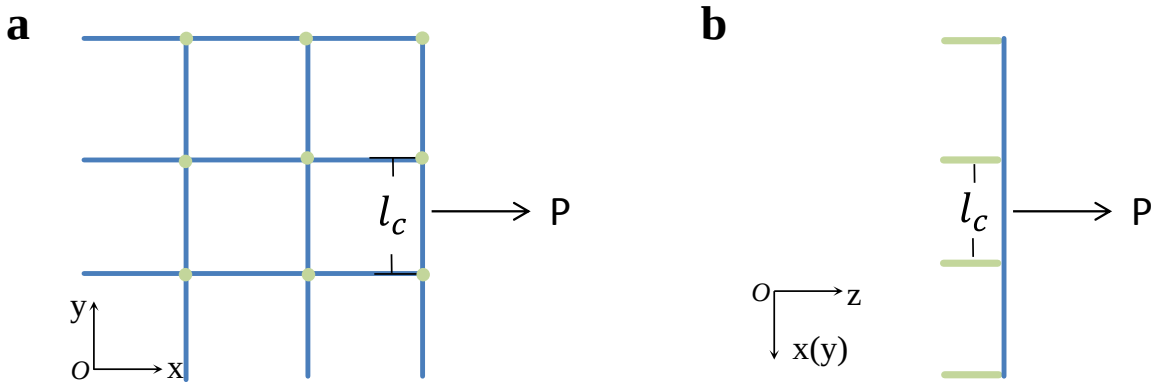

Figure 4.15. Simplified schematic program of the filamentous structure in (a) the plane of isotropy and (b) the plane of anisotropy for dimensional analysis.

4.4.1 The effect of relative density on the Young's modulus in the x direction

As shown in Figure 4.15a, each fibre segment can be regarded as a simply supported beam. When a simply supported beam is subject to a concentrated transverse load *P* in the x direction at the centre, the deflection can be expressed as,

$$\Delta_x = \frac{P {l_c}^3}{48EI} \tag{4.14}$$

where E is the Young's modulus of the solid material and I is the second moment of area of the fibre. For a circular cross-section $I = \frac{\pi d^4}{64}$.

The strain in the x direction is given by,

$$\varepsilon_x = \Delta_x / l_c \tag{4.15}$$

The stress in the x direction is given by,

$$\sigma_x = P/A \tag{4.16}$$

where $A = l_c d$.

The Young's modulus in the x direction can be obtained as follows

$$E_x = \frac{\sigma_x}{\varepsilon_x} = \frac{3\pi E}{4}(\frac{d}{l_c})^3 \tag{4.17}$$

Since the diameter d and length L have fixed values, it indicates that $d/l_c \sim L/l_c$. As shown in Figure 4.6, the relative density of the filamentous structure has a linear correlation with the concentration of the intersections or cross-linkers L/l_c; therefore, the Young's modulus in the x direction of the filamentous structure takes the form,

$$E_x/E = \alpha\rho^3 \tag{4.18}$$

where α is a coefficient.

By dimensional analysis, the relationship between the Young's modulus in the x direction and the relative density of the filamentous structure is revealed. This result shows good agreement with the FE simulation, as shown in Figure 4.7(a), when the relative density is low, proving that strut bending is the dominant deformation mechanism for low-density filamentous networks in the x direction.

4.4.2 The effect of relative density on the Young's modulus in the z direction

In the random beam model, the cross-linkers are represented by inserted beams, based on which a simplified schematic diagram of the fibrous structure in the x-z plane is shown in Figure 4.15b. The inserted beams are parallel to the z direction (thickness direction). Similarly, each fibre segment can be regarded as a simply supported beam. When the beam is subject to a concentrated transverse load, P in the z direction at the centre, the central deflection is given as,

$$\Delta_z = \frac{P{l_c}^3}{48EI} \tag{4.19}$$

where E is the Young's modulus of the solid material and I is the second moment of the beam cross-sectional area. For a circular cross-section, $I = \frac{\pi d^4}{64}$.

The strain in the z direction is given by

$$\varepsilon_z = \Delta_z/d \tag{4.20}$$

In considering the stress, it should be noted that the external force, P is not undergone by only one fibre segment. In the x direction, the analysis unit could be treated as springs in series (see Figure4.15a), whereas in the z direction, the analysis unit could be treated as springs in parallel (see Figure4.15b). Considering an area of $L \times L$ in the x-y plane, the force P is shared by $N_c \times N_c$ units of analysis, where $N_c = L/l_c$. Thus, the stress in the x direction is given by

$$\sigma_z = \frac{P}{L^2 \Big/ {N_c}^2} = \frac{P}{{l_c}^2} \tag{4.21}$$

Young's modulus in the z direction is thus

$$E_z = \sigma_z / \varepsilon_z \tag{4.22}$$

By substituting Eq.(4.20) and Eq.(4.21) into Eq.(4.22), the Young's modulus in the z direction can be specified as

$$E_z = \frac{3\pi E}{4} \left(\frac{d}{l_c}\right)^5 \tag{4.23}$$

As the relative density of the filamentous structure has a linear correlation with the concentration of the intersections or cross-linkers, L/l_c, the Young's modulus in the z direction of the filamentous structure takes the form,

$$E_z/E = \beta \rho^5 \tag{4.24}$$

where β is a coefficient, which could be determined by data fitting.

By dimensional analysis, the relationship between the Young's modulus in the z direction and the relative density of the filamentous structure is revealed. This result is broadly consistent with the FE simulation, as shown in Figure 4.7(b).

4.5 **Discussion**

In this study, the Poisson's ratio of the solid filaments is set at $\nu_s = 0.3$. As demonstrated above, the Poisson's ratio, ν_{12} of the filamentous network remains constant at around 0.3 with the varying degrees of overlap and relative densities. To test if the value of ν_{12} is dependent on ν_s, FE simulations are performed for stochastic filamentous networks with different values of ν_s. As can be seen from Figure 4.16, Poisson's ratio ν_{12} remains almost the same for different intrinsic values of material, which implies that the Poisson ratio ν_{12} of filamentous networks is around 0.3 and independent of the properties of the solid material.

In this study, the flexible cross-linkers in the cytoskeletal network are represented by inserted beams. The determination of the diameter of the inserted beams is from the stand point of structural mechanics by studying the stiffness of the inserted beam, together with the two intersected fibres (beams). However, in the real biomaterial, the diameter of the cross-linkers could vary over a large range. Table 4.9 lists the normalized Young's modulus in the x direction with different diameters of the cross-linkers. Two types of overlap coefficient, i.e., $c = 0.5$ and $c = 0.95$ have been investigated, as the degree of overlap between the two intersected beams would affect the length of the cross-linkers, δ. As seen from Figure 4.17, the non-dimensional Young's modulus in the x direction increases with an increase in the diameter of cross-linker, d'. Moreover, the larger the overlap degree, the smaller the Young's modulus in the x direction will be, which can be explained by the beam bending theory. When the overlap degree is larger, the length of the inserted beam is larger. As the inserted beam is parallel to the z direction, when it is subjected to an external force in the x

direction, the deflection is larger with a longer beam. Thus the strain is larger and the Young's modulus is smaller for $E = \sigma/\varepsilon$.

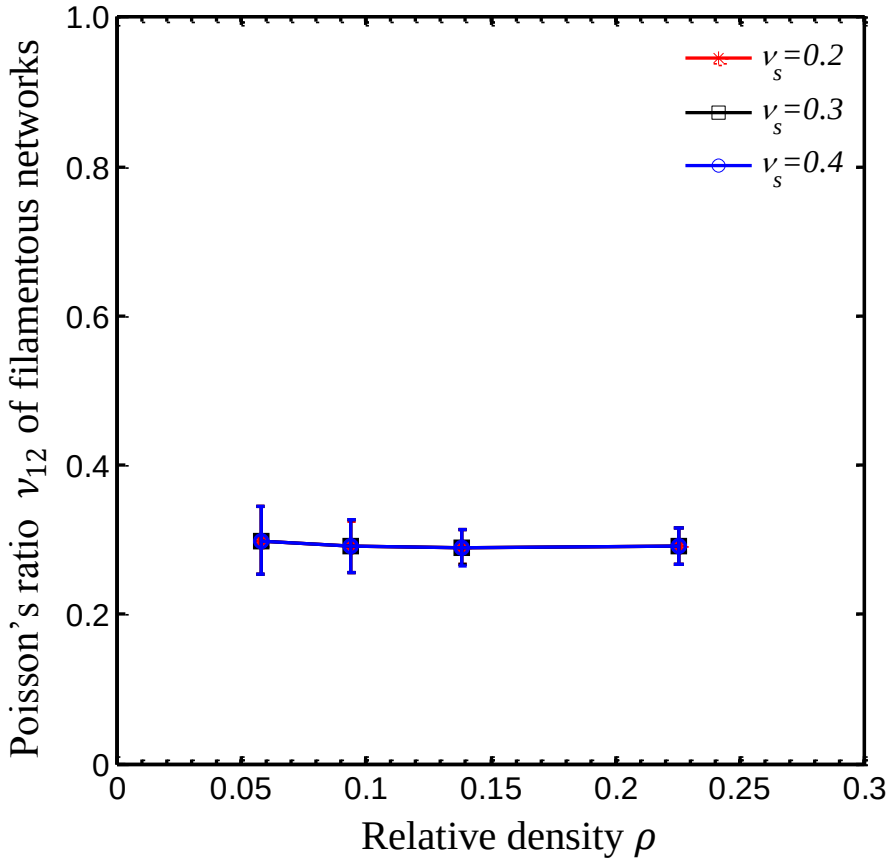

Figure 4.16. Dependence of Poisson ratio ν_{12} on the intrinsic Poisson ratio of filament ν_s.

Table 4.9. The non-dimensional Young's moduli of the same periodic filamentous structures with 200 filaments, the same density of cross-linker $L/l_c = 4$, mean aspect ratio 1.5%, and different diameters of inserted beams.

d'/d	20%	22.2%	25%	28.6%	33.3%	40%	50%	66.7%	100%
$c = 0.5$	1.21e-3	1.43e-3	1.69e-3	1.97e-3	2.30e-3	2.67e-3	3.10e-3	3.61e-3	4.12e-3
$c = 0.95$	1.85e-4	2.37e-4	3.07e-4	3.97e-4	5.13e-4	6.60e-4	8.45e-4	1.08e-3	1.34e-3

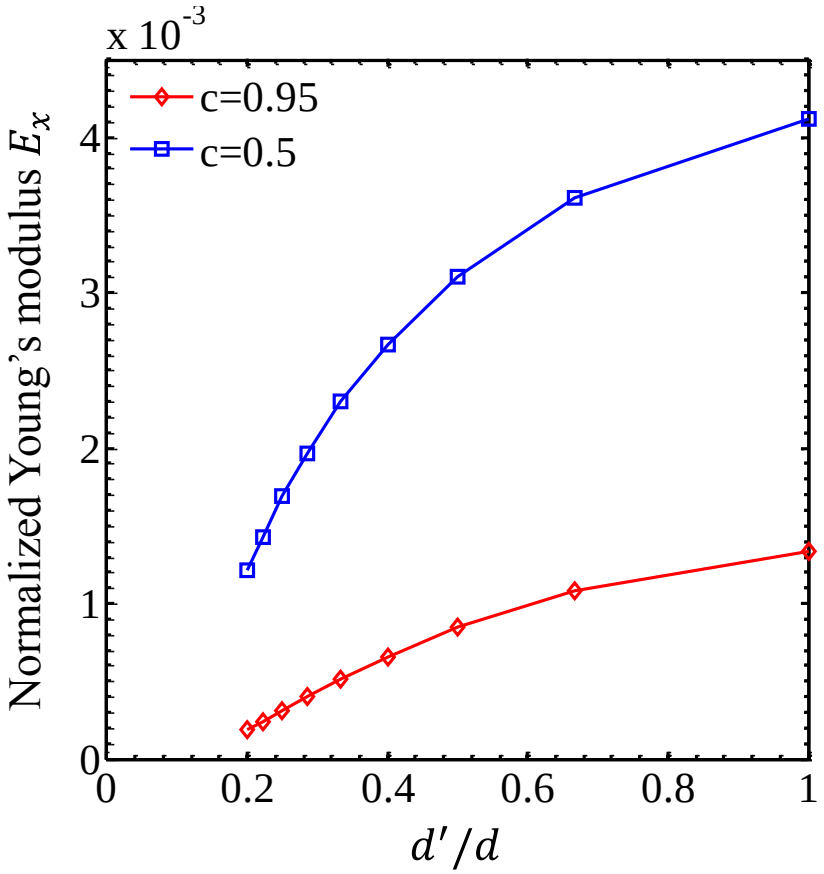

Figure 4.17. The effect of the dimension of inserted beam on the Young's modulus in the x direction.

The five independent elastic constants of two cytoskeletal networks have been tested by FE simulation: one with $c = 0.5$, $d' = 0.667d$, the other with $c = 0.95$, $d' = 0.333d$. The effects of relative density on the mechanical properties of a stochastic filamentous network with $c = 0.5$, $d' = 0.667d$ are shown in Figure 4.18-4.22.

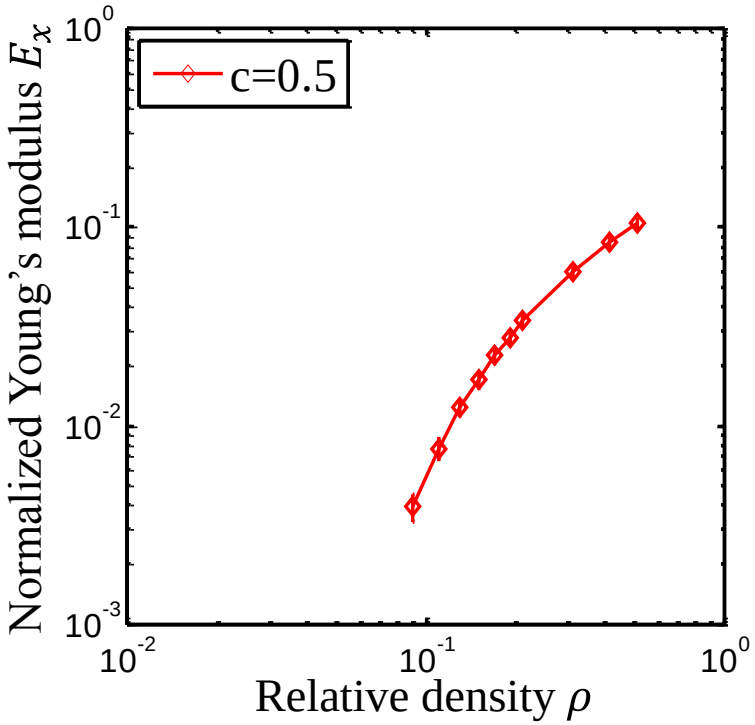

Figure 4.18. Effect of relative density on the non-dimensional Young's modulus in the x direction of filamentous structure having a degree of overlap $c = 0.5$, and diameter of cross-linker $d' = 0.667d$.

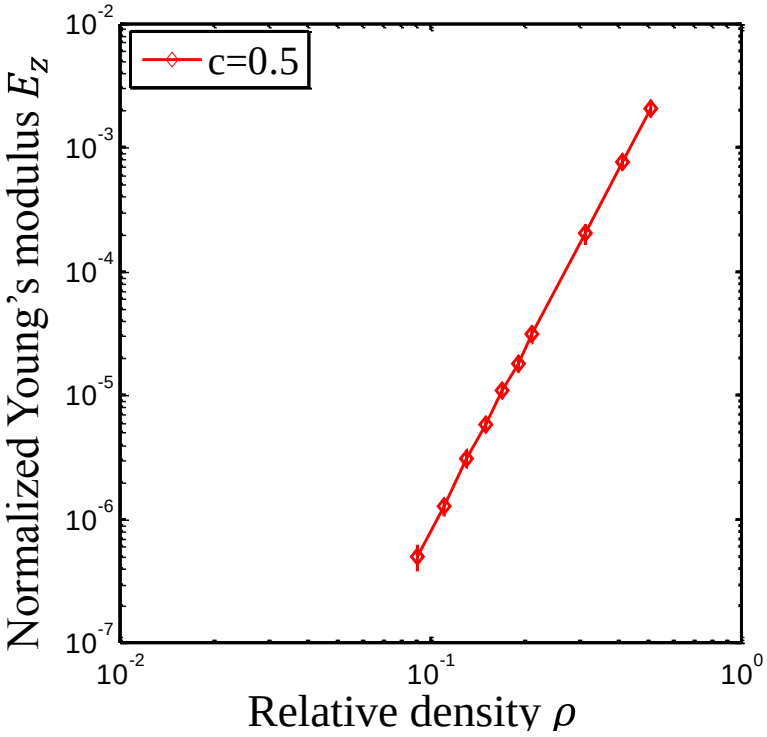

Figure 4.19. Effect of relative density on the non-dimensional Young's modulus in the z direction of filamentous structure having a degree of overlap $c = 0.5$, and diameter of cross-linker $d' = 0.667d$.

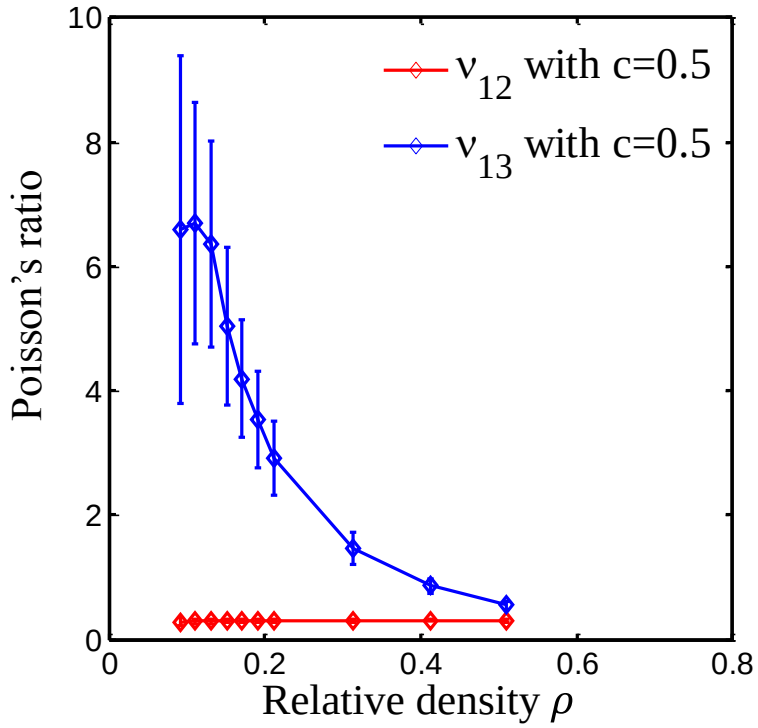

Figure 4.20. Effect of relative density on Poisson's ratios $\nu_{12}$and ν_{13} of filamentous structure having a degree of overlap c = 0.5, and diameter of cross-liker $d' = 0.667d$.

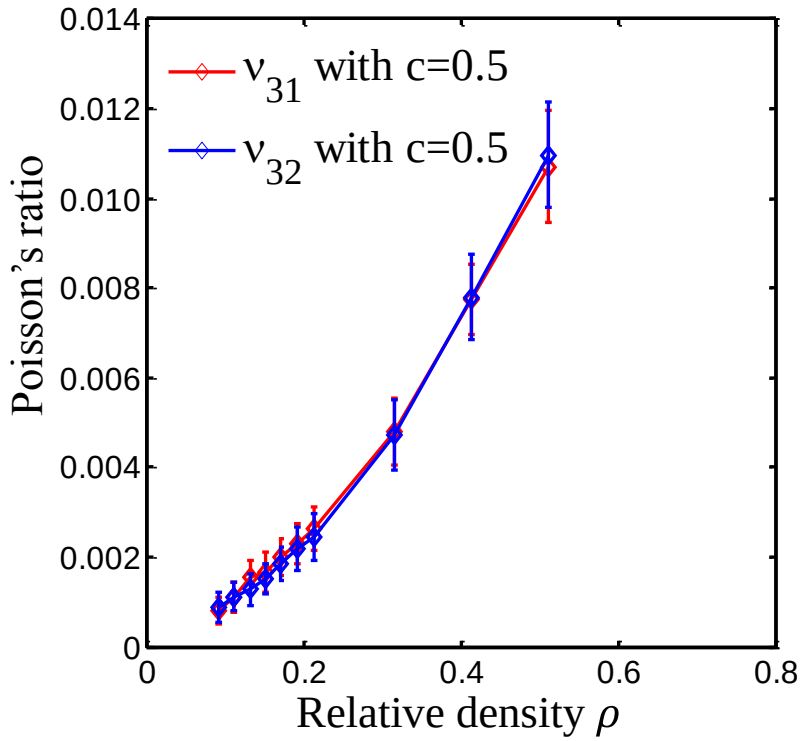

Figure 4.21. Effect of relative density on Poisson's ratios $\nu_{31}$and ν_{32} of filamentous structure having a degree of overlap c = 0.5, and diameter of cross-liker $d' = 0.667d$.

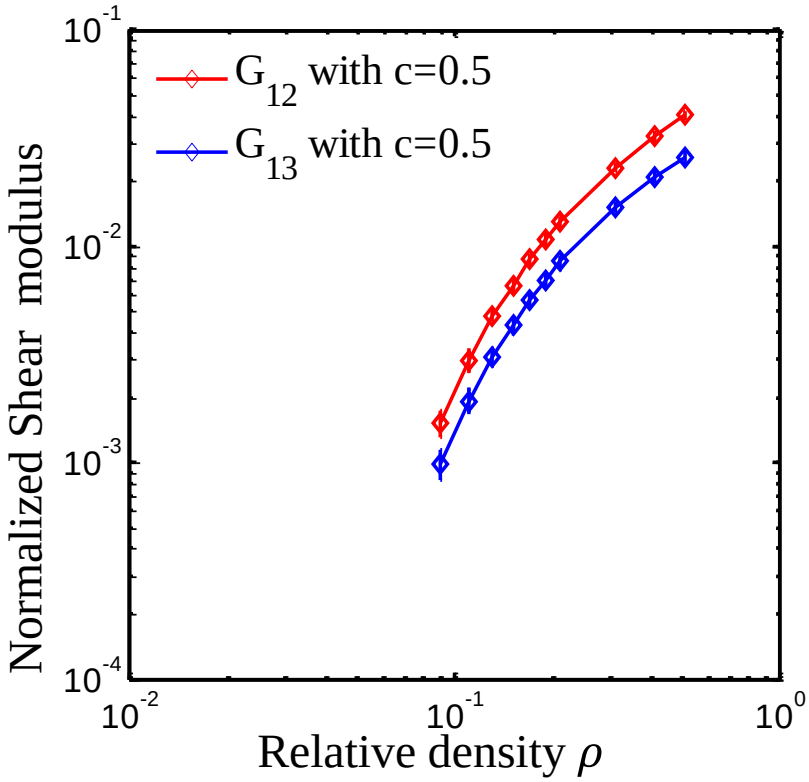

Figure 4.22. Effect of relative density on the non-dimensional shear moduli of filamentous structure having a degree of overlap c = 0.5, and diameter of cross-liker $d' = 0.667d$.

Note that the change of relative density is obtained by adjusting the concentration of cross-linkers. As can be seen from Figures 4.18 and 4.19, there is a discrepancy between the Young's moduli in the x and z directions. The Poisson's ratios in the thickness direction ν_{31} and ν_{32} are very small and close to zero, as shown in Figure4.21.

The effects of relative density on the mechanical properties of filamentous structure having a degree of overlap $c = 0.95$, and diameter of cross-liker $d' = 0.333d$ are shown in Figure 4.23- 4.27.

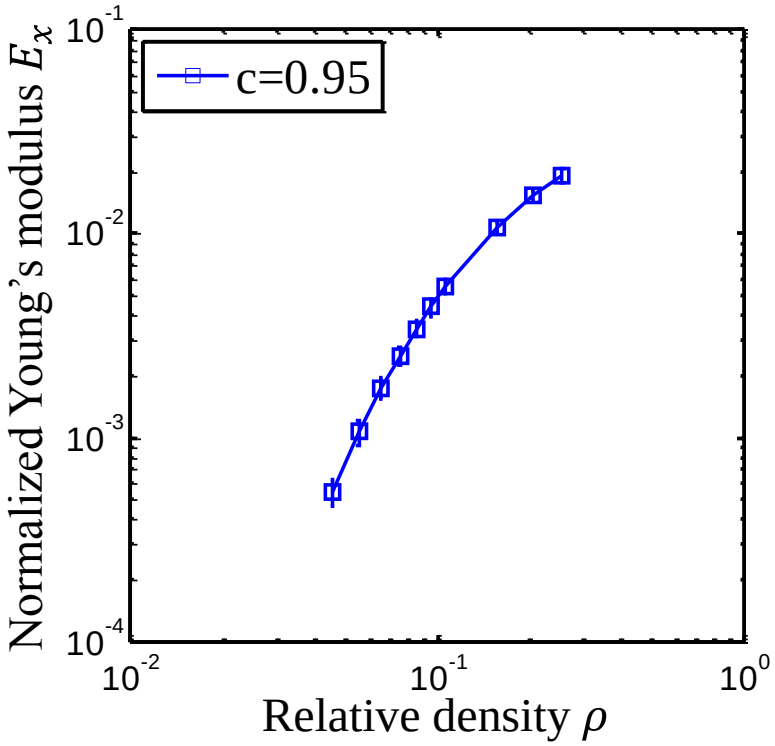

Figure 4.23. Effect of relative density on the non-dimensional Young's modulus in the x direction of filamentous structure having a degree of overlap $c = 0.95$, and diameter of cross-linker $d' = 0.333d$.

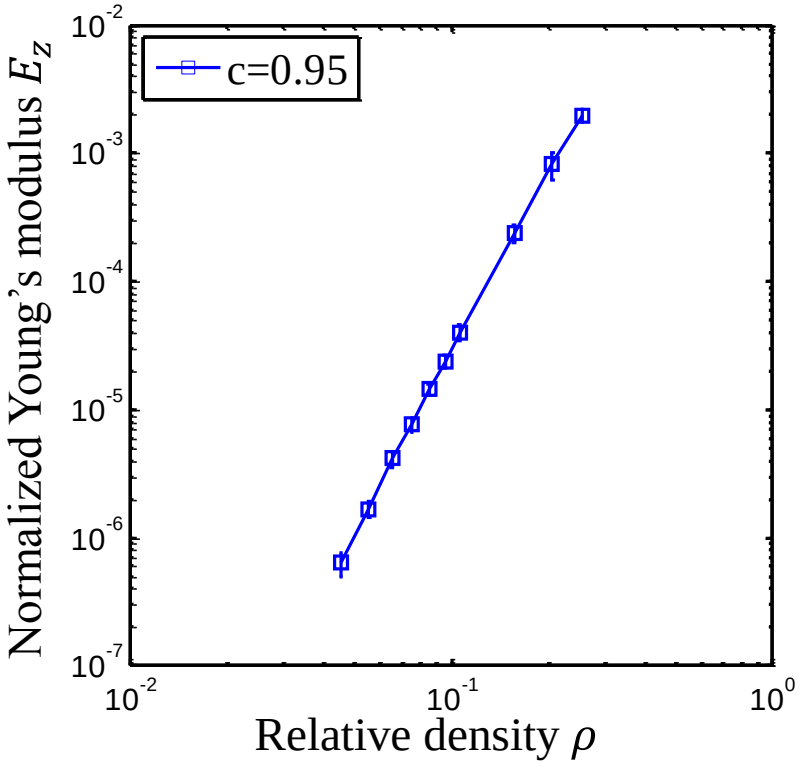

Figure 4.24. Effect of relative density on the non-dimensional Young's modulus in the z direction of filamentous structure having a degree of overlap $c = 0.95$, and diameter of cross-linker $d' = 0.333d$.

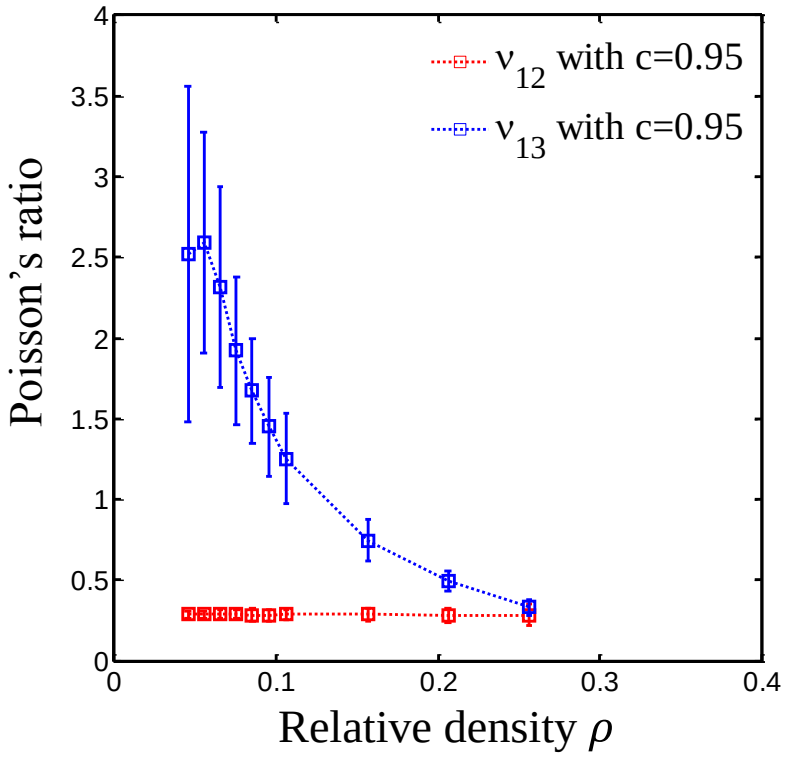

Figure 4.25. Effect of relative density on Poisson's ratios $\nu_{12}$and ν_{13} of filamentous structure having a degree of overlap $c = 0.95$, and diameter of cross-liker $d' = 0.333d$.

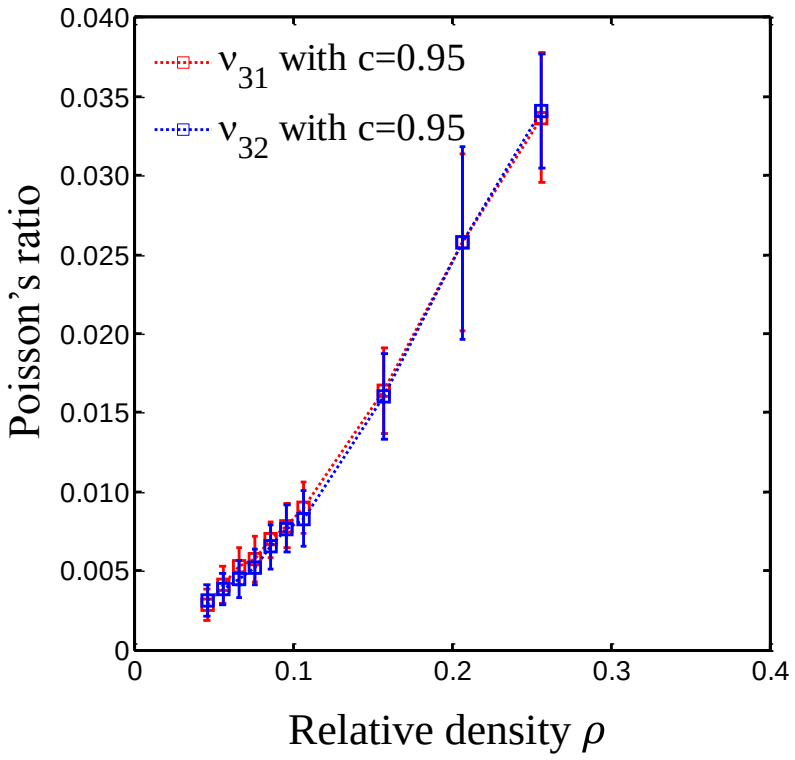

Figure 4.26. Effect of relative density on Poisson's ratios $\nu_{31}$and ν_{32} of filamentous structure having a degree of overlap $c = 0.95$, and diameter of cross-liker $d' = 0.333d$.

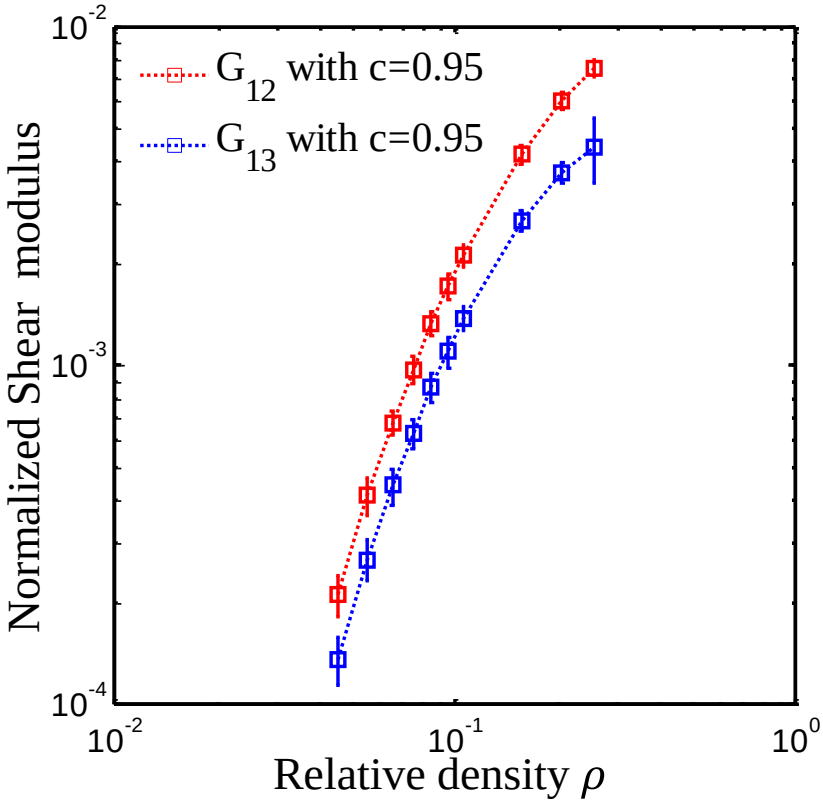

Figure 4.27. Effect of relative density on the non-dimensional shear moduli of filamentous structure having a degree of overlap $c = 0.95$, and diameter of cross-liker $d' = 0.333d$.

The dimensions of the cross-linkers can affect the elastic properties of the stochastic filamentous structure. However, the dominant deformation mechanism remains almost unchanged. In Session 4.4, dimensional analysis has been conducted to reveal the relationships between relative density and Young's moduli in the x and z directions of the filamentous network. For the Young's modulus in the z direction, it shows $E_z/E \propto \rho^5$. A log-log plot of the non-dimensional Young's modulus in the z direction versus relative density is given in Figure 4.19 for network having an overlap degree $c = 0.5$ and in Figure 4.24 for network with $c = 0.95$. The relations are approximately linear and display a slope of 5, which indicates a power law relationship of $E_z/E \propto \rho^5$. The FE simulations with different diameters of cross-linkers are

consistent with the analytical models. The dominant deformation mechanism in the z direction remains the same for filamentous structures having diameters of cross-linkers, $d' = 0.333d$, and $d' = 0.667d$, and for the previous model shown in Section4.3, in which the diameter of the inserted beam is determined by the method of stiffness equivalency.

A log-log plot of the non-dimensional Young's modulus in the x direction versus relative density, is given in Figure 4.18 for network having an overlap degree $c = 0.5$, and in Figure 4.23 for network with $c = 0.95$. The slopes of the lines are not constant, but decreasing with the increasing relative density. It implies that, with the increase of connectivity in the cytoskeleton, the dominant deformation mechanism in the x direction gradually changes from bending to stretching. The dimensions of the cross-linkers does not affect the general deformation mechanism of the filamentous networks. However, it should be noted that the diameter of the cross-linkers and the overlap degree could change the point where the deformation mechanism of filamentous structure switches from bending-dominated to stretching-dominated.

Focused on the zero-frequency, or static linearly-elastic properties of the filamentous structure, the complexities of the networks may be ignored. Instead, the study concentrates on the mechanical properties of the three-dimensional anisotropic systems with different types and concentration of cross-linkers. By massive numerical simulation, we could predict the elastic modulus of the filamentous structure, for instance, the extensional ability, the contractility and the response to shear stress, with different relative densities and overlap coefficients.

4.6 **Conclusions**

In summary, this study has developed a three-dimensional random finite element model to describe the mechanical properties of the stochastic cytoskeletal networks. By creating a simplified geometry of the cytoskeleton with the aid of a computer, some key features in the cytoskeleton have been elucidated. Periodic samples and periodic boundary conditions have been used and the macroscopic stress and strain of the filamentous structure has been revealed over the representative volume element. A novel way to deal with the cross-linkers in the networks is put forward in which beam elements are inserted into the filaments. This type of cross-linkers are treated as deformable springs. Another way is to simply treat the cross-linkers as rigid joints/connections. Comparisons between the two types of cross-linkers show that the stiffness of the network material with deformable cross-linkers is lower than that with rigid cross-linkers. In addition, the higher the concentration of cross-linkers L/l_c, the higher the Young's modulus and shear modulus will be the network. The results show that this model is transversely isotropic in the x-y plane. The relationship, $G_{12}^* = 0.5E_x^*/(1+\nu_{12})$, holds for filamentous structures with different relative densities. The non-dimensional Young's moduli and shear moduli increase with increasing relative density, when the overlap coefficient is fixed. The effective Poisson's ratio can be up to 10 and can be very low, at round 10^{-4}. Future investigations may address pre-stress applied to the networks and the nonlinear elasticity.

Chapter 5 The Yield Behaviour of a Three-Dimensional Stochastic Fibrous Network with Cross-linking

Fibrous materials are a special type of porous materials with low density and high stiffness and strength; however, limited research has been carried out, especially on simulation models and analytical models. A continuum, mechanics-based, three-dimensional, periodic beam model has been constructed to describe stochastic fibrous materials. In the stochastic model the concentration of intersection or cross-linking has been directly related to the relative density. An additional beam has been inserted between intersected fibres, which can be treated as a deformable cross-linker. The objective of this work was to delineate the yield behaviour of stochastic fibrous materials. Characteristic stress and strain, derived from the total strain energy density, have been adopted to reveal the yielding of the fibrous network. The results indicate that the in-plane stiffness and strength are much higher than those in the thickness direction. All the characteristic stress-strain curves, under various loading paths, collapse along one single line in the elastic regime. Also, the concentration of cross-linking and the dimension of inserted beam show a significant effect on the stiffness and strength of stochastic fibrous networks.

5.1 **Introduction**

Porous materials are promising for a wide range of engineering applications due to their attractive thermal, acoustic, electrical and mechanical properties. Foams and honeycombs, which can also be categorized as cellular materials, have been extensively studied[1,3–6,14]. With the same attractive properties as cellular materials, porous fibrous materials are less researched and less understood in comparison, because of their more complex geometry. More detailed information about the fibrous materials can be found in Section 2.1.

Finite element method (FEM) offers a means to probe the mechanical properties of intricate stochastic fibrous materials, and by FEM it is easier and more convenient to control the relative density and other key parameters in the model. In Finite Element (FE) modelling, beams are mostly utilized to represent the fibres and the treatment of connections between beams is crucial. A comprehensive study on the modelling of stochastic fibrous materials by mathematical treatment, for instance, the possibility and distribution can be found in reference[37], however, the connection between fibres was not taken into consideration. Sastry and co-workers[21–23] proposed a technique for modelling fibre-fibre joints, in which connection realized by a torsion spring can be regarded as flexible. However, the mechanical properties of fibrous networks with flexible bonding were not given. The idea that the connectivity between fibres cannot be adequately described by single connection points in the beam modelling is very encouraging. In this study, the concentration of connections or intersections has been incorporated into the model. This is important because the concentration of intersections is directly related to the relative density in stochastic fibrous materials. In the network in this model, there is no fibre entanglement, which is commonly found

in woven fabrics[118]. It is found that the macroscopic stresses and strains can be determined by the microscopic stresses and strains over a representative volume element (RVE). RVE[38] was proposed to reveal the full-scale model by a representative 'cell unit' to significantly reduce the computation complexity. Traditionally the yielding of a solid metal material is defined according to the von Mises yield criterion. However, it cannot be used to describe the yielding of a porous material when it is subjected to hydrostatic loading, as the Mises criterion is based on the distortional part of strain energy, and disregards the hydrostatic loading. Some researchers have put forward characteristic stress and strain, which combine hydrostatic energy density and deviatoric energy density, as a probe for the yielding of two-dimensional isotropic foams[14], two-dimensional anisotropic cellular materials[41] and three-dimensional transversely isotropic foams[42].

It has been suggested that there exists a significant difference between cellular materials, such as foams and honeycombs, and fibrous materials[17,20,24]. It is crucial to build quantitative mechanical models, describing complicated stochastic fibrous materials. Due to the computational limitation, a RVE has been adopted to represent the whole fibrous materials. Characteristic stress and strain are utilized, based on strain energy density, irrespective of loading path. The objective has been to investigate the initial yield surface of 3-D stochastic fibrous material under multi-axial loadings and the dependence of elastic-plastic behaviours on concentration of cross-linkers and relative density.

5.2 **Simulation methods**

5.2.1 Construction of three-dimensional stochastic periodic fibrous structure

X-ray tomography has been utilized to extract the reliable architectural characteristics from the very complicated stochastic porous fibrous network and to reconstruct it[26,28], as shown in Figure 5.1(a). However, this technique is computationally challenging. Finite element models are an attractive approach to construct complex stochastic fibre networks, based on fundamental geometrical parameters extracted from x-ray computed tomography. A three-dimensional random beam model has been constructed by FEM as shown in Figure 5.1(b), which shows a similarity with the geometry from X-ray tomography.

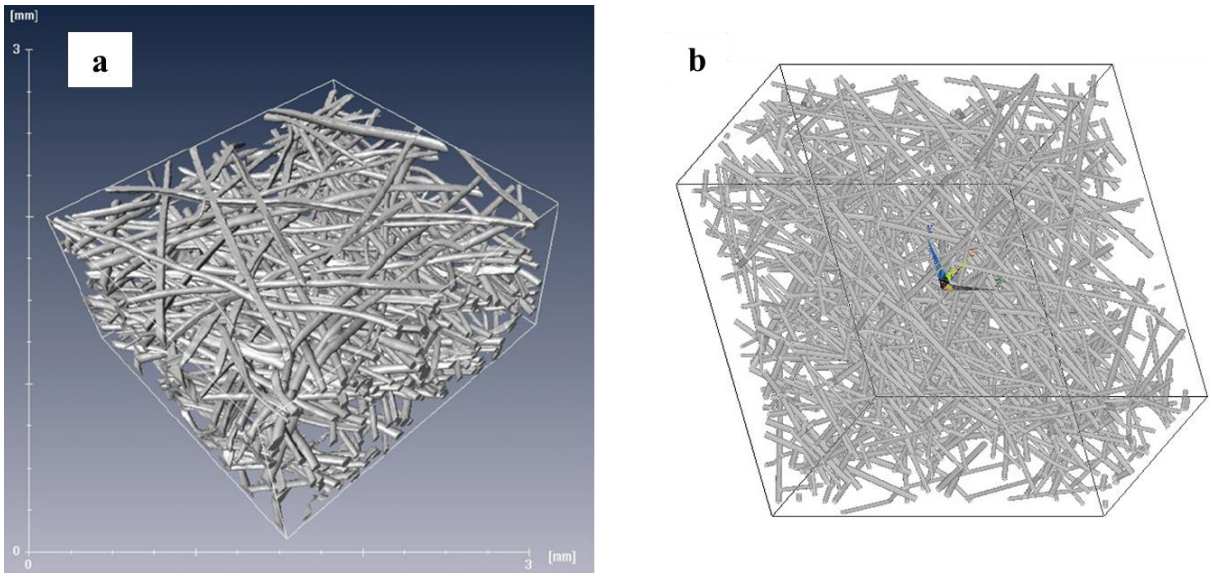

Figure 5.1. The architecture of stochastic fibrous material. (a) 3-D reconstruction from the X-ray computed tomography[28]; (b) 3-D random beam model

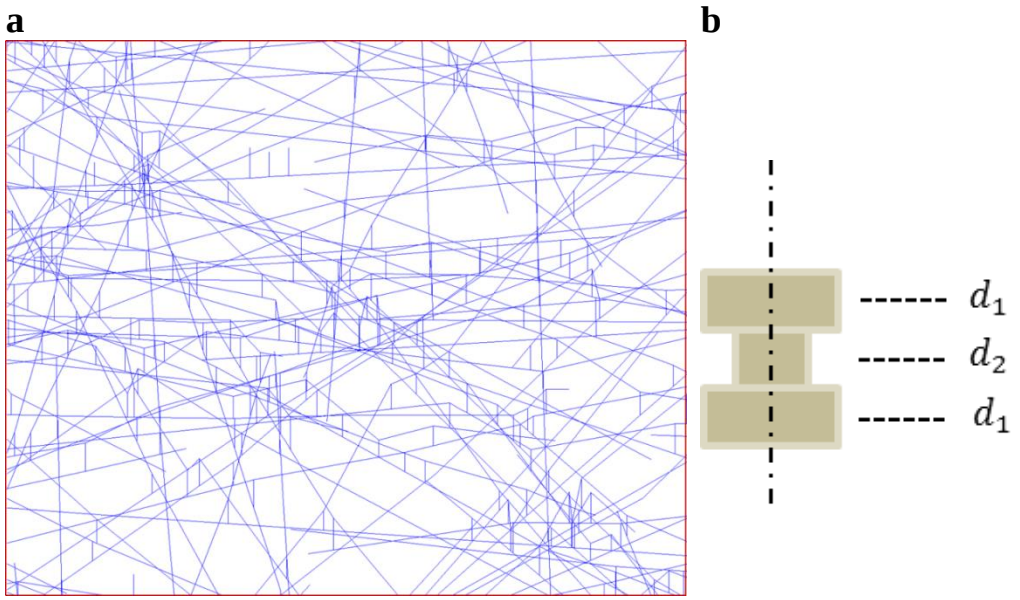

Figure 5.2. (a) The cross-linking of the network represented by the beam element inserted between intersected fibres; (b) three-section inserted beam in the study of plasticity

Full details of the methodology to generate the stochastic fibrous structure can be found in Chapter 3. In the numerical model, an innovative way to deal with cross-linking in the three-dimensional random beam model is introduced. As shown in Figure 5.2(a), an additional beam with three nodes is inserted between the intersected two fibres in the thickness direction (z direction). The inserted beams represent the cross-linkers in the stochastic fibrous network. In this chapter, the length of the inserted beam is set as the average of the diameters of the two intersected fibres. As the strength of the stochastic fibrous material is sensitive to the diameter of the inserted beams, in the study of plasticity, the inserted beams are divided into three sections, with the different/same diameters shown in Figure 5.2(b). The dimensions of the inserted beam can affect the rigidity and strength of the fibrous structure, especially in the z direction, which is parallel to the axial direction of the inserted beams. In an industrial process, if two metal fibres overlapped because of, for instance, high temperature, the middle of the intersection is usually thinner than the two ends. Thus,

a parameter study has been conducted in terms of the diameter, d_1, d_2 of the inserted beam, as detailed in Section 5.6.

The number of intersections is controllable and adjustable, according to specifically manufactured materials, and is defined as $N_c = L/l_c$, where l_c is the mean distance between any two neighbouring intersection points along a fibre of length L. In the three-dimensional model with line segments, the fibre can drop down to connect with more fibres below, in which the fibre volume fraction of the representative volume element(RVE) can be increased dramatically and related to comparable values in real material by adjusting the concentration of cross-linkers. The relative density is a key parameter to elucidate the mechanical behaviour of porous materials, including fibrous materials[1–4,10,119]. In this chapter, dimensional analysis has been conducted to reveal the relationship between the yield strength and relative density of a stochastic fibrous material, as detailed in Section 5.5. The relative density of the fibrous material is specified by:

$$\rho = \frac{\sum_{i=1}^{N} L_i * (\frac{1}{4} * \pi {d_i}^2)}{(1 * 1 * t)} \tag{5.1}$$

where L_i is the fibre length, t is the thickness of the fibre structure, N is the number of fibres and d_i diameters of the circular cross sections (in the model, the diameters are different for different fibres). Since the fibres are randomly distributed with a periodicity of w=1 in x and y directions, 1*1*t refers to the volume of the structure. It is not surprising that the relative density of stochastic fibrous material increases with a rise in the concentration of cross-linkers based on the three-dimensional beam model developed in this study. To obtain more intersections or cross-linkers with other fibres, the fibre has to drop down to connect with more fibres below, thus resulting in a reduction in the thickness of the structure and an increase of the relative density. As it

can be seen from Figure 5.3, the relative density is linearly related to the concentration of cross-linkers, L/l_c. The curve fitting result gives

$$\rho = 0.9 \times 10^{-2} L/l_c \tag{5.2}$$

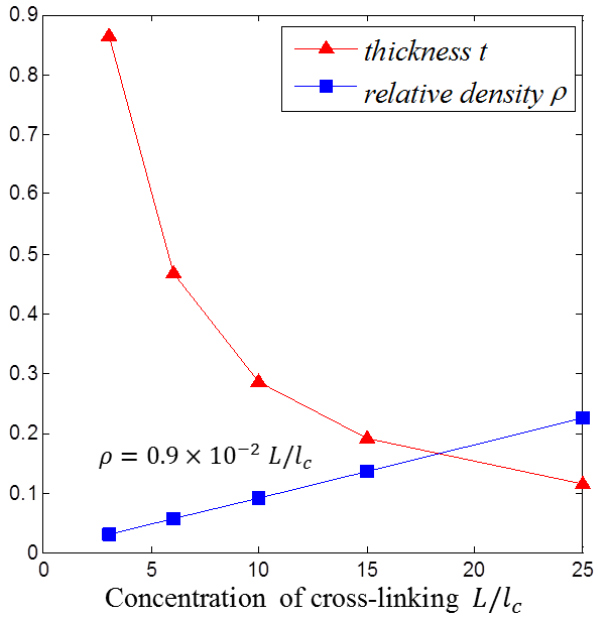

Figure 5.3. The effect of concentration of cross-linking on the thickness and relative density of stochastic fibrous structure.

5.2.2 Mesh and boundary conditions

The periodic geometrical model of fibrous network is made of a large number of randomly located and orientated beams with a circular cross-section and different diameters. The structure is meshed into a large number of BEAM-189 elements. This type of element (BEAM 189) has 3 nodes and is suitable for analysis of slender and moderately stubby/thick beam structures. This element is based on the Timoshenko beam theory and the shear deformation effect is included. The constituting solid fibres are assumed to be elastic and perfectly plastic with Young's modulus, $E_s = 210GPa$, Poisson ratio, $\nu_s = 0.3$, and yield strength, $\sigma_s = 290MPa$.

Choosing an appropriate boundary condition is very important in the numerical simulation. It has been suggested that periodic boundary conditions are more suitable than mixed boundary conditions and prescribed displacement boundary conditions to analyse the mechanical properties of a periodic RVE[1, 2]. Periodic boundary conditions assume that the corresponding nodes on the opposite edge of the mesh have the same expansion in the normal direction, the same displacement in other directions, and the same rotations in all other directions. For uniaxial loading, to take the x-directional loading as an example, the reference node on the left x-boundary is constrained in the x, y and z directions, and a tensile or compressive strain in the x direction is applied to the corresponding node on the opposite boundary. For biaxial loading, or triaxial loading, proportional strain is applied on the reference nodes in two or three directions simultaneously, for instance, $\varepsilon_x : \varepsilon_y = 1:1$, $\varepsilon_x : \varepsilon_z = 1:-1$, $\varepsilon_x : \varepsilon_y : \varepsilon_z = 1:1:2$.

It is necessary to determine the number of fibres, N in the RVE, as N should be sufficient so as to obtain the periodic stochastic fibrous structure. A mesh sensitivity study has been performed by changing the total number of fibres, N for models having the concentration of cross-linkers, L/l_c=6. Twenty random models were investigated for each different number of fibres, N=50, 75, 100, 150, 200, 400. Each fibrous structural model was generated using a different list of random numbers, and had the same diameter range, $d \in [0.01,0.02]$. More details can be found in Chapter 4. Based on the mesh sensitivity study, the finite element results shown below are the mean results over twenty random models, having a number of fibres fixed at N=200.

5.3 **Elasticity**

The three-dimensional stochastic fibrous model has been constructed with cross-linkers inserted between fibres parallel to the out-of-plane direction, i.e., z direction. By finite element analysis, it was found that the model exhibits several distinctive properties, such as transverse isotropy and the same property under tension and compression, which lay the foundation for the plasticity study and the application of the energy-based yield criterion.

5.3.1 Transversely isotropic properties

One of the significant features incorporated into this new three-dimensional beam model is the anisotropic elasticity of the fibrous networks. It is shown that the mean values of the Young's modulus and the Poisson's ratio for 20 samples are almost identical in the x and y directions. From the results it is evident that the shear modulus, Young's modulus and Poisson ratio in the x-y plane meet that the following relationship,

$$\overline{G_{12}} = 0.5\overline{E_x}/(1 + \overline{\nu_{12}}) \tag{5.3}$$

where E_x can be replaced by E_y and ν_{12} can be replaced by ν_{21}. In addition, $\overline{G_{13}} = \overline{G_{23}}$, $\overline{\nu_{13}} = \overline{\nu_{23}}$, $\overline{\nu_{31}} = \overline{\nu_{32}}$. These all suggest that the stochastic fibrous structure is transversely isotropic.

5.3.2 Uniaxial tension and compression

It is interesting to note that the stochastic fibrous structure model shows completely the same stress strain relation up to a well-defined yield point under either uniaxial tension or compression in the x or z direction, and either equi-biaxial tension or equi-

biaxial compression in the plane of isotropy or anisotropy, as shown in Figure 5.5. The model developed in this study therefore is pressure independent.

5.4 **Plasticity**

5.4.1 Characteristic stress and strain

A three-dimensional stochastic beam model has been developed which is transversely isotropic. Ayyagari *et al* [42] developed yield criteria for three-dimensional transversely isotropic foams by hypothesizing that the yielding is driven by the total strain energy density. The uniaxial response of a transversely isotropic material ($E_1 = E_2$) can be schematically represented by the stress-strain graphs in Figure 5.4. Hooke's law for transversely isotropic materials can be expressed as,

$$\begin{aligned}
\varepsilon_1 &= \frac{\sigma_1}{E_1} - \nu_{12}\frac{\sigma_2}{E_1} - \nu_{13}\frac{\sigma_3}{E_1} \\
\varepsilon_2 &= -\nu_{21}\frac{\sigma_1}{E_1} + \frac{\sigma_2}{E_1} - \nu_{13}\frac{\sigma_3}{E_1} \\
\varepsilon_3 &= -\nu_{31}\frac{\sigma_1}{E_3} - \nu_{31}\frac{\sigma_2}{E_3} + \frac{\sigma_3}{E_3} \\
\varepsilon_4 &= \frac{\sigma_4}{2G_{13}} \\
\varepsilon_5 &= \frac{\sigma_5}{2G_{13}} \\
\varepsilon_6 &= \frac{\sigma_6}{2G_{12}}
\end{aligned} \tag{5.4}$$

where the elastic moduli E_1, E_3 and the Poisson ratios have to satisfy the reciprocal relation:

$$\nu_{12} = \nu_{21}(\text{plane of isotropy}) \tag{5.5}$$

$$\frac{\nu_{13}}{E_1} = \frac{\nu_{31}}{E_3} \text{(plane of anisotropy)} \tag{5.6}$$

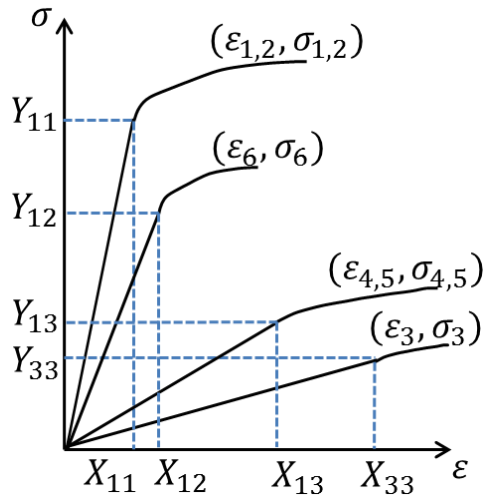

Figure 5.4. The elastic-plastic response of transversely isotropic materials under uniaxial loading and pure shearing.

Also, the shear modulus G_{12} holds the relationship with Young's modulus E_1 due to the isotropy in the x-y plane:

$$G_{12} = \frac{E_1}{2(1+\nu_{12})} \tag{5.7}$$

The total elastic strain energy density function, with shear stresses incorporated, is specialized as,

$$W = \frac{1}{2}(\sigma_1\varepsilon_1 + \sigma_2\varepsilon_2 + \sigma_3\varepsilon_3 + \sigma_4\varepsilon_4 + \sigma_5\varepsilon_5 + \sigma_6\varepsilon_6) \tag{5.8}$$

To obtain a scalar measure of the strain energy density, independent of the loading directions, the stresses and strains in Eq.(5.8) are normalized by the corresponding values at the yield points in the uniaxial tests, or pure shearing tests, as shown in Figure5.4. Thus the normalized strain energy density can be written as,

$$\bar{W} = \frac{1}{2}(\bar{\sigma}_1\bar{\varepsilon}_1 + \bar{\sigma}_2\bar{\varepsilon}_2 + \bar{\sigma}_3\bar{\varepsilon}_3 + \bar{\sigma}_4\bar{\varepsilon}_4 + \bar{\sigma}_5\bar{\varepsilon}_5 + \bar{\sigma}_6\bar{\varepsilon}_6) \tag{5.9}$$

where $\bar{\sigma}_1$, $\bar{\sigma}_2$, $\bar{\sigma}_3$, $\bar{\sigma}_4$, $\bar{\sigma}_5$, $\bar{\sigma}_6$ and $\bar{\varepsilon}_1$, $\bar{\varepsilon}_2$, $\bar{\varepsilon}_3$, $\bar{\varepsilon}_4$, $\bar{\varepsilon}_5$, $\bar{\varepsilon}_6$ are the normalized stresses and strains and can be expressed as,

$$\begin{aligned}
\bar{\sigma}_1 &= \sigma_1/Y_{11} \qquad \bar{\varepsilon}_1 = \varepsilon_1/X_{11} \\
\bar{\sigma}_2 &= \sigma_2/Y_{11} \qquad \bar{\varepsilon}_2 = \varepsilon_2/X_{11} \\
\bar{\sigma}_3 &= \sigma_3/Y_{33} \qquad \bar{\varepsilon}_3 = \varepsilon_3/X_{33} \\
\bar{\sigma}_4 &= \sigma_4/Y_{13} \qquad \bar{\varepsilon}_4 = \varepsilon_4/X_{13} \\
\bar{\sigma}_5 &= \sigma_5/Y_{13} \qquad \bar{\varepsilon}_5 = \varepsilon_5/X_{13} \\
\bar{\sigma}_6 &= \sigma_6/Y_{12} \qquad \bar{\varepsilon}_6 = \varepsilon_6/X_{12}
\end{aligned} \tag{5.10}$$

such that Y_{11}, Y_{33}, X_{11}, X_{33} are the yield stresses and strains along, the x and z directions, for transversely isotropic materials subjected to uniaxial loadings, and Y_{13}, Y_{12}, X_{13}, X_{12} are the shear stresses and strains at yielding along 1-3 and 1-2 directions.

Hooke's law in Eq.(5.4) can be rewritten in the normalized form as

$$\begin{aligned}
\bar{\varepsilon}_1 &= \bar{\sigma}_1 - \nu_{12}\bar{\sigma}_2 - \frac{\nu_{13}}{r_1}\bar{\sigma}_3 \\
\bar{\varepsilon}_2 &= -\nu_{12}\bar{\sigma}_1 + \bar{\sigma}_2 - \frac{\nu_{13}}{r_1}\bar{\sigma}_3 \\
\bar{\varepsilon}_3 &= -\nu_{31}r_1\bar{\sigma}_1 - \nu_{31}r_1\bar{\sigma}_2 + \bar{\sigma}_3 \\
\bar{\varepsilon}_4 &= \bar{\sigma}_4 \\
\bar{\varepsilon}_5 &= \bar{\sigma}_5 \\
\bar{\varepsilon}_6 &= \bar{\sigma}_6
\end{aligned} \tag{5.11}$$

By solving for the normalized stresses from Eq.(5.11), the stresses take the forms

$$\bar{\sigma}_1 = \frac{1}{\nu_{12} - 1 + 2\nu_{13}\nu_{31}}\left(\frac{\nu_{13}\nu_{31} - 1}{\nu_{12} + 1}\bar{\varepsilon}_1 - \frac{\nu_{13}\nu_{31} + \nu_{12}}{\nu_{12} + 1}\bar{\varepsilon}_2 - \frac{\nu_{13}}{r_1}\bar{\varepsilon}_3 \right)$$

$$\bar{\sigma}_2 = \frac{1}{\nu_{12} - 1 + 2\nu_{13}\nu_{31}}\left(-\frac{\nu_{13}\nu_{31} + \nu_{12}}{\nu_{12} + 1}\bar{\varepsilon}_1 + \frac{\nu_{13}\nu_{31} - 1}{\nu_{12} + 1}\bar{\varepsilon}_2 - \frac{\nu_{13}}{r_1}\bar{\varepsilon}_3\right)$$

$$\bar{\sigma}_3 = \frac{1}{\nu_{12} - 1 + 2\nu_{13}\nu_{31}}(-r_1\nu_{31}\bar{\varepsilon}_1 \quad - r_1\nu_{31}\bar{\varepsilon}_2 \quad + (\nu_{12} - 1)\bar{\varepsilon}_3)$$

$$\bar{\sigma}_4 = \quad \bar{\varepsilon}_4$$

$$\bar{\sigma}_5 = \quad \bar{\varepsilon}_5$$

$$\bar{\sigma}_6 = \quad \bar{\varepsilon}_6 \tag{5.12}$$

The normalized strain energy density can be expressed as a function of the normalized stresses by substituting Eq.(5.11) into Eq.(5.9)

$$\bar{W} = \frac{1}{2}\left(\bar{\sigma}_1{}^2 + \bar{\sigma}_2{}^2 + \bar{\sigma}_3{}^2 + \bar{\sigma}_4{}^2 + \bar{\sigma}_5{}^2 + \bar{\sigma}_6{}^2\right) - \nu_{12}\bar{\sigma}_1\bar{\sigma}_2 - \frac{1}{2}\left(\frac{Y_{11}}{Y_{33}} + \frac{X_{33}}{X_{11}}\right)\nu_{31}(\bar{\sigma}_1\bar{\sigma}_3 + \bar{\sigma}_2\bar{\sigma}_3) \tag{5.13}$$

The normalized strain energy density, irrespective of the loading direction, can be decomposed into hydrostatic, $\bar{W}_h$ and deviatoric, $\bar{W}_d$ parts for transversely isotropic materials as follows,

$$\bar{W} = \bar{W}_h + \bar{W}_d \tag{5.14}$$

Upon decomposition, the hydrostatic and deviatoric strain energy densities in terms of stresses are specialized as[42],

$$\bar{W}_h = \frac{1}{18}\left(3 - 2\nu_{12} - 2\nu_{31}\left(\frac{\mathrm{Y}_{11}}{\mathrm{Y}_{33}} + \frac{\mathrm{X}_{33}}{\mathrm{X}_{11}}\right)\right)(\bar{\sigma}_1 + \bar{\sigma}_2 + \bar{\sigma}_3)^2 \tag{5.15}$$

$$\bar{W}_d = \frac{1}{18}\left(6 + 2\nu_{12} + 2\nu_{31}\left(\frac{\mathrm{Y}_{11}}{\mathrm{Y}_{33}} + \frac{\mathrm{X}_{33}}{\mathrm{X}_{11}}\right)\right)\left(\bar{\sigma}_1{}^2 + \bar{\sigma}_2{}^2 + \bar{\sigma}_3{}^2 + \Psi_1\bar{\sigma}_1\bar{\sigma}_2 + \Psi_2(\bar{\sigma}_1\bar{\sigma}_3 + \bar{\sigma}_2\bar{\sigma}_3)\right) + \frac{1}{2}(\bar{\sigma}_4{}^2 + \bar{\sigma}_5{}^2 + \bar{\sigma}_6{}^2) \tag{5.16}$$

where

$$\Psi_1 = -\frac{\left(6 + 14\nu_{12} - 4\nu_{31}\left(\frac{Y_{11}}{Y_{33}} + \frac{X_{33}}{X_{11}}\right)\right)}{\left(6 + 2\nu_{12} + 2\nu_{31}\left(\frac{Y_{11}}{Y_{33}} + \frac{X_{33}}{X_{11}}\right)\right)}, \Psi_2 = -\frac{\left(6 - 4\nu_{12} + 5\nu_{31}\left(\frac{Y_{11}}{Y_{33}} + \frac{X_{33}}{X_{11}}\right)\right)}{\left(6 + 2\nu_{12} + 2\nu_{31}\left(\frac{Y_{11}}{Y_{33}} + \frac{X_{33}}{X_{11}}\right)\right)}.$$

The normalized strain energy densities can also be expressed in terms of strains by substituting Eq.(5.12) into Eq.(5.15) and Eq.(5.16), and given as,

$$\bar{W}_h = \frac{1}{18}\frac{\left(3 - 2\nu_{12} - 2\nu_{31}\left(\frac{Y_{11}}{Y_{33}} + \frac{X_{33}}{X_{11}}\right)\right)}{(\nu_{12} - 1 + 2\nu_{13}\nu_{31})^2}\left(\left(1 + \nu_{31}\frac{Y_{11}}{Y_{33}}\right)(\bar{\varepsilon}_1 + \bar{\varepsilon}_2) + \left(1 - \nu_{12} + 2\nu_{13}\frac{Y_{33}}{Y_{11}}\right)\bar{\varepsilon}_3\right)^2 \tag{5.17}$$

$$\bar{W}_d = \frac{1}{18}\frac{\left(6 + 2\nu_{12} + 2\nu_{31}\left(\frac{Y_{11}}{Y_{33}} + \frac{X_{33}}{X_{11}}\right)\right)}{(\nu_{12} - 1 + 2\nu_{13}\nu_{31})^2}\left(\Theta_1\left(\bar{\varepsilon}_1{}^2 + \bar{\varepsilon}_2{}^2\right) + \Theta_2\bar{\varepsilon}_3{}^2 + \Theta_3\bar{\varepsilon}_1\bar{\varepsilon}_2 + \Theta_4(\bar{\varepsilon}_1\bar{\varepsilon}_3 + \bar{\varepsilon}_2\bar{\varepsilon}_3)\right) + \frac{1}{2}\left(\bar{\varepsilon}_4{}^2 + \bar{\varepsilon}_5{}^2 + \bar{\varepsilon}_6{}^2\right) \tag{5.18}$$

such that

$$\Theta_1 = \left(1 + \nu_{31}\frac{Y_{11}}{Y_{33}}\right)^2 - \frac{9\left(2(1 - \nu_{13}\nu_{31})(\nu_{12} + \nu_{13}\nu_{31}) + \left(2 + \nu_{31}\left(\frac{Y_{11}}{Y_{33}} + \frac{X_{33}}{X_{11}}\right)\right)(1 + \nu_{12})\nu_{31}\frac{Y_{11}}{Y_{33}}\right)}{\left(6 + 2\nu_{12} + 2\nu_{31}\left(\frac{Y_{11}}{Y_{33}} + \frac{X_{33}}{X_{11}}\right)\right)(1 + \nu_{12})}$$

$$\Theta_2 = \left(1 - \nu_{12} + 2\nu_{13}\frac{Y_{33}}{Y_{11}}\right)^2 - \frac{18\nu_{13}Y_{33}\left((1 + \nu_{12})\left(\nu_{13}\frac{Y_{33}}{Y_{11}}\right) + (1 - \nu_{12})\left(2 + \nu_{31}\left(\frac{Y_{11}}{Y_{33}} + \frac{X_{33}}{X_{11}}\right)\right)\right)}{Y_1\left(6 + 2\nu_{12} + 2\nu_{31}\left(\frac{Y_{11}}{Y_{33}} + \frac{X_{33}}{X_{11}}\right)\right)}$$

$$\Theta_3 = 2\left(1 + \nu_{31}\frac{Y_{11}}{Y_{33}}\right)^2 - \frac{18\left((1 - \nu_{13}\nu_{31})^2 + (\nu_{12} + \nu_{13}\nu_{31})^2 + \left(2 + \nu_{31}\left(\frac{Y_{11}}{Y_{33}} + \frac{X_{33}}{X_{11}}\right)\right)(1 + \nu_{12})\nu_{31}\frac{Y_{11}}{Y_{33}}\right)}{\left(6 + 2\nu_{12} + 2\nu_{31}\left(\frac{Y_{11}}{Y_{33}} + \frac{X_{33}}{X_{11}}\right)\right)(1 + \nu_{12})}$$

$$\Theta_4 = \left(2 + 2\nu_{31}\frac{Y_{11}}{Y_{33}}\right)\left(1 - \nu_{12} + 2\nu_{13}\frac{Y_{33}}{Y_{11}}\right) - \frac{9\left(2\nu_{13}\frac{Y_{33}}{Y_{11}}(1 + \nu_{12}) + (1 - \nu_{12} + 2\nu_{13}\nu_{31})\left(2 + \nu_{31}\left(\frac{Y_{11}}{Y_{33}} + \frac{X_{33}}{X_{11}}\right)\right)\right)}{\left(6 + 2\nu_{12} + 2\nu_{31}\left(\frac{Y_{11}}{Y_{33}} + \frac{X_{33}}{X_{11}}\right)\right)}$$

The deviatoric part of strain energy density can be used to define the work conjugate effective stress $\bar{\sigma}_e$ and effective strain $\bar{\varepsilon}_e$ in the following.

The effective stress and effective strain are linearly related as

$$\bar{\sigma}_e = \bar{E}\bar{\varepsilon}_e \tag{5.19}$$

Then the deviatoric strain energy density is given by

$$\bar{W}_d = \frac{1}{2}\bar{\sigma}_e\bar{\varepsilon}_e = \frac{1}{2\bar{E}}\bar{\sigma}_e{}^2 = \frac{1}{2}\bar{E}\bar{\varepsilon}_e{}^2 \tag{5.20}$$

Equating the result in Eq.(5.20), with that in Eq.(5.16), the effective stress, $\bar{\sigma}_e$ can be derived as

$$\bar{\sigma}_e = \sqrt{\bar{\sigma}_1{}^2 + \bar{\sigma}_2{}^2 + \bar{\sigma}_3{}^2 + \Psi_1\bar{\sigma}_1\bar{\sigma}_2 + \Psi_2(\bar{\sigma}_1\bar{\sigma}_3 + \bar{\sigma}_2\bar{\sigma}_3) + \bar{E}\left(\bar{\sigma}_4{}^2 + \bar{\sigma}_5{}^2 + \bar{\sigma}_6{}^2\right)} \tag{5.21}$$

The elastic constant $\bar{E}$ is given by

$$\bar{E} = \frac{9}{\left(6 + 2\nu_{12} + 2\nu_{31}\left(\frac{\mathrm{Y}_{11}}{\mathrm{Y}_{33}} + \frac{\mathrm{X}_{33}}{\mathrm{X}_{11}}\right)\right)} \tag{5.22}$$

Equating the result in Eq.(5.20) with that in Eq.(5.18) , the effective strain, $\bar{\varepsilon}_e$ can be obtained as,

$$\bar{\varepsilon}_e = K_1\sqrt{\Theta_1\left(\bar{\varepsilon}_1{}^2 + \bar{\varepsilon}_2{}^2\right) + \Theta_2\bar{\varepsilon}_3{}^2 + \Theta_3\bar{\varepsilon}_1\bar{\varepsilon}_2 + \Theta_4(\bar{\varepsilon}_1\bar{\varepsilon}_3 + \bar{\varepsilon}_2\bar{\varepsilon}_3) + \Theta_5(\bar{\varepsilon}_4{}^2 + \bar{\varepsilon}_5{}^2 + \bar{\varepsilon}_6{}^2)} \tag{5.23}$$

where

$$K_1 = \frac{\left(6 + 2\nu_{12} + 2\nu_{31}\left(\frac{\mathrm{Y}_{11}}{\mathrm{Y}_{33}} + \frac{\mathrm{X}_{33}}{\mathrm{X}_{11}}\right)\right)}{9(1 - \nu_{12} - 2\nu_{13}\nu_{31})}, \qquad \Theta_5 = \frac{1}{K_1{}^2\bar{E}}.$$

The hydrostatic part of strain energy density can be used to define the work-conjugates: the mean stress $\bar{\sigma}_m$ and volumetric strain $\bar{\varepsilon}_v$ in the following

$$\bar{W}_h = \frac{1}{2}\bar{\sigma}_m\bar{\varepsilon}_v = \frac{1}{2\bar{K}}\bar{\sigma}_m{}^2 = \frac{1}{2}\bar{K}\bar{\varepsilon}_v{}^2 \tag{5.24}$$

where

$$\bar{\sigma}_m = \frac{\bar{\sigma}_1 + \bar{\sigma}_2 + \bar{\sigma}_3}{3} \tag{5.25}$$

Equating the result in Eq.(5.24) with that in Eq.(5.15), the elastic constant $\overline{K}$ can be obtained as

$$\overline{K} = \frac{1}{\left(3 - 2\nu_{12} - 2\nu_{31}\left(\frac{\mathrm{Y}_{11}}{\mathrm{Y}_{33}} + \frac{\mathrm{X}_{33}}{\mathrm{X}_{11}}\right)\right)} \tag{5.26}$$

and the volumetric strain $\bar{\varepsilon}_v$ can be derived as,

$$\bar{\varepsilon}_v = K_2 \left| \left(1 + \nu_{31}\frac{Y_{11}}{Y_{33}}\right)(\varepsilon_1 + \varepsilon_2) + \left(1 - \nu_{12} + 2\nu_{13}\frac{Y_{33}}{Y_{11}}\right)\varepsilon_3 \right| \tag{5.27}$$

where

$K_2 = \frac{\left(3 - 2\nu_{12} - 2\nu_{31}\left(\frac{Y_{11}}{Y_{33}} + \frac{X_{33}}{X_{11}}\right)\right)}{3(1 - \nu_{12} - 2\nu_{13}\nu_{31})}$.

By scaling back, the normalized effective stress and strain, mean stress and volumetric strain, the scalar measures of their counterparts denoted as $\hat{\sigma}_e$, $\hat{\varepsilon}_e$, $\hat{\sigma}_m$, $\hat{\varepsilon}_v$, respectively can be obtained.

$$\hat{\sigma}_e = \bar{\sigma}_e \times Y_{11}$$

$$= \sqrt{{\sigma_1}^2 + {\sigma_2}^2 + \left(\frac{Y_{11}}{Y_{33}}\right)^2 {\sigma_3}^2 + \Psi_1\sigma_1\sigma_2 + \Psi_2\left(\frac{Y_{11}}{Y_{33}}\right)(\sigma_1\sigma_3 + \sigma_2\sigma_3) + \bar{E}\left(\frac{Y_{11}}{Y_{13}}\right)^2 ({\sigma_4}^2 + {\sigma_5}^2) + \bar{E}\left(\frac{Y_{11}}{Y_{12}}\right)^2 {\sigma_6}^2}$$

$$\hat{\varepsilon}_e = \bar{\varepsilon}_e \times X_{11}$$

$$= K_1\sqrt{\Theta_1({\varepsilon_1}^2 + {\varepsilon_2}^2) + \Theta_2\left(\frac{X_{11}}{X_{33}}\right)^2 {\varepsilon_3}^2 + \Theta_3\varepsilon_1\varepsilon_2 + \Theta_4\left(\frac{X_{11}}{X_{33}}\right)(\varepsilon_1\varepsilon_3 + \varepsilon_2\varepsilon_3) + \Theta_5\left(\frac{X_{11}}{X_{13}}\right)^2 ({\varepsilon_4}^2 + {\varepsilon_5}^2) + \Theta_5\left(\frac{X_{11}}{X_{12}}\right)^2 {\varepsilon_6}^2}$$

$$\hat{\sigma}_m = \bar{\sigma}_m \times Y_{11}$$

$$= \frac{\sigma_1 + \sigma_2 + \left(\frac{Y_{11}}{Y_{33}}\right)\sigma_3}{3}$$

$$\hat{\varepsilon}_v = \bar{\varepsilon}_v \times X_{11}$$

$$= K_2 \left| \left(1 + \nu_{31}\frac{Y_{11}}{Y_{33}}\right)(\varepsilon_1 + \varepsilon_2) + \left(\frac{X_{11}}{X_{33}}\right)\left(1 - \nu_{12} + 2\nu_{13}\frac{Y_{33}}{Y_{11}}\right)\varepsilon_3 \right| \tag{5.28}$$

Accordingly, the deviatoric and hydrostatic parts of the normalized strain energy densities can be scaled back and expressed as

$$\widehat{W}_d = \bar{W}_d \times \frac{{Y_{11}}^2}{E_1} = \frac{1}{2\bar{E}}{\bar{\sigma}_e}^2 \times \frac{{Y_{11}}^2}{E_1} = \frac{1}{2}\bar{E}{\bar{\varepsilon}_e}^2 \times {X_{11}}^2 E_1$$
$$= \frac{1}{2\bar{E}E_1}{\hat{\sigma}_e}^2 \quad = \frac{\bar{E}E_1}{2}{\hat{\varepsilon}_e}^2 \tag{5.29}$$

$$\widehat{W}_h = \bar{W}_h \times \frac{{Y_{11}}^2}{E_1} = \frac{1}{2\bar{K}}{\bar{\sigma}_m}^2 \times \frac{{Y_{11}}^2}{E_1} = \frac{1}{2}\bar{K}{\bar{\varepsilon}_v}^2 \times {X_{11}}^2 E_1$$
$$= \frac{1}{2\bar{K}E_1}{\hat{\sigma}_m}^2 \quad = \frac{\bar{K}E_1}{2}{\hat{\varepsilon}_v}^2 \tag{5.30}$$

where E_1 is the Young's modulus in the x direction of the stochastic fibrous material. The scalar measures of the deviatoric and hydrostatic strain energy densities compose the homogenized total strain energy density, irrespective of loading directions, or state of stresses.

$$\widehat{W} = \widehat{W}_d + \widehat{W}_h \tag{5.31}$$

Further, by substituting Eq.(5.29) and Eq.(5.30) into Eq.(5.31), the homogenized total strain energy density can be given in terms of effective and mean stresses:

$$\widehat{W} = \frac{1}{2\hat{E}}({\hat{\sigma}_e}^2 + \kappa^2{\hat{\sigma}_m}^2) \tag{5.32}$$

where

$$\hat{E} = \bar{E}E_1 \tag{5.33}$$

$$\kappa^2 = \frac{\bar{E}}{\bar{K}} \tag{5.34}$$

Also, in terms of effective and volumetric strains, the homogenized total strain energy density can be specified as

$$\widehat{W} = \frac{\hat{E}}{2}({\hat{\varepsilon}_e}^2 + \frac{{\hat{\varepsilon}_v}^2}{\kappa^2}) \tag{5.35}$$

Based on the total strain energy density, the characteristic stress, $\hat{\sigma}$ and characteristic strain, $\hat{\varepsilon}$ can be defined as

$$\hat{\sigma} = \hat{\sigma}_e{}^2 + \kappa^2 \hat{\sigma}_m{}^2 \tag{5.36}$$

$$\hat{\varepsilon} = \hat{\varepsilon}_e{}^2 + \frac{\hat{\varepsilon}_v{}^2}{\kappa^2} \tag{5.37}$$

In the elastic regime, the characteristic stress and strain satisfy

$$\hat{\sigma} = \hat{E}\hat{\varepsilon} \tag{5.38}$$

The introduction of the scalar measures of the characteristic stress and strain helps to reveal the elastic response of transversely isotropic materials under multiaxial loadings, in which all the characteristic stress and strain curves collapse along a master line whose slope is $\hat{E}$. Note that the characteristic stress and strain carry the information on stiffness and strength anisotropy, such as, $Y_{11}, Y_{33}, X_{11}, X_{33}, Y_{13}, Y_{12}, X_{13}, X_{12}$ and $E_1, E_3, \nu_{12}, \nu_{31}$, which can be obtained from just the elastic-plastic response of uniaxial loading in the x and z directions, and pure shearing along 1-3 and 1-2 directions. The elastic properties and yield strength values (MPa) of the stochastic fibrous structure model, extracted from uniaxial and pure shearing FE simulations, are listed in Table 5.1.

Table 5.1 Elastic properties and yield strength values (MPa) of the stochastic fibrous structure model extracted from uniaxial and pure shearing FE simulations. In the model of stochastic fibrous structure, the number of intersections, $L/l_c = 10$, and the fibre aspect ratio, $L/d = 80$, the number of fibres $\mathrm{N} = 200$.

Y_{11}	X_{11}	Y_{33}	X_{33}	Y_{13}	X_{13}	Y_{12}	X_{12}
1.05	0.72e-3	0.035	0.87e-2	0.0453	0.0034	0.4511	8.633e-4
E_1	E_3	ν_{12}	ν_{31}				
1503.31	4.26	0.228	0.856e-2				

5.4.2 Effect of scaling back directions

As the von Mises criterion is only based on the deviatoric part of the strain energy, it is not sufficient to describe the yielding behaviour of a fibrous material when it is

subjected to hydrostatic loading. By combining both the deviatoric and hydrostatic parts of the strain energy, the characteristic stress and characteristic strain are defined to render the plastic response of stochastic fibrous materials.

It is assumed that yielding of the stochastic fibrous structure occurs when the homogenized total strain energy density, $\widehat{W}$ reaches a critical value. Under uniaxial stress state in the x direction, yielding occurs when $\sigma_1 = Y_{11}$, then at yielding

$$\hat{\sigma}_m = \frac{Y_{11}}{3};\ \hat{\sigma}_e = Y_{11} \tag{5.39}$$

The homogenized total strain energy density of the stochastic fibrous structure, subject to uniaxial loading in the x direction, can be specified as

$$\widehat{W}_1 = \frac{1}{2\hat{E}}\hat{\sigma}^2 = \frac{1}{2\hat{E}}\left(\hat{\sigma}_e{}^2 + \kappa^2\hat{\sigma}_m{}^2\right) = \frac{1}{2\hat{E}}\left(1 + \frac{\kappa^2}{9}\right)Y_{11}{}^2 \tag{5.40}$$

Therefore, the yield criterion of the stochastic fibrous structure, under any arbitrary stress state, becomes $\widehat{W} = \widehat{W}_1$, that is

$$\hat{\sigma}_e{}^2 + \kappa^2\hat{\sigma}_m{}^2 = \left(1 + \frac{\kappa^2}{9}\right)Y_{11}{}^2 \tag{5.41}$$

The elastic constants and yield strength values obtained from FE simulation of the stochastic fibrous structure (see Table5.1), are used in Eq.(5.41) to plot the yielding criteria in the plane of mean stress versus effective stress space, as shown in Figure5.6. One must note that the homogenized total strain energy density, $\widehat{W}$ is not exactly the total strain energy density, W, shown in Eq. (5.8). As the homogenized total strain energy density is obtained by scaling back the normalized stresses and strains, based only on the strength and stiffness in the x direction, $\widehat{W}$ can be rewritten as

$$\widehat{\mathrm{W}} = \frac{1}{2}\left(\sigma_1\varepsilon_1 + \sigma_2\varepsilon_2 + \left(\frac{Y_{11}}{Y_{33}}\frac{X_{11}}{X_{33}}\right)\sigma_3\varepsilon_3 + \left(\frac{Y_{11}}{Y_{13}}\frac{X_{11}}{X_{13}}\right)\sigma_4\varepsilon_4 + \left(\frac{Y_{11}}{Y_{13}}\frac{X_{11}}{X_{13}}\right)\sigma_5\varepsilon_5 + \left(\frac{Y_{11}}{Y_{12}}\frac{X_{11}}{X_{12}}\right)\sigma_6\varepsilon_6\right) \tag{5.42}$$

By comparing Eq.(5.42) with Eq.(5.8), it appears that there is a discrepancy between the total elastic strain energy density and its homogenized counterpart. Also, the

homogenized strain energy density depends on the way in which it scales back from the normalized stresses and strains.

The dependence of the homogenized strain energy density, as well as the characteristic stress and strain, on the scaling back directions has been investigated. Scaling back the normalized effective stress and strain, mean stress and volumetric strain, with the strength in the z direction under uniaxial loading, the scalar measures of their counterparts can be given by

$$\hat{\sigma}_e = \bar{\sigma}_e \times Y_{33}$$

$$= \sqrt{\left(\frac{Y_{33}}{Y_{11}}\right)^2 ({\sigma_1}^2 + {\sigma_2}^2) + {\sigma_3}^2 + \Psi_1 \left(\frac{Y_{33}}{Y_{11}}\right)^2 \sigma_1\sigma_2 + \Psi_2 \left(\frac{Y_{33}}{Y_{11}}\right)(\sigma_1\sigma_3 + \sigma_2\sigma_3) + \bar{E}\left(\frac{Y_{33}}{Y_{13}}\right)^2 ({\sigma_4}^2 + {\sigma_5}^2) + \bar{E}\left(\frac{Y_{33}}{Y_{12}}\right)^2 {\sigma_6}^2}$$

$$\hat{\varepsilon}_e = \bar{\varepsilon}_e \times X_{33}$$

$$= K_1 \sqrt{\Theta_1 \left(\frac{X_{33}}{X_{11}}\right)^2 ({\varepsilon_1}^2 + {\varepsilon_2}^2) + \Theta_2 {\varepsilon_3}^2 + \Theta_3 \left(\frac{X_{33}}{X_{11}}\right)^2 \varepsilon_1\varepsilon_2 + \Theta_4 \left(\frac{X_{33}}{X_{11}}\right)(\varepsilon_1\varepsilon_3 + \varepsilon_2\varepsilon_3) + \Theta_5 \left(\frac{X_{33}}{X_{13}}\right)^2 ({\varepsilon_4}^2 + {\varepsilon_5}^2) + \Theta_5 \left(\frac{X_{33}}{X_{12}}\right)^2 {\varepsilon_6}^2}$$

$$\hat{\sigma}_m = \bar{\sigma}_m \times Y_{33}$$

$$= \frac{\left(\frac{Y_{33}}{Y_{11}}\right)(\sigma_1 + \sigma_2) + \sigma_3}{3}$$

$$\hat{\varepsilon}_v = \bar{\varepsilon}_v \times X_{33}$$

$$= K_2 \left| \left(1 + \nu_{31}\frac{Y_{11}}{Y_{33}}\right)\left(\frac{X_{33}}{X_{11}}\right)(\varepsilon_1 + \varepsilon_2) + \left(1 - \nu_{12} + 2\nu_{13}\frac{Y_{33}}{Y_{11}}\right)\varepsilon_3 \right| \tag{5.43}$$

Accordingly, the deviatoric and hydrostatic parts of the normalized strain energy density can be scaled back and expressed as,

$$\widehat{W}_d = \bar{W}_d \times \frac{{Y_{33}}^2}{E_3} = \frac{1}{2\bar{E}}{\bar{\sigma}_e}^2 \times \frac{{Y_{33}}^2}{E_3} = \frac{1}{2}\bar{E}{\bar{\varepsilon}_e}^2 \times {X_{33}}^2 E_3$$
$$= \frac{1}{2\bar{E}E_3}{\hat{\sigma}_e}^2 \quad = \frac{\bar{E}E_3}{2}{\hat{\varepsilon}_e}^2 \tag{5.44}$$

$$\widehat{W}_h = \bar{W}_h \times \frac{{Y_{33}}^2}{E_3} = \frac{1}{2\bar{K}}{\bar{\sigma}_m}^2 \times \frac{{Y_{33}}^2}{E_3} = \frac{1}{2}\bar{K}{\bar{\varepsilon}_v}^2 \times {X_{33}}^2 E_3$$
$$= \frac{1}{2\bar{K}E_3}{\hat{\sigma}_m}^2 \quad = \frac{\bar{K}E_3}{2}{\hat{\varepsilon}_v}^2 \tag{5.45}$$

where E_3 is the Young's modulus in the z direction of the stochastic fibrous material. By substituting Eq.(5.44) and Eq.(5.45) into Eq.(5.31), the homogenized total strain energy density can be obtained, and then the effective and mean stresses, the effective and volumetric strains can be given by Eq.(5.32-5.35). In the elastic regime, the characteristic stress and strain satisfy, $\hat{\sigma} = \hat{E}\hat{\varepsilon}$, where

$$\hat{E} = \bar{E}E_3 \tag{5.46}$$

It is assumed that yielding of the stochastic fibrous structure occurs when the homogenized total strain energy density, $\widehat{W}$, reaches a critical value. Under uniaxial stress state in the z direction, yielding occurs when $\sigma_3 = Y_{33}$, then at yielding

$$\hat{\sigma}_m = \frac{Y_{33}}{3}; \hat{\sigma}_e = Y_{33} \tag{5.47}$$

The homogenized total strain energy density of the stochastic fibrous structure, subject to uniaxial loading in the z direction, can be specified as

$$\widehat{W}_3 = \frac{1}{2\hat{E}}\left(\hat{\sigma}_e{}^2 + \kappa^2\hat{\sigma}_m{}^2\right) = \frac{1}{2\hat{E}}\left(1 + \frac{\kappa^2}{9}\right)Y_{33}{}^2 \tag{5.48}$$

Therefore, the yield criterion of the stochastic fibrous structure, under any arbitrary stress state, becomes $\widehat{W} = \widehat{W}_3$, that is

$$\hat{\sigma}_e{}^2 + \kappa^2\hat{\sigma}_m{}^2 = \left(1 + \frac{\kappa^2}{9}\right)Y_{33}{}^2 \tag{5.49}$$

From Eq.(5.49) and Eq.(5.41), it can be seen that the scaling back direction can affect the size of the yield space of mean stress versus effective stress. In addition, in the elastic regime, the slope, $\hat{E}$ of the characteristic stress-strain curve is different, as shown in Eq. (5.46) and Eq.(5.33).

Similarly, if the normalized effective stress and strain, mean stress and volumetric strain are scaled back, with the yielding points under pure shearing along 1-3 and 1-2 directions, the slope of characteristic stress-strain curve, $\hat{E}$, can be given by

$$\hat{E} = 2\bar{E}G_{13} \qquad (shear\ along\ 1-3\ direction) \tag{5.50}$$

$$\hat{E} = 2\bar{E}G_{12} \qquad (shear\ along\ 1-2\ direction) \tag{5.51}$$

It is assumed that yielding of the stochastic fibrous structure occurs when the homogenized total strain energy density, $\widehat{W}$ reaches a critical value, for example, yielding occurs when $\sigma_4 = Y_{13}$ under pure shearing along 1-3 direction, or when $\sigma_6 = Y_{12}$ under pure shearing along 1-2 direction. The yield surface in the space of mean stress versus effective stress can be specified as,

$$\hat{\sigma}_e{}^2 + \kappa^2\hat{\sigma}_m{}^2 = \bar{E}Y_{13}{}^2 \quad (shear\ along\ 1-3\ direction) \tag{5.52}$$

$$\hat{\sigma}_e{}^2 + \kappa^2\hat{\sigma}_m{}^2 = \bar{E}Y_{12}{}^2 \quad (shear\ along\ 1-2\ direction) \tag{5.53}$$

The above analysis has suggested that the energy-based anisotropic yield criterion for stochastic fibrous structure is a combination of the deviatoric and hydrostatic parts and can be used to render the plastic response of transversely isotropic fibrous materials. However, it should be emphasised that the homogenized total strain energy density is dependent on the way in which the normalized stresses and strains are scaled back.

Characteristic stress-strain curves can be used to determine the yield point for stochastic fibrous material in a unique manner, even under various stress states, as all these curves fall on the same line before yielding. Before describing the yield surface from FE simulation, a critical strain value should be defined for the yield point. The strain offset method has been widely used in determining the yield strength of materials which do not have a clear yield point. The traditional offset strain for mild

steel is 0.2% in experimental studies[14,17]. Usually, it is preferable to use a relatively larger offset value in experimental studies and a smaller value in the numerical simulations. In addition, a small characteristic strain, 0.02%, is adopted, rather than the traditional 0.2%, so as to exclude the effect of hardening by minimizing the difference between the proportional limit and the yield point. It is not hard to understand that adopting different characteristic strain values would trigger different yield points for various stress states and different yield surfaces. Figure 5.6(c) reveals the different yield surfaces with different characteristic strain values. For the yield criterion presented above in Eq.(5.41) and yield surfaces shown in Figure 5.6(c), the characteristic strain value can be calculated as follows,

$$\hat{\varepsilon} = \frac{\hat{\sigma}}{\hat{E}} = \frac{Y_1}{\hat{E}} \sqrt{\left(1 + \frac{\kappa^2}{9}\right)} \tag{5.54}$$

The characteristic strain value from the yield criterion Eq.(5.41) is $\hat{\varepsilon} \approx 0.06\%$. Thus, the adoption of the characteristic strain value at 0.02% to reveal the yielding for FE simulation, irrespective of the strain path or stress state, is reasonable.

Note that, even if a characteristic strain value is adopted, the yield surface is still related to the scaling back directions. For instance, if the characteristic strain value is set at $\hat{\varepsilon} = 0.02\%$ and because

$$\hat{\sigma}_e{}^2 + \kappa^2 \hat{\sigma}_m{}^2 = (\hat{E}\hat{\varepsilon})^2 , \tag{5.55}$$

with different scaling back directions, the slope, $\hat{E}$ is different. Thus the sizes of the yield surface are not the same.

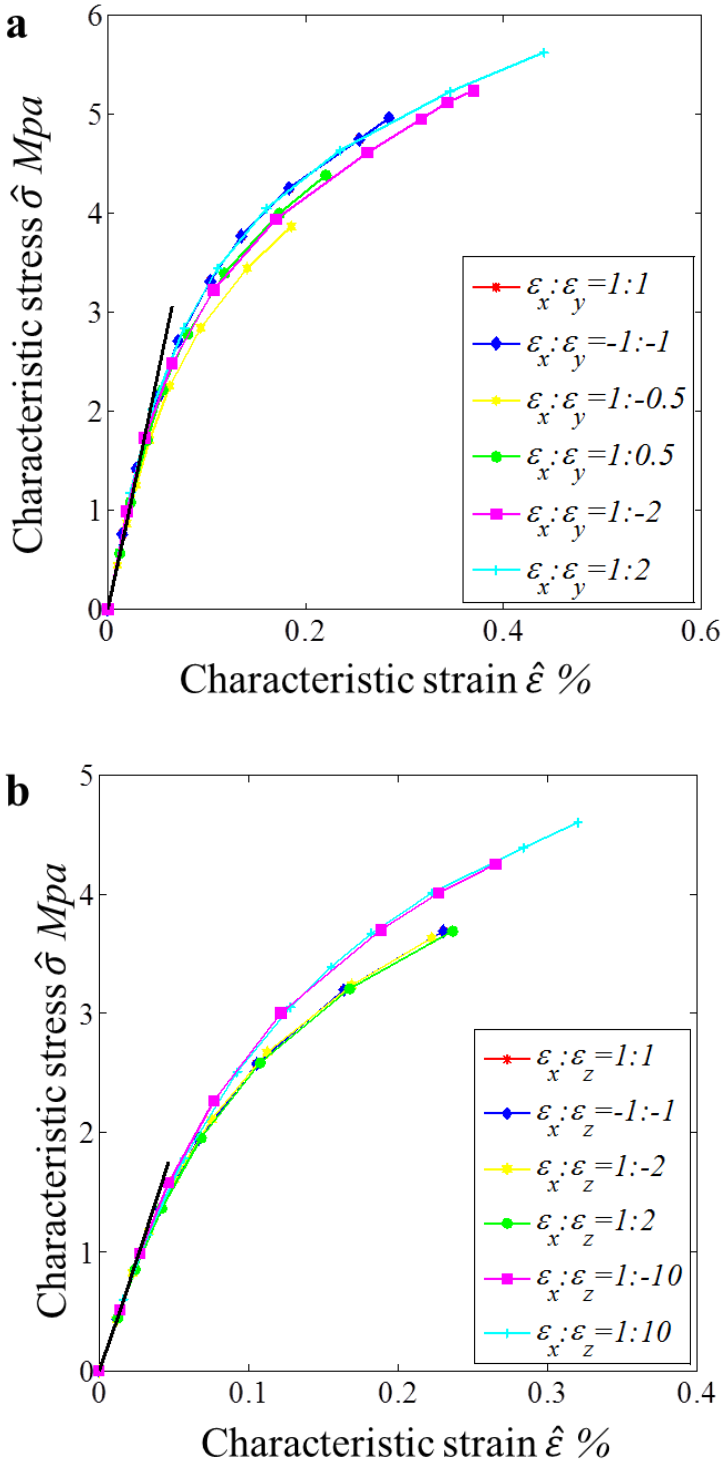

Figure 5.5. Characteristic stress-strain plot under biaxial loading in plane of isotropy(a) and plane of anisotropy(b).

In this study, the homogenized strain energy density is obtained by scaling back the normalized stresses and strains, with yielding under uniaxial tension in the x direction. With the energy-based yield criterion, the yield function can be fully calibrated in

terms of the uniaxial tension (or compression) responses in the x and z directions, and pure shearing responses along the 1-3 and 1-2 directions, rather than complex multiaxial loading responses.

5.4.3 Multiaxial normal stress states

Stress-strain curves of the stochastic fibrous structure under normal stress states were obtained from FE simulation. With the theory given in Section 5.4.1, the characteristic stresses and characteristic strains can be worked out. The characteristic stress-strain curves for various biaxial strain paths in both the plane of isotropy and the plane of anisotropy, are plotted in Figure 5.5. All the data points on the graphs are from the same stochastic fibrous structure with the concentration of intersection $L/l_c = 10$, the fibre aspect ratio$L/d = 80$ and the number of fibres $N = 200$. As it can be seen from Figure 5.5, for biaxial loadings in both the plane of isotropy (x-y plane) and plane of anisotropy(x-z plane), all the characteristic stress-strain curves collapse on a single master line in the elastic regime. It has been mentioned above that the stochastic fibrous structure model shows completely the same properties under uniaxial tension and compression in the x and z directions. In addition, when this material is subjected to equi-biaxial tension in the plane of isotropy ($\varepsilon_x : \varepsilon_y = 1:1$), the response is the same as that of equi-biaxial compression ($\varepsilon_x : \varepsilon_y = -1:-1$). This conclusion is applicable for the plane of anisotropy, as shown in Figure 5.5(b). In the plane of anisotropy for stochastic fibrous structure, the characteristic stress-strain curves under proportional biaxial loadings, such as $\varepsilon_x : \varepsilon_z = 1:1,\ 1:-2,\ 1:2$, show significant similarities. This is mainly attributed to the much larger strength and stiffness in the x direction than in the z direction. As properties of the structure are dominated by the axial loading in the

x direction in the plane of anisotropy, slight changes of loading in the z direction hardly affect the plastic response of the stochastic fibrous structure.

The elastic constants and yield strength values obtained from uniaxial FE simulation of the stochastic fibrous structure (see Table5.1), are used in Eq.(5.41) to plot the yielding criteria in the plane of isotropy (Figure5.6a), plane of anisotropy (Figure5.6b) and mean stress versus effective stress space (Figure5.6c). The strength anisotropy (i.e. Y_1/Y_3) determines the significant change in the tilt of the yield surface in the plane of anisotropy, as shown in Figure 5.6b.

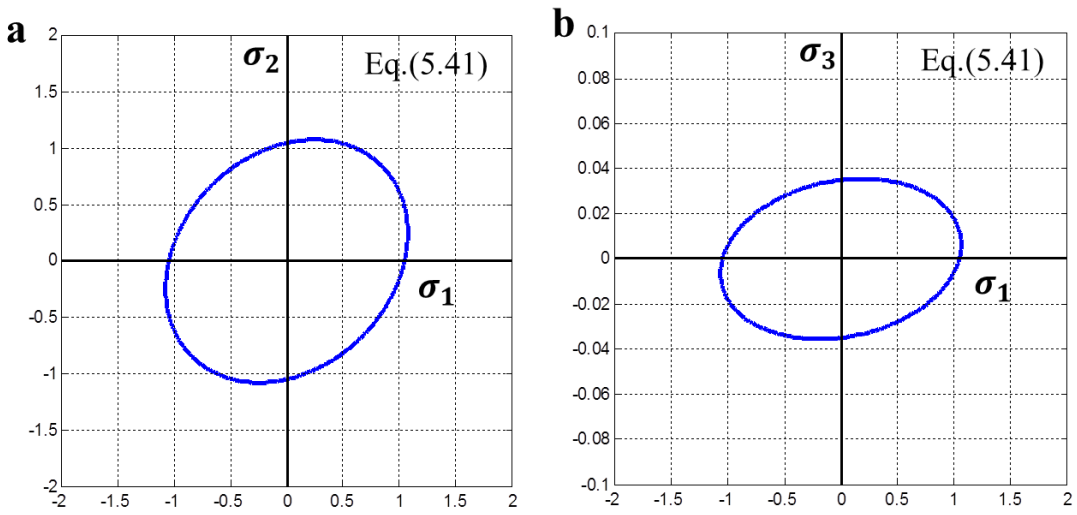

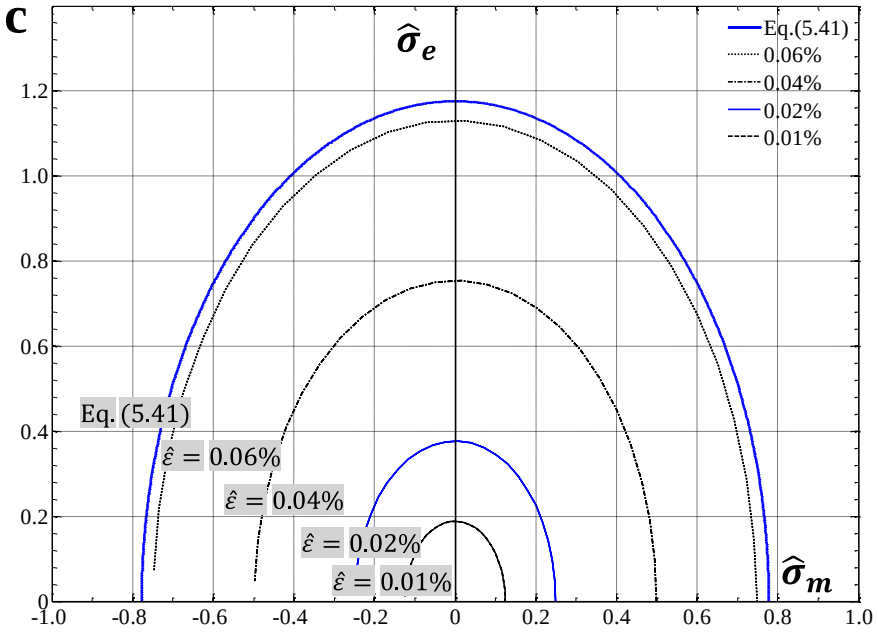

Figure 5.6. Yield surface in the plane of isotropy (a), plane of anisotropy (b) and mean-effective stress space(c). In the space of mean-effective stress, the yield surface shows the same shape, but different size under different characteristic strain offset values.

For the yield points in the plane of isotropy under biaxial proportional loading, for example $\varepsilon_1 : \varepsilon_2 = 1 : p$, the stochastic fibrous structure is subjected to loadings in the x and y direction, so σ_3 is zero. The elastic response can be written as

$$\begin{bmatrix} \varepsilon_1 \\ \varepsilon_2 \end{bmatrix} = \begin{bmatrix} \frac{1}{E_1} & \frac{-\nu_{12}}{E_1} \\ \frac{-\nu_{12}}{E_1} & \frac{1}{E_1} \end{bmatrix} \begin{bmatrix} \sigma_1 \\ \sigma_2 \end{bmatrix} = C_1 \begin{bmatrix} \sigma_1 \\ \sigma_2 \end{bmatrix} \tag{5.56}$$

$$\varepsilon_3 = \frac{-\nu_{31}}{E_3}\sigma_1 + \frac{-\nu_{31}}{E_3}\sigma_2 \tag{5.57}$$

After getting the inverse matrix of C_1, then the stresses σ_1, σ_2 can be expressed by strains ε_1 ε_2

$$\begin{bmatrix} \sigma_1 \\ \sigma_2 \end{bmatrix} = \frac{E_1}{1 - {\nu_{12}}^2} \begin{bmatrix} 1 & \nu_{12} \\ \nu_{12} & 1 \end{bmatrix} \begin{bmatrix} \varepsilon_1 \\ \varepsilon_2 \end{bmatrix} \tag{5.58}$$

Assuming that $\varepsilon_1 = k$, then $\varepsilon_2 = p * k$, the stresses take the forms

$$\sigma_1 = \frac{E_1}{1 - {\nu_{12}}^2}(1 + p\nu_{12})k \tag{5.59}$$

$$\sigma_2 = \frac{E_1}{1 - {\nu_{12}}^2}(\nu_{12} + p)k \tag{5.60}$$

We can obtain ε_3 as a function of k and p by substituting Eq.(5.59-5.60) into Eq.(5.57)

$$\varepsilon_3 = \frac{\nu_{13}(1 + p)}{\nu_{12} - 1}k \tag{5.61}$$

For a specific loading path, the proportion ratio, k is known, by substituting the three principal strains, ε_i $(i = 1,2,3)$ into the characteristic strain $\hat{\varepsilon}$, where $\hat{\varepsilon}$=0.02%, all the strain values can be solved under the condition of initial yielding. With Hooke's law, the principal stresses, and further, the effective stress and mean stress can be obtained. The yield data from FE simulation, when the stochastic fibrous model is subject to biaxial loading in the plane of isotropy, are tabulated in Table 5.2.

Table 5.2. The yield data of transversely isotropic stochastic fibrous material from FE simulation under biaxial loading in the plane of isotropy (1-2 plane) with the characteristic strain offset value at 0.02%.

$\varepsilon_1 : \varepsilon_2$	σ_1(MPa)	σ_2(MPa)	σ_3(MPa)	σ_e(MPa)	σ_m(MPa)
1:1	0.2714	0.2714	0	0.2599	0.1809
-1:-1	-0.2714	-0.2714	0	0.2599	-0.1809
1:-0.5	0.3032	-0.0931	0	0.3622	0.0701
1:0.5	0.3173	0.2074	0	0.2691	0.1749
1:-2	0.0931	-0.3032	0	0.3622	-0.0701
1:2	0.2074	0.3173	0	0.2691	0.1749

The yield point under biaxial loading in the plane of anisotropy, can be derived as follows. When the stochastic fibrous structure is subject to loadings in the x and z directions, so σ_2 is zero. The elastic response can be written as

$$\begin{bmatrix}\varepsilon_1\\ \varepsilon_3\end{bmatrix} = \begin{bmatrix}\frac{1}{E_1} & \frac{-\nu_{13}}{E_1}\\ \frac{-\nu_{31}}{E_3} & \frac{1}{E_3}\end{bmatrix}\begin{bmatrix}\sigma_1\\ \sigma_3\end{bmatrix} = C_2\begin{bmatrix}\sigma_1\\ \sigma_3\end{bmatrix} \tag{5.62}$$

$$\varepsilon_2 = \frac{-\nu_{12}}{E_1}\sigma_1 + \frac{-\nu_{13}}{E_1}\sigma_3 \tag{5.63}$$

After getting the inverse matrix of C_2, then the stresses σ_1, σ_3 can be expressed by strains ε_1 ε_3

$$\begin{bmatrix}\sigma_1\\ \sigma_3\end{bmatrix} = \frac{E_1}{1-\nu_{13}\nu_{31}}\begin{bmatrix}1 & \nu_{31}\\ \nu_{31} & \frac{E_3}{E_1}\end{bmatrix}\begin{bmatrix}\varepsilon_1\\ \varepsilon_3\end{bmatrix} \tag{5.64}$$

Assuming that $\varepsilon_1 = k$, then $\varepsilon_3 = p * k$, the stresses take the forms

$$\sigma_1 = \frac{E_1}{1-\nu_{13}\nu_{31}}(1+p\nu_{31})k \tag{5.65}$$

$$\sigma_3 = \frac{E_1}{1-\nu_{13}\nu_{31}}\left(\nu_{31} + p\frac{E_3}{E_1}\right)k \tag{5.66}$$

We can obtain ε_2 as function of k and p by substituting Eq.(5.65-5.66) into Eq.(5.63)

$$\varepsilon_2 = \frac{\nu_{12}(1+p\nu_{31}) + \nu_{31}(p+\nu_{13})}{\nu_{13}\nu_{31}-1}k \tag{5.67}$$

For a specific loading path, the proportion ratio k is known, by substituting the three principal strains ε_i $(i = 1,2,3)$ into the characteristic strain $\hat{\varepsilon}$, where $\hat{\varepsilon}$=0.02%, all the strain values can be solved under the condition of initial yielding. With Hooke's law, the principal stresses, and further, the effective stress and mean stress can be obtained.

The yield data from FE simulation, when the stochastic fibrous model is subject to biaxial loading in the plane of anisotropy, are tabulated in Table 5.3.

Table 5.3. The yield data of transversely isotropic stochastic fibrous material from FE simulation under biaxial loading in the plane of anisotropy (1-3 plane) with the characteristic strain offset value at 0.02%.

$\varepsilon_1:\varepsilon_3$	σ_1(MPa)	σ_2(MPa)	σ_3(MPa)	σ_e(MPa)	σ_m(MPa)
1:1	0.3379	0	0.0038	0.3003	0.1509
-1:-1	-0.3379	0	-0.0038	0.3003	-0.1509
1:-2	0.3409	0	9.8943e-04	0.3277	0.1235
1:2	0.3325	0	0.0047	0.2924	0.1575
1:-10	0.2618	0	-0.0057	0.3756	0.0300
1:10	0.2600	0	0.0089	0.2687	0.1755

For uniaxial loadings in the x and z directions, the yield point can be derived as follows, based on the fixed characteristic strain value at 0.02%. Once the principal strains, ε_i $(i = 1,2,3)$ are solved, with Hooke's law we can obtain the principal stresses. Then by substituting the principal stresses and strains into Eq.(5.28), the effective stress and strain, mean stress and volumetric strain can be acquired. For uniaxial loading in the x direction, it is assumed that $\varepsilon_1 = k$, and $\varepsilon_2 = -\nu_{12}k$, $\varepsilon_3 = -\nu_{13}k$; for uniaxial loading in the z direction, assuming that $\varepsilon_3 = k$, and $\varepsilon_1 = -\nu_{31}k$, $\varepsilon_2 = -\nu_{31}k$.

When the transversely isotropic material is subjected to triaxial proportional loading, for example, $\varepsilon_1:\varepsilon_2:\varepsilon_3 = 1:p_1:p_2$, the characteristic strain can be obtained from Eq.(5.37). By solving the formula $\hat{\varepsilon} = 0.02\%$, the principal strains ε_i $(i = 1,2,3)$ are acquired. Table 5.4 lists the yield data when the stochastic fibrous material is subjected to uniaxial and triaxial loadings. The yield data of transversely isotropic stochastic

fibrous material from FE simulation under multi-aixal loading are plotted in Figure5.7, in the space of effective stress and mean stress.

Table 5.4. The yield data of transversely isotropic stochastic fibrous material from FE simulation under uniaxial and triaxial loadings with the characteristic strain offset value at 0.02%.

$\varepsilon_1:\varepsilon_2:\varepsilon_3$	σ_1(MPa)	σ_2(MPa)	σ_3(MPa)	σ_e(MPa)	σ_m(MPa)
1:0:0	0.3370	0	0	0.3367	0.1125
0:0:1	0	0	0.0112	0.3370	0.1121
1:1:10	0.2420	0.2420	0.0087	0.0282	0.2486
1:1:-10	0.2599	0.2599	-0.0014	0.2908	0.1593
1:10:1	0.1238	0.3516	0.0042	0.2248	0.2000
1:-10:1	-0.0577	-0.3520	-0.0034	0.2748	-0.1707
1:-2:-5	0.0722	-0.3047	-0.0042	0.3312	-0.1194
1:-4:-4	-0.0076	-0.3397	-0.0039	0.2956	-0.1548
1:-4:7	0.0031	-0.3406	-0.0012	0.3268	-0.1245
1:1:0.5	0.2796	0.2796	0.0051	0.1152	0.2372

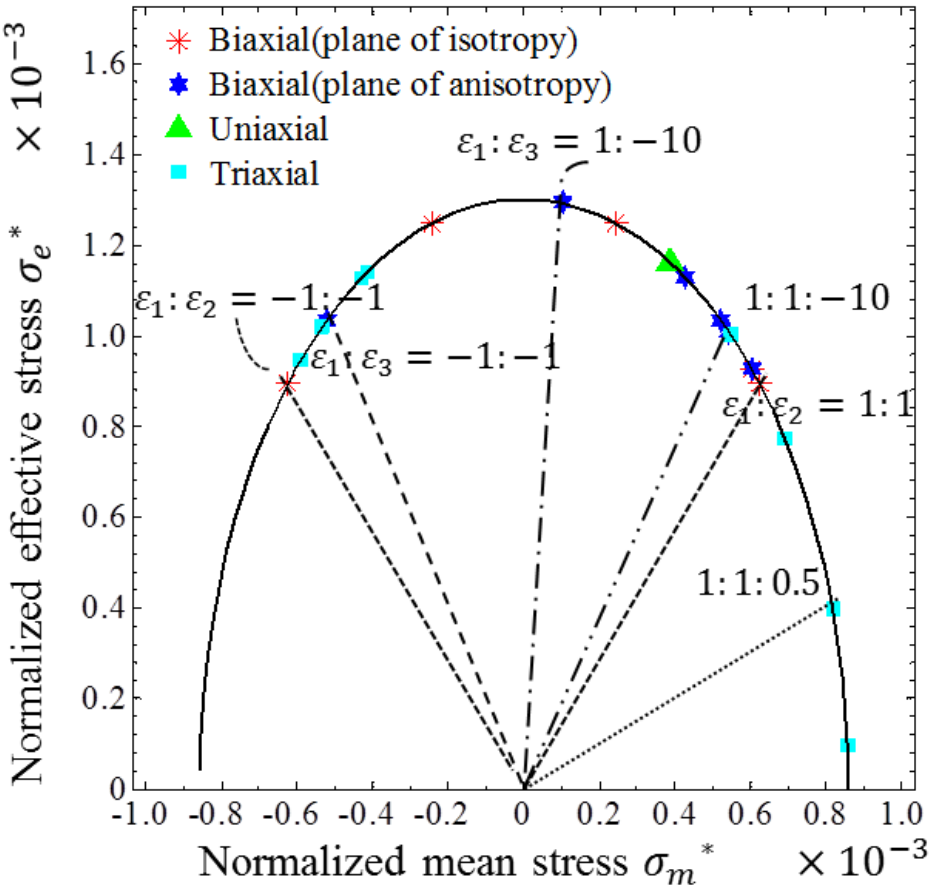

Figure 5.7. The yield data of transversely isotropic stochastic fibrous material from FE simulation under multiaixal loading in the space of effective stress and mean stress. The stresses are normalised against the yield strength of the solid material σ_s.

5.4.4 Combined axial loading and shearing

It should be noted that the introduction of shear component does not affect the form of yield criterion in Eq.(5.41), or in Eq.(5.55) where characteristic strain value $\hat{\varepsilon}$ is adopted. When the homogenized strain energy density is obtained by scaling back the normalized stresses and strains, with the yielding under uniaxial tension in the x direction, the slope, $\hat{E}$ of the characteristic stress-strain curve has no relation to shear terms. Thus, the yield surface in the space of effective stress and mean stress is

independent of the shearing. In contrast, the size of the yield surface in the plane of anisotropy can be adjusted by changing the shear along the 1-3 directions. As can be seen from Figure5.8, when the shear is absent, the size of yield surface in the plane of anisotropy arrives at its maximum. With the increasing of shear, the size decreases.

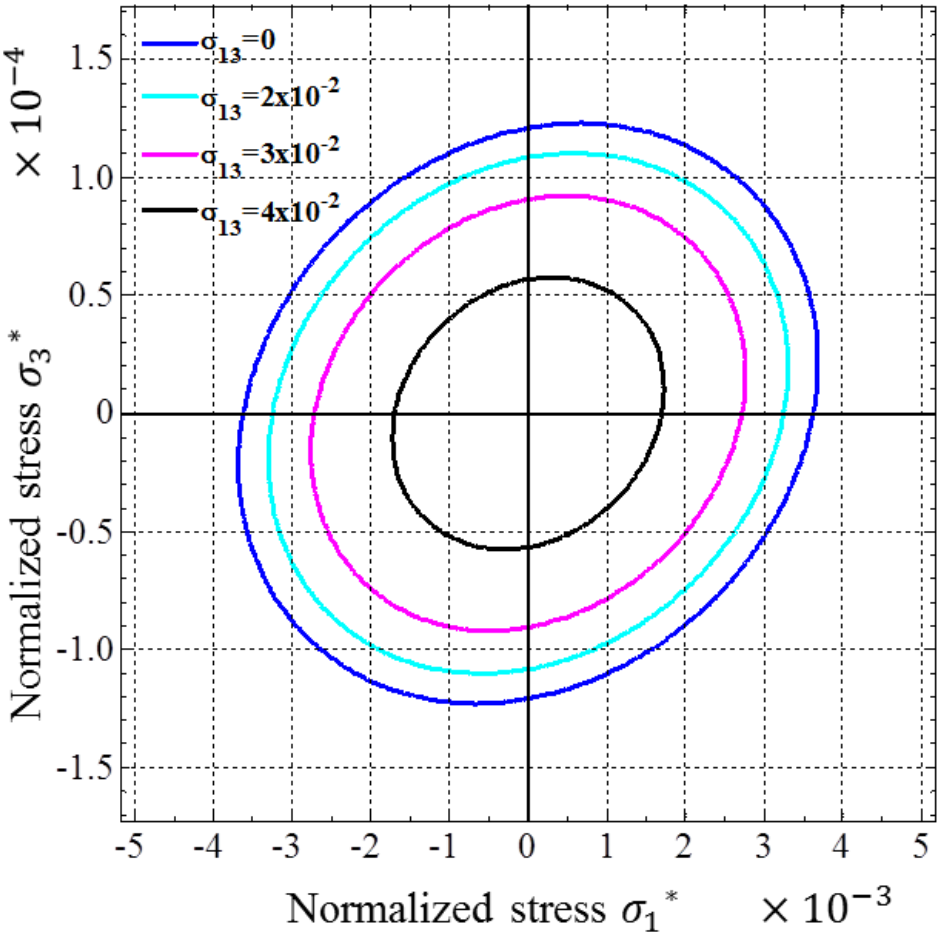

Figure 5.8. Yield surface in the plane of anisotropy with shearing under the yield criterion shown in Eq.(5.41)

5.5 **Results**

5.5.1 Effect of relative density on plastic properties

As can be seen from Figure 5.3, the relative density is linearly related to the concentration of cross-linkers, L/l_c. Thus, the effects of the density of cross-linkers and the relative density on the elastic constants are equivalent with the recognition that

the former is in terms of geometry and the latter is an intrinsic parameter of the structure.

Firstly, the strength of stochastic fibrous materials in the x direction has been investigated. A bilinear constitutive model has been used in the finite element simulation to study the plastic response of the fibrous structure. The stress-strain behaviour of the solid material (fibre itself) in the model is assumed to be bilinear and can be defined by four parameters as shown in Figure 5.9. The solid material of fibre is isotropic with an initial elastic modulus, $E_s = 210Gpa$, Poisson ratio, $\nu_s = 0.3$ and initial yield stress, $\sigma_s = 290MPa$. The tangent modulus after yield is set as $E_t = 4.2Gpa$. Based on the nonlinear constitutive model of solid material, the stress-strain behaviour of stochastic fibrous materials has been obtained from the simulation, as shown in Figure 5.10. To determine the yield strength of stochastic fibrous materials, for instance, with concentration of cross-liner at $L/l_c = 10$, under uniaxial tension in the x direction, curve fitting and interpolation techniques are utilized, together with elasticity analysis. The data on the stress-strain curve are limited, attributed to the number of iterations in the simulation. By drawing a straight line with the slope of Young's modulus E_x, which has been obtained from the study of elasticity, the turning point on the stress-strain curve can be roughly observed. More interpolated values are added on the curve. The yield point (X_{11}, Y_{11}) is determined when the error, γ_x is less than 5%. The error, γ_x takes the form,

$$\gamma_x = \frac{E_x - {\sigma_i}/{\varepsilon_i}}{E_x} \tag{5.68}$$

where σ_i and ε_i are the data on the fitting curve of stress and strain with interpolation.

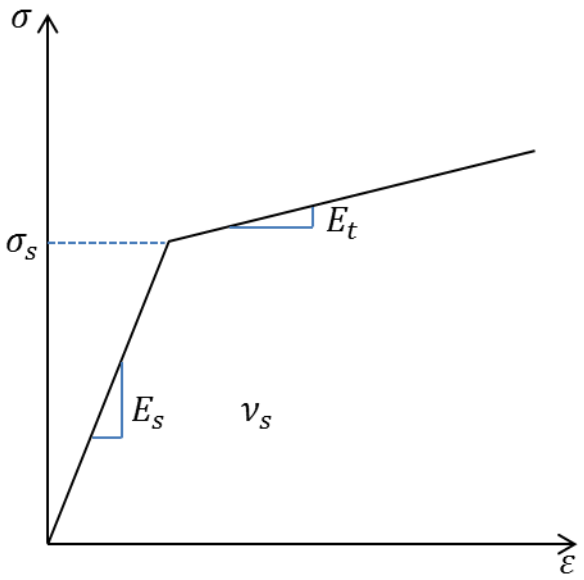

Figure 5.9. The stress-strain behaviour of the bilinear elastic isotropic constitutive model.

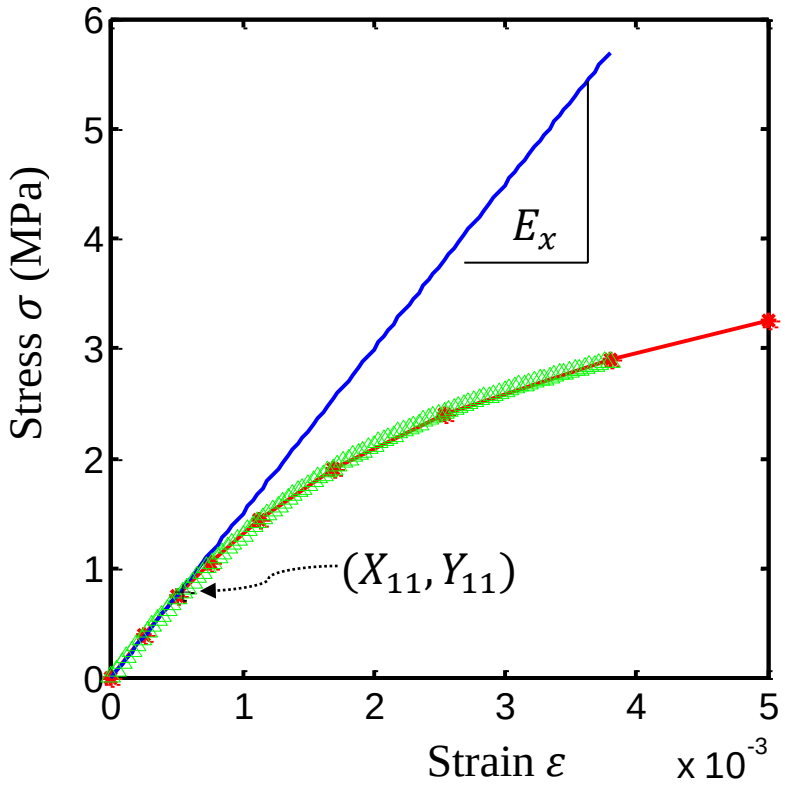

Figure 5.10. Determination of the yield strength of stochastic fibrous structure with concentration of cross-linker at 10 under uniaxial tension in the x direction.

The relative density can be adjusted by changing the concentration of intersections, as mentioned above. The simulation indicates that there is a quadratic function relationship between the yield strength in the x direction and the relative density of the stochastic fibrous structure, as shown in Figure 5.11.

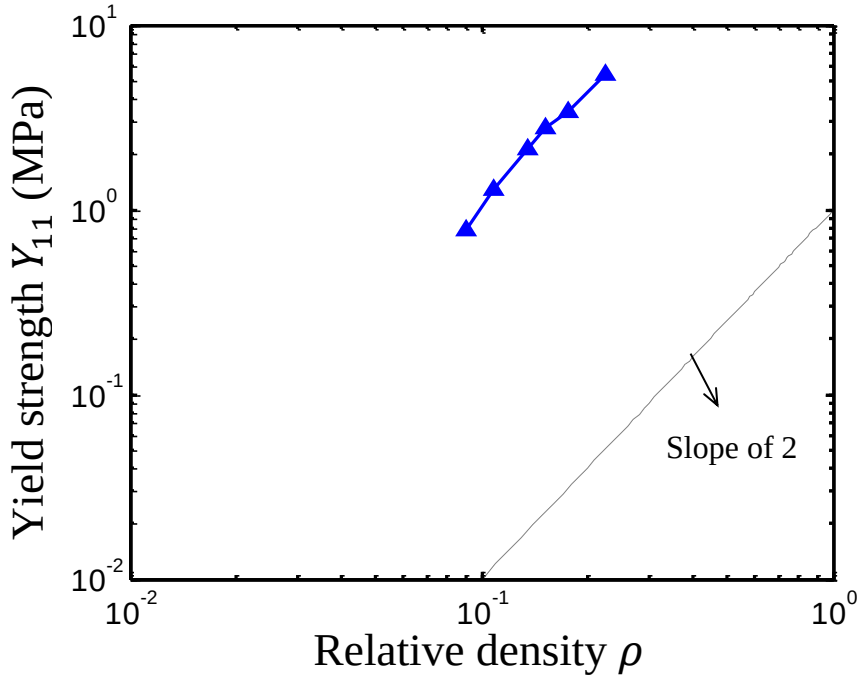

Figure 5.11. The effect of relative density on the yield strength of stochastic fibrous materials in the x direction.

Similarly, in the z direction the yield point (X_{33}, Y_{33}) is determined when the error, γ_z is less than 5%. The error, γ_z takes the form,

$$\gamma_z = \frac{E_z - {}^{\sigma_i}/_{\varepsilon_i}}{E_z} \tag{5.69}$$

where σ_i and ε_i are the data on the fitting curve of stress and strain with interpolation, E_z is the Young's modulus in the z direction obtained from the study of elasticity.

A cubic function relationship between the yield strength in the z direction and the relative density of the stochastic fibrous structure is displayed in Figure 5.12.

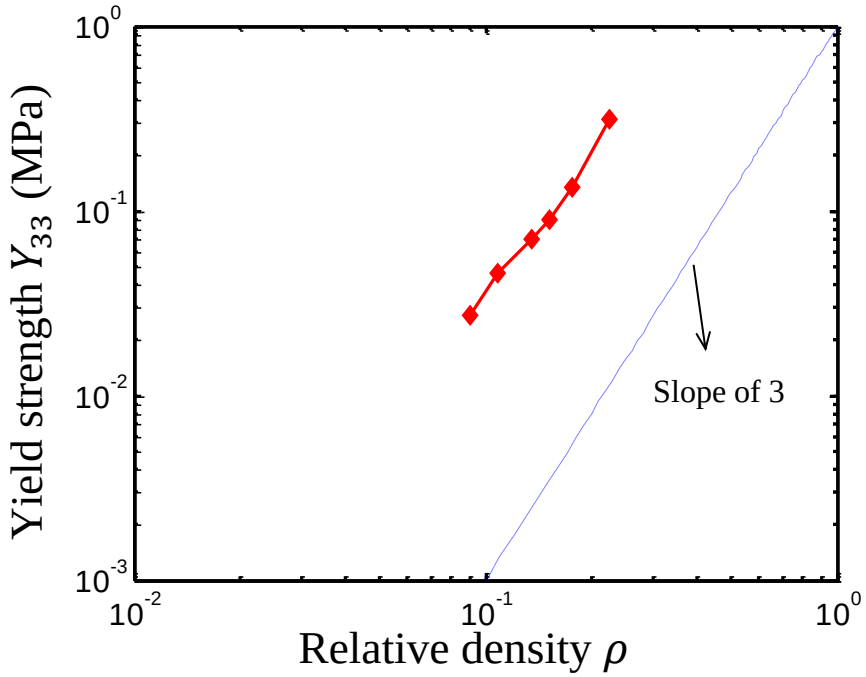

Figure 5.12. The effect of relative density on the yield strength of stochastic fibrous materials in the z direction.

5.5.2 Dimensional analysis of the effect of relative density on the yield strength

It has been suggested that the stochastic fibrous model is transversely isotropic with properties in the x direction the same as those in the y direction. The model is simplified in the x-y plane to conduct the dimensional analysis. As shown in Figure5.13, an external force, P is applied in the x direction. It is assumed that bending dominates the plastic deformation mechanism of the stochastic fibrous structure. As each fibre segment can be regarded as simply supported beam, the maximum bending moment is given by

$$M_{max} = \frac{1}{4} P l_c \tag{5.70}$$

Considering the yield strength locally, i.e., with respect to the solid material, the yielding can be expressed in terms of the maximum internal force, i.e., maximum bending moment,

$$\sigma_s = \frac{M_{max} d}{2I} \tag{5.71}$$

where d is the diameter of the fibre and I is area moment of inertia. For circular cross-section, $I = \frac{\pi d^4}{64}$.

By substituting Eq.(5.70) into Eq.(5.71), we can get

$$\sigma_s = \frac{4 P l_c}{\pi d^3} \tag{5.72}$$

Considering the yield strength globally, i.e, with respect to the fibrous structure, the yielding can be expressed as,

$$Y_{11} = \frac{P}{A} \tag{5.73}$$

where A is the area of the fibre segment, and takes the form,

$$A = l_c d \tag{5.74}$$

So

$$P = Y_{11} l_c d \tag{5.75}$$

By substituting Eq.(5.75) into Eq.(5.72), the yield strength of stochastic fibrous structure under uniaxial loading in the x direction can be specified as

$$Y_{11} = \frac{\pi \sigma_s}{4} (d/l_c)^2 \tag{5.76}$$

Since the diameter d is a fixed value, as well as the length L, it implies that $d/l_c \sim L/l_c$. As discussed above, the relative density is proportional to the concentration of cross-linker, L/l_c, the yield strength takes the form,

$$Y_{11} = \alpha\rho^2 \tag{5.77}$$

where α is a coefficient.

By dimensional analysis, the quadratic function relationship between yield strength in the x direction and the relative density of the stochastic fibrous structure is revealed, which indicates strong agreement with the FE simulation result shown in Figure 5.11.

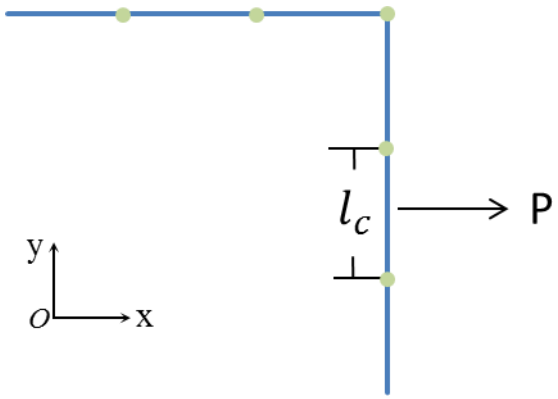

Figure 5.13. Simplified schematic diagram of the fibrous structure in x-y plane for dimensional analysis.

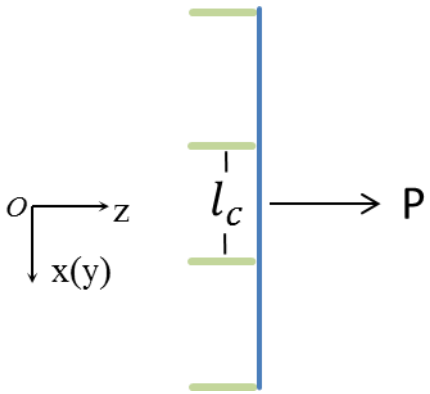

Figure 5.14. Simplified schematic diagram of the fibrous structure in x-z plane for dimensional analysis.

In the random beam model developed in this study, the cross-linkers are represented by inserted beams, based on which a simplified schematic diagram of the fibrous structure in x-z plane is shown in Figure 5.14.

When the fibrous structure is stretched in the z direction, the cross-sectional area of $L \times L$ in the x-y plane can be partitioned into $N_c \times N_c$ units of area ${l_c}^2$. Thus, the yielding in the z direction can be expressed by

$$Y_{33} = \frac{P}{L^2 / {N_c}^2} = \frac{P}{{l_c}^2} \tag{5.78}$$

Based on the beam bending theory, by substituting Eq.(5.78) into Eq.(5.72), the yield strength of stochastic fibrous structure under uniaxial loading in the z direction can be specified as

$$Y_{33} = \frac{\pi \sigma_s}{4} (d/l_c)^3 \tag{5.79}$$

Hence, the relationship between yield strength in the z direction, and the relative density of the stochastic fibrous structure takes the form,

$$Y_{33} = \beta \rho^3 \tag{5.80}$$

where β is a coefficient.

The cubic function from the dimensional analysis has good agreement with the FE simulation, as shown in Figure 5.12.

The relationship between yielding strength and relative density of stochastic fibrous materials indicates the bending dominated deformation mechanism. In contrast, Jin *et al*[10] suggest that the deformation mechanism of porous metal fibre sintered sheets(MFSSs) is stretching dominated.

5.6 **Discussion**

The yield strength and yield surface have been demonstrated for a stochastic fibrous structure with a number of intersections, $L/l_c = 10$, a fibre aspect ratio, $L/d = 80$, with a number of fibres, $N = 200$ and the dimensions of inserted beams, $d_1 = \frac{2}{3}d$; $d_2 = \frac{1}{3}d$, as shown in Figure 5.2(b). The stiffness and the strength of this stochastic fibrous structure in the z direction are much lower than those in the x direction, as shown in Table 5.1, which gives rise to a significant change in the tilt of the yield surface in the plane of anisotropy, as shown in Figure 5.6(b). The stiffness and strength in the z direction are associated with the cross-linkers between any two intersected fibres, dependent upon the concentration and dimensions of the inserted beams that are utilized to represent the cross-linkers. Not surprisingly, the strength and stiffness in the z direction of the stochastic fibrous structure would improve by increasing the dimensions of the inserted beam and the concentration of cross-linking.

5.6.1 Dependence of yielding on the dimensions of inserted beams

The parameter study has been conducted in terms of the diameters, d_1, d_2 of the inserted beams, as shown in Table 5.5, in an attempt to investigate the dependence of yielding on the dimensions of inserted beams in the stochastic fibrous structure. Note that both the Young's modulus in the x and z directions increase with an increase in the dimensions of the inserted beams, whereas the yield strength shows little fluctuation between case 2 and case 3. The mean diameter $(2/3d)$ of the inserted beams in case 2 is lower than that in case 3 $(5/6d)$, but since the dimension is uniform in case 2, it is stronger when the material is subjected to uniaxial loading. As can be

seen from Figure 5.15, the overlapping occurs on the yield surface in the plane of anisotropy between case 2 and case 3. The size of the yield surface on the space of mean-effective stress grows consistently upon raising the dimensions of inserted beams, as shown in Figure 5.16.

Table 5.5. Elastic properties and yield strength values (MPa) of the stochastic fibrous structure model, extracted from uniaxial FE simulations with different dimensions of inserted beams. In the model of stochastic fibrous structure, the number of intersections, $L/l_c = 10$, and the fibre aspect ratio, $L/d = 80$, the number of fibres $N = 200$.

	z direction			x direction		
	E_3	X_3	Y_3	E_1	X_1	Y_1
Case1: $d_1 = \frac{2}{3}d;\ d_2 = \frac{1}{3}d$	4.26	0.87e-2	0.035	1503.31	0.72e-3	1.05
Case2: $d_1 = \frac{2}{3}d;\ d_2 = \frac{2}{3}d$	5.45	0.11e-1	0.059	1776.50	0.87e-3	1.53
Case3: $d_1 = d;\ d_2 = \frac{1}{2}d$	5.54	0.88e-2	0.048	1843.77	0.80e-3	1.47
Case4: $d_1 = d;\ d_2 = d$	6.96	0.12e-1	0.082	2102.28	0.10e-2	2.09

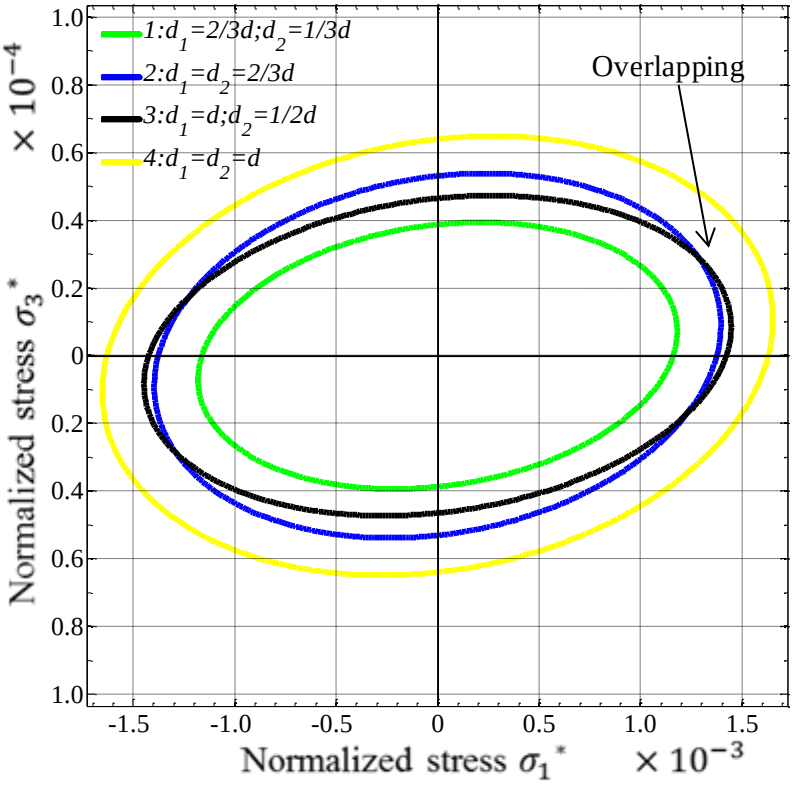

Figure 5.15. Yield surface in the plane of anisotropy for stochastic fibrous structures with different dimensions of inserted beam.

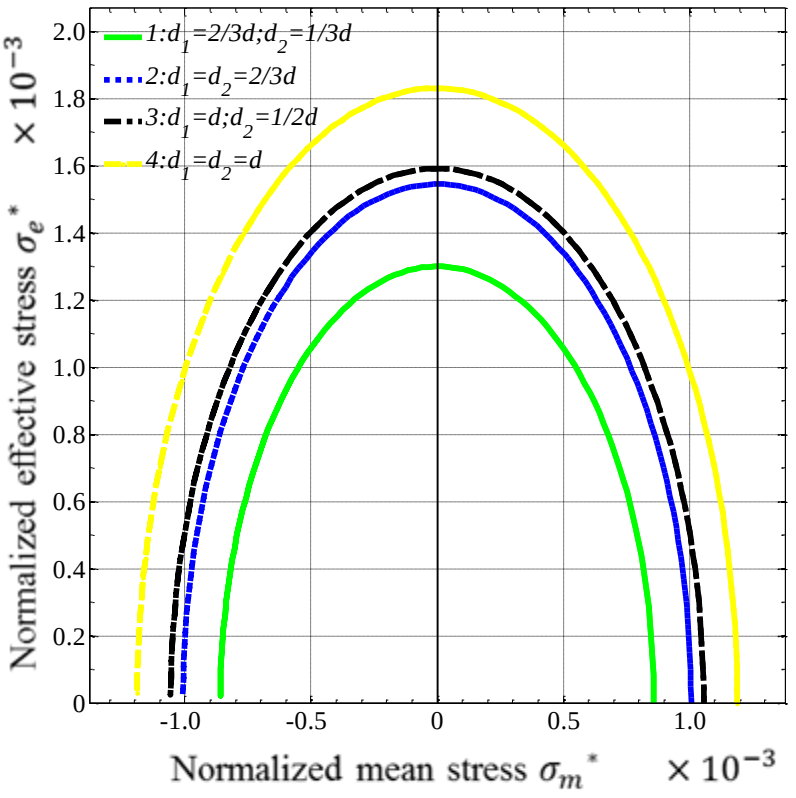

Figure 5.16.Yield surface on the space of mean-effective stress for stochastic fibrous structures with different dimensions of inserted beam.

5.6.2 Dependence of yielding on the concentration of cross-linking

The concentration of cross-linking, L/l_c is a key feature incorporated into the fibrous model. To obtain more intersections or cross-linkers with other fibres, each fibre has to drop down and this thus results in a reduction in the thickness of the structure and, simultaneously, increases the relative density, as shown in Figure 5.3. With more inserted beams the stiffness of the stochastic fibrous structure improves dramatically. The elastic properties and yield strength values (MPa) of the stochastic fibrous structure model, extracted from uniaxial FE simulations with different concentration of cross-linkers, are tabulated in Table 5.6. As can be seen from Figure 5.17-5.18, the strength of the stochastic fibrous structure rises when the concentration of cross-linkers increases. In addition, the yield surface, for the case with concentration of cross-linking at 3, can hardly be seen properly when all the graphs are plotted in one figure, as the discrepancy between sizes of the yield surface with different concentration of cross-linking is significantly large. The strengths in both the x and z directions increase with L/l_c and the magnitude in the x direction is constantly much larger than that in the z direction, however, strength anisotropy (i.e. Y_1/Y_3) reduces gradually. The tilt of the yield surface in the plane of anisotropy becomes larger with the increase of the concentration of cross-linkers. As can be seen from Figure 5.17, the angle of tilt in the plane of anisotropy for a stochastic fibrous structure with $L/l_c = 25$, φ_2 , is larger than φ_1 for the case of $L/l_c = 15$. This indicates that, by increasing the concentration of cross-linkers in the stochastic fibrous structure, the effect of anisotropy can be weakened with respect to the yield strength.

Table 5.6. Elastic properties and yield strength values (MPa) of the stochastic fibrous structure model, extracted from uniaxial FE simulations with different concentration of cross-linkers. In the model of stochastic fibrous structure, the fibre aspect ratio, $L/d = 80$, the number of fibres, $N = 200$ and the dimension of inserted beam, $d_1 = \frac{2}{3}d;\ d_2 = \frac{1}{3}d$.

	z direction			x direction		
	E_3	X_3	Y_3	E_1	X_1	Y_1
$L/l_c = 3$	0.12e-1	0.30e-1	0.34e-3	54.16	0.39e-3	0.021
$L/l_c = 6$	0.32	0.15e-1	0.46e-2	469.20	0.50e-3	0.223
$L/l_c = 10$	4.26	0.87e-2	0.35e-1	1503.31	0.72e-3	1.05
$L/l_c = 15$	27.19	0.40e-2	1.10e-1	3144.77	0.74e-3	2.22
$L/l_c = 25$	250.64	0.19e-2	4.56e-1	5619.92	0.87e-3	4.76

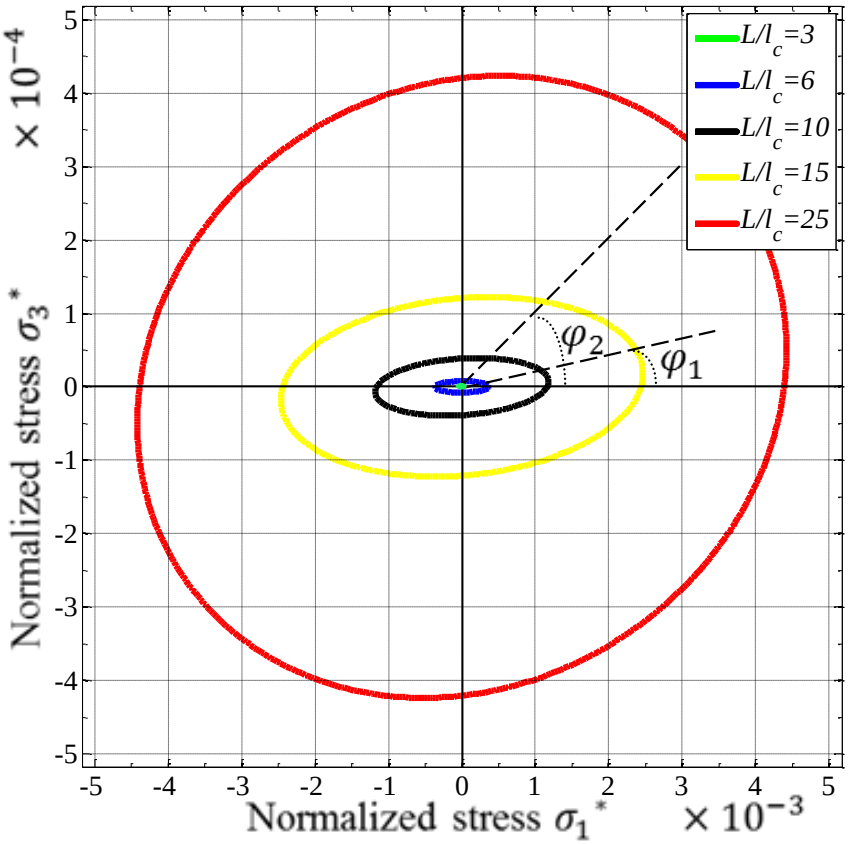

Figure 5.17. Yield surface in the plane of anisotropy for stochastic fibrous structures with different concentration of cross-linkers.

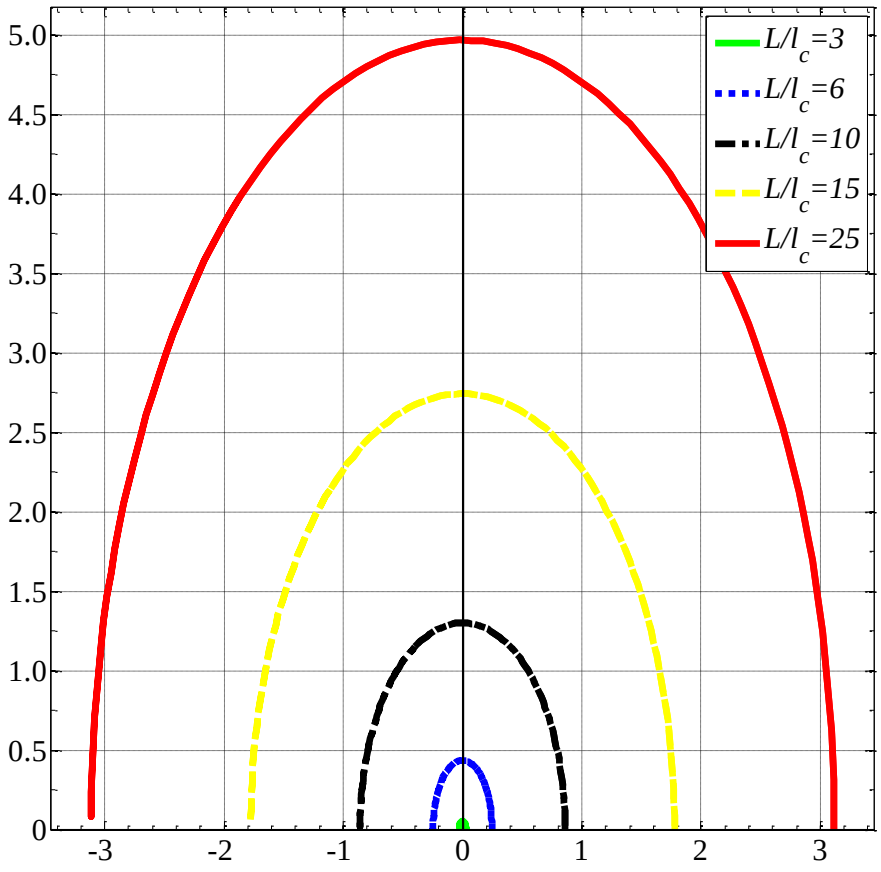

Figure 5.18. Yield surface on the space of mean-effective stress for stochastic fibrous structures with different concentration of cross-linkers.

5.7 **Conclusion**

In this study, a three-dimensional periodic beam model has been developed to investigate the elasto-plastic properties of stochastic fibrous materials with cross-linking. Periodic boundary conditions have been applied to the model and the macroscopic stress and strain of the stochastic fibrous structure have been described over the representative periodic volume element. The concentration of cross-linkers, which have been incorporated into the beam model, plays a significant role in both the stiffness and strength of the stochastic fibrous material. Additional beam between any two fibres, inserted at the intersection points, represents the cross-linking. It has been

suggested that stochastic fibrous material is transversely isotropic, with properties in the x direction identical to those in the y direction. Interestingly, the stochastic model developed in this study is pressure independent, as the response under tension is the same as that under compression. Based on the total strain energy density, the scalar measures of characteristic stress and strain are applied to reveal the mechanical behaviour. The elastic regimes of the characteristic stress-strain curves collapse along a single master line, irrespective of loading path. A critical characteristic strain has been adopted to determine the yield strength of the stochastic fibrous material and it indicates that, with different values of the critical characteristic strain, the yield surface grows or shrinks in the self-similar manner. The yield function can be fully calibrated in terms of the uniaxial tension (or compression) response in the x and z direction, instead of complex multiaxial loading responses. The in-plane stiffness and strength are much higher than those in the out-of-plane direction. By changing the concentration of cross-linkers in the model, the effect of strength anisotropy can be adjusted in terms of the tilt of the yield surface in the plane of anisotropy. The relative density shows a linear relationship with the concentration of cross-linkers. Thus, the dependence of the stiffness and strength of stochastic fibrous materials on relative density is the same as that on concentration of cross-linkers. In addition, it has been showed that the dimension of the inserted beams can also affect the stiffness and strength of stochastic fibrous materials especially in the thickness direction. The effect of relative density on the uniaxial yield strength of stochastic fibrous materials shows a quadratic function in the x direction and a cubic function in the z direction, which have strong agreement with the dimensional analysis.

Chapter 6 Size-dependent and Tunable Elastic Properties of Micro- and Nano-sized Stochastic Fibrous Structures

The effects of strain gradient at the micro-meter scale and the effects of surface elasticity and initial stresses/strains are incorporated into all the deformation mechanisms in the analysis of stochastic fibrous structures. A periodic random beam model with cross-linking has been developed to describe the fibrous networks whose relative density can be adjusted to vary by changing the concentration of cross-linkers. The size-dependent effects on the relationships between the relative density and all the five independent elastic constants of micro- and nano-sized fibrous structures are investigated. In addition, the mechanical and geometrical properties of nano-sized stochastic fibrous networks are tunable and controllable, due to the effects of initial strain, which can be adjusted to vary by the application of external electric/chemical potential.

6.1 **Introduction**

Fibrous materials are a special type of porous materials with low density and high stiffness and strength with promise for a wide range of engineering applications. Fibrous structure can be widely found in biomaterials at micron- and nano-scales. For instance, a typical extra-cellular matrix (ECM) is composed of structural protein nanofibres, such as collagen fibres, with diameters in the order of micrometer[7,60].

Increasing evidence has shown that the mechanical stiffness of ECM plays a significant role in regulating cellular behaviours, including adhesion, proliferation and differentiation of mesenchymal stem cells (MSCs)[52,61,62]. The cytoskeleton (CSK) is a network of filamentous proteins within a cell's cytoplasm, consisting of filamentous actin (F-actin), microtubules and intermediate filaments, with diameters in the order of nanometers[8,120]. The mechanical stiffness of intracellular material, to a great extent, is governed by the cytoskeleton[44]. In industrial engineering, micro and nano-structured fibrous materials can be used in micro-electro-mechanical systems (MEMS) and nano-electro-mechanical systems (NEMS) devices, which are of great interest to scientists and engineers[121].

An understanding of the mechanical properties of macro-sized fibrous materials has been established[10,17]. However, when the dimensions of fibrous structures are reduced to micro- or nano-scale, the stiffness or rigidity is very different from their macro-sized counterparts. In conventional theories, the dimensionless stiffness and strength of fibrous materials are dependent on the relative density, the orientation of the fibres and the slenderness of the fibres, but not on the absolute size. Extensive experimental investigations have shown that the deformation behaviours of metals[67–69] and polymers[70,71] at the micron and sub-micron are size dependent. Some plasticity phenomena have suggested that the smaller is the size, the stronger is the response. Some researchers have been engaging in the development of mechanism-based strain gradient (MSG) theory of plasticity, in which an intrinsic material length scale, l_m is introduced to model the size-dependent effect in the micron to submicron range[79–83]. The strain gradient theory of plasticity assumes that the yield stress depends on not only the strain, but also the strain gradient, which fits the couple stress framework with higher order stress[72–76].

Size-dependence in the nano-sized structural element, in terms of the mechanical properties has also been investigated[89–91,108,122–126]. It has been found that the elastic moduli of silver and lead nanowires of diameter 30nm are almost twice the elastic moduli of bulk Ag and Pb[90]. An intrinsic material length scale l_n , which is defined as the ratio of the surface elastic modulus to the bulk elastic modulus, has been introduced for nano-sized structures[89]. Due to the very large surface-to-volume ratio in nanostructures, surface elasticity and initial surface stress/strain play a dominant role in their mechanical behaviors [89,107,122–126]. The effect of surface elasticity is size-dependent and increases with decreasing size of structure, but the initial surface stress effect can be retained at a constant level, for example, by the application of an electrical potential[101–105]. It is found that the surface stress and the charge in anion adsorption on Au are linearly correlated[104]. Experiments conducted by Biener *et al*[101] have shown that the initial surface stress of nanoporous gold can be controlled to reach 17-26N/m from 1.13N/m, by adjusting the chemical energy.

It is crucial to incorporate the strain gradient effects at the micro-meter scale, and the surface elasticity and initial stress effects at the nano-meter scale into the deformation mechanism of fibrous materials. If the diameter of the fiber is at the nano scale, the elastic properties of a filamentous network are not only size-dependent, but also tunable. To the best of current knowledge, the effect of size dependence on the mechanical behaviour of fibrous materials has not been reported. The objective of this chapter is to investigate the effects of relative density on the size-dependent mechanical properties of micro- and nano-sized fibrous structures. This study could provide fundamental information for scientists in tissue engineering and serve as a guide in the design of MEMS and NEMS.

6.2 **Methodology**

The relative density is a key parameter to elucidate the mechanical behaviour of cellular materials, including fibrous materials[1–3,10]. Gibson and Ashby have put forward that the simplest and most straightforward way to analyse the mechanical properties of cellular materials is to use dimensional analysis[4], which emphasises the dependence of mechanical properties on the relative density of the structure. Finite element method (FEM), which was originally developed for solving solid mechanics problems, offers a means to probe the mechanical properties of stochastic fibrous materials, and by FEM it is easier and more convenient to control the relative density and other key parameters in the model. However, there are no types of elements that could directly incorporate the size-dependent effects into the simulations in commercial finite element software, such as ANSYS. Thus, it is necessary to first work out the equivalent parameters, for instance, diameter, d_e, Young's modulus, E_e, Poisson's ratio, ν_e, for the solid beam whilst taking into account the different size-dependent effects.

6.2.1 Construction of three-dimensional stochastic fibrous structures

A continuum mechanics-based, three-dimensional, periodic beam model has been constructed to describe stochastic fibrous materials. Nanofibrous structure, produced by electrospinning technology, as shown in Figure 6.1(a), displays a great similarity to the random beam model generated, as shown in Figure 6.1(b). In the stochastic model the concentration of intersection or cross-linking has been incorporated, which directly relates to the relative density. As can be seen from Figure 6.2, the cross-linkers between intersected fibres are represented by inserted beams. Full details of the construction of the three-dimensional random beam model with periodicity can be

found in Chapter 3. For the sake of completeness, a brief description of the construction procedure is given as below.

(a) (b)

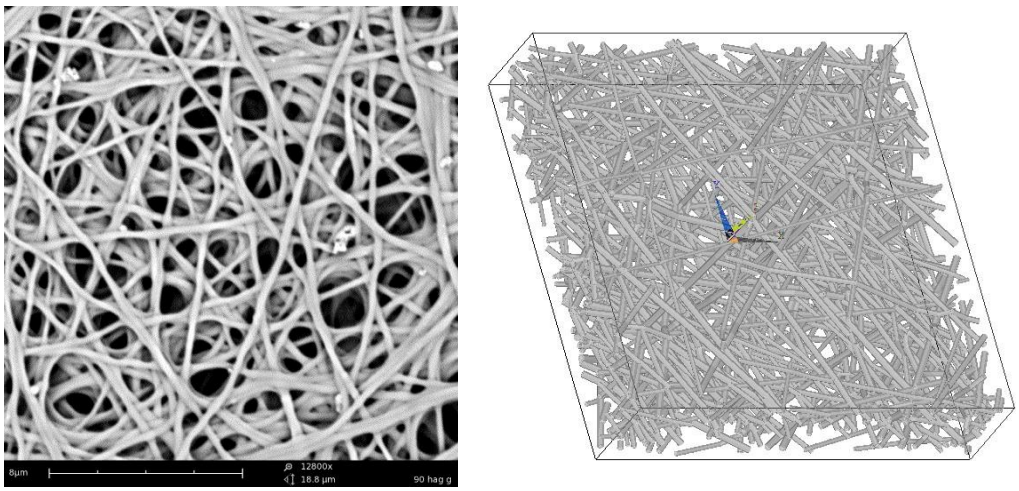

Figure 6.1. (a) SEM images of electrospun HAp/CTS nanocomposite nanofibers[11] and, (b) three-dimensional stochastic fibrous structure generated by ANSYS.

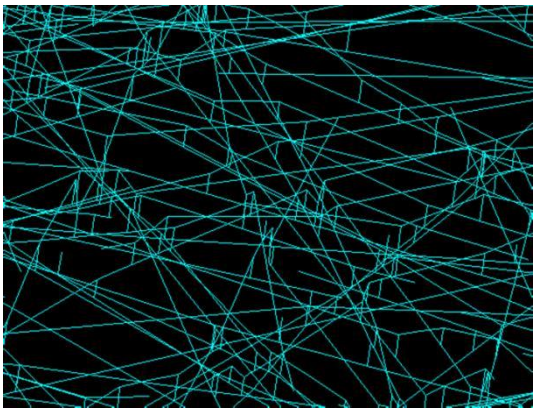

Figure 6.2. Random beam model of the stochastic fibrous structure, in which the fibres are represented by the polylines and the cross-linking of the network is represented by the beam element inserted between intersected fibres.

The establishment of the three-dimensional model is deduced progressively with two-dimensional coordinates being considered first. A representative volume element (RVE) is adopted to investigate the mechanical properties due to computational

limitation. The RVE, which could be called 'unit cell', must be periodic. By creating *3w* x *3w* regions simultaneously in x direction and y direction with periodicity of *w* (*w* is taken to be 1 for simplification), the central region is selected to be periodic. The coordinates in 3-D space of every key point on lines can be derived by the relative positions and 2-D coordinates. In the stochastic model, the length L is not uniform, randomly ranging from 0.8 to 1.2, as we set w as 1. And the orientation, θ ranges from 0 to π. All the fibres represented by beams with a circular cross-section have the same uniform diameter d. The relative density of the fibrous material is specified by:

$$\rho = \frac{1}{4} * \pi d^2 \frac{\sum_{i=1}^{N} L_i}{(1 * 1 * t)} \tag{6.1}$$

where t is the thickness of the fibrous structure, N is the number of filaments. Since the filaments are randomly distributed within the periodicity of w=1 in x and y directions, $1 * 1 * t$ refers to the volume of the structure. The cross-linker concentration is defined by the ratio $N_c = L/l_c$, where l_c is the mean distance between two neighbouring cross-linkers along a filament of length L. To obtain more intersections or cross-linkers with other fibres, each fibre has to drop down, this thus will decrease the thickness of the structure and meanwhile increase the relative density. The relative density is linearly related to the number of cross-linkers. Therefore, the relative density of the stochastic fibrous structure can be adjusted by changing the concentration of cross-linkers.

In addition, it has been suggested that the periodic boundary conditions are more suitable than the mixed boundary conditions and prescribed displacement boundary conditions[1,2]. In the numerical simulation, the three-node beam element (BEAM189) is utilized, based on the Timoshenko beam theory. The constituting solid material of filament is assumed to be elastic, with a Young's modulus $E_s = 200GPa$. The non-

dimensional equivalent Young's modulus is one of the main objects of study with respect to the characteristic of fibrous structure. As it has been indicated, the Poisson's ratio of most solid materials varies between 0.1 and 0.5[109], the Poisson's ratio of the filament is set at 0.3. To measure the Young's moduli or shear moduli of the filamentous network, a uniaxial tensile or shear strain is applied across the periodic boundary conditions.

6.2.2 Size-dependent effects at micro-scale

At micro scale, the strain gradient has a dominant effect on the mechanical behaviour of the stochastic fibrous material. The bending, torsion and axial stretching or compression rigidities of micro-sized structures have been obtained as follows.

For uniform beams with circular cross section at micro-meter scale,

the bending rigidity is given by[122],

$$D_b = \frac{E_s \pi d^4}{64}\left(1 + 8(1+\nu_s)\left(\frac{l_m}{d}\right)^2\right) \tag{6.2}$$

the torsion rigidity is obtained by [77],

$$D_t = \frac{G_s \pi d^4}{32}\left(1 + 24\left(\frac{l_m}{d}\right)^2\right) \tag{6.3}$$

the axial stretching or compression rigidity is presented by[122],

$$D_c = \frac{E_s \pi d^2}{4} \tag{6.4}$$

where l_m is the material length parameter at the micro-meter scale (which can be experimentally measured and is usually in the range between submicron and microns,

and different for different materials), d is the diameter of the circular cross-section. E_s, G_s, ν_s are the Young's modulus, shear modulus and Poisson's ratio of the solid material, respectively.

Since there is no type of elements that could directly incorporate the size-dependent effects into the simulations in commercial finite element software, thus an equivalent solid beam, with diameter d_e, Young's modulus E_e, Poisson's ratio ν_e, is used for the beam element in the finite element simulation [126]. These three equivalent values can be obtained from the following three equations, in which the three rigidities, D_b, D_t, D_c have been presented in Eq.(6.2-6.4).

$$\frac{E_e \pi {d_e}^4}{64} = D_b \tag{6.5}$$

$$\frac{E_e \pi {d_e}^4}{64(1+\nu_e)} = D_t \tag{6.6}$$

$$\frac{E_e \pi {d_e}^2}{4} = D_c \tag{6.7}$$

By solving the Eq.(6.5-6.7), the equivalent three parameters for the BEAM 189 element are given as

$$E_e = \frac{{D_c}^2}{4\pi D_b} \tag{6.8}$$

$$\nu_e = \frac{D_b}{D_t} - 1 \tag{6.9}$$

$$d_e = 4\sqrt{\frac{D_b}{D_c}} \tag{6.10}$$

We can obtain the equivalent parameters of the beam element, that could incorporate the size effect as functions of the intrinsic parameters of the solid material, by substituting Eq.(6.2-6.4) into Eq.(6.8-6.10).

$$E_e = \frac{E_s}{1 + 8(1 + \nu_s)(\frac{l_m}{d})^2} \tag{6.11}$$

$$\nu_e = \frac{(1 + \nu_s)((1 + 8(1 + \nu_s)(\frac{l_m}{d})^2))}{(1 + 24(\frac{l_m}{d})^2)} - 1 \tag{6.12}$$

$$d_e = d\sqrt{(1 + 8(1 + \nu_s)(\frac{l_m}{d})^2)} \tag{6.13}$$

To validate the applicability of the equivalent values of the Young's modulus, Poisson's ratio and the diameter for the beam element in the simulation, a single horizontal micro-sized beam cantilever structure is tested. The left hand side of the cantilever is fixed and a concentrated transverse load (a small load is assumed as $F = 1 \times 10^6 N$) is applied to the free end. The Young's modulus and Poisson's ratio of the solid material are set as 200 GPa and 0.3, respectively. The length and diameter of the cantilever are assumed as L=100μm and 1 μm. The parameter to describe the strain gradient effect, l_m/d , is set as 0.2. According to Eq.(6.11-6.13), the values of the equivalent Young's modulus, Poisson's ratio and the equivalent diameter of the circular cross-section beam are listed in Table 6.1. By applying these values into material properties of BEAM 189 in ANSYS, the deflection is 0.2402 μm. Whereas the theoretical result obtained by Eq.(6.14) for the cantilever beam, in which the size-dependent effect has been incorporated, is 0.2398 μm, which is very close to the numerical result. It suggests that the adoption of the equivalent Young's modulus, E_e, the equivalent Poisson's ratio, ν_e and the equivalent diameter, d_e can be used to

effectively involve the size effect into the finite element simulation. Note that when the size-dependent effect is not incorporated, i.e., $l_m/d = 0$, the deflection of this cantilever beam is 0.3395μm.

$$\Delta = \frac{FL^3}{3D_b} = \frac{64FL^3}{3E_s\pi d^4\left(1 + 8(1+\nu_s)\left(\frac{l_m}{d}\right)^2\right)} \tag{6.14}$$

Table 6.1. The equivalent Young's modulus, Poisson's ratio and equivalent diameter in the finite element simulation to incorporate the size-dependent effects in the micro-scale. The Young's modulus, Poisson's ratio of the solid material are 200e3MPa, 0.3 and the diameter of the fibre is 1 μm

l_m/d	E_e(MPa)	ν_e	d_e (μm)
0.0	2.0000e5	0.3000	1.000
0.2	1.4124e5	-0.0608	1.190
0.5	5.5556e4	-0.3314	1.897
1.0	1.7544e4	-0.4072	3.376

Note that the equivalent Young's modulus and Poisson's ratio, and equivalent diameter, are based on the bending rigidity, D_b, torsion rigidity, D_t and axial stretching (or compression) rigidity, D_c ,without taking the shear rigidity, D_s into consideration. Eq.(6.15) gives the deflection of the cantilever beam with shearing. As can be seen from Table 6.2, the effect of shear can be ignored, especially when the slenderness ratio, *L/d* is larger than 10. In the stochastic fibre model, the diameter of the fibre is uniformly set as 1 μm, while the length ranges from 80 μm to 120 μm, with the mean length at 100 μm, and the slenderness ratio at 100. It should be noted that, since the concentration of intersections, $N_c = L/l_c$ is incorporated, the fibre has been divided into $N_c + 1$ sections, and the slenderness ratio for each beam section drops

down. However, the accuracy of the solution, calculated from Eq.(6.14) is sufficient, even when the slenderness ratio is as small as 4, in which the concentration of intersections in the fibrous structure is more than 20. Thus the equivalent parameters E_e, ν_e, d_e, obtained from bending rigidity, torsion rigidity and stretching or compression rigidity, without taking shear rigidity into consideration, can be used in the finite element simulation to incorporate the size-dependent effects in micro-metre scale.

$$\Delta = \frac{64FL^3}{3E_e\pi {d_e}^4} + \frac{10}{9}\frac{8FL(1+\nu_e)}{E_e\pi {d_e}^2} \tag{6.15}$$

Table 6.2. The comparison between solutions calculated from Eq.(6.14)(which is based on the bending rigidity) and from Eq.(6.15) (which is based on the bending and shear rigidity) as well as the simulation result, in terms of the deflection of the cantilever beam with different slenderness ratio, *L/d*. The Young's modulus, Poisson's ratio of the solid material are 200e3MPa, 0.3 and the diameter of the fibre is 1 μm

L/d	Eq.(6.14)/ μm	Eq.(6.15)/ μm	Simulation/ μm	Error of Eq.(6.14)	Error of Eq.(6.15)
4	0.15346e-4	0.15877e-4	0.15935e-4	3.84%	0.36%
10	0.23978e-3	0.24111e-3	0.24165e-3	0.78%	0.22%
40	0.15346e-1	0.15351e-1	0.15382e-1	0.23%	0.20%
100	0.23978	0.23979	0.24026	0.20%	0.20%

6.2.3 Size-dependent effects at nano-scale

It has been investigated that at the nanometre scale, the surface elasticity and initial strain (stress) effects are of great importance in determining the mechanical behaviour[122–126]. The bending, transverse shear, torsion and axial stretching or compression rigidities of nano-sized structures have been obtained as follows.

For uniform beams with circular cross section at nano-meter scale,

the bending rigidity is given by[93],

$$D_b = \frac{E_s \pi d^4}{64}\left(1 + 8\frac{l_n}{d} + \frac{\nu_s}{1-\nu_s}\varepsilon_0^L\right) \tag{6.16}$$

the torsion rigidity is obtained by[125],

$$D_t = \frac{G_s \pi d^4}{32}\left(1 + 8\frac{l_n}{d}\right) \tag{6.17}$$

the axial stretching or compression rigidity is presented by[125],

$$D_c = \frac{E_s \pi d^2}{4}\left(1 + 4\frac{l_n}{d}\right) \tag{6.18}$$

where l_n is the material intrinsic length at the nano-meter scale, which can be expressed by $l_n = S/E_s$, and typically is in the order of 0.01-0.1nm[89,99], S is the surface elasticity modulus. ε_0^L is the initial strain in the length direction of the beam, whose amplitude can be controlled to vary by an applied electric potential[102,103]. An equivalent solid beam with diameter d_e, Young's modulus E_e, Poisson's ratio ν_e is used for the beam element in the finite element simulation, which is the same approach as that used to deal with the size-dependent effects in the micro-scale.

The equivalent parameters of the beam element, incorporating the size effect in the nano-scale, can be obtained by substituting Eq.(6.16-6.18) into Eq.(6.8-6.10).

Here, the surface elasticity effect and the initial stress or strain effect are considered separately. When the initial stress (strain) is absent, i.e., $\varepsilon_0^L = 0$, the equivalent Young's modulus E_e, equivalent Poisson's ratio ν_e and diameter d_e can be expressed as

$$E_e = \frac{E_s(1+4\frac{l_n}{d})^2}{1+8\frac{l_n}{d}} \tag{6.19}$$

$$\nu_e = \nu_s \tag{6.20}$$

$$d_e = d\sqrt{\frac{1+8\frac{l_n}{d}}{1+4\frac{l_n}{d}}} \tag{6.21}$$

The values of the equivalent Young's modulus, Poisson's ratio and the equivalent diameter of the circular cross-section beam, when the surface elasticity effect in the nano-scale is involved, are listed in Table 6.3.

Table 6.3. The equivalent Young's modulus, Poisson's ratio and equivalent diameter in the finite element simulation to incorporate the surface elasticity effects in the nano-scale. The Young's modulus, Poisson's ratio of the solid material are 200e3MPa, 0.3 and the diameter of the fibre is 1 nm.

l_n/d	E_e(MPa)	ν_e	d_e (nm)
0.0	2.0000e5	0.3000	1.000
0.2	2.4923e5	0.3000	1.202
0.5	3.6000e5	0.3000	1.291
1.0	5.5556e5	0.3000	1.342

When the surface elasticity effect is absent, i.e.,$l_n/d = 0$, and the initial stress or strain is incorporated into the finite element simulation, the equivalent Young's modulus E_e, equivalent Poisson's ratio ν_e and diameter d_e can be expressed as

$$E_e = \frac{E_s}{1+\frac{\nu_s}{1-\nu_s}\varepsilon_0^L} \tag{6.22}$$

$$\nu_e = (1+\nu_s)\left(1+\frac{\nu_s}{1-\nu_s}\varepsilon_0^L\right)-1 \tag{6.23}$$

$$d_e = d\sqrt{1+\frac{\nu_s}{1-\nu_s}\varepsilon_0^L} \tag{6.24}$$

When the initial strain effects are present, the actual beam diameter of the circular cross-section is $d = d_0(1+\varepsilon_0^R)$, where d_0 is the original diameter, ε_0^R is the initial strain in the radial direction $\varepsilon_0^R = \frac{1-3\nu_s}{2(1-\nu_s)}\varepsilon_0^L$[123,125]. Thus the equivalent diameter is written as

$$d_e = d_0\left(1+\frac{1-3\nu_s}{2(1-\nu_s)}\varepsilon_0^L\right)\sqrt{1+\frac{\nu_s}{1-\nu_s}\varepsilon_0^L} \tag{6.25}$$

The amplitude of the initial strain, ε_0^L is set to -0.06, -0.03, 0, 0.03, 0.06, respectively. The values of the equivalent Young's modulus, Poisson's ratio and the equivalent diameter of the circular cross-section beam, when the initial strain effects in the nano-scale are involved, are listed in Table 6.4. One thing that should be mentioned is that, when the effects of initial strain ε_0^L are present, the corresponding nodal coordinates (x, y, z) in the geometry of the periodic fibre model are related to the original coordinates (x_0, y_0, z_0) by

$$x = x_0(1+\varepsilon_0^L) \tag{6.26}$$

$$y = y_0(1+\varepsilon_0^L) \tag{6.27}$$

$$z = z_0(1+\varepsilon_0^R) \tag{6.28}$$

Thus, the length of the fibre is $L = L_0(1+\varepsilon_0^L)$, where L_0 is the original length of the fibre in the structure, when the initial strain effects are present.

Table 6.4. The equivalent Young's modulus, Poisson's ratio and equivalent diameter in the finite element simulation to incorporate the initial strain effects in the nano-scale. The Young's modulus, Poisson's ratio of the solid material are 200e3MPa, 0.3 and the diameter of the fibre is 1 nm.

ε_0^L	E_e(MPa)	ν_e	d_e (nm)
-0.06	2.0528e5	0.2666	0.9828
-0.03	2.0260e5	0.2833	0.9914
0	2.0000e5	0.3000	1.0000
0.03	1.9746e5	0.3167	1.0086
0.06	1.9499e5	0.3334	1.0171

6.3 **Numerical results**

It has been suggested that the random beam model, developed to represent stochastic fibrous networks, is transversely isotropic in the x-y plane, which is perpendicular to the thickness direction (z-axis). Note that the transverse isotropy is size-independent and could apply to micro- and nano-sized fibrous structures. The elastic moduli and the Poisson's ratios of the transversely isotropic fibrous networks have to satisfy the reciprocal relations: $E_x = E_y$; $\nu_{12} = \nu_{21}$; $\nu_{13} = \nu_{23}$; $\nu_{13}/E_x = \nu_{31}/E_z$; $\nu_{31} = \nu_{32}$;$G_{12} = 0.5E_x/(1 + \nu_{12})$; $G_{13} = G_{23}$. All the five independent elastic constants, E_x, E_z, ν_{12}, ν_{13}, G_{13} of micro- and nano-structured fibrous networks are obtained by computer simulation in this section. Since the model is built randomly with the ranges of lengths and orientations of all the filaments taken into consideration, all values are presented as means and standard deviations of twenty independent model calculations. The Young's moduli and shear moduli are normalised against the Young's modulus of the solid material $E_s = 200$ GPa.

6.3.1 Effects of relative density on the size-dependent elastic properties of micro-sized fibrous structures

At the micro scale, the strain gradient has a dominant effect on the mechanical behaviour of stochastic fibrous material. l_m/d is used to describe the strain gradient effects in micro-scale, where l_m is the material length scale at the micro-meter scale (which can be experimentally measured and is usually in the range between submicron and microns, and different for different materials), d is the diameter of the circular cross-section. Simulations for different values of l_m/d ($l_m/d = 0, 0.2, 0.5, 1.0$) have been conducted to investigate the size-dependent effects in micro scale on the elastic properties of stochastic fibrous materials. It is noted that when l_m/d is 0, in which the diameter of the beam is very large compared to the intrinsic material length scale, l_m, the size-dependent effect vanishes and the elastic constants reduce to those of their conventional counterparts[122–126].

For the micro-sized fibrous networks, the size-dependent relationships between the relative density and the non-dimensional Young's moduli in the x and z directions are plotted in Figure 6.3 and Figure 6.4. As can be seen, the smaller the fibre diameter, the larger the dimensionless Young's moduli in the x direction and z directions; and the larger the relative density, the larger the dimensionless Young's moduli.

Figure 6.5 and Figure 6.6 give the size-dependent effects on the relationship between Poisson's ratios, ν_{12} and ν_{13} and the relative density of stochastic fibrous materials at the micro-metre scale. The Poisson's ratio, ν_{12} is almost unchanged, which indicates that ν_{12} is independent of relative density and size of fibre. By contrast, Poisson's ratio, ν_{13} is sensitive to the relative density and the strain gradient effect. ν_{13}, which can be

up to 7, when the relative density is small and the strain gradient effect is absent ($l_m/d = 0$), and decreases with increasing relative density and decreasing diameter.

As can be seen from Figure 6.7, the shear modulus, G_{13} has a similar trend to the Young's moduli. The smaller the diameter, the larger is the dimensionless shear modulus; and the larger the relative density, the larger is the dimensionless shear modulus.

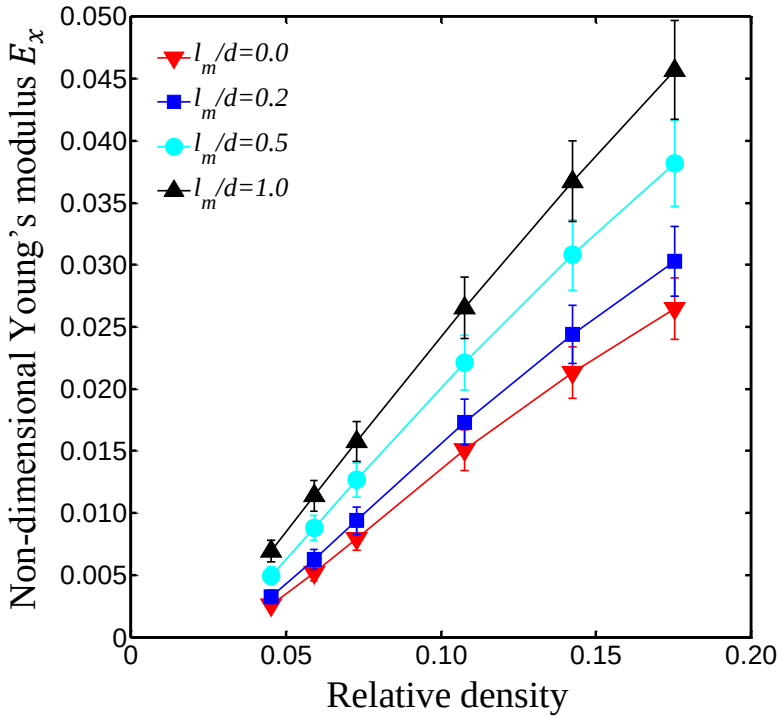

Figure 6.3. Size-dependent effect on the relationship between the non-dimensional Young's modulus in the x direction and the relative density of stochastic fibrous materials at micro-metre scale.

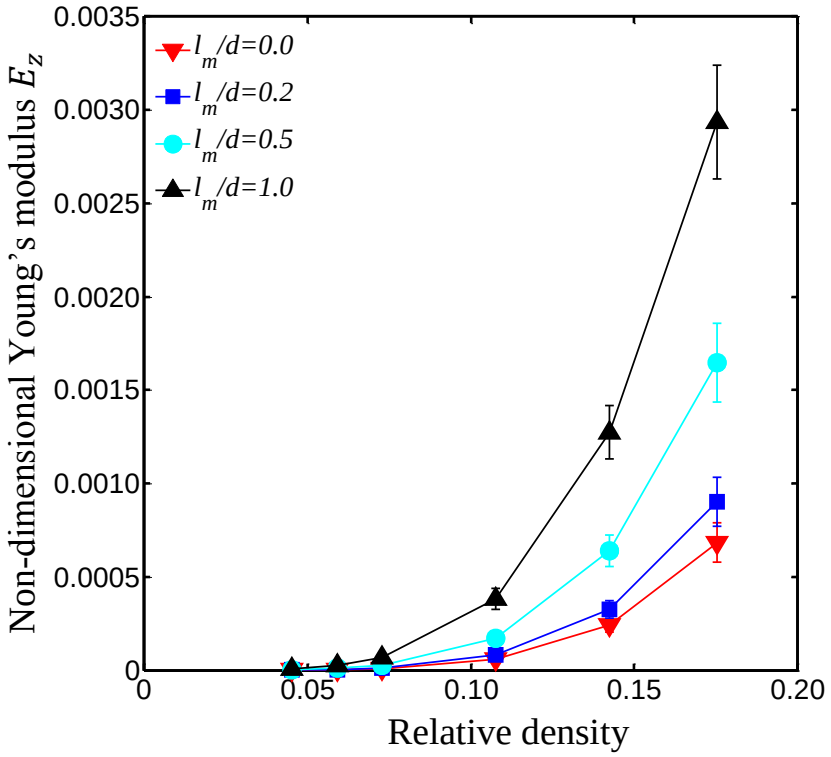

Figure 6.4. Size-dependent effect on the relationship between the non-dimensional Young's modulus in the z direction and the relative density of stochastic fibrous materials at micro-metre scale.

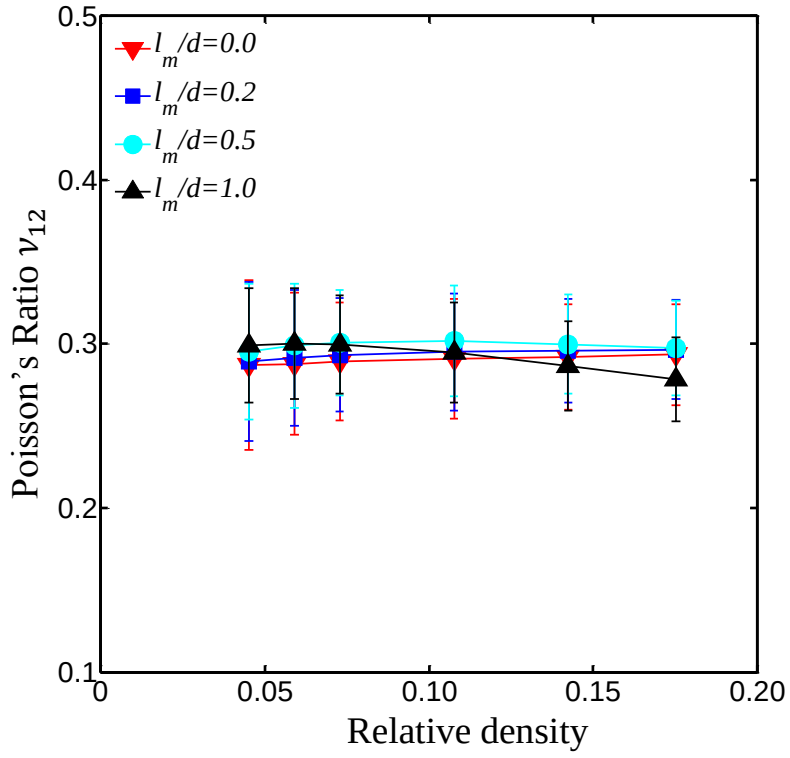

Figure 6.5. Size-dependent effect on the relationship between Poisson's Ratio $\boldsymbol{\nu_{12}}$ and the relative density of stochastic fibrous materials at micro-metre scale.

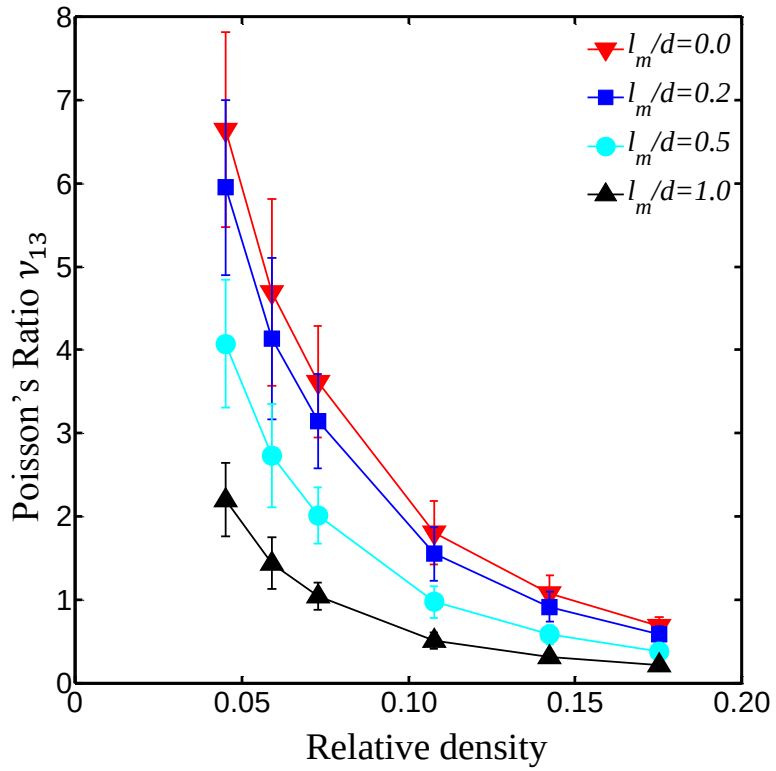

Figure 6.6. Size-dependent effect on the relationship between Poisson's Ratio $\boldsymbol{\nu_{13}}$ and the relative density of stochastic fibrous materials at micro-metre scale.

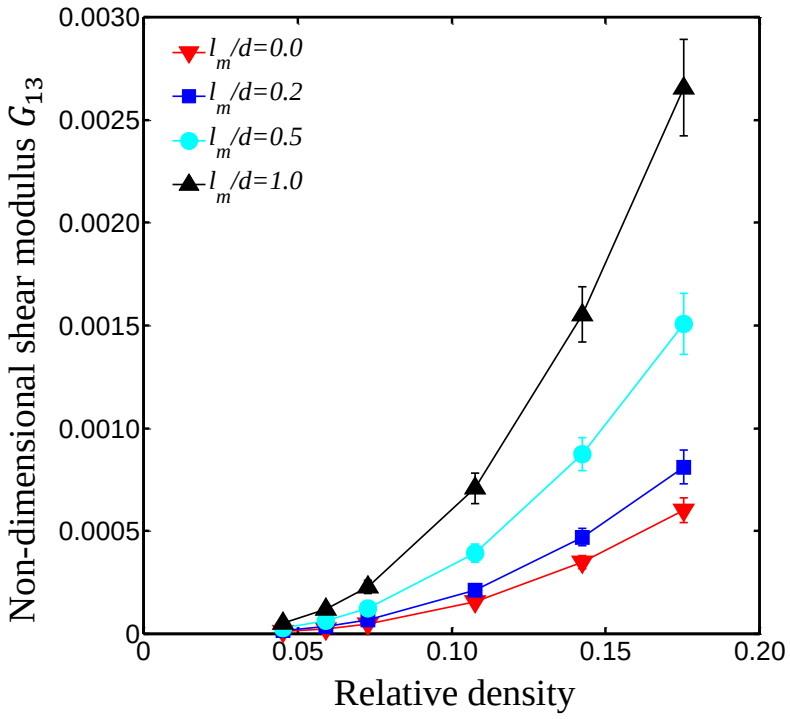

Figure 6.7. Size-dependent effect on the relationship between the non-dimensional shear modulus $\boldsymbol{G_{13}}$ and the relative density of stochastic fibrous materials at micro-metre scale.

6.3.2 Effects of relative density on the size-dependent elastic properties of nano-sized fibrous structures

It has been investigated that at the nano-metre scale, the surface elasticity and initial strain (stress) effects are of great importance in the mechanical behaviour[122–126]. l_n/d is used to describe the surface elasticity effects in nano-scale, where l_n is the material intrinsic length at the nano-meter scale, which can be expressed by $l_n = S/E_s$ (where S is the surface elasticity modulus), and may vary over a range from 0.01nm to 0.1nm for different materials. ε_0^L is the initial strain in the length direction of the beam, whose amplitude can be controlled to vary by an applied electric potential. Simulations in finite element software for different values of l_n/d ($l_n/d = 0, 0.2, 0.5, 1.0$) and ε_0^L ($\varepsilon_0^L = -0.06, -0.03, 0, 0.03, 0.06$) have been conducted to investigate the surface elasticity and initial strain effects separately at nanometre scale on the elastic properties of stochastic fibrous materials. Note that when $l_n/d = 0$ and $\varepsilon_0^L = 0$, the size-dependent effect in nano-scale vanishes and the elastic constants reduce to those of their conventional counterparts.

For the nano-structured fibrous networks, when the effects of the initial stresses/strains are absent, the size-dependent relationships between the non-dimensional Young's moduli and the relative density are shown in Figure 6.8 and Figure 6.9. As can be seen, the smaller the diameter, the larger is the dimensionless Young's moduli; and the larger the relative density, the larger the dimensionless Young's moduli. The trend for Young's modulus is similar to that for shear modulus, as shown in Figure 6.12. The effects of surface elasticity on the relationships between the Poisson's ratios and relative density are given in Figure 6.10 and Figure 6.11.

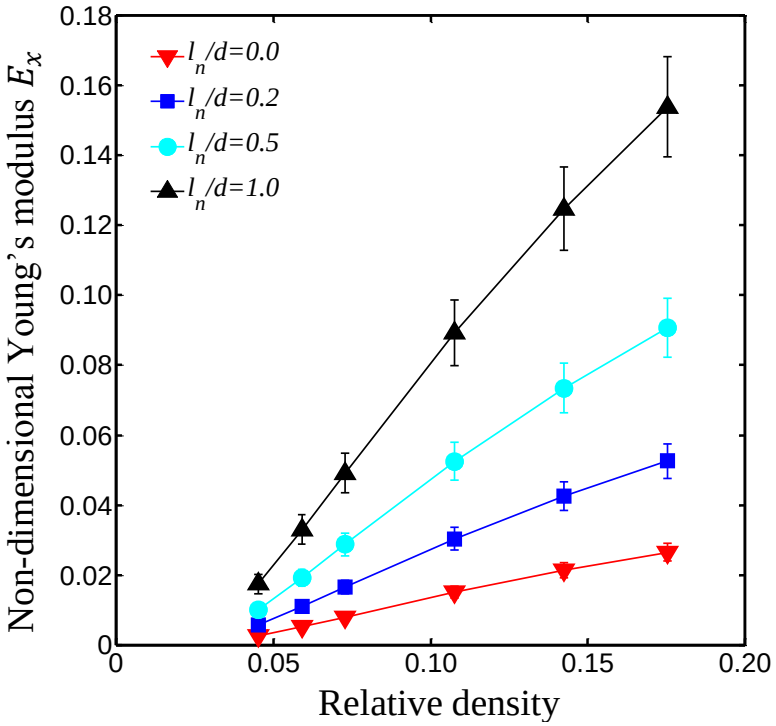

Figure 6.8. Size-dependent effect on the relationship between the non-dimensional Young's modulus in the x direction and the relative density of stochastic fibrous materials at nano-metre scale.

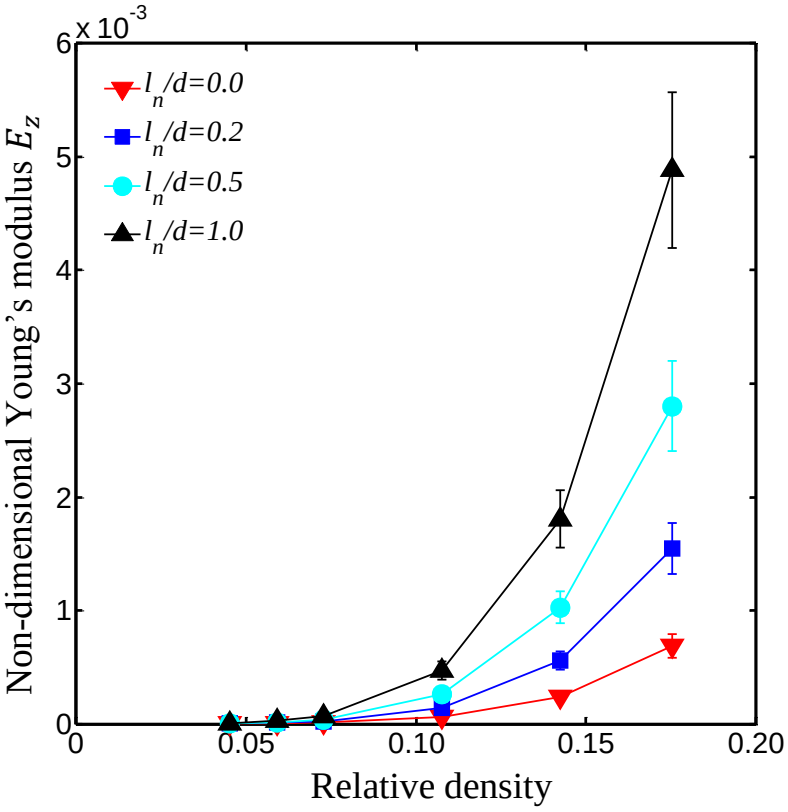

Figure 6.9. Size-dependent effect on the relationship between the non-dimensional Young's modulus in the z direction and the relative density of stochastic fibrous materials at nano-metre scale.

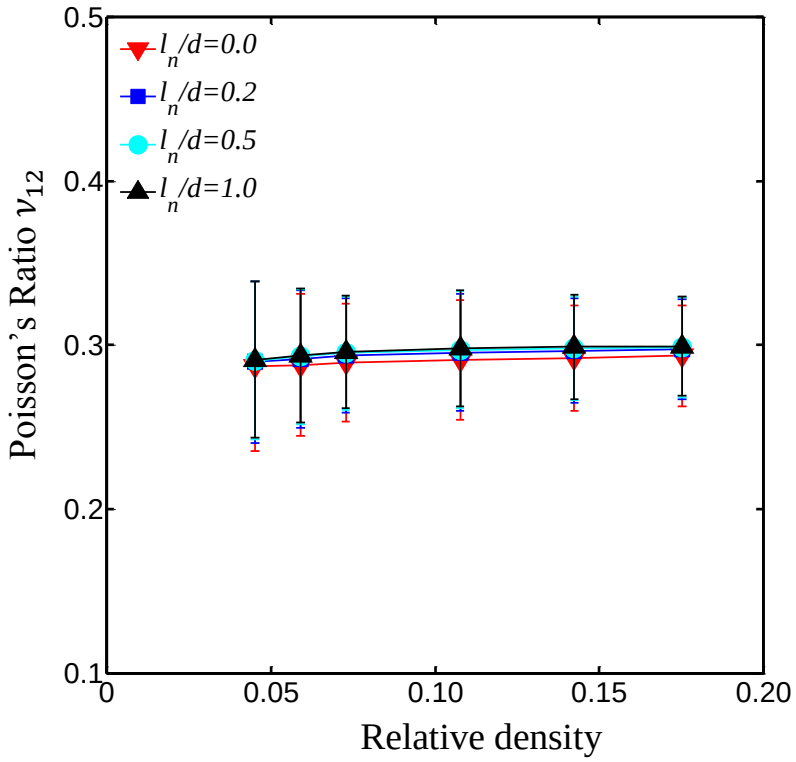

Figure 6.10. Size-dependent effect on the relationship between Poisson's Ratio $\boldsymbol{\nu_{12}}$ and the relative density of stochastic fibrous materials at nano-metre scale.

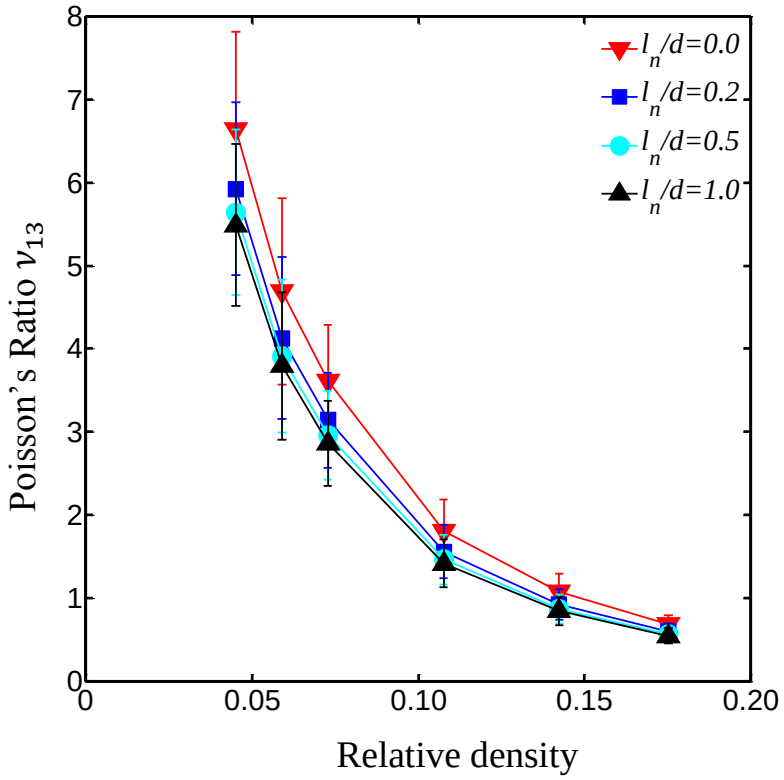

Figure 6.11. Size-dependent effect on the relationship between Poisson's Ratio $\boldsymbol{\nu_{13}}$ and the relative density of stochastic fibrous materials at nano-metre scale.

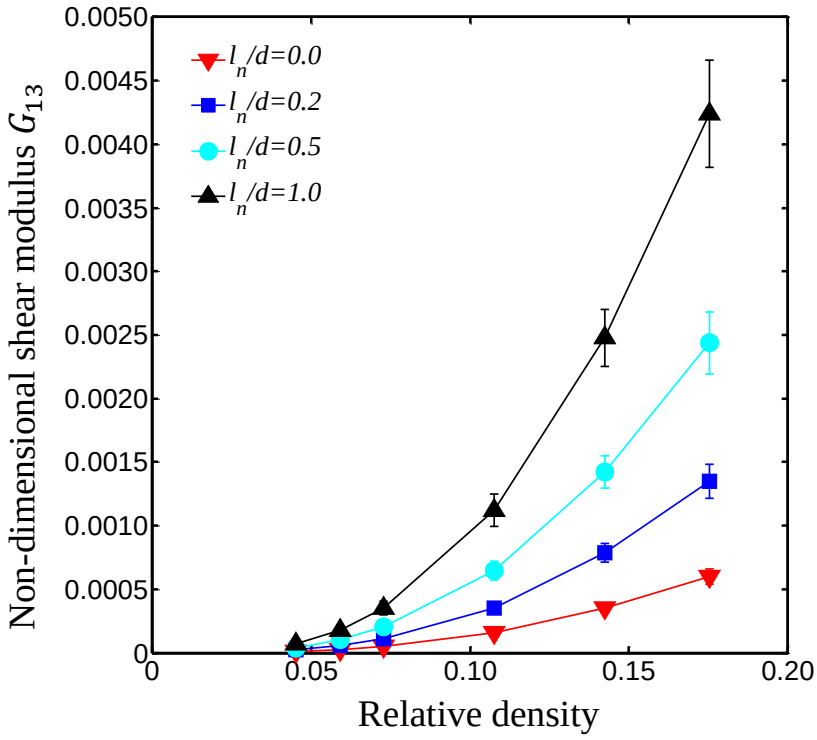

Figure 6.12. Size-dependent effect on the relationship between the non-dimensional shear modulus $\boldsymbol{G_{13}}$ and the relative density of stochastic fibrous materials at nano-metre scale.

When the effects of the surface elasticity are absent (i.e $l_n/d = 0$), the size-dependent relationships between the non-dimensional Young's moduli and the relative density are shown in Figure 6.13 and Figure 6.14. The plot of non-dimensional Young's modulus in the z direction, versus the relative density, is in log-log scale. As can be seen from Figure 6.14, the lines are approximately straight and parallel, indicating a power law relationship between the Young's modulus and the relative density. Moreover, the non-dimensional shear modulus and Poisson's ratio ν_{13} can be controlled to vary by adjusting the amplitude of an applied initial strain, as shown in Figure 6.16 and Figure 6.17. However, the Poisson's ratio ν_{12} is almost constant with different initial strains, as shown in Figure 6.15.

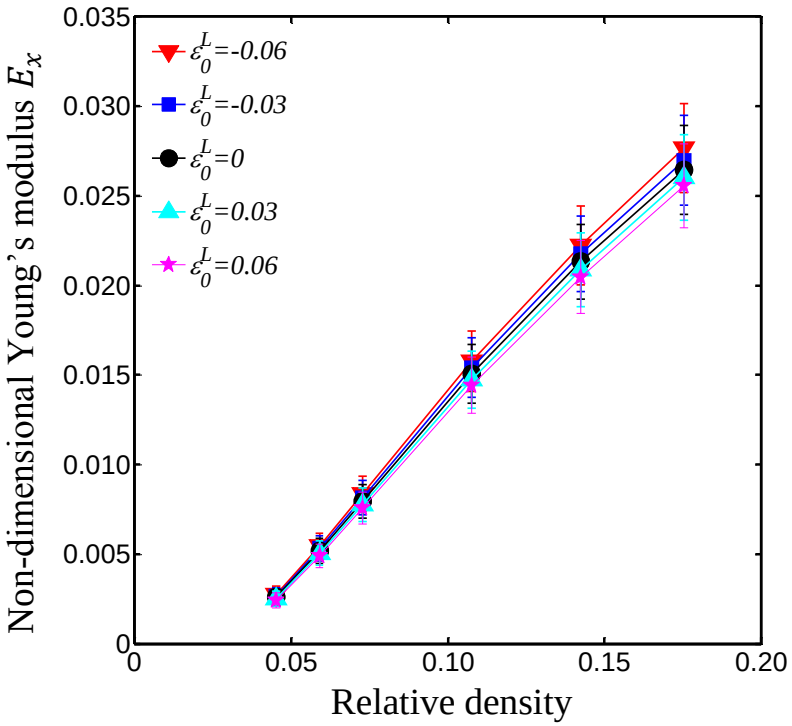

Figure 6.13. Plot of the non-dimensional Young's modulus$\boldsymbol{E_x}$ vs the relative density of nano-sized stochastic fibrous networks with the presence of effects of initial strains/stresses

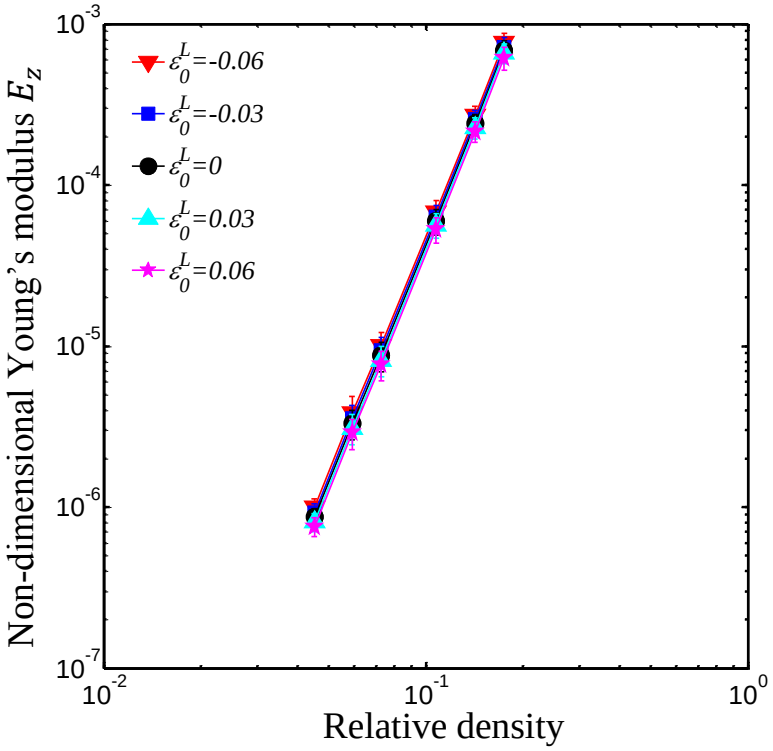

Figure 6.14. Logarithmic plot of the non-dimensional Young's modulus$\boldsymbol{E_z}$ vs the relative density of nano-sized stochastic fibrous networks with the presence of effects of initial strains/stresses

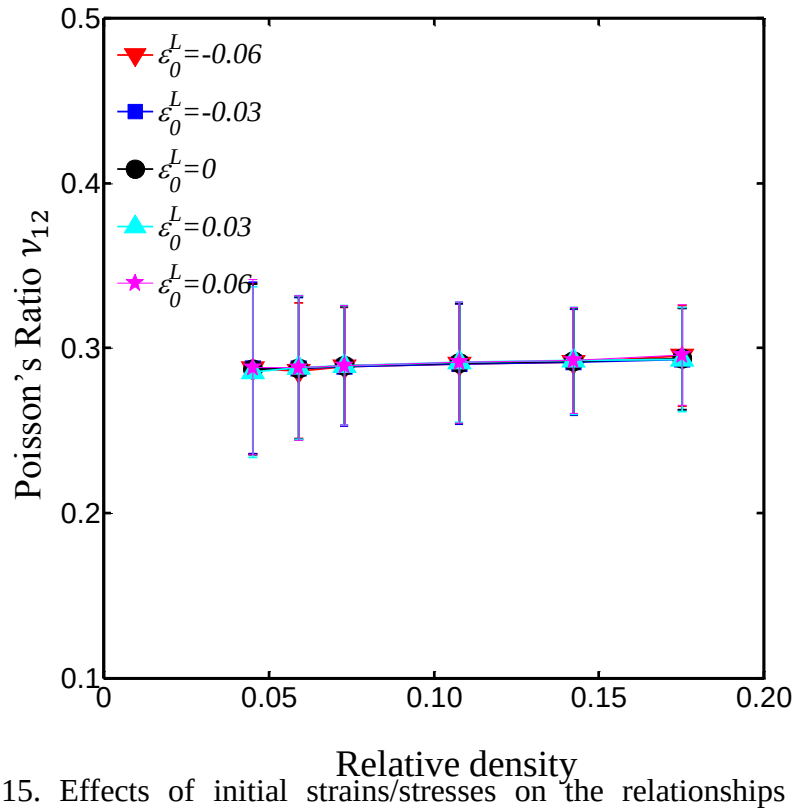

Figure 6.15. Effects of initial strains/stresses on the relationships between the Poisson's ratio $\boldsymbol{\nu_{12}}$ and relative density of stochastic fibrous networks at nano-meter scale.

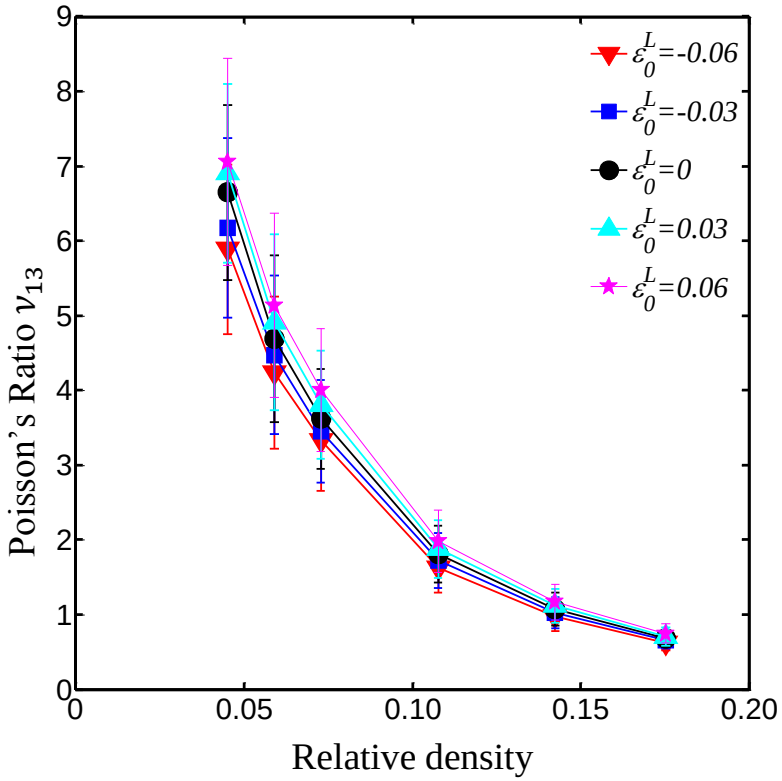

Figure 6.16. Effects of initial strains/stresses on the relationships between the Poisson's ratio $\boldsymbol{\nu_{13}}$ and relative density of stochastic fibrous networks at nano-meter scale.

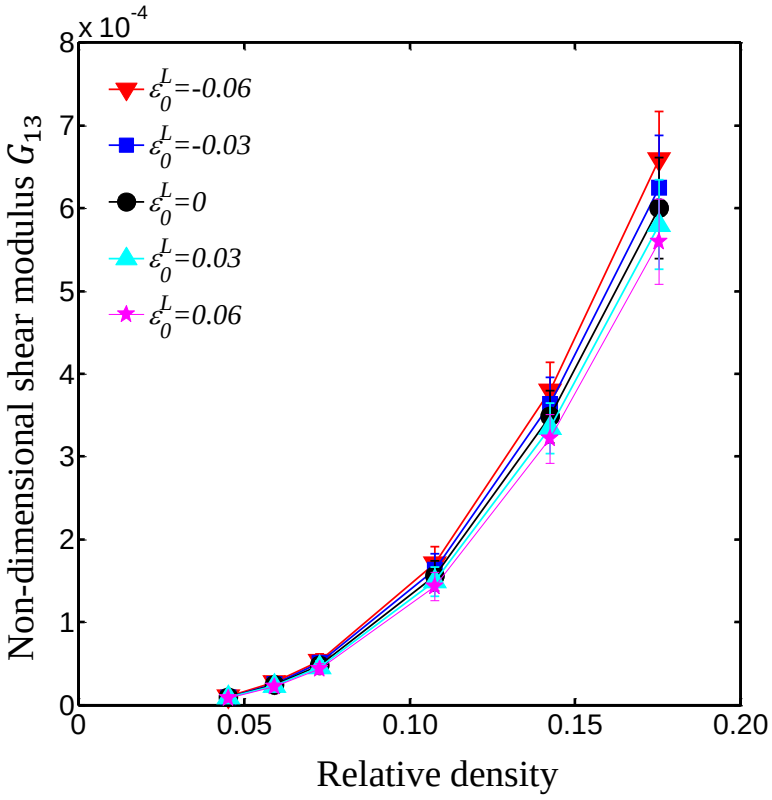

Figure 6.17. Effect of initial strains/stresses on the relationship between the non-dimensional shear modulus $\boldsymbol{G_{13}}$ and the relative density of nano-sized stochastic fibrous materials

6.3.3 Tunable geometrical properties of nano-sized stochastic fibrous structures

For nano-sized stochastic fibrous networks, the amplitude of the recoverable initial elastic strain can be controlled to vary over a range from -0.1 to 0.1 by application of an electric potential [101–105]. Experiments conducted by Weissmuller *et al* showed that the reversible strain of nanoporous Pt increases almost linearly with increasing potential[103]. When the effects of the initial strain are absent, the initial fibre diameter, the area of the void/cell in the x-y plane and the volume of the structure are assumed to be d_0, A_0, V_0, respectively. As the fibre is assumed to be isotropic, when the effects of initial strain ε_0^L are present, those geometrical parameters become

$$\frac{d_1}{d_0} = 1 + \varepsilon_0^R$$

$$\frac{A_1}{A_0} = (1 + \varepsilon_0^L)^2$$

$$\frac{V_1}{V_0} = (1 + \varepsilon_0^R)(1 + \varepsilon_0^L)^2 \tag{6.29}$$

Therefore, the geometrical properties of the nano-sized stochastic fibrous networks can be tuned and controlled.

6.4 **Discussions**

Finite element models of periodic random beams were developed to investigate the size-dependent elastic properties of micro- and nano-structured stochastic fibrous networks. The intrinsic material length scales l_m and l_n are introduced to predict the size-dependence at the micron and nano scales respectively. When the diameter of fibres in the structure is sufficiently large, compared to the intrinsic length scales, i.e., $l_m/d = 0$ or $l_n/d = 0$, the results reduce to those of the macro-sized counterparts.

The intrinsic length scale, l_m in the strain gradient plasticity is given by[80,88]

$$l_m = 3\beta^2(\frac{G}{\sigma_y})^2 b \tag{6.30}$$

where G is the shear modulus, σ_y is the yield strength, b is the magnitude of the Burger's vector and β is an empirical coefficient in the range of 0.2 - 0.5. The intrinsic material length scale, l_m carrying all the information of elasticity(G), plasticity(σ_y), and atomic nature of solids(b) varies from material to material. For typical metallic

materials, the magnitude of Burger's vector, b is in the order of 0.1nm, and $\frac{G}{\sigma_y}$ is in the order of 10^2. Thus, the intrinsic material length, l_m is in the order of microns. The length scale obtained from the micro-bending test of nickel is in the range of 3-5 μm[68]. If we take nickel fibrous structure, with relative density at 4% as an example, when the diameter of the fibre is about 3-5 μm(i.e., $l_m/d = 1$), the Young's modulus in the x direction is about three times of that of nickel fibrous structure with diameter at millimetre, and the Young's modulus in the z direction is more than nine times that of macro-sized nickel fibrous structures.

For nano-sized fibrous networks, Figure 6.13 and Figure 6.14 have suggested that the smaller the diameter of fibre, the larger would be the dimensionless Young's moduli. These results are consistent with the findings of nano-sized regular[122] and irregular honeycombs[126]. Wang *et al*[98] proposed that many properties at the nano-scale obey a simple scaling law. For the non-dimensional mechanical properties of homogeneous nano-structured materials, it is given by,

$$\frac{F(L)}{F(\infty)} = 1 + \alpha \frac{l_{in}}{L} \tag{6.31}$$

where $F(L)$ denotes the mechanical property at nano scale, L; $F(\infty)$ denotes the mechanical property of the bulk material, l_{in} is an intrinsic length scale related to the surface property. It should be noted that α could be different, even with the same effect of surface elasticity l_n/d, as the elasticity of nano-sized fibrous networks is dependent on the relative density. For instance, if we analyse the Young's modulus in the z direction with l_n/d=0.5, the coefficient from the scaling law $\alpha \approx 7$ when the relative density $\rho = 5.9\%$; and when $\rho = 17.5\%$, $\alpha \approx 6$. The simulation results indicate that the non-dimensional Young's modulus for nano-sized fibrous structure increases with

a rise in the relative density and a rise in l_n/d. However, the increase in the relative density suppresses, to a certain extent, the effect of surface elasticity, as the coefficient, α is decreasing. For nanostructures, as the surface-to-volume ratio is large, surface effects play a dominant role in the mechanical behaviour, when the structure dimension is small. The two main factors relevant in surface effects are surface elasticity and initial surface stress/strain. The former is size-dependent and increases with decreasing size of structure; the latter is size-sensitive and can be retained at different constant levels depending on the size, for example, by the application of an electrical potential. Figure 6.13 shows that the dimensionless Young's modulus in the x direction of the nano-sized stochastic fibrous network can be controlled, either to increase about 6%, or to reduce about 8%, when the initial strain is varied from -6% to 6%, respectively. The dimensionless Young's modulus in the z direction for nano-sized fibrous networks can be varied from 17% increment to 13% reduction, as shown in Figure 6.14. It should be noted that when the effect of surface elasticity is present ($l_n/d \neq 0$), the tunable range of the dimensionless Young's moduli remains almost the same as that when the effect of surface elasticity is absent, as was discussed above. Thus, if the applied initial strain is controlled to vary over the same range, the non-dimensional Young's modulus of the nano-sized fibrous structure can be scaled up or down, on the basis of the values obtained from the analysis in the presence of surface elasticity [122–126].

6.5 **Conclusion**

The effects of strain gradient at the micro-meter scale, and the effects of surface elasticity and initial stresses/strains at the nano-meter scale, are incorporated into all

the deformation mechanisms in the finite element simulations to predict the size-dependent behaviours of micro- and nano-sized stochastic fibrous structures. The relationships between all the five independent elastic constants and the relative density are obtained with the size effects taken into account. The relative density is controlled by changing the concentration of cross-linker in the three-dimensional random beam model developed in this study. The simulation results suggest that the Poisson ratio, ν_{12} is irrespective of the size of the fibres and the relative density of the fibrous networks, as well as the initial stresses/strains. By contrast, the Poisson's ratio, ν_{13} is sensitive to geometrical properties of the structure and the applied initial strains. For both micro- and nano-sized fibrous structures, the smaller the fibre diameter, the larger the non-dimensional Young's moduli and shear moduli; and the larger the relative density, the larger the non-dimensional Young's moduli and shear moduli. Generally speaking, the Young's modulus and shear modulus of a nano-sized stochastic fibrous structure are larger than their micro-sized counterparts. In addition, the elasticity of a nano-sized fibrous structure is not only size dependent, but also tunable and controllable, due to the initial stresses/strains. Moreover, when the effects of initial strain are present, the geometrical properties of the nano-sized stochastic fibrous networks can be tuned and controlled by adjusting the applied electric potential. Materials that can change their dimensions in response to an applied voltage can serve as actuators in various applications. The results obtained in this study could provide a guide in the design of MEMS and NEMS. Also, as the micro- and nano-sized stochastic fibrous networks are widely found in biomaterials, this study could give a good reference for scientists engaged in tissue engineering.

Chapter 7 Conclusions and further work

7.1 **Conclusions**

This thesis has revealed the mechanical properties of macro-sized, micro-sized and nano-sized fibrous structures by using a three-dimensional periodic beam model developed in this study by the author.

A novel way to deal with the connections between fibres by inserting additional beams has been introduced. By inserting the beam elements between the fibres the connections can be identified as elastic cross-linkers. It has shown that with the elastic cross-linkers included in the network, the stiffness of the material is 3-4 times lower than the network with rigid connections.

Relative density is a key parameter to elucidate the mechanical properties of porous materials. The relative density of the beam model developed in this thesis can be adjusted by changing the concentration of cross-linkers, the aspect ratio of the fibre and the coefficient of overlap. Finite element models of cytoskeletal networks have been developed to investigate the effects of relative density on all the independent elastic constants. The results show that the model is transversely isotropic in the x-y plane, whose normal direction is the thickness direction. The relationship $G_{12}^{*} = 0.5E_{x}^{*}/(1+\nu_{12})$ holds for filamentous structures with different relative densities. The non-dimensional Young's moduli and shear moduli increase with increasing relative density. The Poisson's ratio ν_{12} of the filamentous structure keeps constant at around 0.3 with varying degrees of overlap and relative densities, and is irrespective of properties of the solid material. By dimensional analysis, the relationships between

the Young's moduli and the relative density of the filamentous structure have been revealed. The analytical models show that Young's modulus in the x direction of the filamentous structure takes the form, $E_x/E = \alpha\rho^3$, and in the z direction, $E_z/E = \beta\rho^5$, which suggests that the strut bending is the dominant deformation mechanism for the stochastic fibrous network. The results from the analytical models are broadly consistent with the FE simulations.

Interestingly, the stochastic model developed in this study is pressure independent, as the response under tension is the same as that under compression. Based on the total strain energy density, the scalar measures of characteristic stress and strain were applied to reveal the yielding of the stochastic fibrous material. The elastic regimes of characteristic stress-strain curves collapse along a single master line irrespective of the loading path. A critical characteristic strain has been adopted to determine the yield strength of the stochastic fibrous material and it indicates that with different critical values, the yield surface grows or shrinks in a self-similar manner. The yield function can be fully calibrated in terms of the uniaxial tension (or compression) response, in the x or z direction, rather than complex multiaxial loading responses. By changing the concentration of cross-linkers in the model, the effect of strength anisotropy can be adjusted in terms of the tilt of the yield surface in the plane of anisotropy. The relative density shows a linear relationship with the concentration of cross- linkers. Thus, the dependence of the stiffness and strength of stochastic fibrous material on relative density is the same as that on concentration of cross-linkers. In addition, it has been showed that the dimensions of the inserted beams can also affect the stiffness and strength of the stochastic fibrous material, especially in the thickness direction. The effect of relative density on uniaxial yield strength of stochastic fibrous material

shows quadratic function in the x direction and a cubic function in the z direction, which have strong agreement with the dimensional analyses.

When the dimensions of the fibrous structures are reduced to the micro- or nano-scale, the stiffness or rigidity is much different from that of their macro-sized counterparts. The strain gradient effects at the micro-meter scale, and the surface elasticity and initial stress effects at the nano-meter scale have been incorporated into the deformation mechanisms of fibrous materials. Since there is no type of elements that could directly incorporate the size-dependent effects into the simulations in commercial finite element software, the equivalent Young's modulus, Poisson's ratio and cross-sectional size of the beam elements have been worked out. The intrinsic material length scale parameters, l_m and l_n were introduced to predict the size-dependence at micron and nano scales, respectively. For both of the micro- and nano-sized fibrous structures, the smaller the diameter, the larger the non-dimensional Young's moduli and shear moduli; and the larger the relative density, the larger the non-dimensional Young's moduli and shear moduli. When the diameter of the fibres in the structure is sufficiently large, compared to the intrinsic length scales, i.e., $l_m/d = 0$ or $l_n/d = 0$, the results reduce to those of the macro-sized counterparts. Generally speaking, the Young's modulus and shear modulus of nano-sized stochastic fibrous structures are larger than their micro-sized counterparts. In addition, the elasticity of nano-sized fibrous structures is not only size dependent, but also tunable and controllable, due to the initial stresses/strains. The results show that the dimensionless Young's modulus in the x direction of the nano-sized stochastic fibrous networks can be controlled, either to increase about 6%, or to reduce about 8%,when the initial strain is controlled to vary from -6% to 6%, respectively. The dimensionless Young's modulus in the z direction for nano-sized fibrous networks can be controlled

to vary from 17% increment to 13% reduction. Moreover, when the effects of initial strain are present, the geometrical properties of the nano-sized stochastic fibrous networks can be tuned and controlled by adjusting the applied electric potential. The size-dependent effects investigated in this thesis could provide good reference points for scientists in tissue engineering and serve as a guide in the design of MEMS and NEMS.

7.2 **Further work**

A three-dimensional random beam model has been developed to represent stochastic fibrous materials. This thesis has covered the geometrical properties, elasticity and plasticity, as well as size-dependent effects of a stochastic fibrous network, but there are a number of limitations and still more research to do in the future.

Firstly, as the attention is focused on the zero-frequency, or static linearly elastic properties of fibrous structures, the complexities of the network may be ignored, especially when it is applied to biomaterials, for instance, the cytoskeleton.

Secondly, in the beam model, all the fibres or filaments are assumed to be the same material. The fibrous structure made of one single material may not be suitable in some cases.

Thirdly, one fibre does not have to connect with another in the cross-linked network. The overlap coefficient could be larger than 1, i.e., the distance between two intersected fibres could be larger than the sum of their radii.

Last, for some stochastic fibrous materials, they have preferred orientations such as cornea.

All of the unexplored researches mentioned above could be done in further simulations. In addition, it will be interesting and productive to compare the data from experiments with the simulation results shown in this thesis.

References

[1] Zhu HX, Hobdell JR, Windle AH. Effects of cell irregularity on the elastic properties of open-cell foams. Acta Mater 2000;48:4893–900.

[2] Zhu HX, Hobdell JR, Windle AH. Effects of cell irregularity on the elastic properties of 2D Voronoi honeycombs. J Mech Phys Solids 2001;49:857–70.

[3] Zhu HX, Knott JF, Mills NJ. Analysis of the elastic properties of open-cell foams with tetrakaidecahedral cells. J Mech Phys Solids 1997;45:319–43. doi:10.1016/S0022-5096(96)00090-7.

[4] Gibson LJ, Ashby MF. Cellular solids: structure and properties. Cambridge university press; 1997.

[5] Banhart J. Manufacture, characterisation and application of cellular metals and metal foams. Prog Mater Sci 2001;46:559–632.

[6] Silva MJ, Gibson LJ. The effects of non-periodic microstructure and defects on the compressive strength of two-dimensional cellular solids. Int J Mech Sci 1997;39:549–63.

[7] Pedersen JA, Swartz MA. Mechanobiology in the third dimension. Ann Biomed Eng 2005;33:1469–90.

[8] Fuchs E, Cleveland DW. A structural scaffolding of intermediate filaments in health and disease. Science (80-) 1998;279:514–9.

[9] Xi Z, Zhu J, Tang H, Ao Q, Zhi H, Wang J, et al. Progress of application researches of porous fiber metals. Materials (Basel) 2011;4:816–24.

[10] Jin MZ, Chen CQ, Lu TJ. The mechanical behavior of porous metal fiber sintered sheets. J Mech Phys Solids 2013;61:161–74.

[11] Zhang Y, Venugopal JR, El-Turki A, Ramakrishna S, Su B, Lim CT. Electrospun biomimetic nanocomposite nanofibers of hydroxyapatite/chitosan for bone tissue engineering. Biomaterials 2008;29:4314–22.

[12] Sill TJ, von Recum HA. Electrospinning: applications in drug delivery and tissue engineering. Biomaterials 2008;29:1989–2006.

[13] Wilhelm J, Frey E. Elasticity of stiff polymer networks. Phys Rev Lett 2003;91:108103.

[14] Chen C, Lu TJ, Fleck NA. Effect of imperfections on the yielding of two-dimensional foams. J Mech Phys Solids 1999;47:2235–72.

[15] Youssef S, Maire E, Gaertner R. Finite element modelling of the actual structure of cellular materials determined by X-ray tomography. Acta Mater

2005;53:719–30.

[16] Redenbach C. Microstructure models for cellular materials. Comput Mater Sci 2009;44:1397–407.

[17] Zhao TF, Jin MZ, Chen CQ. A phenomenological elastoplastic model for porous metal fiber sintered sheets. Mater Sci Eng A 2013;582:188–93.

[18] Zhao TF, Chen CQ. The shear properties and deformation mechanisms of porous metal fiber sintered sheets. Mech Mater 2014;70:33–40.

[19] Symons DD, Fleck NA. The imperfection sensitivity of isotropic two-dimensional elastic lattices. J Appl Mech 2008;75:51011.

[20] Markaki AE, Clyne TW. Mechanics of thin ultra-light stainless steel sandwich sheet material: Part I. Stiffness. Acta Mater 2003;51:1341–50.

[21] Sastry AM, Wang C-W, Berhan L. Deformation and failure in stochastic fibrous networks: scale, dimension and application. Key Eng. Mater., vol. 200, 2001, p. 229.

[22] Wang CW, Berhan L, Sastry AM. Structure, Mechanics and Failure of Stochastic Fibrous Networks: Part1—Microscale Consideration. ASME J Eng Mater Technol 2000;122:450–9.

[23] Wang CW, Sastry AM. Structure, mechanics and failure of stochastic fibrous networks: Part II—Network simulations and application. J Eng Mater Technol 2000;122:460–8.

[24] Qiao J, Xi Z, Tang H, Wang J, Zhu J. Influence of porosity on quasi-static compressive properties of porous metal media fabricated by stainless steel fibers. Mater Des 2009;30:2737–40.

[25] Picu RC. Mechanics of random fiber networks—a review. Soft Matter 2011;7:6768–85.

[26] Clyne TW, Markaki AE, Tan JC. Mechanical and magnetic properties of metal fibre networks, with and without a polymeric matrix. Compos Sci Technol 2005;65:2492–9.

[27] Markaki AE, Clyne TW. Magneto-mechanical actuation of bonded ferromagnetic fibre arrays. Acta Mater 2005;53:877–89.

[28] Tsarouchas D, Markaki AE. Extraction of fibre network architecture by X-ray tomography and prediction of elastic properties using an affine analytical model. Acta Mater 2011;59:6989–7002.

[29] Chung JW, De Hosson JTM. Effects of network morphology on the failure stress of highly porous media. Phys Rev B 2002;66:64206.

[30] Markaki AE, Clyne TW. Magneto-mechanical stimulation of bone growth in a bonded array of ferromagnetic fibres. Biomaterials 2004;25:4805–15.

[31] Markaki AE, Clyne TW. Mechanics of thin ultra-light stainless steel sandwich sheet material: Part II. Resistance to delamination. Acta Mater 2003;51:1351–7.

[32] Baruchel J, Buffiere J-Y, Maire E. X-ray tomography in material science 2000.

[33] Zhu HX, Thorpe SM, Windle AH. The geometrical properties of irregular two-dimensional Voronoi tessellations. Philos Mag A 2001;81:2765–83.

[34] Zhu HX, Thorpe SM, Windle AH. The effect of cell irregularity on the high strain compression of 2D Voronoi honeycombs. Int J Solids Struct 2006;43:1061–78.

[35] Liu Q, Lu Z, Hu Z, Li J. Finite element analysis on tensile behaviour of 3D random fibrous materials: Model description and meso-level approach. Mater Sci Eng A 2013;587:36–45.

[36] Liu Q, Lu Z, Zhu M, Yang Z, Hu Z, Li J. Experimental and FEM analysis of the compressive behavior of 3D random fibrous materials with bonded networks. J Mater Sci 2014;49:1386–98.

[37] Sampson WW. Modelling Stochastic Fibrous Materials with Mathematica. Springer Science & Business Media; 2008.

[38] Hill R. Elastic properties of reinforced solids: some theoretical principles. J Mech Phys Solids 1963;11:357–72.

[39] Silva MJ. The effect of Non-periodic microstructure on the elastic properties of two-dimensional cellular solids. Int J Mech Sci 1995.

[40] Triantafyllidis N, Schraad MW. Onset of failure in aluminum honeycombs under general in-plane loading. J Mech Phys Solids 1998;46:1089–124.

[41] Alkhader M, Vural M. An energy-based anisotropic yield criterion for cellular solids and validation by biaxial FE simulations. J Mech Phys Solids 2009;57:871–90.

[42] Ayyagari RS, Vural M. Multiaxial yield surface of transversely isotropic foams: Part I—Modeling. J Mech Phys Solids 2015;74:49–67.

[43] Deshpande VS, Fleck NA. Isotropic constitutive models for metallic foams. J Mech Phys Solids 2000;48:1253–83.

[44] Alberts B, Bray D, Lewis J, Raff M, Roberts K, Watson JD. Molecular biology of the cell, 1994. Garland, New York 1994:139–94.

[45] Orr AW, Helmke BP, Blackman BR, Schwartz MA. Mechanisms of

mechanotransduction. Dev Cell 2006;10:11–20.

[46] Huang S, Ingber DE. The structural and mechanical complexity of cell-growth control. Nat Cell Biol 1999;1:E131--E138.

[47] Wang N, Butler JP, Ingber DE. Mechanotransduction across the cell surface and through the cytoskeleton. Science (80-) 1993;260:1124–7.

[48] Janmey PA, Euteneuer U, Traub P, Schliwa M. Viscoelastic properties of vimentin compared with other filamentous biopolymer networks. J Cell Biol 1991;113:155–60.

[49] Hirokawa N, Glicksman MA, Willard MB. Organization of mammalian neurofilament polypeptides within the neuronal cytoskeleton. J Cell Biol 1984;98:1523–36.

[50] Panorchan P, Lee JSH, Daniels BR, Kole TP, Tseng Y, Wirtz D. Probing cellular mechanical responses to stimuli using ballistic intracellular nanorheology. Methods Cell Biol 2007;83:113–40.

[51] Radmacher M. Studying the mechanics of cellular processes by atomic force microscopy. Methods Cell Biol 2007;83:347–72.

[52] Discher DE, Janmey P, Wang Y. Tissue cells feel and respond to the stiffness of their substrate. Science (80-) 2005;310:1139–43.

[53] Hinner B, Tempel M, Sackmann E, Kroy K, Frey E. Entanglement, elasticity, and viscous relaxation of actin solutions. Phys Rev Lett 1998;81:2614.

[54] Gardel ML, Kasza KE, Brangwynne CP, Liu J, Weitz DA. Mechanical response of cytoskeletal networks. Methods Cell Biol 2008;89:487–519.

[55] Gardel ML, Nakamura F, Hartwig JH, Crocker JC, Stossel TP, Weitz DA. Prestressed F-actin networks cross-linked by hinged filamins replicate mechanical properties of cells. Proc Natl Acad Sci U S A 2006;103:1762–7.

[56] Xu J, Tseng Y, Wirtz D. Strain Hardening of actin filament networks regulation by the dynamic cross-linking protein α-actinin. J Biol Chem 2000;275:35886–92.

[57] Gardel ML, Shin JH, MacKintosh FC, Mahadevan L, Matsudaira P, Weitz DA. Elastic behavior of cross-linked and bundled actin networks. Science (80-) 2004;304:1301–5.

[58] Chaudhuri O, Parekh SH, Fletcher DA. Reversible stress softening of actin networks. Nature 2007;445:295–8.

[59] Hynes RO. The extracellular matrix: not just pretty fibrils. Science (80-) 2009;326:1216–9.

[60] Baker BM, Trappmann B, Wang WY, Sakar MS, Kim IL, Shenoy VB, et al. Cell-mediated fibre recruitment drives extracellular matrix mechanosensing in engineered fibrillar microenvironments. Nat Mater 2015.

[61] Sun Y, Chen CS, Fu J. Forcing stem cells to behave: a biophysical perspective of the cellular microenvironment. Annu Rev Biophys 2012;41:519.

[62] Trappmann B, Gautrot JE, Connelly JT, Strange DGT, Li Y, Oyen ML, et al. Extracellular-matrix tethering regulates stem-cell fate. Nat Mater 2012;11:642–9.

[63] Collet J-P, Shuman H, Ledger RE, Lee S, Weisel JW. The elasticity of an individual fibrin fiber in a clot. Proc Natl Acad Sci U S A 2005;102:9133–7.

[64] Hutmacher DW. Scaffolds in tissue engineering bone and cartilage. Biomaterials 2000;21:2529–43.

[65] Girard MJA, Suh J-KF, Bottlang M, Burgoyne CF, Downs JC. Scleral biomechanics in the aging monkey eye. Invest Ophthalmol Vis Sci 2009;50:5226–37.

[66] Tanaka Y, Baba K, Duncan TJ, Kubota A, Asahi T, Quantock AJ, et al. Transparent, tough collagen laminates prepared by oriented flow casting, multi-cyclic vitrification and chemical cross-linking. Biomaterials 2011;32:3358–66.

[67] Fleck NA, Muller GM, Ashby MF, Hutchinson JW. Strain gradient plasticity: theory and experiment. Acta Metall Mater 1994;42:475–87.

[68] Stölken JS, Evans AG. A microbend test method for measuring the plasticity length scale. Acta Mater 1998;46:5109–15.

[69] Ma Q, Clarke DR. Size dependent hardness of silver single crystals. J Mater Res 1995;10:853–63.

[70] Lam DCC, Chong A. Indentation model and strain gradient plasticity law for glassy polymers. J Mater Res 1999;14:3784–8.

[71] Chong A, Lam DCC. Strain gradient plasticity effect in indentation hardness of polymers. J Mater Res 1999;14:4103–10.

[72] Toupin RA. Elastic materials with couple-stresses. Arch Ration Mech Anal 1962;11:385–414.

[73] Mindlin RD, Tiersten HF. Effects of couple-stresses in linear elasticity. Arch Ration Mech Anal 1962;11:415–48.

[74] Koiter WT. Couple-stresses in the theory of elasticity, I & II 1969.

[75] Mindlin RD. Micro-structure in linear elasticity. Arch Ration Mech Anal 1964;16:51–78.

[76] Toupin RA. Theories of elasticity with couple-stress. Arch Ration Mech Anal 1964;17:85–112.

[77] Yang F, Chong ACM, Lam DCC, Tong P. Couple stress based strain gradient theory for elasticity. Int J Solids Struct 2002;39:2731–43.

[78] Cosserat E, Cosserat F. Th{é}orie des corps d{é}formables. Paris 1909;3:17–29.

[79] Fleck NA, Hutchinson JW. A phenomenological theory for strain gradient effects in plasticity. J Mech Phys Solids 1993;41:1825–57.

[80] Nix WD, Gao H. Indentation size effects in crystalline materials: a law for strain gradient plasticity. J Mech Phys Solids 1998;46:411–25.

[81] Huang Y, Qu S, Hwang KC, Li M, Gao H. A conventional theory of mechanism-based strain gradient plasticity. Int J Plast 2004;20:753–82.

[82] Han C-S, Gao H, Huang Y, Nix WD. Mechanism-based strain gradient crystal plasticity—I. Theory. J Mech Phys Solids 2005;53:1188–203.

[83] Gao H, Huang Y, Nix WD, Hutchinson JW. Mechanism-based strain gradient plasticity—I. Theory. J Mech Phys Solids 1999;47:1239–63.

[84] Ashby MF. The deformation of plastically non-homogeneous materials. Philos Mag 1970;21:399–424.

[85] Ashby MF. Deformation of Plastically Non-Homogeneous Alloys. Strength Methods Crystals, 1971, 137-192 1971.

[86] Nye JF. Some geometrical relations in dislocated crystals. Acta Metall 1953;1:153–62.

[87] Basinski SJ, Basinski ZS. The nature of the cold worked state. Recrystalization, Grain Growth, Textures, Pap. Present. a Semin. Am. Soc. Met. Met. Park. Ohio, USA, 1966.

[88] Hutchinson JW. Plasticity at the micron scale. Int J Solids Struct 2000;37:225–38.

[89] Miller RE, Shenoy VB. Size-dependent elastic properties of nanosized structural elements. Nanotechnology 2000;11:139.

[90] Cuenot S, Frétigny C, Demoustier-Champagne S, Nysten B. Surface tension effect on the mechanical properties of nanomaterials measured by atomic force microscopy. Phys Rev B 2004;69:165410.

[91] Shenoy VB. Size-dependent rigidities of nanosized torsional elements. Int J Solids Struct 2002;39:4039–52.

[92] Biener J, Hodge AM, Hayes JR, Volkert CA, Zepeda-Ruiz LA, Hamza A V, et

al. Size effects on the mechanical behavior of nanoporous Au. Nano Lett 2006;6:2379–82.

[93] Zhu HX. The effects of surface and initial stresses on the bending stiffness of nanowires. Nanotechnology 2008;19:405703.

[94] Zhu HX, Karihaloo BL. Size-dependent bending of thin metallic films. Int J Plast 2008;24:991–1007.

[95] Tersoff J. Empirical interatomic potential for silicon with improved elastic properties. Phys Rev B 1988;38:9902.

[96] Liang H, Upmanyu M, Huang H. Size-dependent elasticity of nanowires: nonlinear effects. Phys Rev B 2005;71:241403.

[97] Zhang P, Huang Y, Geubelle PH, Klein PA, Hwang KC. The elastic modulus of single-wall carbon nanotubes: a continuum analysis incorporating interatomic potentials. Int J Solids Struct 2002;39:3893–906.

[98] Wang J, Duan HL, Huang ZP, Karihaloo BL. A scaling law for properties of nano-structured materials. Proc. R. Soc. London A Math. Phys. Eng. Sci., vol. 462, 2006, p. 1355–63.

[99] Streitz FH, Cammarata RC, Sieradzki K. Surface-stress effects on elastic properties. I. Thin metal films. Phys Rev B 1994;49:10699.

[100] Duan HL, Wang J, Huang ZP, Karihaloo BL. Size-dependent effective elastic constants of solids containing nano-inhomogeneities with interface stress. J Mech Phys Solids 2005;53:1574–96.

[101] Biener J, Wittstock A, Zepeda-Ruiz LA, Biener MM, Zielasek V, Kramer D, et al. Surface-chemistry-driven actuation in nanoporous gold. Nat Mater 2009;8:47–51.

[102] Kramer D, Viswanath RN, Weissmüller J. Surface-stress induced macroscopic bending of nanoporous gold cantilevers. Nano Lett 2004;4:793–6.

[103] Weissmüller J, Viswanath RN, Kramer D, Zimmer P, Würschum R, Gleiter H. Charge-induced reversible strain in a metal. Science (80-) 2003;300:312–5.

[104] Haiss W, Nichols RJ, Sass JK, Charle KP. Linear correlation between surface stress and surface charge in anion adsorption on Au (111). J Electroanal Chem 1998;452:199–202.

[105] Raiteri R, Butt H-J. Measuring electrochemically induced surface stress with an atomic force microscope. J Phys Chem 1995;99:15728–32.

[106] Viswanath RN, Kramer D, Weissmüller J. Variation of the surface stress-charge coefficient of platinum with electrolyte concentration. Langmuir 2005;21:4604–9.

[107] Cammarata RC. Surface and interface stress effects in thin films. Prog Surf Sci 1994;46:1–38.

[108] Zhu H, Wang J, Karihaloo B. Effects of surface and initial stresses on the bending stiffness of trilayer plates and nanofilms. J Mech Mater Struct 2009;4:589–604.

[109] Crandall SH, Lardner TJ, Archer RR, Cook NH, Dahl NC. An introduction to the mechanics of solids 1978.

[110] Stricker J, Falzone T, Gardel ML. Mechanics of the F-actin cytoskeleton. J Biomech 2010;43:9–14.

[111] Onck PR, Koeman T, Van Dillen T, der Giessen E. Alternative explanation of stiffening in cross-linked semiflexible networks. Phys Rev Lett 2005;95:178102.

[112] Head DA, Levine AJ, MacKintosh FC. Deformation of cross-linked semiflexible polymer networks. Phys Rev Lett 2003;91:108102.

[113] Lieleg O, Bausch AR. Cross-linker unbinding and self-similarity in bundled cytoskeletal networks. Phys Rev Lett 2007;99:158105.

[114] Conti E, MacKintosh FC. Cross-linked networks of stiff filaments exhibit negative normal stress. Phys Rev Lett 2009;102:88102.

[115] Janmey PA, McCormick ME, Rammensee S, Leight JL, Georges PC, MacKintosh FC. Negative normal stress in semiflexible biopolymer gels. Nat Mater 2006;6:48–51.

[116] Tharmann R, Claessens M, Bausch AR. Viscoelasticity of isotropically cross-linked actin networks. Phys Rev Lett 2007;98:88103.

[117] Limozin L, Sackmann E. Polymorphism of cross-linked actin networks in giant vesicles. Phys Rev Lett 2002;89:168103.

[118] Grishanov S, Tausif M, Russell SJ. Characterisation of fibre entanglement in nonwoven fabrics based on knot theory. Compos Sci Technol 2012;72:1331–7.

[119] Won Y, Gao Y, Panzer MA, Xiang R, Maruyama S, Kenny TW, et al. Zipping, entanglement, and the elastic modulus of aligned single-walled carbon nanotube films. Proc Natl Acad Sci 2013;110:20426–30.

[120] Chang L, Kious T, Yorgancioglu M, Keller D, Pfeiffer J. Cytoskeleton of living, unstained cells imaged by scanning force microscopy. Biophys J 1993;64:1282–6.

[121] Sukhoveyev S. Ultra high aspect-ratio MEMS and NEMS on basis of fibrous composite technology. Microsyst Technol 2008;14:1099–110.

[122] Zhu HX. Size-dependent elastic properties of micro-and nano-honeycombs. J Mech Phys Solids 2010;58:696–709.

[123] Zhu H, Wang ZB, Fan TX, Zhang D, others. Tunable bending stiffness, buckling force, and natural frequency of nanowires and nanoplates. World J Nano Sci Eng 2012;2:161.

[124] Zhu HX, Yan LB, Zhang R, Qiu XM. Size-dependent and tunable elastic properties of hierarchical honeycombs with regular square and equilateral triangular cells. Acta Mater 2012;60:4927–39.

[125] Zhu HX, Wang ZB. Size-dependent and tunable elastic and geometric properties of hierarchical nano-porous materials. Sci Adv Mater 2013;5:677–86.

[126] Zhu HX, Zhang HC, You JF, Kennedy D, Wang ZB, Fan TX, et al. The elastic and geometrical properties of micro-and nano-structured hierarchical random irregular honeycombs. J Mater Sci 2014;49:5690–702.

Publications

Journal papers

Ma, Y. H., Zhu, H. X., Su, B., Hu, G. K., Perks, R. The elasto-plastic behaviour of a three-dimensional stochastic fibrous network with cross-linking, under review (JMPS).

Ma, Y. H., Zhu, H. X., Su, B., Liu, X. N., Hu, G. K. Mechanical properties of cytosketetal networks based on a 3-D stochastic filament model with FEA, in preparation.

Ma, Y. H., Zhu, H. X., Su, B. Size-dependent and tunable mechanical properties of micro- and nano-sized stochastic fibrous structures, in preparation.

Conference papers/proceedings

Zhu, H. X., Ma, Y. H., Su, B. 2014. Designing nanofibrous materials for bioscience and medical applications. Presented at: *7th World Congress of Biomechanics*, Boston, USA, 6-11 July 2014.

Ma, Y. H., Zhu, H. X., Su, B. 2014. Mechanical properties of cytoskeletal networks based on 3D stochastic fibre model with FEM. Presented at: *CITER Annual Scientific Meeting 2014: Basic Science to Regenerative Medicine*, Llanelli, Carmarthenshire, 17-18 September 2014.

Ma, Y. H., Zhu, H. X. 2015. The mechanical behaviour of 3D stochastic fibrous materials. Presented at: *4th International Conference on Material Modeling*, Berkeley, CA, 27- 29 May 2015

Ma, Y. H., Zhu, H. X., Su, B. 2016. Size-dependent and tunable mechanical properties of micro- and nano-sized stochastic fibrous structures. Presented at: *24th International Congress of Theoretical and Applied Mechanics, Montreal, Canada, 21-26 August 2016.*